University of Southampton
Faculty of Engineering and the Environment

Development and characterisation of a lightweight alkaline aluminium-air cell

by

Derek Egan

Thesis for the degree of Doctor of Philosophy

November 2015

UNIVERSITY OF SOUTHAMPTON

ABSTRACT

Faculty of Engineering and the Environment

Electrochemical Engineering

Doctor of Philosophy

DEVELOPMENT AND CHARACTERISATION OF A LIGHTWEIGHT, ALKALINE ALUMINIUM-AIR CELL

by Derek Egan

This experimental study examined the development of a lightweight aluminium-air cell. The novelty of this study was the characterisation of the behaviour of the lightweight aluminium-air cell, depending on the choice of aluminium anode and air-cathode. Development of the prototype aluminium-air cell involved three areas of study. For the first two high purity aluminium alloys, Al/0.5 Mg/0.07 Sn and Al/0.4 Mg/0.07 Sn/0.05 Ga, were evaluated as anodes in a half-cell in 4 mol dm^{-3} NaOH at 22 °C and 60 °C and compared against 99.999 %wt aluminium. Alloys were pre-treated by solution heat treating in a furnace at 600 °C for 8 hours followed by a water quench. Corrosion rates were quantified at open-circuit and under galvanostatic discharge via a hydrogen collection method. For the second method of study, the electrochemistry of a $LaCaCo_3$/$LaCaMnO_3$ air-electrode, known as KTH, supplied by a project collaborator, was compared against seven commercial gas diffusion electrodes. The catalysts on the commercial electrodes include Pt, MnO_x, Ag_2O and Co-based. Air-electrodes were compared structurally using scanning electron microscopy, mercury intrusion porosimetry and pycnometry. The KTH electrode outperformed the others with a limiting current density for oxygen reduction of −463 mA cm^{-2} at −0.49 V *vs.* Hg/HgO. In the final area of study three prototype aluminium-air cells were investigated with the third one being selected as the final design. Cell characterisation involved measurement of electrode potentials and cell temperature during variable loading and galvanostatic discharge experiments, and assessing their inter-relationship. The best performing prototype cell with a solution heat treated Al/Mg/Sn anode and KTH air-electrode had a peak power density of 174 mW cm^{-2} at 208 mA cm^{-2}. Under galvanostatic discharge at 100 mA cm^{-2} over an hour duration, this cell had a specific power capability of 62 W kg^{-1} and a specific energy of 66 W h kg^{-1}.

Table of contents

List of figures

Figure 4.4: The effect of refreshing the electrolyte on the open-circuit potential of the same 99.999 % Al sample in 4 mol dm^{-3} NaOH. ○ Initial measurement, ● after refilling with fresh electrolyte. For the initial measurement, the aluminium was mechanically ground by SiC paper, grit P4000. After measuring its open-circuit potential for 3600s the electrolyte was refreshed. Electrode area: 3.5 cm^2.

Figure 4.5: Effect of electrolyte type on the anodic polarisation of 99.999 % aluminium. Sweep rate of 1 mV s^{-1}. The electrodes were held at open-circuit for at least one hour prior to sweeping the potential. Platinum mesh counter electrode. Electrolyte temperature: 22 °C. ● 7 mol dm^{-3} KOH, ○ 4 mol dm^{-3} NaOH.

Figure 4.6: Effect of electrolyte purity on the open-circuit potential of 99.999 % Al in 4 mol dm^{-3} NaOH using two different experimental half-cells. ○ 3-electrode cell with analytical reagent NaOH, ● 3-electrode cell with laboratory reagent NaOH, △ beaker cell with analytical reagent NaOH, ▲ beaker cell with laboratory reagent NaOH. Analytical reagent NaOH had a purity of 98.95 %wt, whereas the laboratory reagent NaOH had a purity of 97 %wt.

Figure 4.7: SEM image showing the effect of electrolyte purity on the surface of 99.999 % aluminium at open-circuit. Electrolyte: 4 mol dm^{-3} NaOH at 22 °C. Sample held at open-circuit for 4800 s in a laboratory reagent of > 97 %wt purity. Electrode area: 3.5 cm^2.

Figure 4.8: Results from galvanostatic tests on 99.999 %wt aluminium in 4 mol dm^{-3} NaOH. (a) Variation of electrode potential *vs.* time at different anodic current densities. (b) Hydrogen volume *vs.* time at different anodic current densities. Electrode area: 3.5 cm^2. Electrolyte temperature: 22 °C. Platinum mesh counter electrode.

Figure 4.9: Dissolution behaviour of 99.999 % Al in 4 mol dm^{-3} NaOH. (a) ○ Polarisation curve constructed from galvanostatic discharge tests over the range, 0 to 80 mA cm^{-2}. —— Linear sweep voltammogram for pure aluminium at 1 mV s^{-1} (b) Corrosion current density determined by hydrogen collection, and discharge efficiency. Electrolyte temperature: 22 °C. Electrode area: 3.5 cm^2.

Figure 4.10: Equilibrium phase diagrams for (a) Al/Sn and (b) Al/Mg binary alloys. Dotted lines indicate how the solubility limits at 600 °C are read from the graphs.

Figure 4.11: Effect of heat treatment temperature on the uniformity of the composition of the Al/Mg/Sn alloy. (a) BEI of homogenised sample, solution heat treated at 600 °C for 8 hours, followed by a water quench. The identified zirconium particle was a contaminant from polishing. (b) BEI of un-homogenised sample, heat treated at 500 °C for 6 hours. Elements of higher atomic mass than the matrix show up as white particles. (c) EDX profile for point A_1. Points A_2 and A_3 were of similar composition. (d) EDX profile for point B.

Figure 4.12: The importance of solution heat treatment on the open-circuit potential and polarisation of Al/Mg/Sn alloy. (a) Open-circuit potential, (b) Polarisation curves at 1 mV s^{-1}. Electrolyte: 4 mol dm^{-3} NaOH at 22 °C. △ Al/0.5 Mg/0.07 Sn un-homogenised, ● Al/0.5 Mg/0.07 Sn homogenised at 600 °C for 8 hours, ○ 99.999 %wt Al, ★ 99.99 % Sn. Electrode area: 3.5 cm^2. Platinum mesh counter electrode.

Figure 4.13: Effect of initial electrode potential on the polarisation of the homogenised Al/Mg/Sn alloy. ····· Initial potential was −1.7 V *vs.* Hg/HgO, ——— initial potential was −2.0 V *vs.* Hg/HgO. Electrolyte: 4 mol dm^{-3} NaOH at 22 °C. Sweep rate: 1 mV s^{-1}.

Figure 4.14: Difficulty in obtaining a solid solution with the Al/Mg/Sn/Ga alloy. (a) Back-scatter electron image (b) EDX profile of the particle labelled A. Solution heat treatment for 8 hours at 600 °C followed by a water quench. 15 kV accelerating voltage.

Figure 4.15: Effect of distance of reference electrode on the anodic linear sweep of the Al/Mg/Sn alloy. ● Tip of the Luggin capillary 2 mm from the Al/Mg/Sn surface. ○ Reference electrode 5 cm away from the Al/Mg/Sn surface. Alloy was solution heat treated. Electrolyte of 4 mol dm^{-3} at 22 °C.

Figure 4.16: Variation of open-circuit potential and hydrogen volume for ●, ■ Al/Mg/Sn and ○, □ 99.999 %wt Al. Electrolyte: 4 mol dm^{-3} NaOH at 22 °C. Electrode area: 3.5 cm^2. Platinum mesh counter electrode.

Figure 4.17: Polarisation resistance of the Al/Mg/Sn alloy compared to that of 99.999 %wt aluminium. Electrolyte: 4 mol dm^{-3} NaOH at 22 °C. Electrode area: 3.46 cm^2. ● Al/Mg/Sn ○ 99.999 %wt Al.

Figure 4.18: Variation with time of the open-circuit corrosion current density of Al/Mg/Sn compared to that of 99.999 %wt Al. Electrolyte: 4 mol dm^{-3} NaOH at 22 °C. ● Al/0.5 % Mg/0.07 % Sn, ○ 99.999 %wt Al. Electrode area: 3.5 cm^2. Platinum mesh counter electrode.

Figure 4.19: Dependence of the transient, extremely negative open-circuit potential of Al/Mg/Sn on the surface condition of the alloy. (a) Open-circuit potential with time. (b) Corrosion current density at open-circuit. ● Sample held at open-circuit for 4800 s, □ Electrolyte refreshed and sample held at open-circuit for a further 4800 s. Electrolyte: 4 mol dm^{-3} NaOH at 22 °C. Electrode area: 3.5 cm^2.

Figure 4.20: Back-scatter electron image showing surface microstructure of the Al/Mg/Sn alloy at open-circuit. Sample held at open-circuit for 4800 s in 4 mol dm^{-3} NaOH. Points A and B highlight two different surface morphologies, which are shown at higher magnification in Figure 4.21(a) and (b) respectively.

Figure 4.21: Non-uniform surface morphology and passive layer of the Al/Mg/Sn alloy after being held at open-circuit for 4800 s in 4 mol dm^{-3} NaOH. (a) Morphology 1; SEM image showing a coarse surface with ridges and cracks. (b) Morphology 2; BEM image showing a finer surface characterised by a mesh of interconnected black regions surrounding white areas. (c) EDX profile of point X. (d) EDX profile of point Y. (e) EDX profile of point Z.

Figure 4.22: Back-scatter electron image showing the cross-section of the Al/Mg/Sn alloy. The face perpendicular to the top edge was immersed in 4 mol dm^{-3} NaOH at 22 °C at open-circuit for 4800 s.

Figure 4.23: Comparison of the linear sweep behaviour of the two aluminium alloys in 4 mol dm^{-3} NaOH at 22 °C. Sweep rate: 20 mV s^{-1}. The electrodes were held at open-circuit for at least one hour prior to the potential sweep. ● Al/Mg/Sn, △ Al/Mg/Sn/Ga, ○ 99.999 %wt Al. The alloys were solution heat treated.

Figure 5.8: Cross section of the OxAg electrode examined via scanning electron microscopy. (a) Plan view of the thickness of the electrode, (b) Back-scattered electron image with EDX analysis insets.

Figure 5.9: Scanning electron microscopy image of the E4A air-electrode at different magnifications. (a) Image showing active layer between metal mesh, (b) Magnification of area highlighted by the white square in image 'a', (c) magnification of area highlighted by the white square in 'b'.

Figure 5.10: Scanning electron microscopy image of the E4 electrode at different magnitudes. (a) Low magnification image with three MnO_x catalyst particles identified, (b) High magnification of area highlighted by the white square in image 'a'.

Figure 5.11: (a) Back scattered electron image of MOC electrode. (b) The same image as in image 'a' as viewed under the scanning electron microscope, with a magnified view of the catalyst inset.

Figure 5.12: Scanning electron microscopy images of the 4 mg cm^{-2} platinum electrode at different magnifications. (a) Scanning electron microscopy image of the face of the active layer, (b) back scatter electron image with inset showing magnified view of selected area, (c) EDX of point 1, (d) EDX of point 2.

Figure 5.13: Scanning electron microscopy images of the 0.5 mg cm^{-2} Pt electrode at three magnifications.

Figure 5.14: Pore distribution curves for the commercial gas diffusion electrodes calculated from mercury intrusion data. ▲ Gaskatel MOC, □ E4A ■ E4, ● E5, ○ 4 mg cm^{-2} Pt.

Figure 5.15: Intrusion gradient for four of the commercial gas diffusion electrodes. (a) E4A, (b) MOC, (c) E4, (d) E5.

Figure 5.16: The importance of electrode preconditioning on the linear sweep voltammogram of the KTH electrode in 4 mol dm^{-3} NaOH solution at 22 °C. The preconditioning procedures were: ▲ ocp 1 hour, ■ −50 mA cm^{-2} 1 hour discharge, △ ocp for 24 hours, □ −100 mA cm^{-2} 1 hr discharge. The back of the electrode was open to atmosphere. Sweep rate: 1 mV s^{-1}.

Figure 5.17: The effect of degassing the electrolyte on the polarisation of the E5 commercial gas diffusion electrode. ——— Solution degassed with N_2 for 40 minutes, ····· Non-degassed normal solution. Electrolyte: 4 mol dm^{-3} NaOH. Sweep rate: 1 mV s^{-1}. Temperature: 295 K. The back of the air-electrode was open to atmosphere.

Figure 5.18: Effect of electrolyte concentration on the polarisation of the Co-based GDE, E5, in NaOH. △ 1 mol dm^{-3}; ● 4 mol dm^{-3}; ○ 8 mol dm^{-3}. Sweep rate: 1 mV s^{-1}. The back of the air−electrode was open to air at atmospheric pressure. Electrolyte temperature: 22 °C. Electrode area: 3.46 cm^2.

Figure 5.19: The effect of electrolyte type on polarisation of the commercial air electrode, E5. ● 4 mol dm^{-3} NaOH, △ 7 mol dm^{-3} KOH. Sweep rate 1 mV s^{-1}. The back of the electrode

was open to atmosphere. Electrolyte temperature: 22 °C. Electrode area: 3.5 cm^2. Platinum mesh counter electrode of area 1.5 cm × 1.5 cm.

Figure 5.20: The effect of electrolyte temperature and electrode pre-treatment on the oxygen reduction reactivity of the E5 commercial gas diffusion electrode. Sweep rate 1 mV s^{-1}. Rear face of the electrode was open to the atmosphere. Electrolyte: 4 mol dm^{-3} NaOH. Electrode area: 3.46 cm^2. Platinum mesh counter electrode of area 1.5 cm × 1.5 cm. ● 22 °C, ▲ 60 °C, ○ pretreated with boiling water.

Figure 5.21: The effect of temperature on linear sweep voltammetry at the KTH electrode. (a) Cathodic linear sweep voltammetry, (b) Tafel plots of these voltammetry sweeps. ▲ 22 °C, △ 60 °C, ■ 22 °C, after a −50 mA cm^{-2} pre-discharge. Electrolyte: 4 mol dm^{-3} NaOH. Electrode area: 3.8 cm^2. The rear face of the electrode was open to the air. Sweep rate: 1 mV s^{-1}.

Figure 5.22: The effect of current collection on oxygen reduction reactivity of 4 mg cm^{-2} Pt gas diffusion electrode in alkaline solution. Static 4 mol dm^{-3} NaOH solution at 22 °C. Electrode area: 3.46 cm^2. Sweep rate: 1 mV s^{-1}. ● 4 mg cm^{-2} Pt GDE without current collector, ○ 4 mg cm^{-2} Pt GDE with current collector. The current collector was a stainless steel foil with a hole in its centre to allow air access at the back of the electrode.

Figure 5.23: (a) Comparison of KTH electrode with the commercial gas diffusion electrodes. The area highlighted by the dotted square is shown in graph 'b'. (b) Close-up of linear sweep at current density below −200 mA cm^{-2}. Linear sweep scans carried out in 4 mol dm^{-3} NaOH at 22 °C. Sweep rate: 1 mV s^{-1}. Area: 3.46 cm^2. The rear face of the electrode was open to air at atmospheric pressure. ✯ 0.5 mg cm^{-2} Pt, ○ 4.0 mg cm^{-2} Pt, ■ E4 MnO_x, ▲ E4A MnO_x, □ MOC, △ E5 Co-catalysed air cathode, ✚ OxAg, ● KTH.

Figure 5.24: Comparison of the gas diffusion electrodes under galvanostatic discharge at 100 mA cm^{-2}. Electrolyte: 4 mol dm^{-3} NaOH at 22 °C. Electrode area: 3.46 cm^2. A larger area of 3.8 cm^2 was used for KTH. ▲ E4A, ● KTH, ✚ AgO. The back of the electrodes were open to the air at ambient pressure.

Figure 5.25: Photograph of discharged OxAg electrode. The light-grey circular area was the discharged area in contact with the electrolyte. The surrounding black area was untested parts of the electrode.

Figure 5.26: Stability of E4A gas diffusion electrode under galvanostatic discharge at −150 mA cm^{-2}. Electrolyte: 4 mol dm^{-3} NaOH at 22 °C. Electrode area: 3.46 cm^2. The rear face of the electrode was open to air at atmospheric pressure. ▲ E4A MnO_x

Figure 6.1: Behaviour of an Al 6101 foam anode in Prototype 1 Al-air cell. Electrolyte: 3 mol dm^{-3} NaOH initially at 22 °C. The electrolyte temperature increased due to Joule heating. Geometrical area of anode: 43 cm^2. The air cathode was a Pt/C GDE with 0.5 mg cm^{-2} platinum loading: ●, ◆, ■ 10 ppi Al 6101 foam, ○ 20 ppi Al 6101 foam. The electrodes were not solution heat treated before use.

Figure 6.2: Cell voltage *vs.* time for the prototype 1 aluminium-air cell employing four different types of aluminium anode: ○ Al 6101 20 ppi foam, ● Al 6101 10 ppi foam, ▲ Al/Mg/Sn/Ga plate, △ Al/Mg/Sn/Ga perforated plate. Electrolyte: 50 cm^3 of 3 mol dm^{-3}

NaOH. Discharge current: 1 A. The air cathode was a Pt/C GDE with a 0.5 mg cm^{-2} platinum loading. The aluminium anodes were not solution heat treated.

Figure 6.3: Photographs of (a) Al 6101 20 ppi foam, (b) Al 6101 10 ppi foam, (c) Al/Mg/Sn/Ga plate, (d) Al/Mg/Sn/Ga perforated plate, after constant current discharge at 1 A in the prototype 1 aluminium-air cell. Electrolyte: 50 cm^3 of 3 mol dm^{-3} NaOH. The air cathode was a Pt/C GDE with 0.5 mg cm^{-2} platinum loading.

Figure 6.4: Measurement of electrode potentials during galvanostatic discharge of the prototype 1 aluminium-air cell using an Al 6101 10 ppi foam anode discharged at 1 A. Electrolyte: 50 cm^3 of 3 mol dm^{-3} NaOH. Air cathode: 0.5 mg cm^{-2} Pt/C GDE. The anode was not heat treated.

Figure 6.5: Effect of electrolyte concentration on the prototype 1 Al-air cell performance. △ 3 mol dm^{-3} NaOH, ● 8 mol dm^{-3} NaOH. (a) Cell voltage *vs.* current density and (b) Power density *vs.* current density. Current and power densities were calculated per unit geometrical area of cathode. The air cathode used was a Pt/C GDE with 0.5 mg cm^{-2} Pt loading. Aluminium anodes were not solution heat treated before use.

Figure 6.6: Determining the area required for a prototype 2 cell. (a) Cell voltage and power versus current. (b) Cell voltage and power density versus current density. ▲ & △ active area of 22 cm^2, ● & ○ active area of 11 cm^2. 99.999 %wt aluminium anode and E5 Co-catalysed commercial gas diffusion electrode. Electrolyte: 4 mol dm^{-3} NaOH initially at 22 °C.

Figure 6.7: Effect of ratio of anode to cathode area on the performance of the prototype 2 Al-air cell. □ & ■ anode:cathode area of 4:1. △ & ▲ anode:cathode area of 1:1. Electrolyte: 4 mol dm^{-3} NaOH, initially at 22 °C. 99.999 %wt aluminium anode and commercial E5 GDE air cathode.

Figure 6.8: Effect of air-cathode current collection and platinum loading on cell performance. (a) Cell voltage and (b) Power density *vs.* current density for the prototype 2 Al-air cell employing three different air-cathodes: ○ 0.5 mg cm^{-2} Pt, no copper wire, ▲ 0.5 mg cm^{-2} Pt, with copper wire, ● 4.0 mg cm^{-2} Pt, with copper wire. Current densities relative to area of the air-cathode of 20 cm^2. Anode area of 21.5 cm^2. The cells were tested using an Al/Mg/Sn/Ga plate anode immersed in 10 cm^3 of 3 mol dm^{-3} NaOH, initially at 20 °C. The alloy was not solution heat treated before these studies.

Figure 6.9: Variable load test on aluminium-air battery consisting of 5 of the prototype 2 Al-air cells connected in series. (a) Battery voltage and power *vs.* current (b) Battery voltage and power density *vs.* current density. Alloy, Al/Mg/Sn/Ga plate (22 cm^2), not heat treated. 0.5 mg cm^{-2} Pt/C GDE. 50 cm^3 of 3 mol dm^{-3} NaOH solution, initially at 22 °C. Current and power densities were calculated per unit projected area of the cathode.

Figure 6.10: Variation of cell voltage with current for each of the five cells connected in series to form the light-weight aluminium-air battery shown in Figure 6.12(a). The cells were tested with an Al/Mg/Sn/Ga plate anode and a gas diffusion electrode with 0.5 mg cm^{-2} platinum loading. The electrolyte was 3 mol dm^{-3} NaOH, initially at 22 °C. The anode of cell 1 formed the battery negative terminal, while the cathode of cell 5 formed the battery positive terminal. The aluminium anodes were not solution heat treated before use.

Figure 6.11: The five Al/Mg/Sn/Ga anodes after performing a load test on the Al-air battery. Original dimensions: 50 × 30 × 1 mm. The battery consisted of 5 cells in series, each cell containing 10 cm^3 of 3 mol dm^{-3} NaOH, initially at 22 °C. In each cell the cathode was a 0.5 mg cm^{-2} loaded Pt/C GDE. The active area of each anode was 22 cm^2. The anodes pictured above belong to cells 1 through 5 from left to right. Anode in cell 1 formed the negative terminal of the battery while cathode in cell 5 formed the positive terminal. The aluminium anodes were not solution heat treated.

Figure 6.12: 5 cell aluminium-air battery driving the motor, delivering 0.5 A (24 mA cm^{-2}) at 7.7 V. Each cell is made from a U-shaped PVC body, with an air cathode glued to the front and back faces and a flat plate Al anode in the centre. Wet mass 109 g. The motor was driving a ca. 180 mm diameter 2-blade, propeller at adjustable speed.

Figure 6.13: Side view of prototype 3 Al-air cell held between PTFE insulators in the clamp.

Figure 6.14: Importance of insulating the Al-air cell to isolate it from its surroundings. ●, ◆, ■ insulated cell. ○, ◇, □ grounded cell. (a) Al-air cell with the KTH cathode (b) Al-air cell with the E4A cathode. Anode: Al/Mg/Sn. Electrolyte: 4 mol dm^{-3} NaOH, initially at 22 °C. Cathode area: 14.4 cm^2. Current density relative to an anode area of 20 cm^2.

Figure 6.15: Transient behaviour of the open-circuit cell potential of the prototype 3 Al-air cell. ● Al/Mg/Sn, ○ 99.999 % Al. Air cathode: E5 Co-catalyst. 15 cm^3 of 4 mol dm^{-3} NaOH electrolyte, initially at 22 °C. Interelectrode gap: 5 mm.

Figure 6.16: Effect of aluminium alloy on the performance of the Al-air cell. (a) Potential and cell temperature versus current density, (b) Magnified view of anode potential and cell temperature versus current density. ●, ◆, ■, ▲ cell with Al/Mg/Sn. ○, ◇, □, △ cell with 99.999 % Al. Current density relative to anode area, 22 cm^2. Cathode area: 15 cm^2. KTH air-electrode. Electrolyte: 15 cm^3 of 4 mol dm^{-3} NaOH initially at 22 °C. 5 mm interelectrode gap.

Figure 6.17: Comparison of the Al/Mg/Sn alloy and 99.999 % aluminium in the Al-air cell under galvanostatic discharge at 100 mA cm^{-2}. E4A air cathode. Electrolyte: 4 mol dm^{-3} NaOH. Anode area: 21 cm^2. Cathode area: 15 cm^2. 5 mm inter-electrode gap. ●, ◆, ■, ▲ for Al/Mg/Sn. ○, ◇, □, △ are for 99.999 % aluminium

Figure 6.18: Discharge of the aluminium-air cell at the peak power point at 170 mA cm^{-2}. Anode: Al/Mg/Sn, area 22 cm^2. Cathode: E4A MnOx, area 15 cm^2. Electrolyte: 15 cm^3 of 4 mol dm^{-3} NaOH.● E_{cell}, ◆ E_c, ■ E_a, ▲ Temperature.

Figure 6.19: Comparison of the performance of the aluminium-air cell using different air electrodes. □, ◇, ○ OxAg; ●, ◆, ■ KTH; ◍, ◈, ▣ E4A. Anode, Al/Mg/Sn. Anode, Al/Mg/Sn solution heat treated. Electrolyte: 15 cm^3 of 4 mol dm^{-3}, initially at 22 °C. Cathode area: 15 cm^2. Current density calculated relative to an anode area of 21 cm^2.

Figure 6.20: The influence of the different air-cathodes on the galvanostatic discharge of the Al-air cell at 100 mA cm^{-2}. □, ◇, ○ OxAg; ●, ◆, ■, ▲ KTH; ◍, ◈, ▣, △ E4A. (a) Comparison of cell and reference potentials versus time. (b) Comparison of cathode reference potential for cells with KTH and E4A air-electrodes. Anode Al/Mg/Sn. Electrolyte: 15 cm^3 of

4 mol dm^{-3} NaOH, initially at 20 °C. Anode area: 21 cm^2. Cathode area: 15 cm^2. Interelectrode gap: 5 mm.

List of tables

Author’s declaration

I declare that this study is work done wholly or mainly by me while in candidature for a research degree at the University of Southampton. I confirm that I have attributed published sources I have consulted or quoted and acknowledged all main sources of help.

_____

Derek Egan

Acknowledgements

Firstly I would like to thank my supervisors Dr. Carlos Ponce de Leon and Prof. Robert Wood for guiding me through the duration of this experimental study. I appreciate their guidance in helping with experimental ideas, acting as mentors and sharing their research skills. I would like to thank Prof. Frank Walsh for sharing some of his vast experience in batteries, corrosion and industrial electrochemistry. I appreciate the advice of Prof. Keith Stokes in contributing ideas of areas to explore during the study.

I appreciate the collaboration with and generosity of Dr. Yohannes Kiros of KTH Royal Institute of Technology, Sweden for providing samples of his team's gas diffusion electrode design. I am grateful to Dr. Christopher Gribble for mercury intrusion analysis of air cathode samples.

I am extremely grateful to Dr. Louise Hespel who is an excellent friend to me.

I would like to thank my family, especially my Mom, Dad and brother. I am extremely grateful that they were there for me as a pivotal support to see me complete this research degree.

I would like to thank Lee Mulholland, Paul Frampton and Przemyslaw Tryc for their glass-blowing skills in skilfully making the various glass-three electrode cells in this study particularly with an enclosed, vertical spout to accommodate hydrogen collection measurements and a water-jacket to facilitate experiments at high temperature.

I would like to thank the team of Rob Dalley in the Chemistry workshop who offered me advice when working with polymers in the assembly of a prototype aluminium-air cell and also helped with cell construction. I would like to thank all the friends I have made and supported me during this thesis who include Ruben Poras, Dr. Irene Merino, Dr. Rachel McKerracher, Dr. Nadia Van Pelt, Dr. Andrea Boghi, Dr. Mihaela Stevar, Maria Kourasi, Luis-Fernando Arenas, Muthu Krishna, Recep Kahraman , Dr. Ravichandra Tangirala, Dr. Jacki Leung, Dr. John Low, Dr. Intan Osman, and Dr. Natalya Doroshenko.

List of symbols and abbreviations

Symbol	Meaning	Units
CR	Corrosion rate	mg cm^{-2} day^{-1}
d	Pore diameter	mm
E_{cell}	Cell voltage	V
E_c	Cathode potential	V *vs.* Hg/HgO
E_a	Anode potential	V *vs.* Hg/HgO
F	Faraday constant	96,485 C mol^{-1}
I	Current	A
I_{cor}	Corrosion current	A
$I_{cor,p}$	Corrosion current for pure aluminium	A
$I_{cor,a}$	Corrosion current for aluminium alloy	A
j_{cor}	Corrosion current density	
n	Amount of material	mol
P	Pressure	N m^{-2}
R_u	Universal gas constant	8.314 J mol^{-1} K^{-1}
t	Time	s
T	Temperature	°C or K
V	Volume	m^3 or cm^3
$\dot{V}$	Volumetric flow rate	m^3 s^{-1}
z	Number of electrons in the electrode process	Dimensionless

φ_{inh}	Open-circuit inhibition efficiency	%
φ_{dis}	Discharge efficiency	%
γ	Interfacial tension	N m^{-1}
θ	Mercury contact angle	degree

Abbreviation	Meaning
3-D	Three dimensional
AB	Acetylene black
Ag	Silver
Al	Aluminium
$AlCl_3$	Aluminium chloride
Al_2O_3	Aluminium oxide
$Al(OH)_3$	Aluminium hydroxide
$Al(OH)_4^-$	Aluminate
BEI	Back-scatter electron imaging
B	Boron
Bi	Bismuth
[BMIm]TFB	1-butyl-3-methylimidazolium tetrafluoroborate

Abbreviation	Meaning
([BMP]TFSI)	1-butyl-1-methylpyrrolidinium bis(trifluoromethylsulfonyl)imide
C	Carbon
CB	Carbon black
Cd	Cadmium
Cu	Copper
Cl^-	Chlorine ion
Co	Cobalt
CTAB	Cetyltrimethylammonium bromide
CTAC	Cetyltrimethylammonium chloride
e^-	electron
EDX	Energy dispersive X-ray
EMIC	1-Ethyl-3-methylimidazolium chloride
([EMIm]TFSI)	1-ethyl-3-methylimidazolium bis(trifluoromethylsulfonyl)amide
F^-	Fluorine ion
Fe	Iron
Fe^{2+}	Ferous ion
FIB/SIMS	Focused ion beam/secondary ion mass spectroscopy
Ga	Gallium
GaO_3^{2-}	Gallate
GDE	Gas diffusion electrode
GDMS	Glow discharge mass spectroscopy
Ge	Germanium
Hg/HgO	Mercury/mercurous oxide
HPG	Hydrophonics gel
H_2	Hydrogen
H_2O	Water
H_2O_2	Hydrogen peroxide
ICP-MS	Inductively coupled plasma mass spectroscopy
In	Indium
InO_2^-	Indate
InO_3	Indium trioxide
$In(OH)_3$	Indium hydroxide
KB	Ketjan black
$KMnO_4$	Potassium permanganate
KOH	Potassium hydroxide
$LaMnO_3$	Lanthanum manganite
Mg	Magnesium
Mn	Manganese
MnO_x	Manganese oxide
NaCl	Sodium chloride
NaOH	Sodium hydroxide
Na_2SnO_3	Sodium stannate
N-BPC	N-Butylpyridinium chloride

Abbreviation	Meaning
O_2	Oxygen
$O_2^{\bullet-}$	Superoxide ion
OH^-	Hydroxyl ion
PAA	Polyacrylic acid
Pb	Lead
PEM	Proton exchange membrane
PEMFC	Proton exchange membrane fuel cell
ppi	Pores per linear inch
PTFE	Polytetrafluoroethylene
($P_{14,6,6,6}$TFSI)	[(Trihexl-tetradecyl)phosphonium] bis(trifluoromethylsulfonyl)imide
PVA	Polyvinyl alcohol
PVC	Polyvinyl chloride
S	Sulfur
Sb	Antimony
SCE	Saturated calomel electrode
SEM	Scanning electron microscopy
Sn	Tin
SnO_3^{2-}	Stannate
SnH_4	Tin hydride
SOP	Standard of practice
TMPAC	Trimethylphenylammonium chloride
TMPATFSI	Trimethyl-n-propylammonium bis(trifluoromethylsulfonyl)imide
UAV	Unmanned aerial vehicle
W_2C	Tungsten carbide
Zn	Zinc
ZnO	Zinc oxide
Zr	Zirconium

Chapter 1. Introduction

1.1 General introduction

Energy storage systems play a vital role in modern life. The breath of energy storage systems is as diverse as the variety of electronic technology experienced. Stationary storage systems tend to be large scale, an increasingly important example being redox flow batteries potentially integrated with renewable energy technology. Storage systems for portable electronic applications, for consumer electronics and transport routinely use batteries. These portable systems are designed to have a maximum energy density. Lithium ion batteries dominate the consumer electronics market and are also used in hybrid and all-electric vehicles. Metal-air batteries provide important alternative high energy density batteries. Zinc-air is the most widely commercialised type, being routinely used in consumable portable goods and for specialised applications such as hearing-aid batteries. Aluminium-air batteries, with a higher energy density, are an attractive alternative for study.

An aluminium-air battery is a primary electrochemical cell where during discharge aluminium oxidises at the anode and oxygen from the air is reduced on catalysts at the cathode, yielding the overall discharge reaction given in reaction 1.1. The aluminium-air battery is studied as a potential high-energy density power source because of the lightness of the aluminium anode and the characteristic that the cathode reactant is not carried within the cell, it is supplied externally from the air. At the University of Southampton, an aluminium-air battery was considered for development as a primary power source for a micro-unmanned Aerial Vehicle (UAV) [1]. This research project was first undertaken by Andrew Kay [2] and succeeded by Dr. Maria Nestoridi [3], who pursued PhD work on saline aluminium-air batteries [1, 4, 5].

$$4Al + 3O_2 + 6H_2O \rightarrow 4Al(OH)_3 \qquad E_{cell} = 2.7\ \text{V} \qquad (1.1)$$

Nestoridi studied a number of aluminium alloys in 12 % w/v NaCl solution [1]. That work showed that the discharge profile for aluminium in NaCl was enhanced upon the addition of alloying elements such as Mg, Sn and Ga. A literature search indicated that an alloy AB50V, Al-0.6 % Mg-0.1 % Sn-0.05 % Ga, was the most suitable material as anode for a saline

aluminium-air battery. The mechanism of the alloy dissolution was associated with the formation of rounded pits, and the tin inclusions played a key role in the formation of these pits [5]. The number and size of these pits increased with dissolution time and anodic current density. At open-circuit in saline solutions, hydrogen evolution was directly associated with pit growth [5]. During anodic dissolution, streams of H_2 gas bubbles emanated from specific points within rounded pits. A given stream of hydrogen bubbles would continue to evolve for $20 - 30$ seconds. The gas evolution then stopped for a few seconds before recommencing with an associated 'explosive' bursting of a solid crust in the pit. No hydrogen bubbles were formed on the rest of the surface [5].

Developing an aluminium-air battery as a power source for a micro-unmanned aerial vehicle is financially very attractive as by 2020 the UAV Market is estimated to be worth $80 billion [6]. Micro-UAVs are used for strategic military applications such as battlefield reconnaissance and for civil missions such as search and rescue, border patrol, air sampling and police surveillance [7]. The idea of using aluminium-air batteries to power micro-UAVs is not a new one. Alupower built a prototype micro-UAV powered by an Al-air battery with an energy density of 120 W h kg^{-1} and power density of 60 W kg^{-1} in 1987 [8, 9]. The Australian Defence Science and Technology Organisation also looked at using aluminium-air batteries to power a UAV in 1995 [8].

1.2 Research objectives

The main deliverable of this PhD is to develop a lightweight aluminium-air cell and to characterise its behaviour utilising different aluminium anodes and air-cathodes. Electrochemical characterisation is to be achieved via measurement of electrode potentials and cell temperature during galvanostatic discharge and variable load experiments. Target specifications include: battery weight of 50 g and an average power output of 20 W with an operation time of 1 hour [1, 2]. The design brief calls for an expendable Al-air cell capable of operating for one hour in applications such as an unmanned air vehicle [10]. These specifications equate to an energy density of 400 W h kg^{-1}, which is achievable by an aluminium-air battery. The power density of this specification, 400 W kg^{-1}, is, however, higher than that attained by previous aluminium-air systems. Typically, an aluminium-air battery with an alkaline electrolyte can deliver 175 W kg^{-1} [11]. The project goal of

developing a lightweight aluminium-air cell was achieved through the following aims and is illustrated in Figure 1.1:

1. A detailed review of the available literature on aluminium-air batteries including the corrosion of aluminium in alkaline solutions. The review focuses on alkaline solutions, because alkaline aluminium-air batteries deliver higher power and energy densities than neutral chloride systems [11]. The review examines the effect of alloying elements on breaking down the aluminium passive hydroxide layer and at inhibiting the reduction of water on the aluminium surface. The review seeks to identify an aluminium alloy suitable for aluminium-air batteries on the basis of having the lowest overpotential and self-corrosion rates in alkaline solutions.
2. Characterisation of the corrosion and dissolution behaviour of the super-pure aluminium alloy, Al/Mg/Sn, identified from the literature. Suppliers of this material are identified. Characterisation of its behaviour involved comparing its electrochemical behaviour against that of 99.999 % Al and an Al/Mg/Sn/Ga alloy studied in the research of Nestoridi. Both of these alloys are patented for use in aluminium-air cells.
3. A high performance air-cathode that can reduce oxygen at high current densities, with a low overpotential is identified. A critical review of air-breathing cathodes for oxygen reduction reaction in alkaline solutions has been carried out. This technology has been widely reviewed for metal-air battery and fuel cell applications [12-16]. As the Al-air cell would be potentially expendable then use of non-noble catalysts as alternatives to platinum are considered. Commercial air cathodes are compared against an electrode designed by a collaborator from KTH University, Sweden whom has extensive expertise in air cathodes.
4. A prototype aluminium-air cell is developed to target the above specifications. The aluminium alloy and the air cathode selected from earlier in the studies are incorporated along with lightweight materials for the battery structure and assembly, to manufacture the prototype aluminium-air cell.

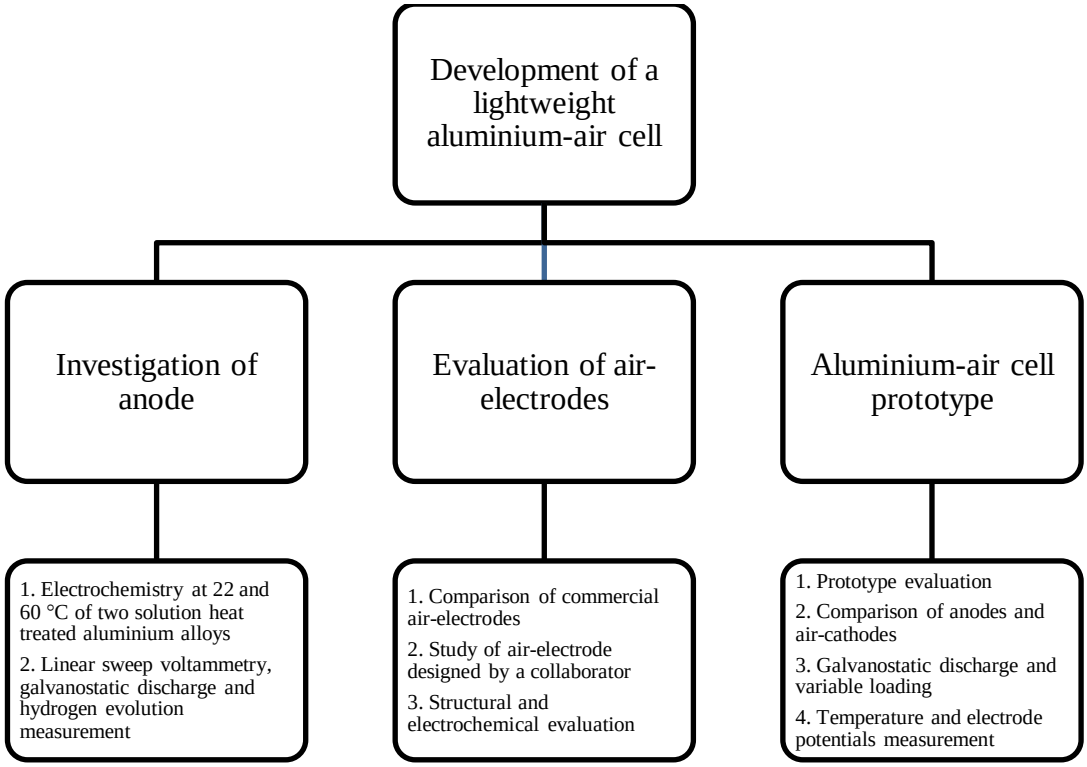

Figure 1.1: Illustration of the goals of this experimental study.

1.3 Research novelty

Alkaline aluminium-air cells have seen periodic bursts of research interest since their invention in 1962 [17]. Previous research typically aimed at developing aluminium-air batteries in the kW range for applications requiring long discharge times, such as electric vehicles [18-21] and reserve power units for back-up telecommunications equipment [22]. These large scale systems incorporated a flowing electrolyte integrated with heat exchangers to operate at an optimal temperature, avoiding overheating and boiling of the electrolyte. The electrolyte circuit would have also included a filter/crystalliser unit to remove crystallised reaction products to maintain solution conductivity and prevent clogging of the pores in the air-cathode.

The novelty of this study is to develop a small, lightweight aluminium-air cell and to contribute knowledge of how this system behaves electrochemically utilising different aluminium anodes and air-cathodes with a variety of catalysts. The target power of the cell falls between 1 and 5 W and the cell uses a static alkaline electrolyte of less than 15 cm^3 volume. Such a small volume electrolyte is susceptible to a temperature increase due to the exothermic nature of aluminium oxidation and the simultaneous reduction of water on its

surface [23]. The cell temperature is monitored to identify the difference in cell and electrode behaviour between a cold start-up and discharge at the steady operational temperature.

Aluminium anodes selected for testing in the aluminium-air cell are evaluated in half-cell tests. Previous studies on suitable anodes have examined the behaviour of various aluminium alloys in flowing electrolytes at 22 and 60 °C. Among the patented alloys, Al/Mg/Sn and Al/Mg/Sn/Ga, showed highly active anode potentials of −1.62 V *vs.* Hg/HgO in an Al-air battery discharged at 715 mA cm^{-2} in 25 % KOH/3.5 % NaCl at 80 °C [24, 25]. An electrolyte of 25 % or 5.5 mol dm^{-3} KOH was used because that is close to the concentration with peak conductivity for KOH. In this thesis, the electrolyte in the aluminium-air cell is static and heated solely by the exothermic oxidation at the anode, so half-cell tests are conducted to compare the behaviour of the alloys over a wide temperature range of 22 to 70 °C. The optimum operational temperature for an aluminium-air cell is 60 °C [26]. In previous research on Al-air cells, there was ambiguity over the oxidation and corrosion behaviour of some alloys due to the heat treatment used after alloy casting. Some studies have involved solution heat treated alloys while others did not. This present work illustrates the importance of a controlled solution heat treatment of the alloys since this affects microstructure and electrochemical performance. Similarly, half-cell electrochemical tests are used to evaluate several commercial gas diffusion electrodes against an electrode designed by a project collaborator at KTH University, Sweden. These experiments are used to narrow down the number of air-electrodes to be evaluated in the prototype, lightweight aluminium-air cell.

1.4 Thesis outline

The thesis consists of seven chapters. This introduction chapter outlines the reason for looking at the aluminium-air system as a lightweight battery. It outlines how this study expands the knowledge of the performance of a lightweight aluminium-air cell, highlighting the novelty of this work. Chapter 2 provides a literature review, examining the extensive research into high-purity aluminium alloys designed to oxidise at high current densities with minimal parasitic corrosion due to hydrogen evolution. The rationale behind the choice of alloying element and its percentage to alloy with is identified. For the air-cathode side, as the design brief called for an aluminium-air cell with a short discharge time, the stability of the air-cathode was not a concern. This meant air-cathodes with a high activity for the oxygen reduction reaction, normally not considered because of poor stability over long discharge,

could be considered and were reviewed. It is from this review work that a collaborator in KTH University, Sweden was contacted and agreed to supply an air-cathode design for evaluation.

Chapters 4, 5 and 6 are devoted to the experimental results and their discussion. Chapter 4 covers the electrochemical behaviour of two high-purity aluminium alloys in alkaline solution, with 99.999 %wt aluminium used as a comparison. The anodic behaviour is quantified using linear sweep voltammetry and galvanostatic discharge. The corrosion behaviour is quantified via a hydrogen collection method. The effect of heat treatment and electrolyte temperature on their behaviour is explored. The purpose of these half-cell experiments is to confirm the choice of alloy to be used as the anode in the prototype aluminium-air cell. Chapter 5 compares the oxygen reduction behaviour of several commercial gas diffusion electrodes against an electrode manufactured by a project collaborator. The electrodes were compared via a structural investigation with electron microscopy and mercury intrusion porosimetry. The investigation analysed the operational variables needing adjustment to optimise the oxygen reduction behaviour of the air-electrodes: these included electrolyte temperature and concentration as well as electrode pre-treatment. The electrochemistry of the electrodes is compared using linear sweep voltammetry and galvanostatic discharge studies. From these results the choice of air-electrodes for testing in the prototype aluminium-air cell are selected.

Chapter 6 concerns the evolution of the design of the prototype aluminium-air cell. The design process focused on minimising weight, ensuring rigidity, stable to alkaline solution and ease with which to assemble for experimental repeatability. The aluminium alloy from chapter 4 and the air-cathodes evaluated in chapter 5 were tested in the final aluminium-air cell prototype. The purpose of the experiments on the prototype aluminium-air cell was to characterise the electrochemical and thermal behaviour, and their inter-relationship, of a lightweight aluminium-air cell, while examining different aluminium anodes and air-cathodes. Chapter 7 highlights conclusions from the research on the lightweight aluminium-air cell prototype and concisely provides recommendations for further research and development.

Chapter 2. Literature Review and Theory

Current research across the breath of energy storage technologies is focused on reducing system weight and volume to improve energy density [27]. For example a power source for a micro-UAV would need to be lightweight and have a compact volume so as to be easily fitted into the aerodynamic design of a micro-UAV. The lightness of aluminium energy storage technologies, such as Al-H_2O_2 or Al-S systems, has meant that they have received renewed interest for a variety of applications [28, 29]. Among these systems is the aluminium-air battery with a practical specific energy density of 400 W h kg^{-1} [25, 30-32], surpassing that of lithium-ion batteries at 100 to 150 W h kg^{-1} [33]. The aluminium-air cell illustrated in Figure 2.1 is a primary metal-air battery with an aluminium anode and an air-breathing cathode in contact with an aqueous electrolyte, typically sodium hydroxide, potassium hydroxide or sodium chloride [34]. The discharge reaction involves the oxidation of the aluminium anode and reduction of oxygen at the air-cathode. The lightness of the aluminium and the fact that the cathode reactant is supplied from the atmosphere rather than carried in the cell give aluminium-air batteries high energy to weight ratios. Other advantages of this system include the geological abundance of aluminium metal, a recyclable reaction product of $Al(OH)_3$ and the ability to offer rapid, mechanical recharging. Aluminium also has a very negative thermodynamic electrode potential in pH 14 alkaline solutions of ca. −2.25 V *vs.* Hg/HgO, as indicated by the Pourbaix diagram in Figure 2.2 [35].

The Pourbaix diagram for aluminium in Figure 2.2 represents the corrosion of aluminium in aqueous media based on fundamental thermodynamic data, assuming equilibrium conditions and ignoring the limiting effects of reaction kinetics. However the Pourbaix diagram does not predict two behaviours which are continuing issues with aluminium-air batteries. These are (a) the parasitic corrosion of the aluminium, at open-circuit and under discharge, due to the reduction of water on the anode surface and (b) the passive hydroxide layer that forms on the aluminium surface in alkaline solutions, which inhibits dissolution and shifts its potential to more positive values. This means in practice, the open-circuit potential of aluminium is more positive than −2.25 V *vs.* Hg/HgO at −1.66 V *vs.* Hg/HgO [36], due to the competition between the numerous electrode processes that take place on the aluminium surface [37]: (i) formation and/or dissolution of an initial Al_2O_3 and subsequent $Al(OH)_3$ layer, (ii) three-electron charge transfer yielding Al^{III} species, (iii) formation of corrosion products, $Al(OH)_4^-$

and $Al(OH)_3$, as well as (iv) a parasitic corrosion reaction involving the reduction of water at localised cathodic centres on the aluminium surface, which releases hydrogen [38]. This self-corrosion at open-circuit prevents the storage of wet aluminium-air batteries and reduces their discharge efficiency. Research has focused on ways to enhance the aluminium oxidation rate while inhibiting the self-corrosion reaction.

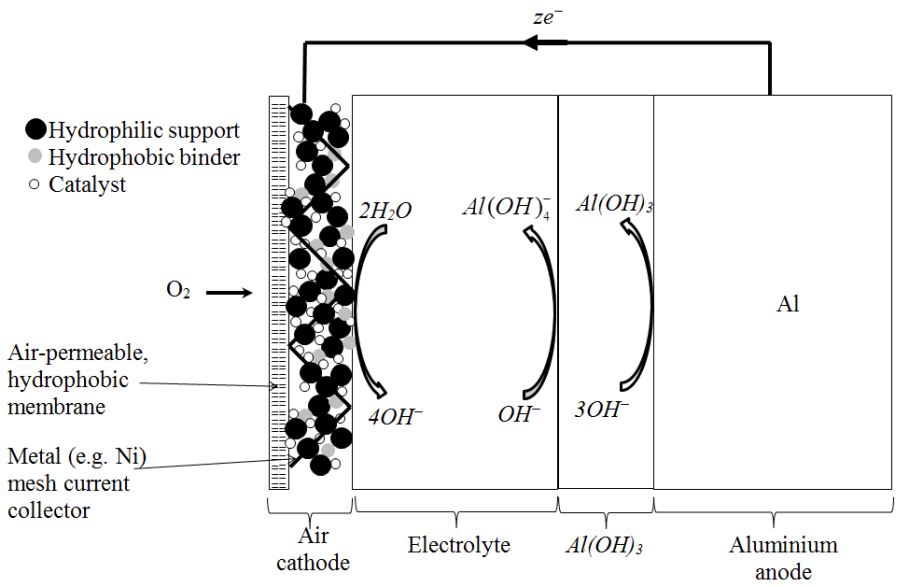

Figure 2.1: Illustration of the structure of an aluminium-air battery using a 3-layer gas diffusion electrode and, in this case, pure aluminium as anode with its passive hydroxide layer.

The literature on aluminium-air batteries spans fifty years as chronicled in Figure 2.3, some of which is accessible as publications and patents while others, such as internal company reports, are more restricted. The extent to which this large body of work has been reviewed is variable. For example some surveys covering the variety of aluminium energy storage systems devote a subsection to the aluminium-air battery electrochemistry [28, 29]. Others focus solely on aluminium-air batteries and detail the advances made together with their developing applications [10, 19, 39-44], such as a power source for electric vehicles [45, 46]. There are specialised reviews that examine aluminium corrosion mechanisms in saline solutions for the cathodic protection of marine structures [47] and under open-circuit conditions in alkaline solutions with relevance to nuclear engineering [48].

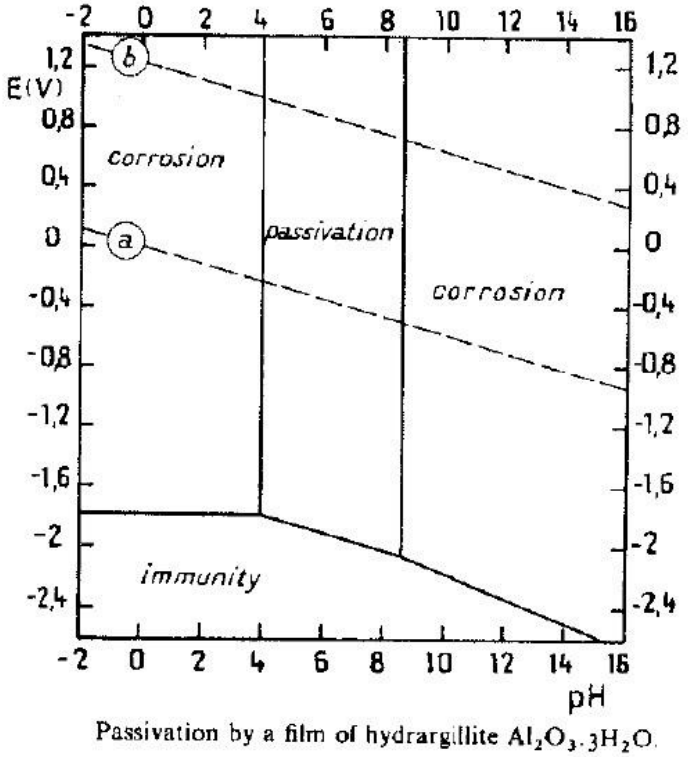

Figure 2.2: The potential-pH diagram for the Al – H_2O system showing the regions of active, passive and immune corrosion behaviour [49].

In this review, experimental data from the literature is critically compared with the aim of examining the choice of different aluminium alloys and alkaline electrolytes for an aluminium-air battery so as to reduce the parasitic corrosion and overcome the passive hydroxide layer, often referred to as 'activating' the aluminium. Research has focused on alloying 99.99 %wt aluminium with certain elements such as Mg, Sn, In and Ga, to achieve such activation. The rationale behind the choice of alloying elements, their concentration and the mechanisms by which they activate the aluminium to yield higher anodic currents is discussed. The percentage of the electrical energy input used during the smelting of aluminium that can be recovered through the discharge of an aluminium energy storage system is 22 % [28]. Since the production of aluminium is an energy intensive process, one lower cost alternative to high-purity alloys involves using commercial grade aluminium and adding inhibitors to the electrolyte. The effectiveness of these inhibitors, singularly and in combination, and in different concentrations is reviewed. The performance of air cathodes with high activity for oxygen reduction in alkaline electrolytes are compared in terms of their

catalyst choice, design and fabrication procedure. Novel methods to overcome the self-corrosion problem are discussed which include using anionic membranes and gel electrolytes or identifying alternative solvents, such as alcohols or ionic liquids, to replace aqueous solutions. Future opportunities and directions for the development of aluminium-air cells are highlighted.

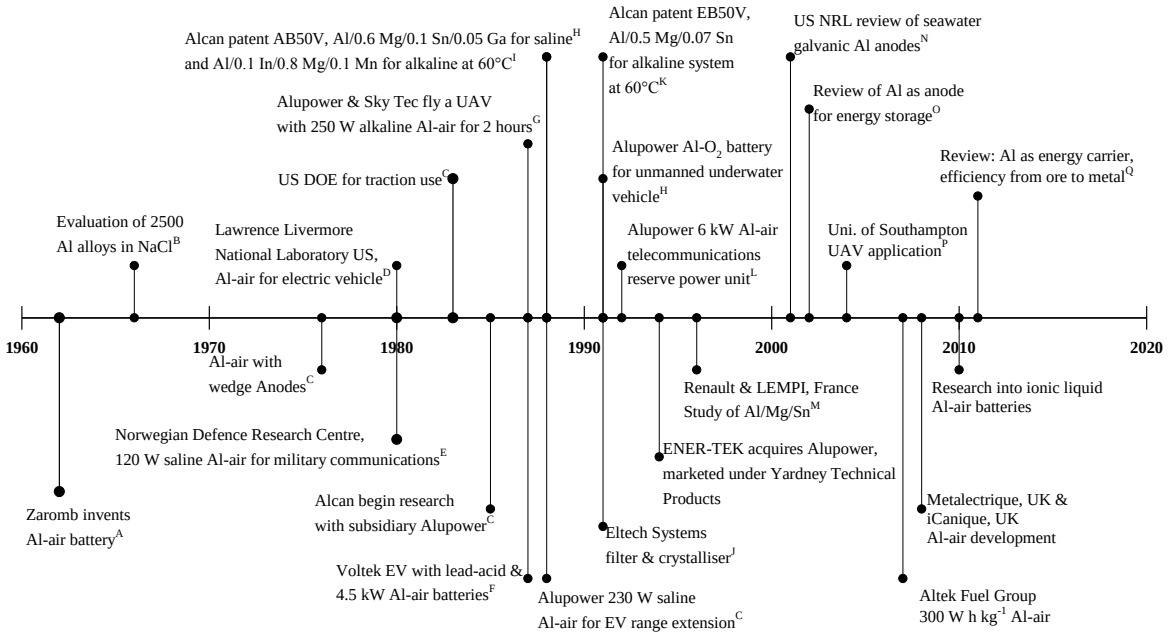

Figure 2.3: Timeline of the history of the development of aluminium-air batteries. [A] [17], [B] [50], [C] [19], [D] [18], [E] [51], [F] [20], [G] [8, 9], [H] [10], [I] [52], [J] [53], [K] [24], [L] [22], [M] [21], [N] [47], [O] [29], [P] [1, 2], [Q] [28]. EV is electric vehicle; UAV is unmanned aerial vehicle.

2.1 Corrosion of 99.999 %wt aluminium in alkaline solutions

Aluminium-air batteries employing alkaline electrolytes are primary energy storage devices since electrodeposition of aluminium from alkaline solutions is not thermodynamically feasible due to its negative standard potential, which will lead to hydrogen evolution at the negative electrode before any aluminium can be deposited [54, 55]. Mechanically recharging is possible by replacing the aluminium anode after each discharge [56].

The positive electrode is an air or gas diffusion electrode, conventionally comprising a carbon-based structure which brings oxygen and the electrolyte into contact with a catalyst resulting in oxygen reduction [1]:

$$O_2 + 2H_2O + 4e^- \rightarrow 4OH^- \qquad E_c = 0.3 \text{ V } \textit{vs.} \text{ Hg/HgO} \qquad (2.1)$$

At the negative electrode the overall anodic reaction involves the oxidation of aluminium to aluminate ions [57]

$$Al + 4OH^- \rightarrow Al(OH)_4^- + 3e^- \qquad E_a = -2.4 \text{ V } \textit{vs.} \text{ Hg/HgO} \qquad (2.2)$$

In parallel with the oxidation of aluminium there is a parasitic reaction involving the reduction of water resulting in hydrogen gas evolution:

$$2H_2O + 2e^- \rightarrow H_2 + 2OH^- \qquad E = -0.93 \text{ V } \textit{vs.} \text{ Hg/HgO} \qquad (2.3)$$

Reactions (2.2) and (2.3) are competing reactions on the surface of aluminium exposed to an alkaline electrolyte. The net current, I, that flows through the external circuit is the difference in magnitude of the dissolution of aluminium, I_d, and corrosion current, I_{cor}.

$$I = I_d - I_{cor} \qquad (2.4)$$

The corrosion behaviour of aluminium and its alloys can be compared by evaluating the corrosion current at open-circuit potential and under discharge. Suitable methods are discussed in the next section.

2.1.1 Evaluating the electrochemical behaviour of aluminium

A quantitative technique for evaluating the corrosion behaviour of aluminium involves measuring the corrosion current as a function of applied discharge current [23, 36, 37, 58-62]. The corrosion rate of aluminium alloys in alkaline solutions varies with time [63], which is particularly evident at open-circuit for aluminium alloys when the changes in the rate of hydrogen evolution exactly mirror the changes in the open-circuit electrode potential with time [49]. Upon immersion, the open-circuit potential of aluminium alloys shifts to a very negative value of −2.0 V *vs.* Hg/HgO due to the presence of aluminium hydrides, AlH_3, [64, 65], and possibly hydrides of the alloying elements, creating a hydroxide-free surface and a high rate of hydrogen evolution [49]. The aluminium hydrides could form from a reaction between aluminium and hydrogen gas, evolved from water reduction [64, 65]. Once the alloy surface becomes passivated by a hydroxide layer, its potential shifts more positively, which is accompanied by a reduction in the rate of hydrogen evolution.

The variable nature of the corrosion rate means that mass loss data, for example, recorded at the end of an experiment, would not give an accurate measure of the steady-state corrosion current. An in-situ technique would be preferred such as oxidising the evolved hydrogen on platinised nickel foam [58] or on the platinum ring of a rotating ring-disc electrode (RRDE) [37]. The RRDE had a collection efficiency of 22.5 % and consisted of a central aluminium disc as working electrode and a concentric platinum ring. During linear sweep voltammetry, hydrogen evolving from the aluminium disc was oxidised on the platinum ring so as to quantify the corrosion current due to water reduction on the aluminium surface. Such techniques, however, have uncertainties as to whether all the evolved hydrogen is detected, particularly during periods of high hydrogen evolution. Another quantitative technique involves calculating the corrosion current from the volume of evolved hydrogen gas, collected during galvanostatic tests [36]. The corrosion current, I_{cor}, is calculated from the volume of hydrogen using equation (2.5), derived from Faraday's laws of electrolysis and the ideal gas law [66]:

$$I_{cor} = \frac{zFP\dot{V}}{tR_uT} \tag{2.5}$$

Where z is the number of electrons consumed to form hydrogen gas, F is the Faraday constant, P is atmospheric pressure, R_u is the molar gas constant, T is the temperature and $\dot{V}$ is the volumetric rate of hydrogen evolution given by

$$\dot{V} = \frac{(V_{t_2} - V_{t_1})}{(t_2 - t_1)} \tag{2.6}$$

Using Faraday's law, the corrosion current density, j_{cor} is related to the corrosion rate (CR), as follows

$$CR = \frac{j_{cor} M_w}{zF} \tag{2.7}$$

where z is the two electrons consumed to reduce water to hydrogen, F is Faraday's constant, M_w is the molar mass of aluminium, 27 g mol^{-1}, P is atmospheric pressure, V is the volume of hydrogen evolved, t is time for which hydrogen was collected, R_u is the universal gas constant, 8.314 J mol^{-1} K^{-1} and T is the temperature in Kelvin.

In this review, the corrosion currents for alloys reported in the literature are quantitatively compared using two parameters: the open-circuit inhibition efficiency, φ_{inh} and the discharge efficiency, φ_{dis}. The open-circuit inhibition efficiency indicates the percentage difference between the corrosion of the alloy and that of pure aluminium.

$$\varphi_{inh} = \left(\frac{I_{cor,p} - I_{cor,a}}{I_{cor,p}} \right) * 100 \tag{2.8}$$

Where $I_{cor,p}$ and $I_{cor,a}$ are the corrosion currents for pure aluminium and the alloy, respectively, at open-circuit. If the inhibition efficiency of an alloy is positive at open-circuit, then its corrosion current is lower than that of pure aluminium, i.e. $I_{cor,a} < I_{cor,p}$, which is desirable of a suitable anode material in an Al-air battery. An alloy with negative inhibition efficiency indicates that its open-circuit corrosion current is worse than that of pure aluminium. The vector for evaluating the corrosion behaviour of the aluminium alloys under discharge is the discharge efficiency, φ_{dis}, which is the ratio of the discharge current, I, to the sum of discharge and corrosion current, I_{cor},:

$$\varphi_{dis} = \frac{I}{I + I_{cor}} * 100 \qquad (2.9)$$

2.1.2 Choice of electrolyte for aluminium-air cells

The electrolyte used in aluminium-air cells is typically an aqueous alkaline solution such as sodium hydroxide or potassium hydroxide. Neutral saline electrolytes have also been used [1, 5, 56, 67-72], because compared with caustic solutions they exhibit a lower open-circuit corrosion rate and pose a lower risk to health [73, 74]. Carbonation of the alkaline electrolyte by carbon dioxide in the air can impede air access and cause mechanical damage to the gas diffusion electrode [29]. However the higher conductivity and $Al(OH)_3$ solubility of alkaline solutions [56] allows high specific power (175 W kg^{-1}) and energy densities (400 W h kg^{-1}) to be attained compared to saline systems (30 W kg^{-1}, 220 W h kg^{-1}) [24]. This is attractive for high-power applications such as standby batteries together with propulsion of unmanned underwater vehicles and electric vehicles.

Some papers have reported using sulphuric acid as an electrolyte for aluminium-air cells, in which the theoretical cell potential differences are higher than in alkaline electrolytes and carbonation problems for the air electrode can be avoided [75, 76]. However, aluminium is passivated by a relatively thick oxide layer in concentrated sulphuric acid solutions [75], necessitating the addition of Cl^- or F^- ions to partially destroy the oxide through pitting [75, 77]. These ions adversely affect the air electrode by adsorption on the platinum catalyst diminishing the amount of platinum oxide that can be formed and increasing the overpotential for oxygen reduction [75, 78]. Hence, this review will focus on alkaline solutions as electrolytes for aluminium-air batteries.

Preferred electrolytes for aluminium-air batteries are 4 mol dm^{-3} NaOH and 7 mol dm^{-3} KOH, which correspond to their peak electrolytic conductivities [23, 24, 60, 61, 79]. The purity of the electrolyte must be of analytical grade, as any electrolyte impurities such as Fe^{2+} ions would reduce on the aluminium surface creating preferential sites for hydrogen evolution, adversely affecting the corrosion and electrode potential [36, 79]. The peak electrolytic conductivity of 7 mol dm^{-3} potassium hydroxide at 0.7 S cm^{-1} [80], is superior to that of 4 mol dm^{-3} sodium hydroxide, 0.39 S cm^{-1} [79]. Also KOH shows superiority to NaOH

solutions for oxygen reduction because of higher solubility for oxygen, higher oxygen diffusion coefficients and lower viscosity [81]. However KOH solution does not allow the recycling of alumina via the industrial Hall−Héroult process because the potassium ions interfere at the cathode of the electrolysis cell used during the recycling process [21]. This would be important for mass-production of aluminium−air cells requiring the recycling of spent electrolytes [29].

Considering the amount of aluminate reaction product that can dissolve into the electrolyte, aluminate has a solubility of 6 g per 100 g in 7 mol dm^{-3} KOH solution compared to 4 g per 100 g of electrolyte for a 4 mol dm^{-3} NaOH solution [82, 83]. This is an additional benefit of being able to select a higher concentration KOH over NaOH. The solubility of aluminate in the electrolyte is an important consideration for aluminium-air batteries using static electrolytes as when the saturation level for $Al(OH)_4^-$ is reached, it precipitates out as $Al(OH)_3$ also known as the hydrargillite phase. The $Al(OH)_3$ binds to water, reducing its availability for oxygen reduction at the cathode and blocks pores. In water, the diffusion coefficient for OH^- ions is 5.273 cm^2 s^{-1} [84, 85]. The accumulation of the $Al(OH)_4^-$ in static electrolyte aluminium-air batteries results in a viscous gel layer, slowing the diffusion of OH^- ions towards the Al surface and reducing the rate of aluminium dissolution [36]. In addition, the consumption of OH^- ions to form $Al(OH)_4^-$ lowers electrolyte conductivity allowing the hydroxide film to thicken impeding further dissolution [23]. Conductivity rises again once precipitation of $Al(OH)_3$ liberates OH^- ions via reaction 2.13.

To overcome these issues of fluctuating electrolyte conductivity and accumulation of $Al(OH)_3$ at the electrodes, large scale aluminium-air systems typically employ a circulating electrolyte pumped from an external tank. This prevents hydroxide build-up and cathode pore blocking [86], removes hydrogen bubbles from the aluminium surface [21] and allows integration of peripherals such as a heat exchanger or filter/crystalliser unit [40]. A heat exchanger helps to cool down the electrolyte, preventing it from boiling [87], while a crystalliser promotes the crystallisation of $Al(OH)_4^-$ into insoluble $Al(OH)_3$, increasing the OH^- ion concentration, via reaction (2.13). The subsequent rise in electrolytic conductivity helps to maintain a steady cell potential difference for a longer time, enhancing the energy density of the cell for a given electrolyte tank volume [88]. Initial fluctuations in electrolyte conductivity can be avoided by adding seed crystals of $Al(OH)_3$, typically 1 μm in size, to the

electrolyte to saturate it with aluminate. Additional aluminate ions formed during the oxidation of the aluminium anode would immediately precipitate to form aluminium hydroxide [11], which is filtered from the electrolyte [1, 4, 19, 29].

2.1.3 Mechanism of super-pure aluminium corrosion in alkaline solutions

In open atmosphere, the surface of aluminium is covered by a 4 nm thick oxide film of Al_2O_3 [89]. Upon initial immersion of 99.99 wt% aluminium in a 4 mol dm^{-3} sodium hydroxide solution, the Al_2O_3 layer is rapidly dissolved under a high rate of hydrogen evolution as a result of the alkalinisation of the electrode surface [36, 48].

At this point, the electrode potential at open-circuit is −1.69 V *vs.* Hg/HgO as shown in Figure 2.4. Values as negative as −1.73 V *vs.* Hg/HgO are reported in the literature [90]. This is a mixed electrode potential owing to the oxidation of aluminium, the reduction of water and the growth of aluminium hydroxide layer. The surface then undergoes dissolution via a series of 3 one-electron steps and hydroxide addition, leading to the final tri-hydroxide, $Al(OH)_3$ [36]:

$$Al + OH^- \rightarrow Al(OH)_{ads} + e^- \tag{2.10}$$

$$Al(OH)_{ads} + OH^- \rightarrow Al(OH)_{2ads} + e^- \tag{2.11}$$

$$Al(OH)_{2ads} + OH^- \rightarrow Al(OH)_{3ads} + e^- \tag{2.12}$$

An $Al(OH)_3$ film is formed because Al^{3+} ions are thermodynamically unstable in the alkaline solution. The final step involves the dissolution of the hydroxide film forming soluble aluminate ions in the electrolyte and the regeneration of a bare aluminium surface site.

$$Al(OH)_3 + OH^- \rightarrow Al(OH)_4^- \tag{2.13}$$

At the same time, water is reduced on the aluminium surface according to a Volmer−Heyrovsky mechanism [36, 91]. The Volmer reaction (2.14) describes how a water molecule reduces at a cathodic site on the aluminium surface forming an adsorbed hydrogen atom (H_{ads}) on the surface and a hydroxyl ion in the electrolyte. The subsequent Heyrovsky reaction (2.15) describes how this adsorbed hydrogen atom reacts with an additional water

molecule and electron to form a hydroxyl ion and hydrogen that bubbles away from the surface.

$$H_2O + e^- \rightarrow H_{ads} + OH^- \tag{2.14}$$

$$H_{ads} + H_2O + e^- \rightarrow H_2 + OH^- \tag{2.15}$$

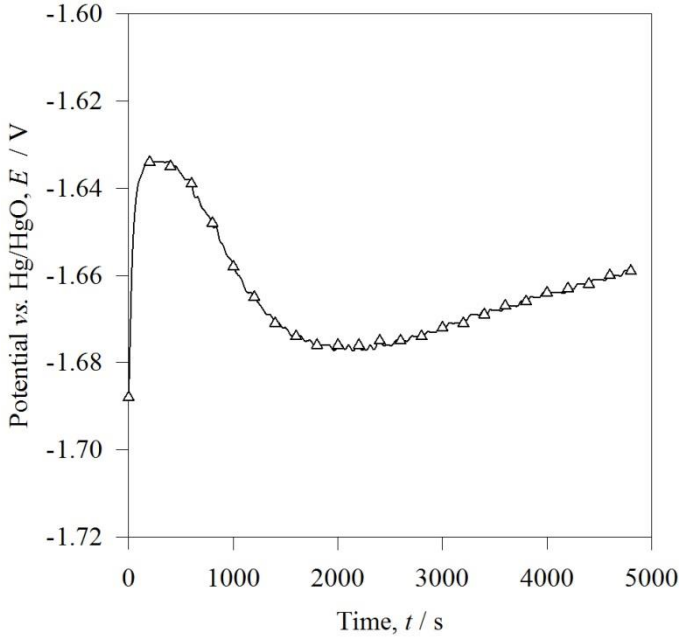

Figure 2.4: Variation of the open-circuit potential of 99.999 % aluminium upon initial immersion in 4 mol dm^{-3} NaOH at 22 °C. Electrode surface ground to a mirror finish prior to immersion.

At longer times, the open-circuit potential shifts to more positive values and eventually stabilises at −1.66 V *vs.* Hg/HgO. This positive shift in open-circuit potential upon initial immersion is due to a lowering of solution pH. As the aluminium oxidises, OH^- ions are consumed at the interface and $Al(OH)_4^-$ ions are produced leading to passivation of the surface by a thicker $Al(OH)_3$ film [36, 57]:

$$2Al + 2OH^- + 6H_2O \rightarrow 2Al(OH)_4^- + 3H_2 \tag{2.16}$$

Anodic discharge of aluminium proceeds via the direct and indirect metal dissolution [57]. The direct dissolution of the aluminium metal involves OH^- ions from the electrolyte migrating through the passive layer, via reaction (2.13) towards the interface between the

aluminium and the hydroxide film [36], incurring resistive losses. The indirect dissolution reaction involves the consecutive film formation and dissolution into $Al(OH)_4^-$.

2.2 Aluminium alloys

The discussion above has shown that super-pure aluminium, in an uninhibited alkaline electrolyte, is unsuitable for use as the anode of an Al-air battery since (i) its surface is covered by a passive hydroxide layer creating high overpotentials during anodic dissolution and (ii) it suffers from high corrosion currents as water reduces on preferential surface sites evolving hydrogen. Alloying aluminium with particular elements improves its electrochemistry or activates it. The purpose of activation is to (a) reduce the overpotential for the oxidation by breaking down the passive hydroxide layer and (b) to increase the overpotential for the reduction of water on the surface.

Aluminium of purity greater than 99.99 wt%, should be used as feedstock for the alloy because impurities such as copper, iron and silicon aggravate self-corrosion [49, 79, 92]. Such contaminants form cathodic sites of localised galvanic cells on the aluminium surface where hydrogen evolves because of their low overpotential for the hydrogen evolution reaction, see Table 2.1 [93, 94]. In purity grades, such as 99.9 wt% aluminium, the levels of impurities such as iron exceed their solubility limit in aluminium and precipitate out as second phase particles; for example Al_3Fe can act as cathodic centres for the generation of hydrogen, resulting in higher corrosion rates of the lower purity grades of aluminium [49, 79].

2.2.1 The influence of alloying elements and activation mechanisms

An effective alloying element should possess the following properties: (i) a melting point below the melting temperature of aluminium (657 °C), (ii) good solid solubility in the aluminium matrix, (iii) a higher nobility than aluminium in the electrochemical series as determined from the Pourbaix Diagram [43, 95], (iv) good solubility in an alkaline electrolyte [49] and (v) a high hydrogen overpotential [19, 96]. These properties are pivotal to the mechanisms by which the alloying elements activate the aluminium in alkaline solutions. Research on alloys for aluminium-air batteries has focused on Mg, Zn, Pb, Sn, Ga, In and Mn as alloying elements, because these elements have lower melting temperatures than aluminium (with the exception of Mn), have a degree of solubility in aluminium, are more noble than aluminium (with the exception of Mg), are soluble in alkaline electrolytes and

have a high hydrogen overpotential, as shown in Table 2.1. The benefit these properties confer to an aluminium alloy anode is discussed below.

	Region of stability in pH 14 electrolyte						
Metal	Reduced species *vs.* Hg/HgO / V		Oxidised species *vs.* Hg/HgO / V		T_m / °C	η_{H2} / V	Solubility limit in Al
Fe				-1.06	1540	0.41	0.025 % at 600 °C
Cu				-0.55	1080	0.59	2.97 % at 600 °C
Pb				-0.83	328	1.05	0.15 % at 658 °C
Bi	BiH_3	-1.70	BiO_2^-	-0.61	272	0.96	< 0.10 % at 657 °C
Cd			$HCdO_2^-$	-1.06	322	0.85	0.25 % at 600 °C
Sb	SbH_3	-1.32	SbO_3^-	-0.90	631	0.70	< 0.10 % at 657 °C
Sn	SnH_4	-2.05	SnO_3^{2-}	-1.27	232	1.00	0.10 % at 600 °C
In				-1.15	157		0.13 % at 600 °C
Ga			$Ga(OH)_4^-$	-1.61	29		6.00 % at 600 °C
Zn			ZnO_2^{2-}	-1.61	420	1.10	14.6 % at 600 °C
Mn				-1.74	1250	0.76	1.03 % at 600 °C
Al			$Al(OH)_4^-$	-2.48	657	0.47	
Mg			$Mg(OH)_2$	-2.79	650	1.47	3.6 % at 600 °C

Table 2.1: The region of stability for metals in pH 14 alkaline electrolytes. Compiled from Pourbaix Diagrams [35], together with hydrogen overpotential and melting temperature for various metals in 6 mol L^{-1} NaOH solution at 25 °C [97, 98]. T_m is melting temperature. η_{H_2} is hydrogen overpotential.

The melting temperature of the alloying element should be lower than that of pure aluminium so as to facilitate its diffusion in the aluminium matrix via solution heat treatment to form a solid solution alloy. A solid solution aluminium alloy is one where the atoms of the alloying element occupy places in the crystal structure that would be occupied by aluminium atoms. Tin, for example, has a melting temperature of 232 °C and a maximum solubility in aluminium of 0.1 % when solution heat treated at 600 °C, as detailed in Table 2.1. Alloying elements will only activate the aluminium when they are in solid solution with the aluminium matrix, yielding higher anodic currents compared to if the alloying elements are present as precipitates [47, 88, 99]. In precipitate form, the alloying elements aggravate the self-corrosion of the aluminium and decrease its discharge efficiency [24, 52, 96]. Heating for 8 hours at 600 °C, followed by rapid cooling or quenching in water to suppress precipitation of alloying elements is a suitable heat treatment to achieve a solid solution alloy [52, 96, 100].

The heat treatment temperature can be determined from the phase diagram of the particular alloy [101, 102].

The third desirable property of the alloying element is that it should be more noble than aluminium in the galvanic series [43, 95]. This is key to the mechanism by which the alloying element activates aluminium in alkaline solutions, the metal dissolution−deposition process [43, 47, 103, 104], which will be described in relation to a binary Al/0.12 Sn solid solution alloy. The anodic behaviour of Al/0.12 Sn is superior to that of pure aluminium, as shown in Figure 2.5, over a potential range corresponding to the region of stability for tin in pH 14 electrolyte i.e. between the SnH_4 / Sn reversible potential of −1.86 V *vs.* Hg/HgO to the Sn / SnO_3^{2-} reversible potential of −1.06 V *vs.* Hg/HgO, predicted by the Pourbaix Diagram [49, 105].

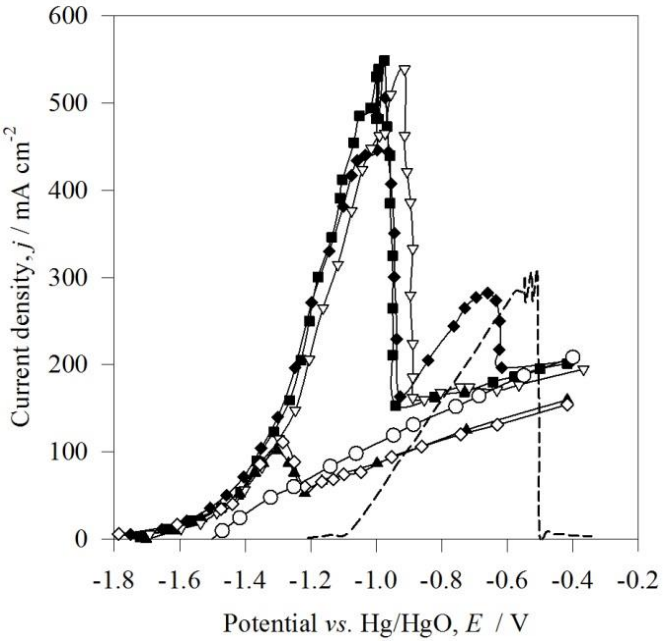

Figure 2.5: Effect of tin concentration on improving the anodic polarisation of binary aluminium alloys compared to pure aluminium in alkaline solutions at 25 °C. Data from rotating disc, potential sweep experiments performed on six Al/Sn alloys in 4 mol dm^{-3} NaOH [25, 49]. Potential was swept from −2.1 V to −0.5 V *vs.* Hg/HgO, but only shown from the open-circuit potential in this graph. Alloys were heat treated at 600 °C for 2 hours followed by a water quench. Electrode area: 0.5 cm^2. Potential sweep rate: 5 mV s^{-1}. 20 Hz rotation speed. Counter-electrode, platinised titanium strip. ○ 99.995 % Al, ▲ Al/0.044 wt% Sn, ◇ Al/0.089 wt% Sn, ■ Al/0.12 wt% Sn, ▽ Al/0.23 wt% Sn, ◆ Al/0.45 wt% Sn, − − − − pure Sn.

As the Al/0.12 Sn alloy undergoes anodic polarisation in Figure 2.5, tin atoms in solid solution become exposed to the electrolyte and subsequently oxidise [95]. These oxidised species of tin are only present in the outermost few monolayers of the aluminium alloy passive film, as indicated by Auger depth profiling in Figure 2.6 [106]. The oxidised tin is soluble in alkaline solutions and dissolves into the electrolyte as stannate ions, SnO_3^{2-}, and if the potential of the alloy is more negative than the Sn/SnO_3^{2-} reversible potential, the SnO_3^{2-} ions reduce at cathodic sites on the aluminium alloy surface to form metallic tin, as illustrated in Figure 2.7 [95]. Auger depth profiling in Figure 2.6 verified that there was a high concentration of metallic tin on the outer surface of the alloy, which gradually decayed towards its bulk value in the metal [106].

The forming of tin deposits serves three functions: (a) it promotes the further dissolution of aluminium alloy, by destabilising the passive layer, (b) it prevents the electrolyte becoming saturated with stannate ions and (c) it reduces the self-corrosion of the aluminium alloy, as tin's overpotential for hydrogen evolution is higher than it is for pure aluminium, as indicated in Table 2.1 [49]. Once the potential of aluminium becomes more positive than the Sn/SnO_3^{2-} reversible potential, the anodic behaviour of the alloy reverts back to the oxidation behaviour of 99.995 % aluminium, see Figure 2.5. This is because SnO_3^{2-} ions in the electrolyte no longer redeposit onto the electrode surface and their concentration in the alkaline electrolyte increases. When the saturation level for SnO_3^{2-} ions in the electrolyte is reached, any further tin atoms in the solid solution alloy that become exposed and oxidised no longer dissolve into the electrolyte and remain on the aluminium surface, passivating it.

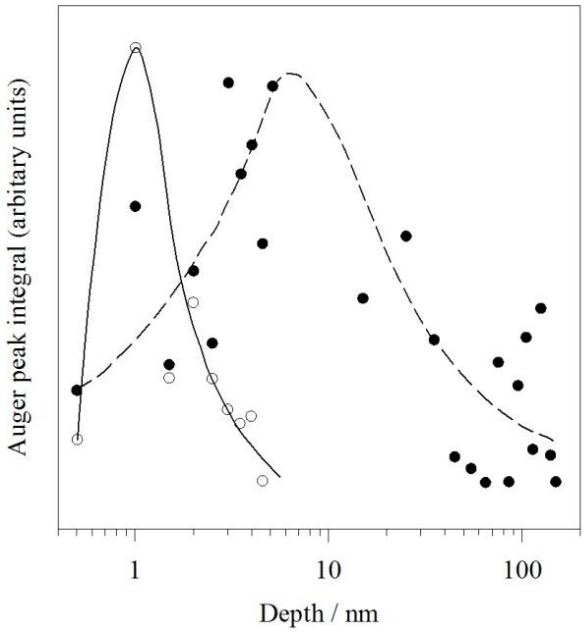

Figure 2.6: Auger depth profiles of oxidised and metallic tin on an Al/0.1 Sn alloy exposed for 1 hour in 1 mol dm^{-3} NaOH at an applied current density of 1 mA cm^{-2} [106]. Depth is measured from the top of the surface hydroxide layer. The alloy was heat treated at 620 °C for 16 hours and water quenched. Electrolyte temperature: 25 °C. ○ oxidised tin, ● metallic tin. (b) The activation mechanism.

An alternative activation mechanism, the point defect effect one [43, 100, 107], proposes that the metal ions of the alloying element are present within the passive layer itself and reduce to form deposits at the interface between the alloy and the passive layer. Local swelling, during growth of these deposits, causes partial destruction and thinning of the passive film forming surface pits. One discrepancy with this mechanism is that it does not explain the activation of pure aluminium solely by metal ions introduced to the electrolyte as additives.

Regardless of the discrepancy between the dissolution−deposition and point defect mechanisms, there is a general consensus that the reduced species of the alloying element is in intimate contact with the base alloy. The observation that the amount of gallium on the surface of an anodically discharged Al/Ga alloy had diminished following several days storage is evidence of back diffusion into the alloy bulk, facilitated by the intimate contact with the gallium and the aluminium alloy. A driving force for back diffusion exists because of the lower concentration of the gallium in the bulk. The diffusion coefficient for gallium in aluminium is 9×10^{-4} cm^2 s^{-1} [100], which proceeds by surface and grain boundary diffusion. Back diffusion could play a determining role as to whether a certain concentration

of an alloying element enhances the anodic behaviour of the aluminium since a particular minimum surface concentration of the reduced metal species must be present to achieve activation [100].

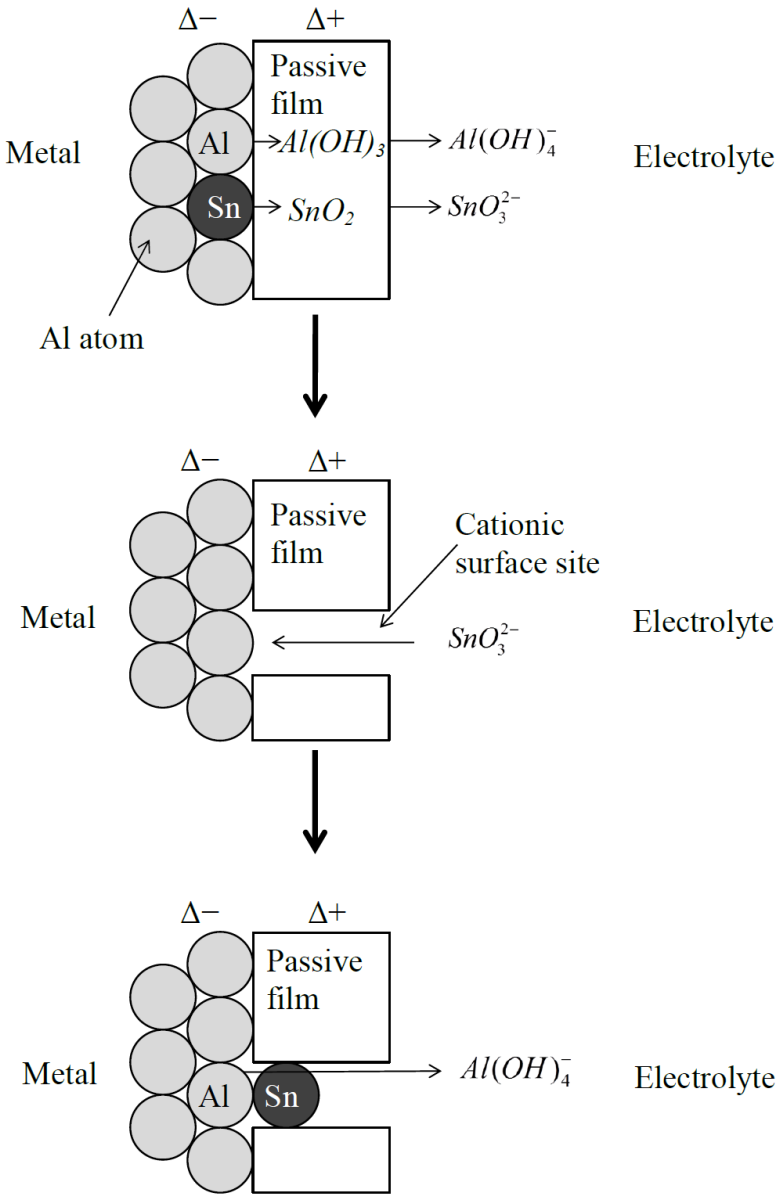

Figure 2.7: Illustration of the dissolution-deposition activation mechanism of aluminium alloys in alkaline electrolyte.

These reduced deposits on the alloy surface are free of a passive hydroxide layer and the aluminium diffuses through them to be oxidised [49, 100, 106]. The deposits are likely in a liquid state owing to the low melting temperature of some of the alloying elements, in particular gallium, and also due to the anodic current concentrating at these surface deposits creating extremely large current densities [42]. Differential scanning calorimetry supports the likelihood of liquid surface deposits through which the aluminium can diffuse [108, 109].

The next section discusses how the anodic behaviour and corrosion of super-pure aluminium alloys in alkaline solutions is influenced by different alloying elements. The alloys discussed were cast using super-pure aluminium base with a minimum purity of 99.99 wt%. Several studies have looked at the effect of alloying elements on more commercially pure aluminium alloys [93, 110-114]. The data on the commercially pure alloys have not been included in this review for the purpose of highlighting the effect of individual alloying elements, without any misreading results from impurities such as iron and copper. Studies where the alloys were not solution heat treated or homogenised prior to testing were not included in this review [21, 103, 115-118], since as discussed above, the alloying elements must be in solid solution to be effective at activating the aluminium alloy surface.

2.2.2 Alloying elements

2.2.2.1 Tin

The dissolution behaviour of Al/Sn binary alloys is influenced by the structure, concentration and electrochemistry of tin along with the electrolyte temperature. The tin must be in solid solution with the aluminium. This is achieved by heat treatment, such as heating at 600 °C for two hours, then water quenching [24, 25, 102, 119]. A water quench involves instantly taking the heat treated aluminium sample from the furnace at 600 °C and dipping into water at 22 °C. Different tin concentrations over the range of 0.044 to 0.45 % tin had different effects on improving the anodic behaviour of Al/Sn alloys compared to pure aluminium. At 25 °C, an Al/0.12 Sn alloy showed the most anodic behaviour in Figure 2.5 among the range of Al/Sn binary alloys in a 4 mol dm^{-3} NaOH solution. This alloy showed enhanced anodic currents compared to pure aluminium over a potential range corresponding to the region of stability for tin, as discussed earlier [49, 105]. The Al/0.12 Sn alloy showed the best anodic behaviour compared to the other tin concentrations because 0.12 wt% tin is the maximum amount of tin that can be accommodated in solid solution in the aluminium matrix. Concentrations of tin lower than 0.12 % in a 25 °C electrolyte most likely had fewer tin deposits formed during the

dissolution−deposition process to accommodate film-free dissolution of aluminium. The alloys with tin levels greater than 0.12 % did not improve the anodic current peak at −1.0 V *vs.* Hg/HgO in Figure 2.5 because the excess tin, that couldn't be accommodated in the solid solution, was present as second phase particles or precipitates. These precipitates were present on the grain boundaries and are ineffective at activating aluminium, as discussed earlier [49]. The anodic peak at −0.66 V *vs.* Hg/HgO in Figure 2.5 for Al/0.45 Sn alloy was due to the oxidation of these precipitates, which resulted in pronounced grain boundary attack and potential disintegration of surface grains upon anodic discharge, as verified under the SEM [49].

Since the maximum solubility limit of 0.12 % Sn changes when alloying with a ternary element, lower concentrations of tin would be required when forming a ternary or quaternary alloy to ensure a solid solution can be achieved. The effect of lower tin concentrations is strongly influenced by the electrolyte temperature. At 25 °C, low tin concentrations did little to improve upon the anodic currents observed for pure aluminium, shown in Figure 2.5, whereas at 60 °C binary alloys with concentrations ranging from 0.022 up to 0.12 % Sn showed identical anodic behaviour [49]. This is indicated by the marginal differences among the galvanostatic discharge potentials shown in Table 2.2. It was the corrosion behaviour that was the segregating feature among the tin concentrations at 60 °C, with Al/0.12 Sn exhibiting the highest inhibition and discharge efficiencies, as shown in Table 2.2.

Why some Al/Sn alloys were active at 60 °C and not at 25 °C, can be explained by the higher solubility of aluminate with increasing temperature allowing more of the $Al(OH)_3$ passive film to dissolve into the electrolyte [36, 103]. The subsequent thinner passive film allowed easier transfer of OH^- ions to pass through it quickening the rate of aluminium dissolution [23]. However a thinner passive film also lowers resistance to the conduction of electrons to the cathodic sites on the aluminium surface, where they are consumed by the reduction of water evolving hydrogen [91]. Consequently, the corrosion current also increases. The improved anodic behaviour at the elevated temperature may also be due to a faster rate of diffusion of aluminium through the surface tin, higher solubility for the SnO_3^{2-} ion in the electrolyte and the reversible potential for Sn / SnO_3^{2-} may be shifted more positive. This would also explain why the potential range of enhanced anodic behaviour observed in the anodic polarisation curves at 25 °C was absent at 60 °C, under the experimental conditions.

2.2.2.2 Gallium

The electrochemistry of Al/Ga alloys in alkaline electrolytes is dependent on the gallium content in the alloy, the electrolyte temperature and the electrochemistry of gallium. At an electrolyte temperature of 25 °C, gallium contents of 0.055 wt% or higher were required to enhance the anodic currents of pure aluminium, see Figure 2.8(a) [49]. At 60 °C, at least 0.1 % Ga was required to achieve a more active behaviour than pure Al, as shown in Figure 2.8(b). A certain level of surface gallium is required to activate the aluminium [100]. Whether an alloy achieves this critical level is dependent on the rate of dissolution of the aluminium, the formation of gallium deposits via the dissolution−deposition process and the rate of back diffusion of gallium from the surface into the alloy bulk.

The corrosion behaviour of Al/Ga alloys in an alkaline electrolyte at 60 °C is shown in Table 2.2 [49, 99]. At open-circuit, the corrosion rate of all the binary Al/Ga alloys was extremely high with very negative inhibition efficiencies. The effect of gallium content on discharge efficiency was dependent on whether the alloy was activated or not, with the activated alloys showing very poor discharge efficiencies, i.e. those with gallium levels above 0.1 %. In the case of Al/2.3 % Ga, scanning electron microscopy examination showed that it suffered severe grain boundary attack leading to disintegration. Activation of Al/Ga alloys coincided with gallium deposits found at the base of pits on the alloy surface, as confirmed by energy dispersive x-ray analysis, and on top of the surface hydroxide layer [100]. The evidence of pits on the surface of an Al/0.05 Ga alloy in Figure 2.9(a), in a 4 mol dm^{-3} NaOH solution at 60 °C flowing at 500 cm^3 min^{-1}, indicates that the anodic current is concentrated at very small sites on the surface [120, 121]. Prolonged discharge saw pit growth and coalescence of the pits [100]. The flowing electrolyte in this example, 500 cm^3 min^{-1}, did not hinder the pit growth. At 60 °C, the gallium deposits at the base of the pits would have been in a liquid state, allowing the underlying aluminium to diffuse through it to be oxidised. Diffusion coefficients for aluminium through liquid gallium of 0.64 cm^2 s^{-1} have been reported in the literature [100]. Corrosion data for Al/Ga alloys at 25 °C or other intermediate temperatures was not evident in the literature. It is likely that at temperatures below the low melting temperature of gallium, 29 °C, the diffusion of aluminium through solid gallium deposits would be slower and hence the rate of water reduction and corrosion would be less [100].

Alloy	% Inhibition efficiency at open circuit	% Discharge efficiency under galvanostatic discharge				Electrode potential during galvanostatic discharge			
	% φ_{inh}	% φ_{dis} at j in mA cm^{-2}				*E vs.* Hg/HgO / V			
		50	200	300	600	E_{oc}	E_{50}	E_{200}	E_{600}
Binary alloys									
Tin									
Al/0.022 Sn [a]	-597	9	12			-1.78	-1.79	-1.70	
Al/0.044 Sn [a]	26	15	45				-1.73	-1.67	
Al/0.089 Sn [a]	44	25	62			-1.77	-1.74	-1.62	
Al/0.12 Sn [a]	67	35	68			-1.70	-1.73	-1.63	
Gallium									
Al/0.013 Ga [a]	-370			58		-1.78			
Al/0.026 Ga [a]	-1370			61		-1.85			
Al/0.055 Ga [a]	-1627			50		-1.86			
Al/0.10 Ga [a]	-4324			7		-1.85			
Al/0.24 Ga [a]	-2839			7		-1.89			
Al/2.3 Ga [a]	-7036			3		-1.89			
Indium									
Al/0.02 In [a]	65	35	63			-1.88	-1.78	-1.68	
Al/0.037 In [a]	85	51	65			-1.85	-1.76	-1.72	
Al/0.074 In [a]	95	7	40			-1.80	-1.78	-1.71	
Al/0.16 In [a]	88	5	23			-1.77	-1.78	-1.72	
Al/0.21 In [a]	26	5	21			-1.79	-1.78	-1.70	
Al/0.42 In [a]	96	5	21			-1.74	-1.77	-1.70	
Al/0.15 Mn [b]	76		55		passive	-1.69		-1.52	
Al/0.04 Fe [b]	-89		40		74	-1.45		-1.39	-1.34
Al/0.81 Mg [b]	-1876		4		11				

Table 2.2: The open-circuit corrosion characteristics and discharge efficiencies of various binary aluminium alloys in half-cell tests at 60 °C. References [a] [25, 49], [b] [52, 122]. Electrolyte: 4 mol dm^{-3} NaOH. Solution heat treatments: 600 °C for [a] 2 h and [b] 8 h followed by water quench. φ_{inh} is the inhibition efficiency at open-circuit, defined as the percentage change of the corrosion current of the alloy compared to that of pure aluminium. φ_{dis} is the discharge efficiency.

This contrasts with the surface of 99.999 % aluminium in Figure 2.9(b) which was characterised by a network of broad shallow pits of between 3 and 10 μm diameter [49]. These pits were formed via galvanic corrosion initiated by a potential difference on the aluminium surface [120, 121]. Si, Fe and Cu, left from the manufacturing process, reduced and concentrated on cathodic regions of the aluminium surface. These regions formed the boundaries of the subsequent shallow pits, as confirmed by the EDX profile for one of the boundaries in Figure 2.9(b). This explains why the boundaries of the pits were brighter than the pit centres. With Cu and Fe now reduced at the pit boundaries, the pit centres which were covered by a passive hydroxide layer formed the anode of the galvanic cell. At the pit centres, OH^- ions migrated through the hydroxide layer to oxidise the underlying aluminium. The released electrons were conducted through the external circuit but also towards the pit boundaries, which were more cathodic or positive to the pit centres. Here the electrons were consumed by the reduction of water to evolve hydrogen. The hydrogen evolution reaction generated OH^- ions maintaining a high pH at the boundaries, preventing their passivation. The pits on the 99.999 % Al surface were broad, shallow and interconnected indicating the anodic current density was reasonably distributed across the whole aluminium surface.

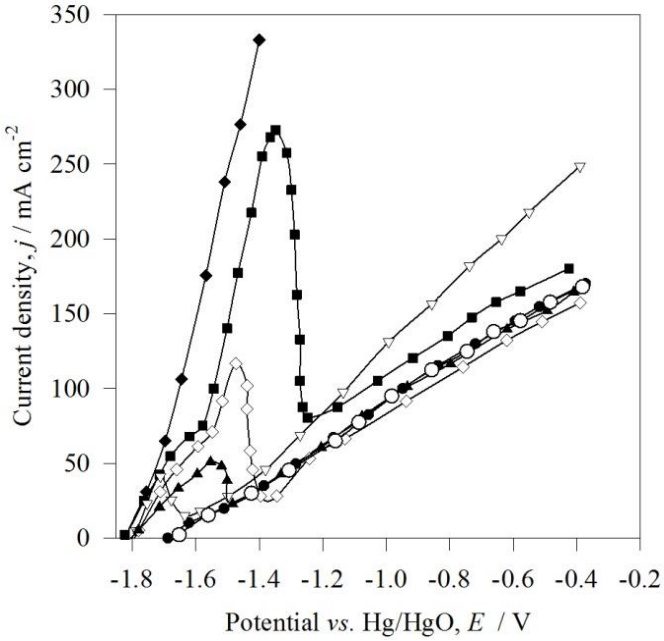

(a)

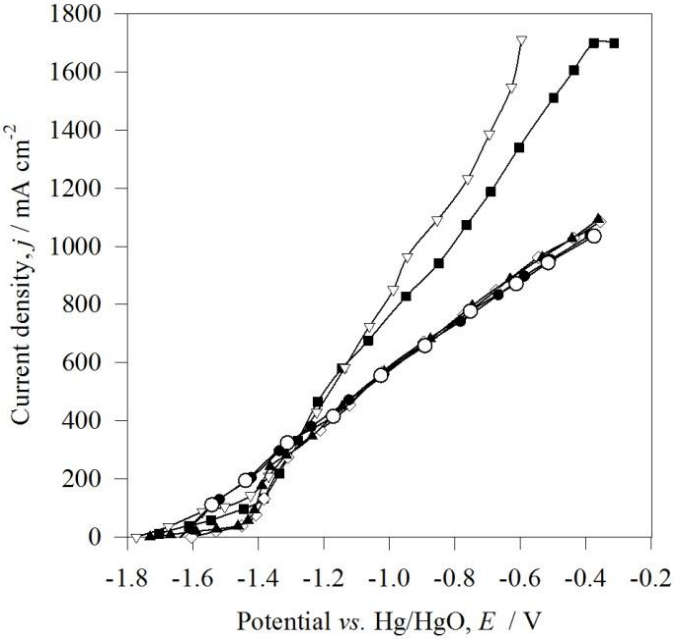

(b)

Figure 2.8: Effect of gallium content on the polarisation behaviour of Al/Ga alloys in a 4 mol dm^{-3} NaOH solution at (a) 25 °C and (b) 60 °C [49]. Results from rotating disc electrode tests. Electrode area: 0.5 cm^2. Potential sweep rate: 5 mV s^{-1}. Rotation speed: 20 Hz. Counter-electrode: platinised titanium strip. Alloys were heat treated at 600 °C for 2 hours followed by a water quench. ○ 99.995 % Al, ● Al/0.013 % Ga, ▲ Al/0.026 % Ga, ◇ Al/0.055 % Ga, ■ Al/0.10 % Ga, ▽ Al/0.24 % Ga, ◆ Al/2.3 % Ga.

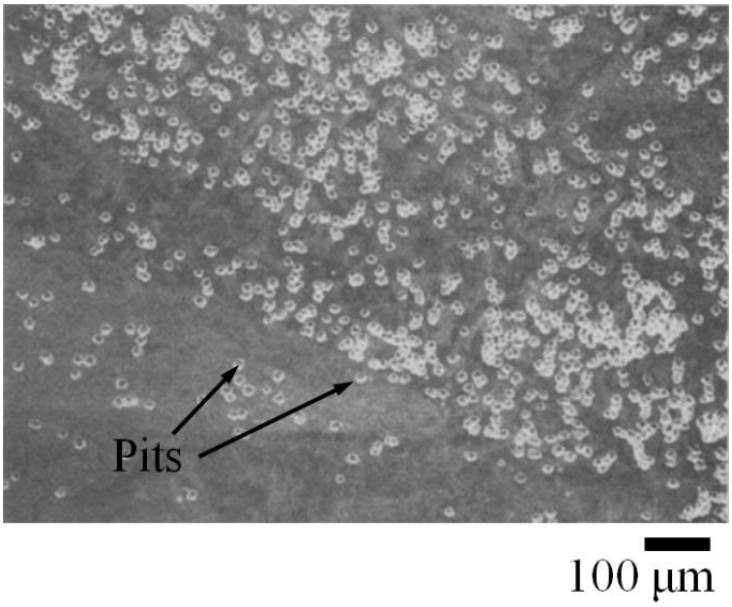

(a)

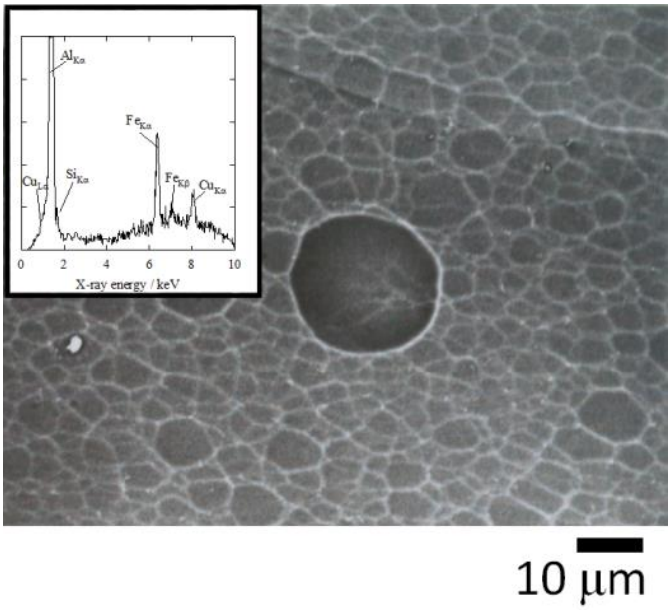

(b)

Figure 2.9: Comparison of the surface morphology of Al/0.05 % Ga alloy and 99.999 % Al under galvanostatic discharge. (a) SEM image of Al/0.05 Ga alloy discharged with a 100 Ω load 4 s after activation [100]. Discharge in a micro Al-air cell with a 4 mol dm^{-3} NaOH solution at 60 °C and flowrate of 500 cm^3 min^{-1}. Anode area: 1 cm^2. Co-catalysed air cathode supplied by Electromedia Corp. Alloy heat treated at 600 °C for at least 2 hours followed by a water quench. (b) Back scatter electron image of 99.999 % Al discharged at 300 mA cm^{-2} for 5 minutes in an Al-air cell [49]. Inset: EDX of the boundary of the large shallow pits.

2.2.2.3 Indium

The electrochemistry of Al/In alloys is dependent on the amount of indium in the alloy, the electrolyte temperature and the electrochemistry of indium [49, 99]. The desirable amount of indium in a binary aluminium alloy for use in aluminium-air batteries is 0.16 %, which is close to the solid solubility limit for indium in aluminium at a heat treatment temperature of 640 °C. Al/0.16 In showed the highest anodic currents in a solution of 4 mol dm^{-3} NaOH at 25 °C compared to other indium compositions examined over the range 0.02 to 0.42 %, see Figure 2.10(a) [49]. Higher indium concentrations of 0.21 % and 0.42 % showed no further improvement in the anodic behaviour, indicating that the polarisation behaviour was entirely controlled by the indium present in solid solution rather than by second phase particles or precipitates. The anodic linear sweep curves for Al/0.21 In and Al/0.42 In were identical to that of Al/0.16 In and are excluded from Figure 2.10 to simplify the graphs.

Indium concentrations lower than the maximum solubility level only showed more active behaviour at an elevated temperature of 60 °C, as indicated in Figure 2.10(b), or by increasing the electrolyte flow rate [49]. The enhancement in anodic behaviour with increase in electrolyte flow indicates that the alloys behaviour is not limited by the surface charge transfer, as is the case for pure aluminium in 4 mol dm^{-3} NaOH [23, 36, 79]. Increasing electrolyte flow rate results in fast supply of OH^- ions to the metal/solution interface and rapid removal of $Al(OH)_4^-$ ions away from the aluminium surface, allowing more of the $Al(OH)_3$ layer to dissolve into the electrolyte, see reaction (2.13) [57]. Among the literature, there has been no rotating disc electrode study evaluating the effect of rotation rate on the anodic and cathodic behaviour of aluminium alloys in alkaline solutions.

In terms of corrosion behaviour of Al/In alloys at 60 °C, the data in Table 2.2 shows that inhibition and discharge efficiencies for Al/In alloys are dependent on the percentage of indium in solid solution. The Al/In alloys with the lowest indium concentrations showed the higher discharge efficiencies. In general the corrosion/hydrogen evolution behaviour of Al/In alloys is very complex depending on the discharge time, current density, indium level and the degree of surface roughening [49].

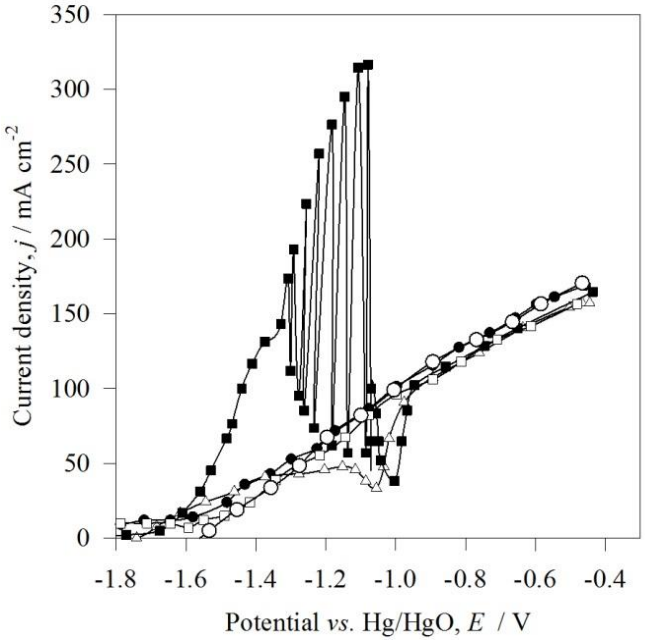

(a)

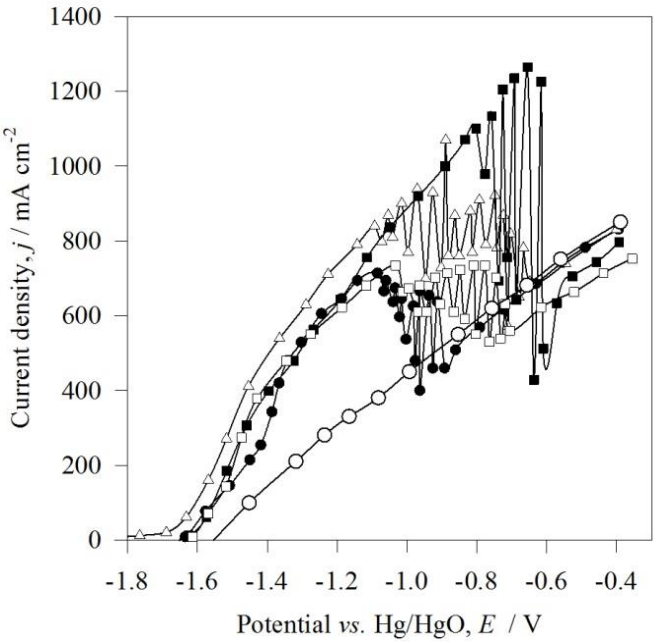

(b)

Figure 2.10: Effect of indium concentration on the polarisation behaviour of Al/In electrodes in 4 mol dm^{-3} NaOH at (a) 25 °C and (b) 60 °C [49]. Results from rotating disc electrode tests. Electrode area: 0.5 cm^2. Potential sweep rate: 5 mV s^{-1}. Rotation speed: 20 Hz. Counter-electrode: platinised titanium strip. Alloys were heat treated at 600 °C for 2 hours followed by a water quench. ○ 99.995 % Al, ● Al/0.02 In, □ Al/0.037 In, △ Al/0.074 In, ■ Al/0.16 In.

Figure 2.10 shows that there is a potential range over which the Al/In alloys exhibit enhanced anodic currents compared to pure aluminium. This potential range corresponds with the region of stability of indium metal in pH 14 electrolyte predicted by the Pourbaix Diagram, as discussed earlier for Al/Sn alloys. The surface of Al/In alloys with enhanced anodic behaviour changed as discharge progressed. Initially the surface would be uniformly pitted with indium agglomerates at the base of the pits. Areas of the alloy surface with indium agglomerates present showed enhanced dissolution compared to areas of the surface not covered with indium, which showed more passive behaviour. As discharge continued, the surface would become characterised by a network of shallow scallops and be heavily covered in indium agglomerates of $0.5 - 5$ μm diameter. These indium deposits on the surface of the passive layer were the active sites causing local destruction of this layer [63, 123].

The anodic polarisation curve for Al/0.16 % In alloy at 25 °C in Figure 2.10(a) exhibited periodic current fluctuations between −1.3 and −1.05 V *vs.* Hg/HgO, indicating that the alloy was alternating between a more active state and the state exhibited by pure aluminium. These fluctuations could have been caused by successive destruction and build-up of a passive hydroxide layer due to local variations in pH at the active sites [63]. A more likely reason to account for these fluctuations is variations in the local concentration of indate in the alkaline electrolyte [49]. As the aluminium and indium dissolved from the alloy into the electrolyte, the local concentration of indate, InO_2^-, increased and eventually reached saturation in the electrolyte. At this point any further oxidised indium remained on the alloy surface as In_2O_3, passivating the active sites. After a brief period of time when the local indate concentration fell below the solubility limit in the electrolyte (by diffusion or convection), the In_2O_3 on the alloy surface could then dissolve into the electrolyte and the rate of oxidation of the alloy increased again. There were similar current fluctuations for an Al/Sn alloy in Figure 2.5, but they were lower than that observed for the Al/In alloys because SnO_3^{2-} is more soluble in pH 14 media than InO_2^-. Similarly GaO_3^{2-} is more soluble in alkaline electrolyte than either SnO_3^{2-} or InO_2^-, explaining why the Al/Ga alloys showed no current fluctuations in Figure 2.8(a). This hypothesis for the observed current fluctuations bolsters the theory that the mechanism of activation of aluminium alloys in alkaline electrolyte is controlled by the dissolution−deposition process i.e. the oxidation of the alloying element into the electrolyte and the subsequent reduction of the oxidised species from the electrolyte onto a cathodic site on the alloy surface.

The data in Figure 2.5, Figure 2.8 and Figure 2.10 was from rotating disc electrode studies to simulate a flowing electrolyte environment. Compared to in a static electrolyte, in a flowing electrolyte environment mass transport will be enhanced. The diffusion of OH^- ions towards the aluminium surface being oxidised will be enhanced. There would be increased diffusion of aluminate ions away from the oxidised surface preventing build-up of aluminate at the electrode surface and therefore promoting further dissolution of the aluminium hydroxide layer. There would also be enhanced diffusion of the dissolved alloying element from the electrode surface preventing local saturation of that species. These would help promote steady dissolution of an aluminium anode over the duration of discharge of an aluminium-air cell with a flowing electrolyte.

2.2.2.4 Other binary aluminium alloys

Examining other binary alloying elements, 0.15 % Mn reduced the self-corrosion of 99.99 % Al with an inhibition efficiency of 76 % at open-circuit, shown in Table 2.2, and enhanced the anodic behaviour with a very negative potential of −1.52 V *vs.* Hg/HgO at 200 mA cm^{-2}. The drawback is that Mn aggravated the parasitic corrosion during discharge, with a discharge efficiency of 55 % [52]. Using manganese as an alloying element has been shown to reduce the rate of corrosion of 99.9 % aluminium which contains high levels of iron [88].

The linear sweep voltammograms for a range of other binary aluminium alloys are shown in Figure 2.11. These alloying elements seem to have no improvement on the anodic behaviour of pure aluminium because their alloying levels are well below their solid solubility limit, listed in Table 2.1. A potential investigation could examine if there is any improvement in anodic behaviour if the alloying levels of the elements in Figure 2.11 were increased to the limit of their solid solubility in aluminium.

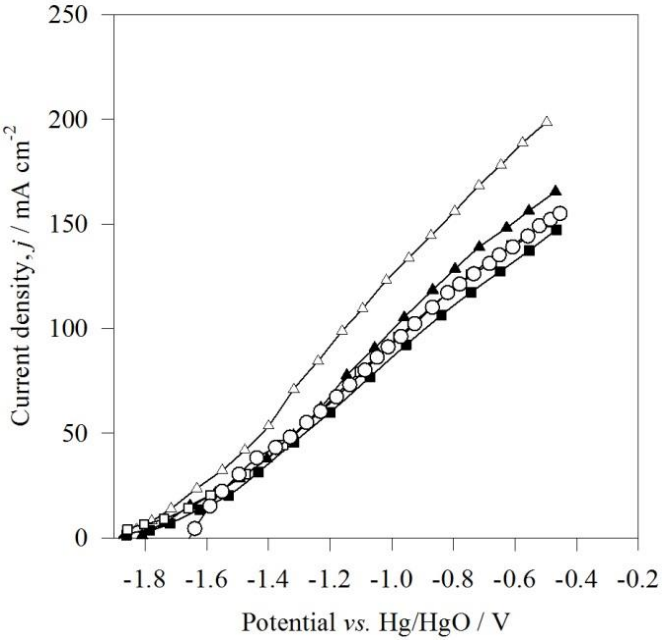

(a)

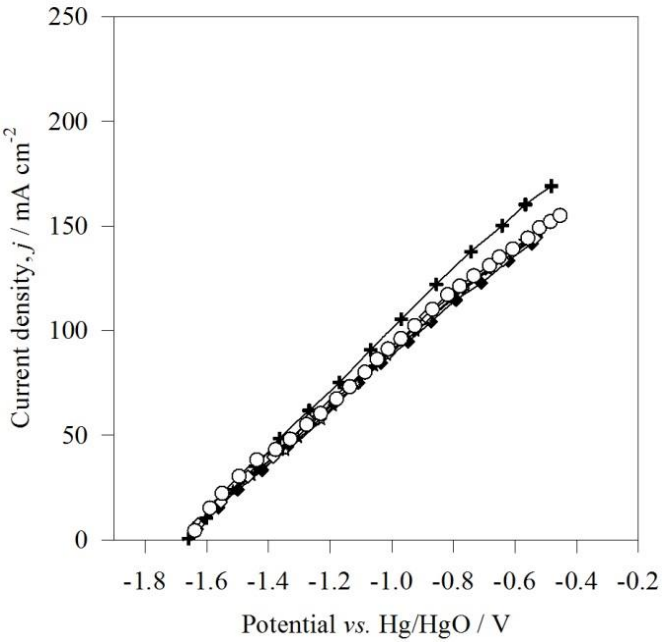

(b)

Figure 2.11: Anodic linear sweep voltammograms of other binary aluminium alloys in 4 mol dm^{-3} NaOH solution at 25 °C [49, 124]. Results from rotating disc electrode tests. Electrode area: 0.5 cm^2. Potential sweep rate: 5 mV s^{-1}. Rotation speed: 20 Hz. Counter-electrode: platinised titanium strip. Alloys were heat treated at 600 °C for 2 hours followed by a water quench. (a) ○ 99.995 % Al, △ Al/0.004 P, ▲ Al/0.02 Sb, ■ Al/0.02 Cd, □ Al/0.004 C. (b) ○ 99.995 % Al, ◆ Al/0.01 Bi, + Al/0.01 Zn, ★ Al/0.005 Si, ✯ Al/0.02 B, ◇ Al/0.04 Ge.

Some binary aluminium alloys such as Al/Zn exhibit open-circuit potentials close to the potential at which the alloying element is oxidised in alkaline solutions. In comparison, other alloying elements like indium and tin shift the open-circuit potential of aluminium towards the potential at which they are reduced in alkaline solutions. This may be due to indium and tin having a wider stability window than zinc in alkaline solutions and the more negative potential of the aluminium base shifts the potential of the tin and indium towards their reversible reduction potentials. In the case of lead, heat treatment of an Al/0.006 Pb alloy at 630 °C followed by water quenching showed that lead has a tendency to become enriched at the aluminium oxide interface, as indicated by depth profiling [125]. The segregations formed because of the extremely small solid solubility of lead in aluminium [125].

The addition of magnesium to aluminium improves its impurity intolerance most probably because the magnesium forms compounds with elements like silicon, preventing them from reducing on cathodic sites to act as centres for hydrogen evolution [11, 91]. It also improves the mechanical properties of aluminium such as its hardness and strength [91, 126]. A magnesium concentration of 0.81 % significantly aggravated the self-corrosion of 99.99 % Al at open-circuit and during discharge with a discharge efficiency of 4 %, as indicated in Table 2.2 [52]. As Mg is more anodic than aluminium, it will not redeposit from the electrolyte at the cathodic sites on the aluminium surface. These sites are left exposed to the solution upon which water reduces, evolving hydrogen gas. The characteristics of the passive films formed on Al/Mg alloys were investigated using in-situ ellipsometry [127]. Those results are not detailed here because limitations of the technique meant the use of potentials more positive than those experienced by the aluminium anode in an aluminium-air battery [127, 128].

2.2.2.5 Ternary and quaternary aluminium alloys

Several studies have shown that the discharge and polarisation characteristics of alloys containing two or more alloying elements are controlled by one dominant species [49, 123]. There exists a dominance sequence among tin, indium and gallium, with tin being dominant in an Al/Sn/In/Ga alloy and indium being dominant in an Al/In/Ga alloy. This dominance was verified by overlapping anodic polarisation curves between ternary or quaternary alloys and the binary alloy of the dominant species. The dominance sequence corresponds with the order of the melting points of the alloying elements and their rate of diffusion. As the oxidised alloying elements plate out from the electrolyte onto the surface of the aluminium

alloy, a concentration gradient of the alloying element is set up, with a high concentration on the surface, decreasing towards the bulk of the alloy. This concentration gradient provides a driving force for the diffusion of the alloying element from the surface towards the bulk. The higher the melting point of an element in a solid solution alloy with aluminium, the slower its back diffusion from the surface of the alloy [49]. This extends its retention on the surface allowing it to control the thinning of the passive film and diffusion of aluminium towards a film-free surface to be oxidised. The dominance of one element upon the discharge characteristics does not mean that it is the only one retained as an agglomerate on the alloy surface. In the case of Al/Sn/In/Ga alloy, all three alloying elements were retained upon the surface after discharge.

Researchers have tested a variety of ternary and quaternary aluminium alloys, of which the corrosion and anodic discharge characteristics are compared in Table 2.3. The general aim, when alloying different elements together with aluminium, was to improve upon the behaviour of the binary alloys discussed above, such as to enhance the anodic currents delivered by Al/Sn alloys or to reduce the self-corrosion of Al/In alloys. An alloy that received much attention was named Alloy BDW, Al/0.84 Mg/0.13 Mn/0.11 In [52]. It attained discharge efficiencies over 90 % at 600 mA cm^{-2} at a potential of −1.64 V *vs.* Hg/HgO in a solution at 60 °C, which is one of the highest performance among the alloys evaluated in Table 2.3.

The aluminium alloy optimised for an Alupower™ battery was 99.999 % aluminium alloyed with 0.07 wt % tin and 0.5 wt % magnesium, known as EB50V [21, 24]. Its discharge efficiencies exceeded 90 % at current densities above 50 mA cm^{-2}, see Table 2.3. These efficiencies were higher than those attained by a binary Al/Sn alloy. Perhaps the magnesium is contributing to reducing the parasitic corrosion when added to an Al/Sn alloy [127]. The composition of this alloy was optimised for use under these nominal conditions: 8 mol dm^{-3} KOH, 60 °C with addition of 0.01 mol dm^{-3} sodium stannate as a corrosion inhibitor [21].

All the aluminium alloys in Table 2.3 were evaluated at an elevated temperature of 60 °C which is the optimum temperature for an aluminium-air system [26]. This is due to enhanced oxidation of aluminium and its alloys in alkaline electrolyte at higher temperature. This is because of a thinner passive film, faster diffusion of aluminium through surface deposits of the alloying element and faster back plating of the dissolved alloying element from the

electrolyte. For example an Al/0.12 Sn alloy had a potential of −1.63 V *vs.* Hg/HgO at 200 mA cm^{-2} at 60 °C (Table 2.2) compared to −1.22 V *vs.* Hg/HgO at the same current density at 25 °C (Figure 2.5). Among the research that adhered to the sample preparation requirements regarding solution heat treatment, none of them carried out tests at intermediate temperatures between 20 and 60 °C. An alloy attaining high discharge rates at 60 °C, may not attain the same anodic currents at room temperature, as shown for Al/Ga alloys in Figure 2.8. This is significant for small scale Al-air batteries in the several watts range employing a simple static electrolyte system at ambient temperature upon start-up. If the system is starting from room temperature, an applicable alloy would have to be chosen. If an alloy from Table 2.3 is selected, external pre-heating of the electrolyte may be feasible to activate the alloy or a run-in time would have to be accommodated for as the electrolyte heats up. Experiments have shown that during discharge the electrolyte temperature will increase from 20 to 60 °C after at least 1 hour discharge [26].

Alloy	% Inhibition eff. at open circuit	% Discharge efficiency under galvanostatic discharge				Electrode potential during galvanostatic discharge			
	% φ_{inh}	% φ_{dis} at j in mA cm^{-2}				*E vs.* Hg/HgO / V			
		50	200	300	600	E_{oc}	E_{50}	E_{200}	E_{600}
Ternary & Quaternary Alloys									
Al/0.5 Mg/0.07 Sn [i] (EB50V)			99		99				
Al/0.84 Mg/0.13 Mn/0.11 In [ii] (Alloy BDW)	94		91		90	-1.70		-1.69	-1.64
Al/0.12 Mn/0.11 In [ii]	79		86		88	-1.76		-1.79	-1.58
Al/0.8 Mg/0.097 In [ii]	96		87		87	-1.70		-1.70	-1.59
Al/0.40 Mg/0.04 Ga/0.10 Sn [ii] (AB50V)	60		86		100	-1.73		-1.63	-1.63
Al/0.1 Ga/0.1 In/0.1 Pb [iii]	90								
Al/0.14 Mn/0.84 Mg [ii]	-1876		4		11				
Al/0.80 Mg/0.04 Ga [ii]	-1876		4		11	-1.87		-1.73	-1.65

Table 2.3: The open-circuit corrosion characteristics and discharge efficiencies of various ternary and quaternary aluminium alloys in half-cell tests at 60 °C. References [i] [24], [ii] [52, 122], [iii] [129]. Solution heat treatments: 600 °C for [ii] 8 h and [iii] 4 h followed by water quench. φ_{inh} is the inhibition efficiency at open-circuit. φ_{dis} is the discharge efficiency.

2.2.3 Grain size

The effect of grain size on the corrosion and anodic behaviour of aluminium alloys in alkaline solutions was not discussed in the above studies. It may be an important point to consider as the grain size of the alloys will vary depending on the duration of the solution heat treatment. A fine-grained structure will have a high density of inter-crystalline areas such as grain boundaries and triple junctions which increase the reactivity of the surface through increased electron activity and diffusion [130]. Passive film formation and adhesion would improve as a result, reducing the alloy's anodic behaviour. Also the enhanced diffusion may reduce the length of time at which surface deposits of the alloying element, formed via the dissolution−deposition mechanism, are retained on the surface. This would dictate whether a particular minimum surface concentration of the reduced metal species is retained on the surface to reach activation [100]. Other factors to consider include the processing route used to manufacture the electrodes, because this leads to microstructural changes, develops alloy texture and introduces internal stresses, which may impart cracks into the passive film [130, 131].

2.3 Effect of electrolyte additives on an aluminium anode

Manufacturing super-pure aluminium alloys with trace amounts of elements such as tin, magnesium and indium is expensive. An alternative method of reducing the corrosion of aluminium in alkaline solutions, without adversely affecting its dissolution characteristics, is to add inhibitors to the electrolyte [60]. They are advantageous because (a) they allow inexpensive scrap aluminium to be used as anodes instead of expensive high-purity aluminium alloys, (b) they increase the overpotential for parasitic hydrogen evolution [36] and (c) inhibition of the cathodic water reduction reaction shifts the open-circuit potential of the aluminium to more negative values [60]. The solution phase inhibitors chosen are typically the same as the elements used to form the high-purity aluminium alloys [60]. Additives can also be added to cause the aluminium hydroxide to form into a crystalline powder form, falling to the bottom of the cell leaving the reaction surface at the anode clear and active [132].

Gallium as an alkaline electrolyte additive was found not to be viable as a solution phase inhibitor as it resulted in the rapid corrosion and consumption of the aluminium [60]. Difficulties associated with employing solution phase additives include: (i) electrolyte

composition change and (ii) formation of large insoluble precipitates which could block and short-circuit the cells as well as interfere with the performance of the air cathodes and the precipitation kinetics of $Al(OH)_3$ [96]. This section examines the effect of electrolyte additives on the electrochemical behaviour of pure aluminium, of 99.99 % purity or higher, unless otherwise stated. Studies which investigated the effect of additives on commercial grade aluminium alloys have not been included in this review [133].

2.3.1 Stannate ion

Stannate, SnO_3^{2-}, has varying effects on the corrosion and dissolution of 99.99 % aluminium in alkaline solutions, depending on the quantity used. Among a range of concentrations in a 4 mol dm^{-3} KOH solution at 50 °C, 1×10^{-3} mol dm^{-3} Na_2SnO_3 was found to be ideal, as it showed discharge efficiencies as high as 95 %, see Table 2.4. The tin plated out of the electrolyte onto cathodic sites on the surface of the aluminium inhibiting the water reduction reaction [60]. A concentration of 1×10^{-3} mol dm^{-3} Na_2SnO_3 also resulted in the least change in anodic behaviour of 99.99 % Al under galvanostatic discharge, as indicated in Table 2.4 [60]. There is no evidence of a well-defined potential range over which the stannate ion exerts an effect on the aluminium at 50 °C, corresponding to the stability range for tin. Comparison with the anodic behaviour of Al/Sn binary alloys in Figure 2.5 indicates that this defined potential range, is only observed at 25 °C and not at elevated temperatures.

At stannate concentrations greater than 1×10^{-2} mol dm^{-3}, tin plating on the aluminium may give rise to dendritic growths which would short circuit the battery or damage any electrolyte circulation system [24, 52]. The stannate interferes with electrolyte management by making it difficult to maintain the required electrolyte concentration due to the precipitation of Sn in insoluble oxides [99]. It can also retard the growth of aluminium hydroxide crystals reducing the efficiency of any regenerative crystalliser unit [24, 52, 96]. An aluminium-air cell using stannate as an inhibitor in a 7.5 mol dm^{-3} KOH solution had an energy density of 106 W h kg^{-1} [87], which is approximately one-quarter of the energy density of commercial Al-air cells.

2.3.2 Indate ion

Additions of $In(OH)_3$ are beneficial for enhancing the anodic behaviour of 99.99 % aluminium as shown in Table 2.4, with 1×10^{-2} mol dm^{-3} $In(OH)_3$ inducing the most negative potentials at a given discharge current. In a similar fashion to Al/In alloys, indium

hydroxide additives exerted an influence over 99.99 % Al over a defined potential range corresponding to its region of stability. Within this potential region, indium plated out of the electrolyte onto the aluminium surface, helping to break down the passive hydroxide layer to promote oxidation of the underlying aluminium. $In(OH)_3$ electrolyte additions aggravated the corrosion of the 99.99 % aluminium, compared to its behaviour in an uninhibited electrolyte, giving negative inhibition efficiencies and low discharge efficiencies, as shown in Table 2.4 [60]. The higher the $In(OH)_3$ concentration the worse the inhibition efficiency at open-circuit. This aggravated corrosion was due to the rate of hydrogen evolution being much faster reaction on indium than on aluminium [60].

Synergistic effects have been demonstrated among solution phase inhibitors. One example includes 1×10^{-2} mol dm^{-3} Na_2SnO_3 and 1×10^{-2} mol dm^{-3} $In(OH)_3$, combining the corrosion inhibiting effect of Na_2SnO_3 and the dissolution promoting effect of $In(OH)_3$. This pair induced a high inhibition efficiency of 73 % at open-circuit and discharge efficiencies as high as 96 %, as shown in Table 2.4. The results of galvanostatic discharge tests in Table 2.4 show that they also favourably shifted the potential of pure aluminium from −1.41 V *vs.* Hg/HgO to –1.47 V *vs.* Hg/HgO at 200 mA cm^{-2} discharge [60]. A combination of 1×10^{-3} mol dm^{-3} K_2MnO_4 with 1×10^{-3} mol dm^{-3} $In(OH)_3$ in 4 mol dm^{-3} KOH was not as effective at inhibiting the open-circuit corrosion or at reducing the electrode overpotential [60].

2.3.3 Cationic surfactants

Evolution of hydrogen arises from water reduction at cathodic sites on the aluminium surface. Cationic surfactants could inhibit this reaction by blocking the cathodic sites on the aluminium [134]. One such cationic surfactant, cetyltrimethylammonium bromide (CTAB) weakly inhibited the corrosion of 99.6 % aluminium in 2 mol dm^{-3} NaOH, with only 14 % inhibition efficiency at open-circuit, see Table 2.4 [135]. In addition, the CTAB restricted the anodic oxidation of the aluminium by adsorbing at the aluminium/alkaline solution interface reducing the active area [135]. A similar inhibitor, cetyltrimethylammonium chloride (CTAC), tested in the concentration range, 0.15 to 1.7×10^{-3} mol dm^{-3}, was also poor at inhibiting the open-circuit corrosion of 99.95 % Al in 1.5 mol dm^{-3} NaOH [134]. The open-circuit inhibition efficiency for 0.5×10^{-3} mol dm^{-3} CTAC was 40 %. In a similar manner to CTAB, the CTAC inhibited the anodic discharge of aluminium [134].

2.3.4 Zinc oxide

The addition of zinc oxide, in a concentration range of 50 to 600 $\times$ 10^{-3} mol dm^{-3}, was investigated as a corrosion inhibitor for 99.9995 % Al in 4 mol dm^{-3} KOH, under open-circuit conditions [66, 90, 136]. A maximum inhibition efficiency of 97.5 % was recorded via a hydrogen collection method with a concentration of 200 $\times$ 10^{-3} mol dm^{-3} ZnO, see Table 2.4 [66]. The zinc deposited on the aluminium surface, increasing the overpotential for hydrogen evolution. The zinc deposit shifted the anodes open-circuit potential in the positive direction, from −1.7 to −1.3 V *vs.* Hg/HgO because the electrode potential of zinc is more positive than that of aluminium [66, 90]. The anodic polarisation curve for 99.9995 % aluminium in a 200 $\times$ 10^{-3} mol dm^{-3} zincate solution shows a peak in current at −1.07 *vs.* Hg/HgO. This is due to the oxidation of the zinc deposit in addition to the oxidation of the aluminium. The current peak indicates the point at which all of the zinc had re-dissolved back into the electrolyte and the behaviour returned to that of pure aluminium.

Inhibitor / mol dm^{-3}	% Inhibition eff. at open-circuit % φ_{inh}	% Discharge Efficiency under galvanostatic discharge % φ_{dis} at j in mA cm^{-2}			Electrode potential during galvanostatic discharge *E vs.* Hg/HgO / V			
-		100	200	400	E_{oc}	E_{100}	E_{200}	E_{400}
99.99 % Al in unhibitied solution [a]		70	89		-1.71	-1.56	-1.41	
Stannate								
10^{-4} Na_2SnO_3 [a]	-94				-1.61			
10^{-3} Na_2SnO_3 [a]	24	79	95		-1.73	-1.54	-1.44	
10^{-2} Na_2SnO_3 [a]	67	63	77		-1.68	-1.48	-1.3	
Indium hydroxide								
10^{-4} $In(OH)_3$ [a]	97		50		-1.75		-1.6	
10^{-3} $In(OH)_3$ [a]	-178				-1.74			
10^{-2} $In(OH)_3$ [a]	-195	30	49		-1.73	-1.65	-1.55	
10^{-3} K_2MnO_4 [a]	32	91	99		-1.73	-1.5	-1.3	
10^{-3} K_2MnO_4 + 10^{-3} $In(OH)_3$ [a]	-5	70	87	96	-1.71	-1.55	-1.32	-1.1
10^{-3} K_2MnO_4 + 10^{-2} $In(OH)_3$ [a]	26	69	87		-1.7	-1.4	-1.1	
10^{-2} Na_2SnO_3 + 10^{-3} $In(OH)_3$ [a]	80	76	88	96	-1.72	-1.55	-1.4	-1.1
10^{-2} Na_2SnO_3 + 10^{-2} $In(OH)_3$ [a]	73	79	89	96	-1.75	-1.5	-1.47	-1.38
0.2 M ZnO [d]	98				-1.31			
Cationic surfactants								
1.8×10^{-4} CTAB [b]	14				-1.42			
0.5×10^{-3} CTAC [c]	40							
2.976 g L^{-1} lupine [b]	63				-1.47			

Table 2.4: Effect of solution phase inhibitors on inhibiting the corrosion rate of Al in alkaline solutions at open-circuit and under discharge in half-cell tests. [a] [60], [b] [135], [c] [134], [d] [66]. Anode and electrolyte temperature [a] 99.99 % Al, 50 °C; [b] 99.6 % Al; [c] 99.95 % Al, 30 °C; [d] 99.9995 % Al, 25 °C.

2.3.5 Plant extracts

Plant extracts are being considered as a corrosion inhibitor for aluminium in alkaline solutions as a replacement of toxic chemicals widely used in industry and to reduce the

operating cost [135]. An example of plant extracts includes the extract from the seeds of the lupine plant. The extract from lupine seeds consists of 50 % protein, 20 % lipids and 5 % quinolizidine alkaloids. This extract was found to inhibit the open-circuit corrosion of a 99.6 % Al alloy in 2 mol dm^{-3} NaOH by 63 %, due to adsorption of its active ingredient onto the alloy surface and reducing the active area [135]. However, it also impeded the anodic discharge of the aluminium.

2.4 The air (gas diffusion) electrode

The air cathode (often a gas diffusion electrode) is one of the most expensive components of a metal-air battery and is largely responsible for determining the cell performance [14, 56]. Air cathode technology has been reviewed for PEM fuel cell [137, 138], metal-air cell [12, 14, 16, 139, 140] and alkaline fuel cell applications [13, 15], and so the description below gives a synopsis of high-activity air-cathodes.

The high current densities attainable with the aluminium alloys (600 mA cm^{-2}), identified in Table 2.3, make the aluminium-air battery versatile for a wide-range of applications depending on what electrocatalyst is selected in the air-cathode. Should one of the inexpensive, high-activity catalysed air electrodes shown in Table 2.5 be chosen, then the aluminium-air battery could be used for a short-discharge high-power density application. It would be limited to a short-discharge owing to the poor durability of many high-activity catalysts, such as $LaMnO_3$ [14]. Reviewing the design of the high-activity electrodes in Table 2.5 shows they all have a double-layered structure of gas diffusion and active layers laminated with a nickel-mesh current collector [138, 141]. The ratio of carbon/binder in the respective layers is very similar across the electrodes, forming a bimodal pore network to optimise the wetting of the electrodes without flooding and impeding oxygen diffusion [142-146]. The degree of porosity is highly dependent on the sintering times and lamination pressures used during manufacture [147]. The pressing pressure is a compromise between ensuring cohesion of the carbon, PTFE, metal mesh and hydrophobic membrane while maintaining a porous structure for movement of oxygen and electrolyte through the electrode. The high-activity of the perovskite electrodes is in part due to the promotion of the direct four-electron oxygen reduction as well as catalytically decomposing the peroxide that is formed at the carbon [146, 148]. The resistance associated with peroxide diffusion from the carbon to the catalyst can be minimised through the use of a high surface area carbon of 1200 m^2 g^{-1} in the active layer [149]. Some of the highest current densities upwards of 3000 mA

cm^{-2} were attainable when pure oxygen was used as the reactant instead of air [150], while elevated pressures examined up to 10 bar will also have a similar effect [151].

The catalyst preparation route impacts the level of activity of the electrodes shown in Table 2.5. For example a reverse micelle preparation of perovskites compared to an amorphous malate precursor route achieves a higher dispersion of catalyst on the carbon support and perhaps better catalyst utilisation [152]. The synthesis method will also influence the surface area of the catalyst [153]. In the case of the porphyrins a subsequent heat treatment of the catalyst is required to enhance their activity and stability [154-157]. As a result of the heat treatment there is a reduction in surface area of the carbon support, which necessitates the use of additional fresh carbon in the active layer to maintain high electrode porosity [154]. Clearly there is great complexity in the design of a high-activity gas diffusion electrode. In terms of high-energy density applications, manganese oxide has received increased attention due to its high chemical stability as well as low cost and low toxicity and high catalytic activity [141, 158]. The oxygen reduction reactivity of MnO_x in a coin-type Al-air cell has been compared against that of platinum for galvanostatic discharge at 0.4 mA using aluminium powder as the anode [158]. The choice of electrolyte, a KOH/ethanol mixture for this comparison was not appropriate because ethanol is oxidised by platinum to form carbon dioxide [15, 159]. The discharge density for the button cell with the MnO_x catalyst was 512 W h kg^{-1}-Al, which is a fraction of the theoretical specific energy of 8,100 W h kg^{-1}-Al for an aluminium anode [158].

Some of the mixed metal-oxide catalysts such as the perovskites are electrically insulating and so the carbon support is used to enhance conductivity. This addresses an area of development in gas diffusion electrodes aimed at minimising the voltage drop associated with the transfer of electrons to the reaction site. At present, gas diffusion electrodes are manufactured by pressing a carbon/catalyst mixture in between the pores of a metal mesh. This means that the catalyst is not in direct contact with the metal mesh current collector, so there is an associated voltage drop. The ohmic losses associated with the gas diffusion electrode would be reduced by directly bonding the catalyst to the metal mesh current collector [160, 161]. Electrodeposition of catalysts such as, platinum [162, 163] or manganese oxide [164-166], is seen as a feasible way of achieving this [163, 167].

Gas diffusion layer composition	Catalyst	Preparation of carbon supported catalyst	Active layer composition	I_L / mA cm^{-2}	Reference
Perovskite type					
CB, 4.7 m^2 g^{-1}, 30 % PTFE	1.9 mg cm^{-2} $La_{0.6}Sr_{0.4}Mn_{0.8}Fe_{0.2}O_3$	Reverse micelle	KB 1270 m^2 g^{-1}, 15 % PTFE	500 mA cm^{-2} at −67 mV *vs.* Hg/HgO, oxygen flow	[168]
CB 74 m^2 g^{-1}, 15-25 % PTFE	3.5-9.9 mg cm^{-2} $La_{0.6}Ca_{0.4}CoO_3$	Amorphous citrate precursor	CB 830 m^2 g^{-1}, 15-25 % PTFE	3000 mA cm^{-2} at −125mV *vs.* Hg/HgO oxygen flow; 166 mA cm^{-2} at −125mV vs. Hg/HgO air flow	[169]
70 % AB, 30 % PTFE	50% $La_{0.6}Ca_{0.4}CoO_3$	Amorphous citrate precursor	35 % KB 1300 m^2 g^{-1}, 15 % PTFE	300 mA cm^{-2} at −200 mV vs. Hg/HgO, air flow	[149]
30-50 % carbon, 50 - 70 % PTFE	$La_{0.6}Ca_{0.4}CoO_3$	Amorphous citrate & drip pyrolysis	Graphite/graphitised AB, 25 % PTFE	1000 mA cm^{-2} at −275 mV *vs.* Hg/HgO, oxygen flow	[170]
70 % CB 47 m^2 g^{-1}, 30 % PTFE	6 mg cm^{-2} $LaMnO_3$	Reverse micelle	85 % KB 1270 m^2 g^{-1}, 15 % PTFE	300 mA cm^{-2} at −300 mV *vs.* Hg/HgO, air flow	[152]
70 % CB 47 m^2 g^{-1}, 30 % PTFE	6 mg cm^{-2} $LaMnO_3$	Reverse micelle	KB 1270 m^2 g^{-1}, 15 % PTFE	400 mA cm^{-2} at −100 mV *vs.* Hg/HgO, air flow	[171]
70 % CB 47 m^2 g^{-1}, 30 % PTFE	$LaMnO_3$, 20-30 nm	NAC-FAS & milling	KB 1270 m^2 g^{-1}, 15 % PTFE	300 mA cm^{-2} at −80 mV *vs.* Hg/HgO, air flow	[172]
40 % AB/active carbon mixture, 60 % PTFE	10 % $La_{0.6}Sr_{0.4}MnO_3$, 20 - 50 nm	Sol-gel & ultrasonic dispersion	50 % CB, 40 % PTFE	324 mA cm^{-2} at −200 mV *vs.* Hg/HgO	[173]
70 % CB 47 m^2 g^{-1}, 30 % PTFE	$La_{0.4}Ca_{0.6}Mn_{0.9}Fe_{0.1}O_3$, 15 nm	Reverse micelle	KB 1270 m^2 g^{-1}, 15 % PTFE	500 mA cm-2 at −50 mV *vs.* Hg/HgO, oxygen flow	[174]

Gas diffusion layer composition	Catalyst	Preparation of carbon supported catalyst	Active layer composition	I_L / mA cm^{-2}	Reference
Porphyrin					
65 % Vulcan HT, 35 % PTFE	Co-TMPP	Sigma Aldrich & dispersion with n-hexane	70 % Vulcan, 30 % PTFE	500 mA cm^{-2} at −250 mV *vs.* Hg/HgO, air	[175]
30-50 % carbon, 50 - 70 % PTFE	Co-TPP, 10-80 nm	Acetate precursor method	Vulcan 254 m^2 g^{-1}, 10 - 20 % PTFE	1000 mA cm^{-2} at −186 mV *vs.* Hg/HgO, oxygen flow	[154]
Spinel					
70 % EB, 30 % PTFE	25 % $LiMn_2Co_1O_4$	Amorphous citrate method	60 % CB, 15 % PTFE	500 mA cm^{-2} at -400 mV *vs.* Hg/HgO, oxygen flow	[176]
70 % EB, 30 % PTFE	25% $LiMn_{1.4}Co_{0.6}O_4$	Amorphous citrate method	60 % CB, 15 % PTFE	2500 mA cm^{-2} at −300 mV *vs.* Hg/HgO, oxygen flow	[177]
40 % AB, 60 % PTFE	$MnCo_2O_4$	Nitrate percursor in microwave oven	acetylene black	250 mA cm^{-2} at −140 mV *vs.* Hg/HgO, air	[178]
Catalyst mixtures					
40 % Vulcan XC-72, 60 % PTFE	9.5 mg cm^{-2} $La_{0.1}Ca_{0.9}MnO_3$/1.5 mg cm^{-2} CoTPP	Direct precipitation	Ketjen Black & Vulcan	300 mA cm^{-2} at −190 mV *vs.* Hg/HgO	[153]

Table 2.5: Survey of high-activity gas diffusion electrode designs. CB is carbon black, AB is acetylene black, KB is Ketjen black. All of the designs incorporated a nickel-mesh current collector.

2.5 Future prospects for aluminium-air batteries

2.5.1 Identification of new aluminium alloy anodes via combinatorial chemistry approaches

Manufacture and electrochemical testing of super-pure aluminium alloys with varying compositions is an expensive and time-consuming process. Combinatorial chemistry would allow the simultaneous synthesis and screening of a large number of alloys under identical conditions relevant to the aluminium-air environment. This technique is growing in popularity to optimise the composition of materials having specific physical or chemical properties [179]. Using this technology, a 10 × 10 array of individually addressable aluminium alloy electrodes could be fabricated onto a silicon nitride capped silicon wafer in a high-throughput physical vapour deposition system. The array would contain a gradient of varying aluminium alloy composition [179, 180]. Screening would involve carrying out simultaneous half-cell tests on each of the Al alloy electrodes [179]. This would allow identification of the alloying elements, either in binary or ternary alloys that enhance the anodic behaviour of aluminium in alkaline solutions at different temperatures, ranging from 20 to 60 °C. This is important since previous published research has focused on characterising suitable alloys at 60 °C. A similar high-throughput screening technique has been used for the evaluation of micro zinc-air [181] and tin-air cells [182].

2.5.2 Three-dimensional aluminium alloy anodes

A three-dimensional aluminium electrode is advantageous to increase the active surface area to enable discharge at high currents [70]. Forms of high surface area aluminium include foams, meshes and honeycombs [2]. Commercial suppliers of 3-D aluminium metal include: (a) ERG Materials and Aerospace Corporation supply aluminium 6101 foams, (b) COREX, who supply 3003 and 5052 aluminium honeycomb and (c) M-Pore who supply 99 wt% aluminium foam [183]. A comprehensive list of aluminium foam suppliers is available [184].

One method to fabricate a 3-D aluminium macroporous electrode includes the replication process [185, 186]. This consists of a pressure filtration technique where a solid material such as NaCl particles is used as a pore shaping template. Molten aluminium is then poured under pressure of 1 MPa into the porous NaCl template and allowed to cool down. The template is subsequently removed by dissolution. There may be difficulty maintaining the high-purity of the aluminium alloy during the manufacture of the foam via the replication technique [186].

Another 3-D anode design is aluminium nanorods, 30−90 nm diameter, 1−2 μm length, produced by chemical vapour deposition [187]. The chemical vapour deposition process involved heating 99.99 % aluminium powder at 1000 °C for 10 hours in a tube furnace in an argon atmosphere. Prototype aluminium-air button cells of 20 mm diameter employing the 99.99 % pure aluminium nanorods and an air cathode consisting of $La_{0.6}Ca_{0.4}CoO_3$ perovskite catalyst had an energy density of 458 W h kg^{-1} at a very low discharge current density of 0.7 mA cm^{-2}. This is superior to that of a similar cell using 99.99 %wt aluminium powder as the anode (236 W h kg^{-1}). The larger surface area of the Al nanorods allowed them to deliver more current compared to the Al powder. The use of granular Al, 8−12 mm in diameter, as a high surface area anode, has also been explored [188].

2.5.3 Anionic membranes

Researchers have explored the use of anionic membranes in aluminium-air batteries to restrict the amount of water making contact with the aluminium surface to reduce the parasitic corrosion reaction. One novel approach employed a polymer mixture of polyacrylic acid (PAA) encapsulating particles of aluminium powder (11.5−45 μm) and facilitating hydroxyl ion conduction [189]. This technique meant that the reaction product, $Al(OH)_3$, remained mostly entrapped by the PAA, helping to maintain electrolyte conductivity throughout the discharge. However if the $Al(OH)_3$ cannot dissolve into the electrolyte as aluminate ions then the growing amount of $Al(OH)_3$ would passivated the anode. Consequently the energy density of an Al-air cell constructed with this anode was very low at 199 W h kg^{-1}−Al. Anion exchange membranes have also been used as a solid polymer electrolyte at the interface between the electrolyte and the air electrode [16]. Two of the functions of this membrane were to prevent the $Al(OH)_3$ clogging the pores of the air cathode and to prevent neutralisation of the alkaline electrolyte by carbon dioxide.

2.5.4 Gel and solid polymer electrolytes

A potassium hydroxide solution gelled with hydrophonics gel (HPG) has been used as an electrolyte for an aluminium-air cell in order to trap the solution and minimise any electrolyte leakage [190]. The energy density was very low at 183 W h kg^{-1}−Al due to the extremely high cell resistance of 11.1 Ω which restricted the discharge current density to below 10 mA cm^{-2}. A large inter-electrode gap of 29 mm, the use of a 95 %wt pure anode and anode passivation by a layer of $Al(OH)_3$ also contributed to the low energy density of the cell with the gel electrolyte [190]. The conductivity of gel electrolytes would need to be improved in order for this system to be viable. In another Al-air cell design an alkaline membrane

synthesised from polyvinyl alcohol (PVA) and polyacrylic acid polymer were used as solid polymer electrolyte. A $KMnO_4$ catalysed air electrode formed the cathode and a 99.99 %wt Al plate was the anode. The cell discharge performance was extremely poor with a peak power density of 1.2 mW cm^{-2} at a low current density of 1.2 mA cm^{-2} due to passivation of the aluminium surface by the discharge product [191]. Gel and solid polymer electrolytes have low solubility for $Al(OH)_4^-$ ions meaning that during anodic discharge the $Al(OH)_3$ cannot dissolve into the electrolyte to form aluminate. The conductivity of these electrolytes is also insufficient to replenish the OH^- ions consumed at the electrode surface, resulting in passivation of the aluminium.

2.5.5 Mixed electrolytes and alternative solvents

The aluminium anode in aqueous solutions undergoes self-discharge with the production of a large amount of hydrogen gas via reaction (2.3). Water, with its high protic activity, is largely responsible for the large corrosion rate of the aluminium anode in alkaline aqueous solutions [192]. The substitution with an aprotic solvent that neither donates nor accepts H^+ ions, while providing sufficient ionic conductivity, may effectively inhibit the corrosion of aluminium.

2.5.5.1 Alcohols

Alcohols used to form both aqueous and non-aqueous alkaline KOH solutions for aluminium corrosion tests include methanol [193, 194], ethanol [195] and propanol [196]. Without any water, there was no hydrogen evolution from the surface of the aluminium in these alkaline alcohol solutions. The open-circuit corrosion current density of 99.999 wt% Al was extremely low at 0.0041 mA cm^{-2} in a 4 mol dm^{-3} KOH ethanol solution at 25 °C [195]. However these solutions almost completely inhibited the oxidation of aluminium as replacing water with the other solvents decreases the ionic conductivity of the electrolyte and the hydration of the surface product layer [192, 193]. The rate of oxidation of the aluminium improved on mixing the alkaline alcohol solutions with water, although it was still inferior to the performance in a 100 % aqueous solution.

The suitability of alcohols as electrolytes in Al-air batteries depends on their stability in contact with the catalysed air electrode. A platinum catalysed air electrode would be unsuitable for use with methanol or ethanol electrolytes, as they are oxidised by platinum releasing carbon dioxide gas [15, 159]. Alternative catalysts, such as tungsten carbide-silver

composite (Ag-W_2C/C) [197] and a $La_{0.6}Ca_{0.4}CoO_3$ perovskite have been successfully used for the reduction of oxygen in alkaline alcohol/water mixtures [187].

2.5.5.2 Ionic liquid electrolytes

As mentioned earlier, aluminium-air batteries are primary sources of energy because aluminium cannot be electrodeposited from aqueous solutions due to its negative standard potential leading to hydrogen evolution before aluminium deposition can occur at the negative electrode [54, 55]. A suitable electrolyte for a rechargeable aluminium-air battery is one that is aprotic such as ionic liquids and electrolytes based on organic aprotic solvents [55, 198]. The disadvantages of organic solvents, such as tetrahydrofuran, include a narrow electrochemical window, low electrical conductivity and high volatility and flammability [199]. Details and current challenges with ionic liquids are briefly discussed below. More detailed reviews covering the history and use of ionic liquids can be found elsewhere [200-203].

Research into ionic liquids for metal-air batteries has received enormous investment. For example, in November 2009, the U.S. Department of Energy awarded a $5.13 million research grant to Fluidic Energy towards the development of a metal-air battery using an ionic liquid electrolyte [204]. Ionic liquids are room-temperature molten salts, composed mostly of organic ions that can be used as solvents for the electrodeposition of metals or as the electrolyte for batteries [201]. Compared to in aqueous electrolytes, aluminium is not prone to the parasitic hydrogen generation reaction in ionic liquid electrolyte [205].

Chloroaluminate ionic liquids may be considered as the first generation of ionic liquids used for the electrodeposition of aluminium [54, 206, 207]. These are prepared by combining highly hygroscopic $AlCl_3$ with a suitable organic chloride such as N-butylpyridinium chloride (N-BPC) and 1-ethyl-3-methylimidazolium chloride (EMIC) [208]. Several researchers have explored the use of chloroaluminate ionic liquids as electrolytes for aluminium batteries [198, 209]. Drawbacks include they are expensive chemicals and their preparation is difficult due to the highly exothermic reaction between 1-ethyl-3-methylimidazolium chloride (EMIC), and $AlCl_3$ [198, 210, 211]. Other chloroaluminate ionic liquids such as trimethylphenylammonium chloride (TMPAC)-$AlCl_3$ are easy and inexpensive to prepare in a relatively high state of purity since TMPAC is commercially available in high-purity [212].

The conductivity of the $AlCl_3$/EMIC ionic liquids is significantly inferior to that of aqueous solutions at 0.017 S cm^{-1} [210] compared to 0.7 S cm^{-1} for 7 mol dm^{-3} KOH at 30 °C [80]. Due to their hygroscopic nature, chloroaluminate ionic liquids must be handled under an inert-gas atmosphere or at least under dry air [54, 199, 200]. This rules them out for use as an electrolyte in aluminium-air batteries unless the battery could be sealed and an O_2-permeating membrane placed on the external surface of the air cathode to prevent moisture, from the air, ingressing into the cell [213]. Cycling of ionic liquid $AlCl_3$/EMIC ionic liquid resulted in changes in electrolyte composition, which limited the cyclability of the deposited aluminium [209].

An alternative to the chloroaluminate ionic liquids is air and water stable ionic liquids such as 1-ethyl-3-methylimidazolium bis(trifluoromethylsulfonyl)amide ([EMIm]TFSI), 1-butyl-1-methylpyrrolidinium bis(trifluoromethylsulfonyl)imide ([BMP]TFSI), [(Trihexl-tetradecyl)phosphonium] bis(trifluoromethylsulfonyl)imide ($P_{14,6,6,6}$TFSI) [54, 214] and 1-butyl-3-methylimidazolium tetrafluoroborate, [BMIm]TFB [192]. Mixing these liquids with $AlCl_3$ and following successive aluminium deposition and stripping cycles, charge efficiencies of 100 %, 4 % and 87 % respectively were recorded at 25 °C [54]. [EMIm]TFSI was superior to the other two because its lower viscosity allowed it to deliver a higher peak discharge current density of 12 mA cm^{-2} compared to 0.1 mA cm^{-2} for [BMP]TFSI and 0.4 mA cm^{-2} for $P_{14,6,6,6}$TFSI at 25 °C [54]. Although these ionic liquids are still novel and expensive, their cost should come down if they go into large-scale production for aluminium electrodeposition [202].

The charge−discharge behaviour of an air electrode in the ionic liquid, TMPATFSI (Trimethyl-n-propylammonium bis(trifluoromethylsulfonyl) imide, has been investigated [215]. The air electrode was a mixture of nickel particles bound with PTFE particles, with one side in contact with the electrolyte and the other open to the air. The mechanism of oxygen reduction proceeds via a reversible $1e^-$ step to form the superoxide ion, $O_2^{\bullet -}$ [216, 217]. A one−electron transfer step at the air cathode would, however, limit the power density of rechargeable ionic liquid aluminium-air batteries.

Several novel developments in aluminium-air battery research have been discussed above. The performance of these systems, such as the gel−electrolyte based one, in terms of

maximum discharge current density and energy density is far inferior to the conventional Al-air cell design employing a re-circulating electrolyte, as indicated in Figure 2.12. Of the systems, a maximum of 3900 W h kg^{-1}−Al at a discharge current density of 50 mA cm^{-2} was delivered by an aluminium-oxygen system incorporating an Al/Mn/In/Mg alloy [88]. This cell delivered reasonable cell potential differences up to a current density of 200 mA cm^{-2}. The other flowing electrolyte system shown in Figure 2.12, a bipolar design, could not be discharged at such high current densities because it used 99.99 wt% Al as the anode which was inferior to the Al/Mn/In/Mg alloy used by the other system [76].

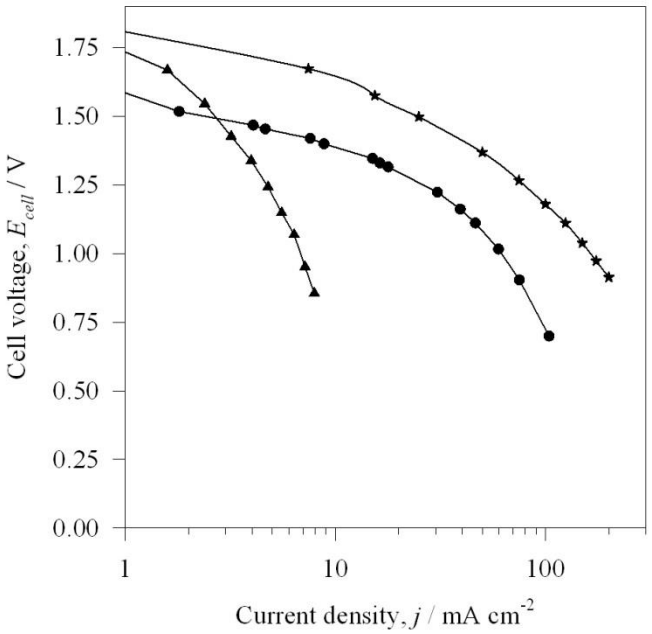

Figure 2.12: Comparison of performance data for some Al-air cells. Cell potential difference versus current density curves. The distinguishing features of each of the systems is: ▲ Gel−electrolyte [190], ● Bipolar Al-air cell with 99.99 % Al [76], ★ Al-O_2 system with flowing electrolyte [88].

2.6 Summary of literature review

1. The corrosion and oxidation of pure aluminium in alkaline solutions is dependent on a number of variables including the electrolyte properties: temperature and its type, its flow rate and concentration, along with the purity of the aluminium. Pure aluminium in an uninhibited alkaline solution oxidises at a high overpotential because of a passive hydroxide layer and has low discharge efficiency because of a parasitic reaction involving the reduction of water.

2. Alloying aluminium with particular elements or adding inhibitors to the electrolyte can reduce the self-corrosion and enhance its oxidation rate. Properties of a suitable alloying element include: (i) a low melting temperature to form a solid solution with aluminium, (ii) solubility with aluminium, (iii) higher nobility than aluminium in the electrochemical series, (iv) solubility in the electrolyte and (v) a high hydrogen overpotential.
3. The electrochemistry of the alloys is determined by the electrochemistry of the alloying element and is highly dependent on the electrolyte temperature. An alloy that has enhanced anodic behaviour at 60 °C may not display this enhanced behaviour at 25 °C. There is a shortage of anodic polarisation, galvanostatic discharge and corrosion data for aluminium alloys in alkaline solutions at 25 °C.
4. Alloys desirable at 60 °C that exhibited extremely high anodic currents, upwards of 600 mA cm^{-2} at potentials of −1.64 V *vs.* Hg/HgO and discharge efficiencies greater than 90 % include Al/0.5 Mg/0.07 Sn, known as EB50V, and Al/0.84 Mg/0.13 Mn/0.11 In. A more detailed experimental study is required on the effect of other alloying elements such as antimony, bismuth, cadmium and zinc in quantities closer to their solubility limit in aluminium.
5. The rationale behind the choice of electrolyte inhibitor is similar to that of alloying elements. A suitable inhibitor pair is 10 mmol dm^{-3} Na_2SnO_3 + 10 mmol dm^{-3} $In(OH)_3$ which were tested at 50 °C. Many studies of electrolyte inhibitors have evaluated effectiveness solely on its inhibition efficiency at open-circuit. Further work should be carried out on low cost electrolyte additives like ZnO, to elucidate their effectiveness at inhibiting the hydrogen evolution under discharge. Investigations can explore synergies between corrosion inhibiting additives such as cetyltrimethylammonium bromide and activating additives such as indium hydroxide. The solubility limit of inhibitors in alkaline solutions needs to be characterised to determine their desired concentration.
6. The design of gas diffusion electrodes plays as an important role as the material electrochemistry. An alternative design of gas diffusion electrodes can involves binding the electrocatalyst directly to the metal mesh current collector to minimise resistance to transfer of electrons to the reaction sites.

2.7 Future developments in Al-air batteries

Finally, likely future developments in alkaline aluminium-air batteries are considered. Although several alloys have been identified with lower corrosion currents compared to pure aluminium, their rate of self-corrosion particularly at open-circuit is still of the order of 10 mA cm^{-2} which is unacceptable when compared with that shown by zinc (ca. 0.1 mA cm^{-2}). This problem of self-corrosion, coupled with the high cost for manufacture of high-purity aluminium alloys, excludes aluminium-air batteries for use as commercial portable batteries employing a static electrolyte design. The issue of cost can be addressed by reviewing the literature on the corrosion and anodic behaviour of commercially available alloys in alkaline solutions and comparing it with that of the high-purity alloys identified in this review. The challenge of open-circuit self-corrosion can be overcome by integrating an Al-air battery with a flowing electrolyte system, where the electrolyte can be stored externally to the cell when not in use, although operational hydrogen management would still be required. The irreversibility of the aluminium oxidation reaction means that a flowing electrolyte system may be less favourable compared to an electronically rechargeable battery. Currently, knowledge gained in trying to minimise the volume of evolved hydrogen from the aluminium alloy surface is being used to design aluminium alloys as portable sources of hydrogen, to overcome the technical challenges associated with hydrogen transport for fuel cell applications. Al-air batteries have also received interest for niche military applications requiring an expendable, light-weight high-power density battery such as those required in a micro-unmanned aerial vehicle.

Chapter 3. Experimental details

This chapter describes the procedures used for conducting the experimental work during the project. The experimental work was divided into three sections: two focused on the individual electrodes of the Al-air cell, the aluminium anode and air-cathode. Following on from the findings of the studies on the individual electrodes, the third section looks at the design and evaluation of a lightweight prototype Al-air cell. Conveniently this chapter is divided with respect to the three experimental sections, highlighting the samples and equipment used along with the electrochemical procedures.

3.1 Aluminium anode experiments

3.1.1 Aluminium samples

Four aluminium samples were examined as potential anodes for the aluminium-air cell. They included two high purity aluminium alloys, a commercial Al 6101 foam and super-pure aluminium. The super-pure aluminium was used as a comparison for the other alloys. The super-pure aluminium, purchased from Goodfellows, was 99.999 %wt pure and had a rolled temper. The rolled temper signifies that the aluminium plates were rolled to their 3 mm thickness through rollers which were heated to impart a desired heat treatment. Details of the impurity concentrations of the super-pure aluminium are given in Table 3.1.

Impurity	Concentration / ppm wt
Copper	0.25
Iron	1.09
Magnesium	1.05
Silicon	1.02

Table 3.1: Concentration of impurities in the 99.999 %wt aluminium supplied by Goodfellows .

The two high-purity aluminium alloys examined in this work were Al/0.5 Mg/0.07 Sn and Al/0.4 Mg/0.07 Sn/0.05 Ga, cast with a 99.999 %wt pure aluminium base. The Al/Mg/Sn alloy was cast by N-Tec Ltd. as 10 individual discs, 60 mm in diameter and 8 mm thick, and subsequently machined by N-Tec to 3 mm thick. The second alloy, Al/Mg/Sn/Ga, was cast by Innoval Ltd. as a 5 kg cylindrical ingot and used during the research of Dr. Maria

Nestoridi and its composition as reported in her work is shown in [1]. N-Tec carried out compositional analysis of the Al/Mg/Sn sample via a spark atomic emission spectrometer. The results shown in Table 3.3 quantified the Mg level at 0.5 %wt and the Sn at 0.07 %wt. Most of the impurity levels were down below 10 ppm, with the exception of lithium which was being recorded as less than 0.1 %wt. The spark arc analysis showed that any impurities such as iron and copper were at very low concentrations, less than 10 ppm wt. At higher concentrations these would otherwise act as cathodic centres in the alloy in an alkaline electrolyte and galvanically aggravate the corrosion due to bimetallic effects [49].

Element	Composition / %wt
Al	Base
Mg	0.4
Sn	0.07
Ga	0.05

Table 3.2: Elemental composition of the Al/Mg/Sn/Ga alloy cast by Innoval Ltd. as reported in the work of Dr. Maria Nestoridi [1].

Focused ion beam secondary ion mass spectrometry, FIB/SIMS, was used to detect the elements present in the Al/Mg/Sn alloy (Figure 3.1). This was also to ensure that any lithium in the alloy was much less than the 0.1 % maximum range value reported from the spark arc analysis. In addition to the aluminium matrix, the FIB/SIMS detected the desired alloying elements, magnesium and tin. The only impurities detected were silicon and zirconium which were contaminants from the grinding and polishing of the sample. To verify the composition of the Al/Mg/Sn alloy, a sample was sent to Evans Analytical Group SAS in France to test via an inductively coupled plasma mass spectrometer (ICP-MS) and a glow discharge mass spectrometer (GDMS). The ICP-MS was used to determine the major elements, Mg and Sn, in the alloy. It verified the composition of the Mg at 0.49 % and Sn at 0.077 %. ICP-MS is an expensive technique costing €35 per element and €40 calibration per element plus €40 for sample preparation. GDMS is useful for acquiring all the traces and ultra-traces in a material. The GDMS cost €190 to analyse the Al/Mg/Sn alloy, so was cheaper per detected element than ICP-MS. GDMS confirmed that any impurities present were below levels of 10 ppm wt (Table 3.4).

Element	Composition / %wt
Li	<0.1000
Be	<0.0010
B	<0.0005
Na	0.0001
Mg	0.545
Al	>99.39
Si	<0.0010
P	<0.0010
Ca	<0.0001
Ti	<0.0010
V	<0.0010
Cr	<0.0010
Mn	<0.0020
Fe	<0.0010
Ni	<0.0010
Cu	<0.0010
Zn	<0.0020
Ga	<0.0005
Sr	<0.0005
Zr	<0.0010
Sn	0.0707
Sb	<0.0020
Pb	0.0012
Bi	<0.0010

Table 3.3: Spark arc compositional analysis carried out by N-Tec on the Al/Mg/Sn alloy.

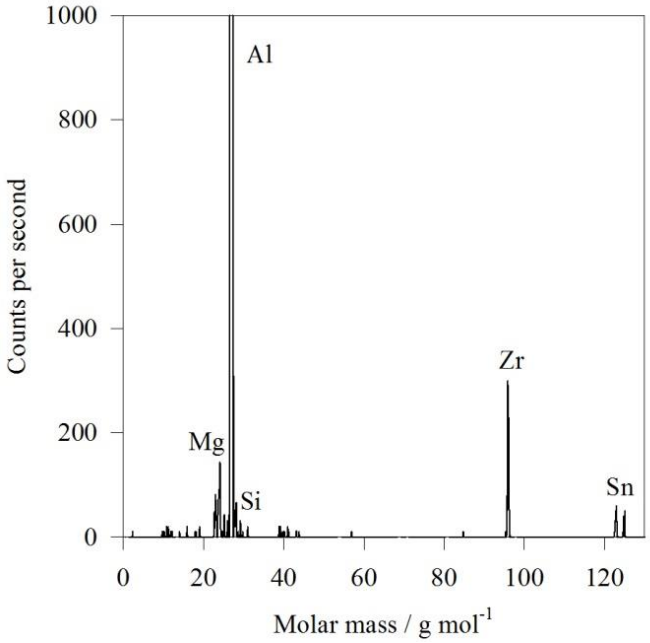

Figure 3.1: Elemental analysis of a sample of the Al/0.5 Mg/0.07 Sn alloy via secondary ion mass spectrometry (SIMs).

Element	Concentration / ppm wt
Li	< 10
Mg	~ 0.49 %wt
Al	Matrix
Si	< 10
Ti	< 10
Cr	< 10
Mn	< 10
Fe	< 10
Ni	< 10
Cu	< 10
Zn	< 10
Ga	< 10
Zr	< 10
Ag	< 10
Sn	~ 0.077 %wt

Table 3.4: Compositional analysis of the Al/Mg/Sn alloy performed by Evans Analytical Group in France. The Mg and Sn were quantified by ICP-MS. All other elements were analysed via GDMS.

The commercial Al 6101 foam was supplied by ERG Aerospace Corporation and branded as Duocel Aluminium Foam. Two different pore densities were used: 10 and 20 pores per linear inch (ppi). They were tested as anodes in the prototype 1 cell. The foam dimensions were 8.8 cm long, 3.8 cm wide and 0.6 cm thick. They had a mass of 4.8 g in the case of 10 ppi and 4.2 g in the case of 20 ppi.

3.1.2 Preparation of the aluminium

It is common practice to grind and polish the surface of the samples prior to testing. This allows removal of any surface contaminants left from sample manufacture, creation of a reproducible surface area between tests and re-use of samples after testing. Working electrodes were wet polished down to grade P1200 abrasive using semi-automatic polishing machines, followed by rinsing in distilled water for three minutes. Some samples were ground to P4000 with SiC paper then machine polished with 1 μm diamond paste on a microcloth to give a mirror finish [60]. These samples were analysed under the scanning electron microscope to ensure there were no precipitates of Mg and Sn present within the alloy after the heat treatment. The absence of precipitates would confirm that the magnesium

and tin alloying elements had gone into solid solution following heat treatment. Silicon carbide grit paper was used rather than aluminium oxide grinding paper since most wet grinding paper for semi-automatic rotating grinding wheels is produced with silicon carbide grit. Electropolishing was considered, but was not employed since the time required to perfect the technique would detract from the other studies. Electropolishing is not a practical procedure as many of the solutions used are either hazardous or form toxic bi-products, such as sulfates formed when mixing methanol with sulphuric acid [218]. After the grinding or polishing step, samples were held at open-circuit for 1 hour to wait for a steady potential prior to corrosion testing, to ensure a reproducible surface condition [136].

3.1.3 Electrochemical apparatus and procedures

Half-cell tests, including galvanostatic discharge and linear sweep voltammetry, were carried out on aluminium samples using the glass three-electrode cell shown in Figure 3.2. The working electrode was clipped to the undivided, three-electrode cell as shown in Figure 3.2. This meant the surface of the working electrode was orientated vertically during the linear sweep and galvanostatic discharge tests. Working electrodes were 50 × 50 mm square and 2 mm thick, see Figure 3.3. The active area of the working electrode exposed to the electrolyte was 3.5 cm^2 which was defined by a rubber gasket having a circular hole. The potential of the working electrode was measured versus a Hg/HgO reference electrode of type Radiometer XR440, supplied by Hach Lange Ltd. filled with a 1 mol dm^{-3} NaOH solution [36]. The counter electrode was a 1.5 × 1.5 cm platinum wire mesh, with 0.7 mm mesh spacing. The mesh structure gave the counter electrode a large active area. Analytical reagent grade sodium hydroxide (Merck) with a purity of 99 % was used. A similar cell with the addition of a water jacket, was used for conducting experiments at elevated temperature, see Figure 3.4 and with dimensions in Figure 3.5. The physical set-up of the working, counter and reference electrodes, as just described, was the same between the two glass cells.

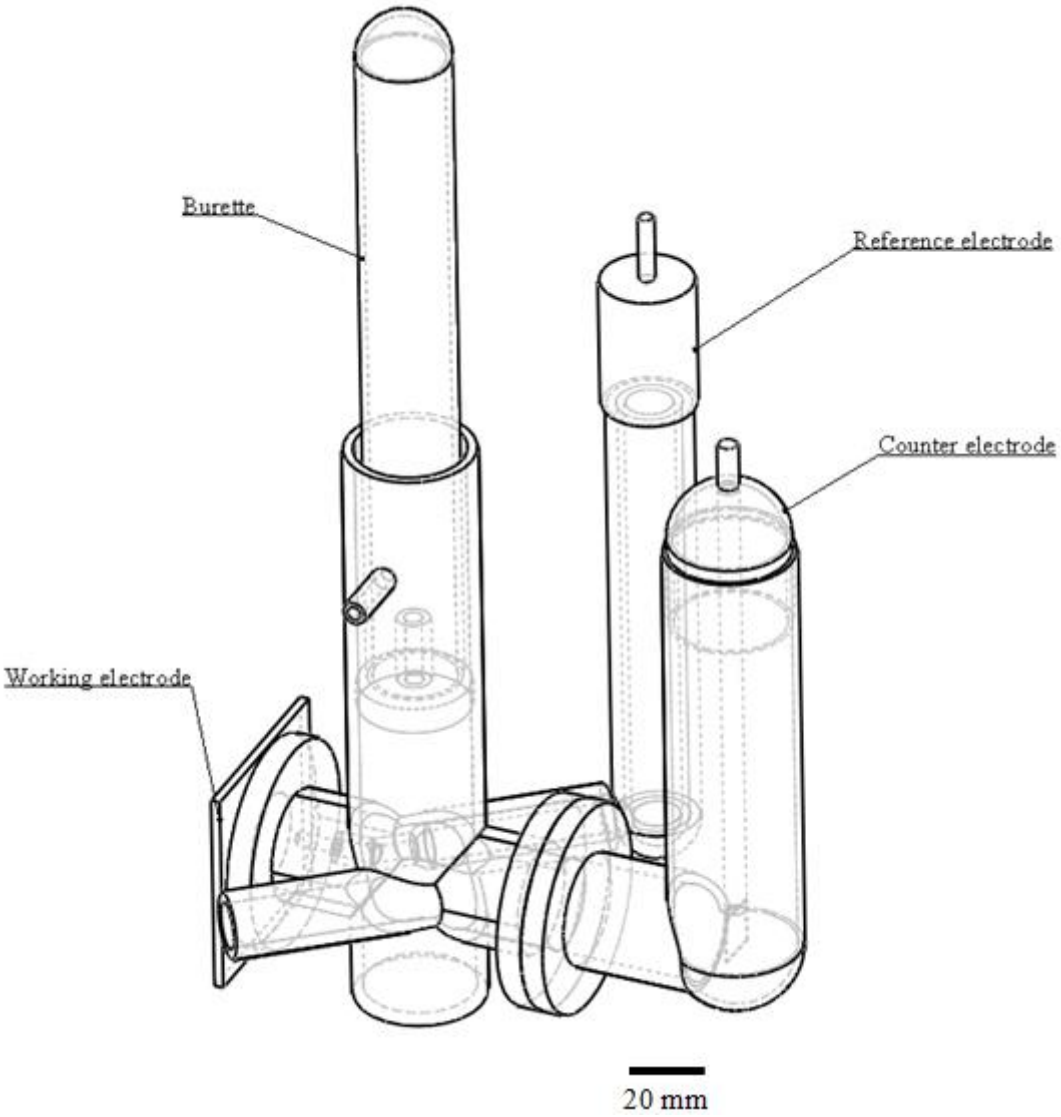

Figure 3.2: Glass, three-electrode cell used for carrying out galvanostatic discharge and linear sweep voltammetry tests on an aluminium working electrode. The burette facilitated measurement of the volume of evolved hydrogen during galvanostatic discharge.

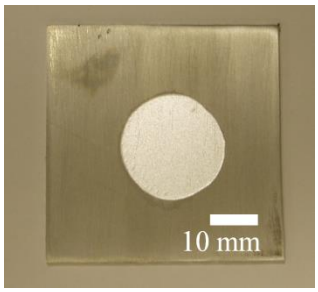

Figure 3.3: 99.999 %wt aluminium working electrode after galvanostatic discharge at a current density of 50 mA cm^{-2} for 4800 s using the three-electrode cell. The circular, bright area (3.5 cm^2), was exposed to the alkaline electrolyte which was a static electrolyte of 4 mol dm^{-3} NaOH at 22 °C.

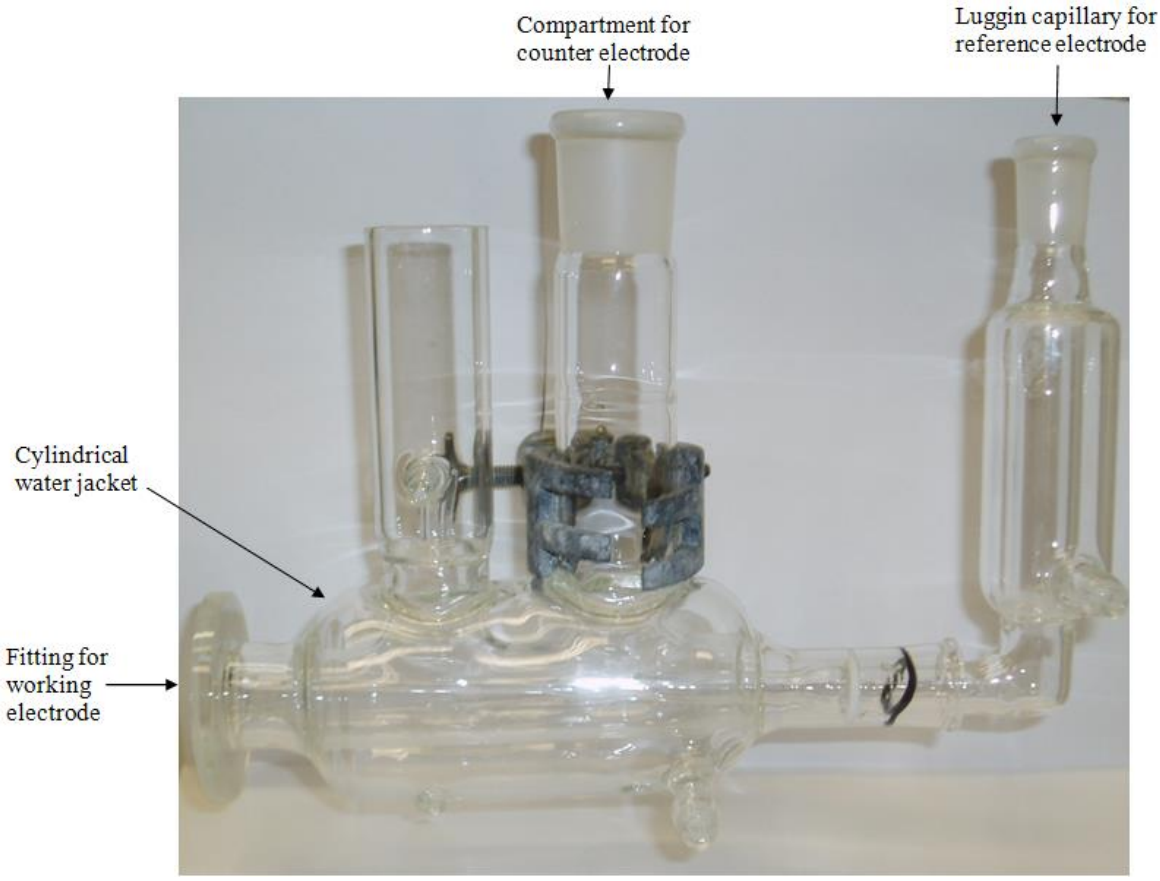

Figure 3.4: Water jacketed, glass three-electrode cell used for conducting linear sweep and galvanostatic discharge experiments at elevated temperature.

A technique which yields quantitative information about the corrosion behaviour of an aluminium electrode, involves applying a range of anodic currents to the aluminium and simultaneously measuring the rate of hydrogen evolution [23, 36, 37, 58, 59, 61]. Galvanostatic studies were carried out for 1 hour, over the range of 0 to 200 mA cm^{-2}, with an Ecochemie Autolab, PGSTAT30, computer controlled potentiostat using the General Purpose, Electrochemical Software, GPES, Version 4.5. A new aluminium sample and fresh electrolyte, 4 mol dm^{-3} NaOH, were used for each test. Prior to each galvanostatic discharge test, the aluminium electrode was held at the open-circuit for 1 hour to allow its open-circuit electrode potential to stabilise as demonstrated for an Al/Mg/Sn sample in Figure 3.6. While applying an anodic current, the volume of hydrogen evolving from the surface of the aluminium was collected and measured in an inverted burette as a function of time (Figure 3.2). An upward facing spout in the three electrode cell fitted into the opening of the upturned burette and funnelled the hydrogen gas into it. The quantifiable analysis conducted on the hydrogen volume data was the same as that previously used to compare corrosion results from the literature in Ch. 2 Literature Review. The corrosion current, I_{cor}, resulting from the

reduction of water on the aluminium surface, reaction (2.3), was calculated from the volume of evolved hydrogen using equation (2.5), which is derived from Faraday's Law and the Ideal gas law. When calculating the corrosion current a steady-state value for the rate of hydrogen evolution, $\dot{V}$, was always used to account for the transient behaviour observed by the rate of hydrogen evolution [63]. At open-circuit the calculated corrosion current was used to compute the inhibition efficiencies, φ_{inh}, for the alloy which indicates the percentage difference between the corrosion of the alloy and pure aluminium, equation (2.8) The vector for evaluating the corrosion behaviour of the aluminium alloys under discharge was the discharge efficiency, φ_{dis}, which is the ratio of the discharge current, I, to the sum of discharge and corrosion current, I_{cor}, calculated via equation (2.9).

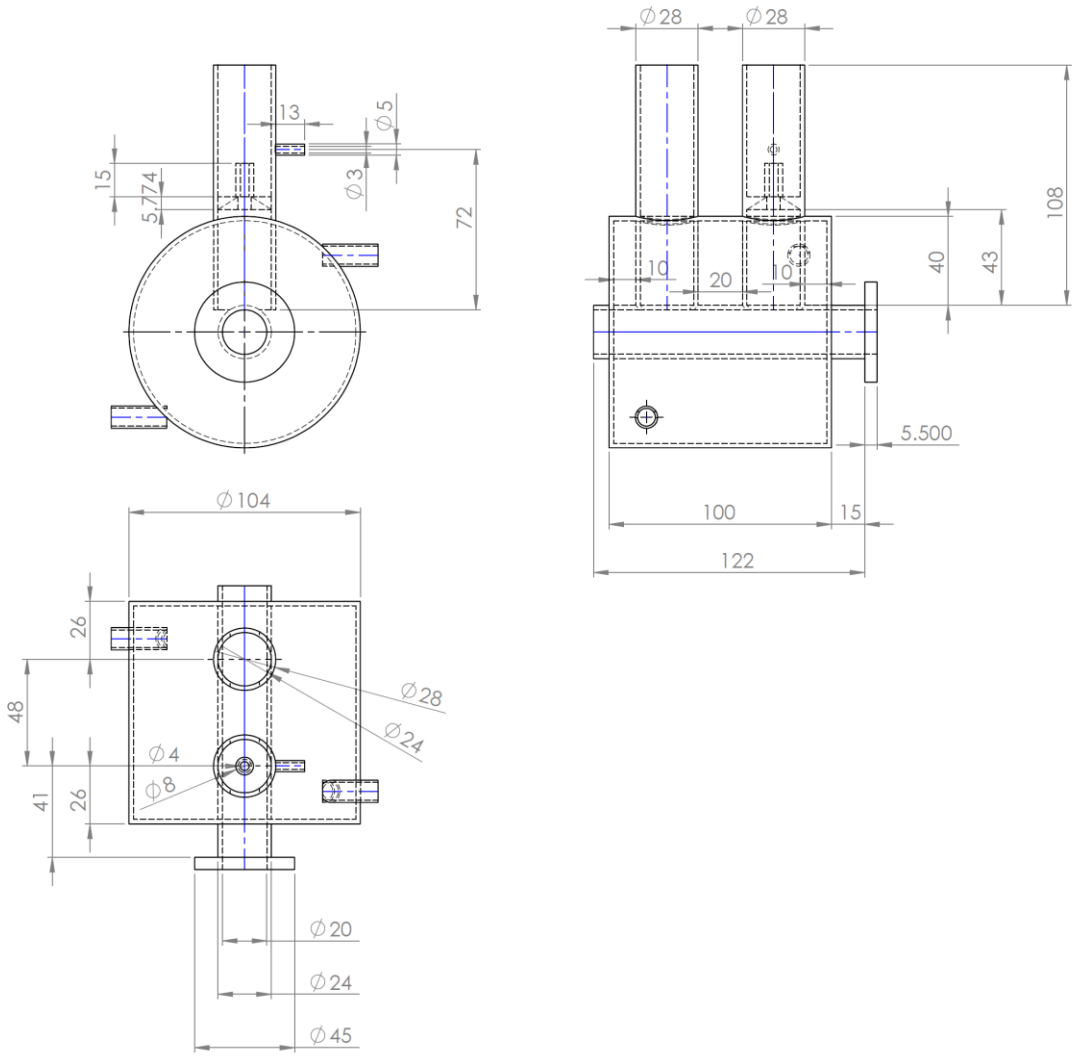

Figure 3.5: Dimensioned drawings of the water jacketed, glass three-electrode cell shown in Figure 3.4. It was used for conducting linear sweep and galvanostatic discharge experiments at elevated temperature.

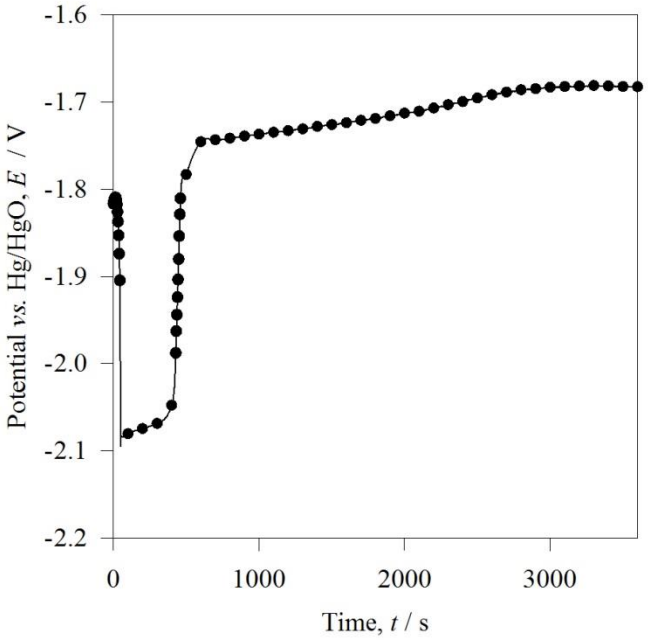

Figure 3.6: Holding Al/Mg/Sn electrode at open-circuit for 3600 s to allow its open-circuit potential to stabilise in 4 mol dm^{-3} NaOH. Electrolyte temperature 22 °C.

In addition to the galvanostatic tests, anodic linear sweep voltammetry was also used to compare the two aluminium alloys with 99.999 % aluminium. Before a linear sweep a sample was held at open-circuit for 1 hour to allow it reach a steady open-circuit value. Linear sweep voltammetry was conducted from the open-circuit potential to more positive values to a limit of −0.5 V *vs.* Hg/HgO as shown in Figure 3.7 for 99.999 % Al. At room temperature, 22 °C, a sweep rate of 1 mV s^{-1} was used. At the higher test temperatures up until 70 °C a faster sweep rate of 20 mV s^{-1} was used to ensure isothermal conditions. An Omega Type T thermocouple connected to a National Instruments data logger was used to monitor temperature during linear sweep scans at elevated temperature.

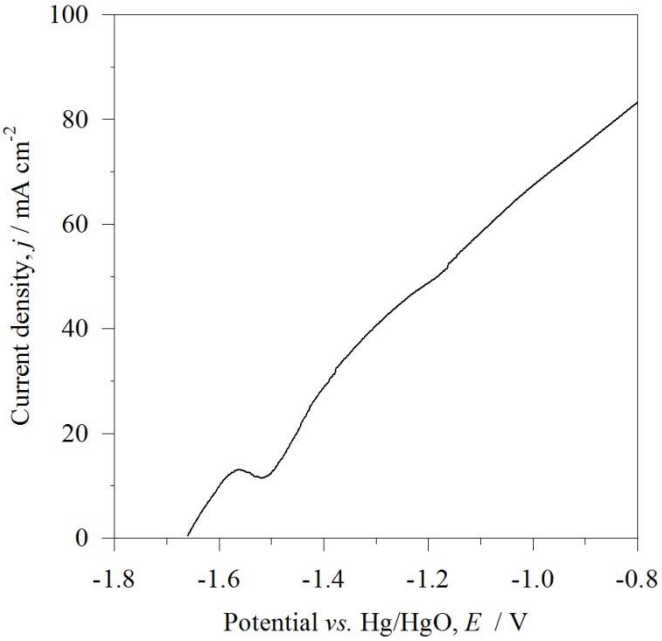

Figure 3.7: Linear sweep voltammogram for 99.999 % Al in 4 mol dm^{-3} NaOH at 22 °C. Sweep rate of 1 mV s^{-1}. Electrode area was 3.46 cm^2.

Linear polarisation resistance experiments were carried out on the Al/Mg/Sn alloy at open-circuit in 4 mol dm^{-3} NaOH. This involved linearly sweeping the potential ±20 mV either side of the open-circuit potential at 120 s intervals for 4800 s. The application of a small potential range meant the measurements were non-destructive, which allowed for successive measurements on the same sample at 120 s intervals [91]. Linear polarisation resistance is a technique that uses polarisation behaviour to determine the corrosion rate of metals [219]. Within ±20 mV of the corrosion potential of a metal in a corrosive solution, the applied potential displays a linear behaviour with the measured current. The slope of this linear polarisation curve, $\triangle E/\triangle I_{app}$, is proportional to the corrosion rate of the metal in the solution. The relationship of the slope of the linear polarisation curve to the corrosion current, I_{corr}, and the anodic and cathodic Tafel slopes, β_a and β_c, is given by equation (3.1). The corrosion current is the current resulting from the anodic oxidation of the aluminium and the cathodic reduction of water on its surface. Measurement of a linear polarisation curve at 120 s intervals while the alloy was open-circuit indicated how the corrosion rate varied with time upon initial immersion in the electrolyte.

$$\frac{\Delta E}{\Delta I_{app}} = \frac{\beta_a \beta_c}{2.3\left(I_{corr}\right)(\beta_a + \beta_c)} \tag{3.1}$$

Rotating disc electrode studies were carried out on the Al/Mg/Sn sample at 0, 200 and 400 rpm using the apparatus shown in Figure 3.8(a). The working electrode was a small disc 0.96 cm in diameter and 0.29 cm thick encased in epoxy as shown in Figure 3.8(b). Electrical contact was made with the back of the disc by a metal screw which was pressed against the sample before and during the moulding in epoxy. The epoxy mould formed a cylindrical electrode 3.0 cm in diameter. The metal screw protruded from the top of the cylindrical epoxy mould and was used to fix the cylindrical electrode to the rotating disc apparatus. A more comprehensive rotating disc study, using higher rotation speeds, was not undertaken. For such a study it would have been preferable to have the working electrode as a 30 mm long cylinder, 0.96 cm in diameter, instead of the 0.29 cm thick disc that was used. As a 30 mm long cylinder, the working electrode would have protruded from the top of its epoxy casing and it would have been easier to ensure electrical contact with it. This would have been more appropriate for a more comprehensive rotating disc electrode study. This was not undertaken because the focus of this research was on static alkaline electrolytes appropriate to a lightweight aluminium-air cell employing a static electrolyte.

3.1.4 Metallographic analysis

The microstructure of samples was analysed under a scanning electron microscope, type Jeol JSM-6500F at an accelerating voltage of 15 kV and a spot size of 11. The spot size refers to the diameter of the electron beam at the surface of the specimen. Selecting a high spot size is beneficial for capturing a good resolution image. Surfaces for microstructural examination were prepared by grinding with SiC paper down to P4000 abrasive and polishing with 1 μm diamond paste.

A BEI is a backscatter electron image used for identifying elements of different atomic mass in a sample. There is a backscatter electron coefficient which is the number of backscattered electrons emitted from the specimen for each incident electron. The backscatter electron coefficient increases with increasing atomic number [220]. Therefore elements of heavy atomic mass relative to the matrix material in a sample will show up brightly under the backscatter detector in the SEM. For example, catalysts in a gas diffusion electrode sample would show up brightly under the backscatter detector. The backscatter detector allows areas of interest to be identified and further analysed by energy dispersive x-ray analysis.

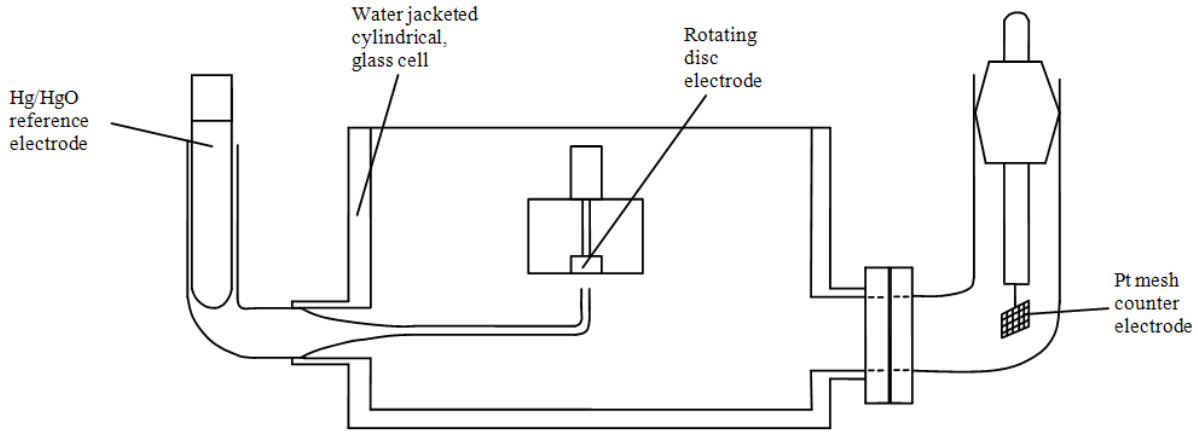

(a)

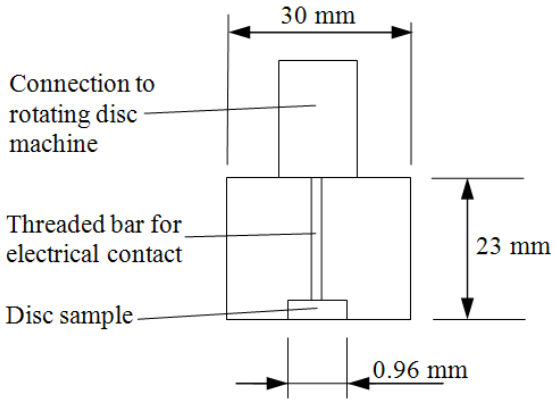

(b)

Figure 3.8: Rotating disc electrode set-up. (a) Water jacketed, cylindrical glass cell, (b) rotating disc electrode.

3.1.5 Reference electrode

A Hg/HgO reference electrode was selected for all experiments in this study. It was a type XR440 supplied by Hach Lange Ltd. The filling solution was 1 mol dm^{-3} NaOH. The mercury(II) oxide (mercuric oxide) is suited for use in highly alkaline electrolytes [221]. The controlling redox process is

$$HgO + 2e^- + H_2O \rightleftharpoons Hg + 2OH^- \qquad E^o_{Hg/HgO} = 0.098 \text{ V } \textit{vs.} \text{ NHE (25 °C)} \qquad (3.2)$$

To convert potentials from SHE into potentials relative to Hg/HgO involves the following calculation:

$$E \textit{ vs.} \text{ Hg/HgO} = E \textit{ vs.} \text{ SHE} - 0.098 \text{ V} \quad (3.3)$$

All the electrode potential values reported in this thesis are those attained by direct measurement. The values were not adjusted for the different temperatures used during the half-cell tests or for the uncontrolled temperature rise during full Al-air cell tests. The sensitivity of the Hg/HgO electrode to temperature was not found in the literature. By way of illustration, in the case of the mercury/mercury chloride electrode, also known as saturated calomel electrode (SCE), it has a potential of 0.241 V *vs.* SHE at 25 °C. At 60 °C the potential of SCE is 0.216 V *vs.* SHE. This potential difference of 0.025 V for SCE due to different electrolyte temperatures is small relative to the values of the anode potential of −1.43 V *vs.* Hg/HgO recorded in the Al-air cell experiments in this study. For that reason the values of the electrode potentials versus Hg/HgO in these experiments were not adjusted for temperature.

3.2 Air electrode experiments

Eight types of gas diffusion electrodes (GDEs) were tested in these experiments, as detailed in Table 3.5. The first one, labelled KTH, was manufactured and supplied by a project collaborator. The other seven were acquired from commercial suppliers.

Linear potential sweep experiments were carried out on the gas-diffusion electrodes in 4 mol dm^{-3} sodium hydroxide solution at 22 °C using the glass three-electrode cell shown in Figure 3.2. Working electrodes were 50 × 50 mm square and 1 mm thick. The air-cathodes were clamped to the three-electrode cell between a glass circular ring and a rubber gasket. The rubber gasket prevented electrolyte leakage and had a circular hole in its centre of area 3.5 cm^2, which defined the active area of the air-cathode in contact with the electrolyte. The glass circular ring provided rigidity to distribute the pressure of the clamps evenly across the back of the air-cathode. It had a hole in its centre matching that of the rubber gasket to allow air contact with the back of the air-cathode. In the case of the two platinum catalysed electrodes, a 1 mm thick stainless steel foil was used as a current collector by placing it between the back of the platinised air electrodes and the glass circular ring. The stainless steel foil, too, had a circular hole in its centre to allow air access and it was not in contact with the electrolyte. The potential of the working electrode was measured versus a Hg/HgO reference electrode with a

1 mol dm^{-3} NaOH filling solution [36]. The counter electrode was a 1.5 × 1.5 cm platinum wire mesh with 0.7 mm mesh spacing. Analytical reagent grade sodium hydroxide (Merck) with a purity of 98.95 %wt was used. A new gas diffusion electrode and fresh electrolyte were used for each experiment. The potential was swept from +0.05 V *vs.* Hg/HgO until the limiting current density for oxygen reduction was reached [222], at a sweep rate of 1 mV s^{-1} [223]. Prior to the electrochemical tests on the air-cathodes, the electrodes were always held at open-circuit in contact with the electrolyte for 3600 s by which point a stable open-circuit potential was reached, as shown in Figure 3.9 for the E4A electrode. This procedure facilitated wetting of the electrodes. Galvanostatic experiments were conducted using the same experimental set-up as for the linear sweep experiments. Linear sweep experiments at 60 °C were conducted using the water jacketed, glass three-electrode cell as shown in Figure 3.4.

Electrode name	Catalyst & loading	Structure	Supplier
KTH	$LaCaCo_3/LaCaMnO_3$	Double layer electrode of catalyst/carbon mixture laminated with a metal mesh on the rear face	Project collaborator
E5	Cobalt based	Catalyst/carbon mixture embedded into a nickel mesh and laminated to a porous PTFE film	Electric Fuel Ltd. [a]
OxAg	100 mg cm^{-2} Ag_2O	Catalyst/carbon mixture embedded into a gold plated nickel mesh and laminated to a porous PTFE film	Gaskatel [b]
MOC	10 mg cm^{-2} Manganese oxide	Catalyst/carbon mixture embedded into a nickel mesh and laminated to a porous PTFE film	Gaskatel [b]
W18365 ELE0072 Graphite paper	4 mg cm^{-2} platinum	Platinised carbon on thin, rigid graphite sheet	E-Tek
E4A	Manganese oxide	Catalyst/carbon mixture embedded into a nickel mesh and laminated to a porous PTFE film	Electric Fuel Ltd. [a]
E4	Manganese oxide	Catalyst/carbon mixture embedded into a nickel mesh and laminated to a porous PTFE film	Electric Fuel Ltd. [a]
W11529-346 Graphite paper	0.5 mg cm^{-2} platinum	Platinised carbon on thin, flexible carbon cloth	E-Tek

Table 3.5: Details of the commercial gas diffusion electrodes evaluated in this work [a] [224], [b] [225].

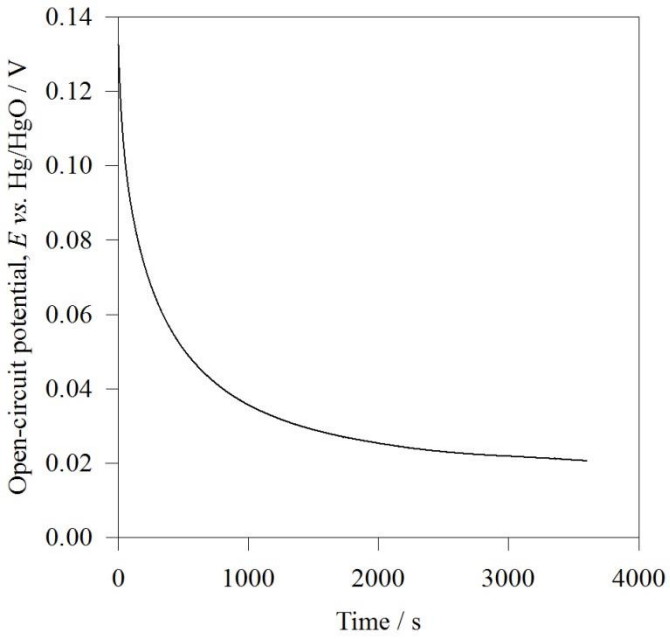

Figure 3.9: Variation of open-circuit potential for the E4A electrode upon initial immersion with 4 mol dm^{-3} NaOH at 22 °C.

3.2.1 Mercury intrusion porosimetry and pycnometry

This technique was used to analyse the structure of the E4, E4A, E5, MOC, 0.5 mg cm^{-2} Pt and 4 mg cm^{-2} Pt air electrodes. These samples were stored in a dessicator for a week prior to analysis, to remove any residual moisture and so improve the performance of the pycnometers. The samples were analysed using a Thermo Fisher Pascal 140 low pressure mercury porosimeter and a Thermo Fisher Pascal 440 high pressure mercury porosimeter. The instruments cover a pore diameter range from approximately 360 to 0.003 μm. The Pascal porosimeters measure the volume distribution of pores in materials by mercury intrusion or extrusion. Mercury has a high surface tension and is non-wetting to all materials with the exception of a few noble metals. These properties cause a mercury surface in contact with a solid to assume the minimum surface area, hence largest possible radius of curvature at a given pressure. An increase in pressure on the mercury shifts the balance between surface tension and surface area toward a smaller radius of mercury curvature. When the radius is equal to that of the pore entrance, mercury fills the volume within the pore.

The instrument was calibrated according the SOPs contained within the Record Manuals for the Pascal mercury porosimeters using the appropriate reference materials. All calibrations

runs were checked against the reference standards source file. Samples were analysed using the SOPs for analysis with Thermo Fisher Pascal porosimeters.

Gas displacement pycnometry was performed on a Micromeritics AccuPyc 1330 gas displacement pycnometer. The pycnometer determines the volume and hence density of the solid phase of a sample by measuring the pressure changes of a gas in a calibrated volume. Geo-pycnometry was carried out using a Micromeritics GeoPyc 1360 instrument which measures envelope volume and hence envelope density by displacement of a powder. The results from the two density techniques were combined to determine the porosity of the sample.

The Laplace equation relates the diameter of the pore (d), with the pressure (P), interfacial tension (γ) and mercury contact angle (θ)

$$d = \frac{-4\gamma \cos\theta}{P} \tag{3.4}$$

The Laplace equation can be simplified to equation (3.5) when the mercury/solid/vacuum interfacial tension is assumed to be 0.480 N m^{-1} (480 dyne cm^{-1}) and the mercury contact angle is 130 degrees.

$$d = \frac{213}{P} \tag{3.5}$$

The E4, E4A, E5, MOC, 0.5 mg cm^{-2} Pt and 4 mg cm^{-2} Pt air electrodes were analysed using Micromeritics AccuPyc 1330 gas displacement pycnometer which measures the solid-phase volume of porous or solid objects of irregular or regular shape whether powdered or in one piece. The instrument calculations are based on the ideal gas law

$$PV = nR_uT \tag{3.6}$$

where P is pressure, V is volume, n is amount of material, R_u is the universal gas constant and T is the temperature of the system. Assume that the volume of the cell, V_{cell}, and the expansion volume, V_{exp}, are at ambient pressure, P_a, and at ambient temperature, T_a, and that

the valve connecting the two is closed. The pressure in V_{cell} is elevated, P_1, so that the mass balance equation becomes:

$$P_1(V_{cell} - V_{samp}) = n_c RT \tag{3.7}$$

Where n_c is the number of moles of sample gas in the sample cell. The mass equation for the expansion volume is:

$$P_a V_{\exp} = n_{\exp} RT \tag{3.8}$$

Where n_{exp} is the number of moles of gas in the expansion volume. When the valve is opened, the pressure will fall to an intermediate value, P_2, and the mass balance equation becomes

$$P_2(V_{cell} - V_{samp} + V_{\exp}) = n_c RT + n_{\exp} RT \tag{3.9}$$

Substituting the equations for n_cRT and $n_{exp}RT$ into equation (3.9)

$$V_{cell} - V_{samp} = \frac{P_a - P_2}{P_2 - P_1} V_{\exp} \tag{3.10}$$

Adding and subtracting P_a in the denominator, followed by dividing the numerator and denominator by $(P_a - P_2)$ gives:

$$V_{samp} = V_{cell} - \frac{V_{\exp}}{\frac{P_1 - P_a}{P_2 - P_a} - 1} \tag{3.11}$$

Since P_1, P_2 and P_a are expressed in equation (3.7) through (3.11) as absolute pressures and in equation (3.11) are arranged so that P_a is subtracted from both P_1 and P_2 before use, new P_{1g} and P_{2g} may be defined as gauge pressures, which allows equation (3.11) to be rewritten to form the working equation (3.12) for the pycnometer.

$$V_{samp} = V_{cell} - \frac{V_{\exp}}{\frac{P_{1g}}{P_{2g}} - 1} \tag{3.12}$$

The gas used with the gas displacement pycnometer for the analysis of the samples was helium with a purity of > 99.9 %vol. Upon determining the volume of the sample the density was calculated using the relationship of volume, mass and density.

Samples were also analysed using a Micromeritics GeoPyc 1360 power displacement pycnometer, which measures the envelope volume of solid objects. The envelope volume of the sample was determined by difference in how far a plunger was driven by a stepping motor into a cylinder containing only a powder standard material called 'DryFlo', and then when the sample was added. The steps of the samples, *C*, were counted and used to calculate the volume. The counts were converted to volume by multiplying them by a conversion factor ν in cm^3 $counts^{-1}$ provided by the instrument manufacturer. The envelope volume of the sample, *V*, was then the difference in the counts with the sample present and with it absent multiplied by the conversion factor:

$$V = \left(C_{present} - C_{absent}\right)\nu \tag{3.13}$$

Upon determining the envelope volume of the sample the envelope density was calculated using the relationship of mass, volume and density. If the absolute density of the sample is known, by previous measurement with helium pycnometry, or by other means, the GeoPyc 1360 also calculates the percent porosity of the sample.

There are several limitations associated with the mercury-porosimetry technique. The technique assumes a cylindrical pore shape. Results are influenced by the mode used, continuous or incremental and the time set for equilibrium before a data point is read. Applying the pressure in increments offers more assurance that a true equilibrium time is reached for each data point. This is beneficial for avoiding compressive heating effects and hindered mercury flow at the high pressure/small pore size range [226]. Compressive heating leads to temperature fluctuations creating volume expansion effects in the mercury and sample. Mercury porosimetry will always show smaller pore sizes than in reality as the entrance to a pore or throat is typically smaller than its internal cavity. A pore will be filled once its size is equal to a pore size at a given pressure but also assuming there is a continuous flow of mercury to it. For example, a large pore surrounded by much smaller pores will not be filled at the pressure for its size because a higher pressure is needed to fill the smaller

pores that surround it. During extrusion, mercury becomes trapped within the pores due to an insufficient equilibration time leading to a marked hysteresis between the intrusion and extrusion curves [226]. Another reason for the trapped mercury is because the entrance to the pores is smaller than the internal cavity so that during extrusion the mercury breaks the narrow connections between pores and becomes trapped inside [226]. As a result of the number of assumptions made with this technique, mercury porosimetry is mainly useful for comparative studies of similar materials where the various assumptions have similar validity among the samples.

3.3 Evolution of prototype aluminium-air cell

3.3.1 Prototype 1 aluminium-air cell

The prototype 1 aluminium-air cell, tested in this work, is shown in Figure 3.10. It consisted of an aluminium anode placed between two electrically connected air cathodes. The cell was made from a white polymer block, potentially of nylon material, 70 mm wide, 80 mm high and 30 mm thick. A rectangular open-ended slot, 50 mm × 30 mm, traversed the thickness of the block, forming a hollow section for the electrolyte compartment and openings in two of the faces. An air-cathode was placed over each of these openings, sandwiched between two rubber gaskets, and compression fitted in place with a flange of 70 × 80 × 10 mm. The flange had a matching slot, 50 × 30 mm in size, to expose the outward face of the air-cathode to the air. The cathode current collector was a stainless steel foil frame, of the same dimensions as the flange, and 1.25 mm thick. It was also compressed against the air-cathode by the flange. The edges of the rubber gaskets were sealed with PTFE tape to avoid electrolyte leaks. The cathode was the platinum gas diffusion electrode supplied by E-Tek with a platinum loading of 0.5 mg cm^{-2}. The inter-electrode gap between the aluminium and each cathode was approximately 16 mm when the aluminium anode was inserted into the top of the cell. The dry weight of the cell, excluding the aluminium anode, was 294 g and it was 231 cm^3 in volume. There was a nozzle at the base of the cell to facilitate oxygen/air aeration of the electrolyte, although in these experiments this feature was not used. Two small holes in the side of the cell accommodated Luggin capillary tubes to measure the electrode potentials. Four different types of aluminium anodes were tested: an Al/Mg/Sn/Ga plate, Al/Mg/Sn/Ga perforated plate and Al 6101 foams of two different pore densities, 10 and 20 pores per inch (ppi). Electrolyte concentrations of 3 and 8 mol dm^{-3} NaOH were tested. It was later

identified that the peak conductivity for NaOH occurs at 4 mol dm^{-3} NaOH which was used for the majority of other tests in this thesis unless otherwise stated. The electrolyte was made from NaOH pellets, supplied by Fisher Scientific, of laboratory grade with purity greater than 97 %.

In the case of the constant current discharge tests, mass loss for the anodes was computed by weighing the initial and final mass and the fragments of unreacted anode which had broken away into the electrolyte. From this data the charge efficiency, specific energy and capacity of the cell were calculated. It was very difficult to accurately calculate the area of the foams.

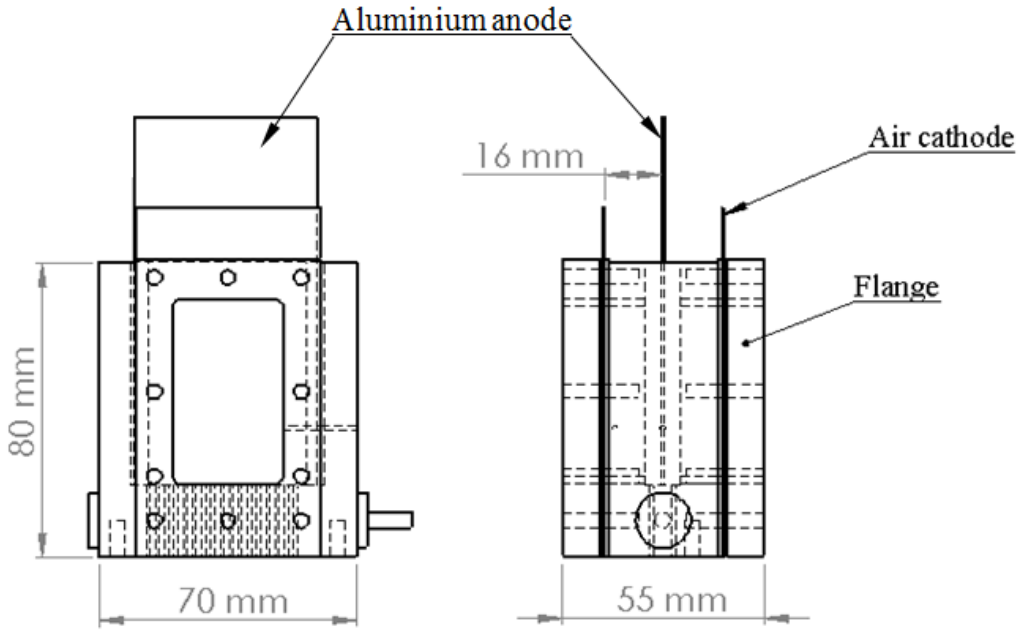

(a) (b)

Figure 3.10: The prototype 1 Al-air cell with a dry mass of 294 g, and a wet mass of 361 g with 50 cm^3 of electrolyte and an anode of 10 g. (a) Front view, (b) side view.

3.3.2 Prototype 2 aluminium-air cell

The second prototype aluminium-air cell tested was lighter than prototype 1. It comprised a U-shaped body made of 1 mm thick polyvinyl chloride, PVC, with an air cathode glued to the front and back faces (Figure 3.11). The two air-cathodes were electrically connected. The glue was Marley Solvent Cement containing Bisphenol A Epichlorohydrin Epoxy Resin. The anode tested was an Al/Mg/Sn/Ga plate (3.3 × 5.0 × 0.1 cm) and 99.999 % Al 3mm thick

plate which was inserted in the middle of the cell leaving an inter-electrode gap of approximately 5 mm. The electrolyte was 4 mol dm^{-3} NaOH. The electrolyte was made from NaOH pellets, from Fisher Scientific, of laboratory grade with purity greater than 97 %.

Two versions of prototype 2 were used depending on the thickness of the aluminium anode. Experiments conducted using 1 mm thick Al/Mg/Sn/Ga plate used a 11 mm thick cell that accommodated an electrolyte volume of at most 10 cm^3 and had a wet mass of 20 g. When a 3 mm thick 99.999 % Al plate was used as the anode a 12 mm thick cell was used which accommodated 15 cm^3 of electrolyte and had a wet mass of 30 g. In both instances the area of anode and cathode were the same: 21.5 cm^2 for the anode and 20 cm^2 for the cathode. Two faces of the anode, each of dimensions 3.3 × 3.0 cm, were exposed to the electrolyte giving the anode area of 21 cm^2, including the area of the edges. Green polyester tape was applied to inactive areas of the anode to prevent them from being oxidised by the electrolyte as indicated in Figure 3.11(d). The green polyester tape was supplied by Cole Parmer. It is ideal for high temperature masking applications in corrosive solutions. Current and power densities are calculated relative to anode area unless otherwise stated.

In the prototype 1 aluminium-air cell, a current collector was under compressive contact with the air-cathodes to facilitate adequate current collection. As this was a heavy approach, an alternative was needed so as to reduce the weight of the prototype 2 cell. Most of the air-cathodes tested were fabricated with their own metal mesh current collector with the exception of the two platinum electrodes, 0.5 mg cm^{-2} and 4 mg cm^{-2} Pt. Several methods of collecting the current from the platinum air cathodes were investigated. In one case, silver paint was applied around the perimeter of the electrode and a copper wire attached via epoxy. Double-sided adhesive copper tape was also tested. The method that offered the least electrical resistance involved a combination of copper wire woven around the perimeter of the cathode and silver paint applied over the wire.

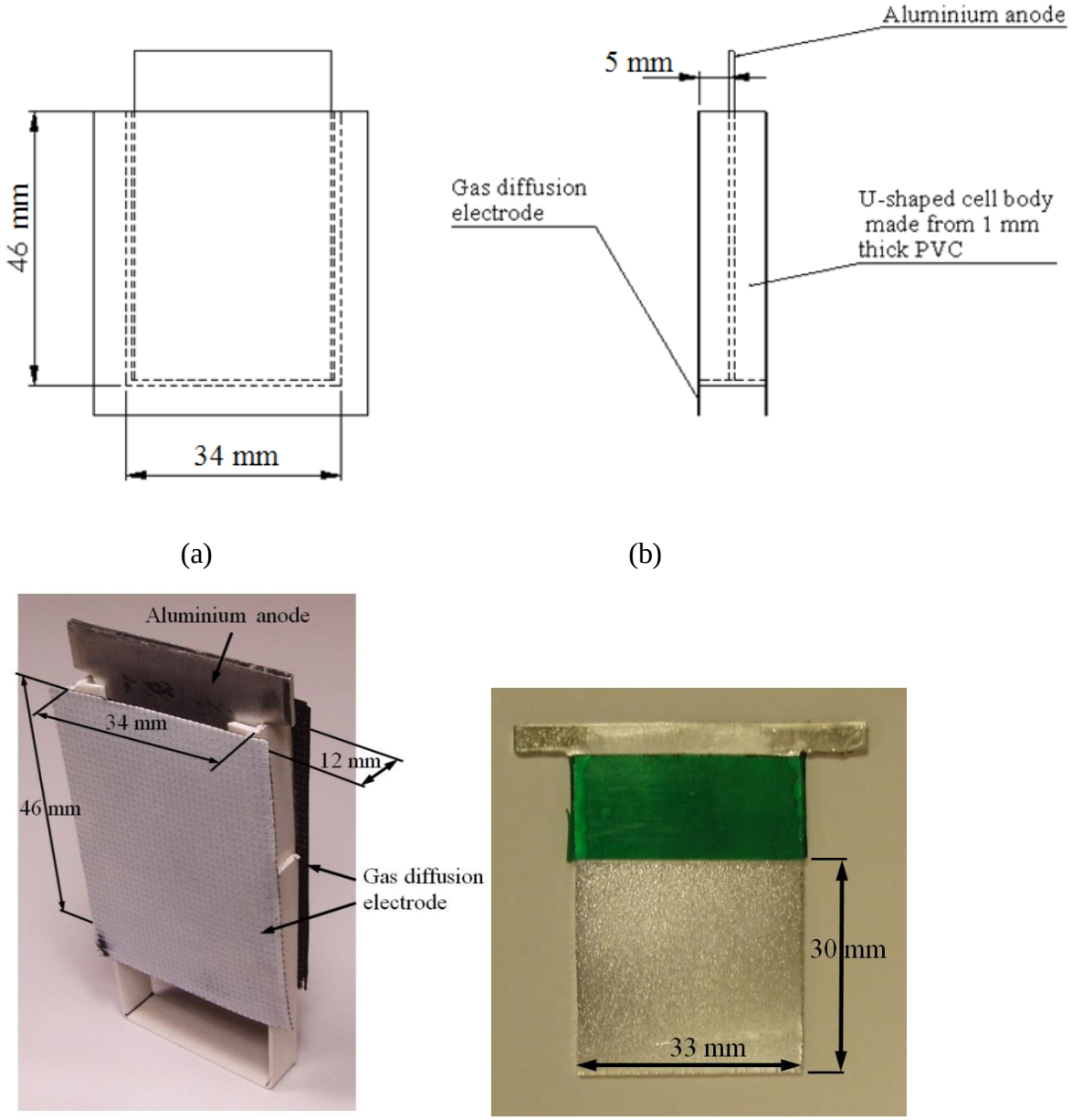

Figure 3.11: Prototype 2 Al-air cell with a wet mass of 30 g with 14 cm^3 of 3 mol dm^{-3} NaOH. (a) Front view of cell, (b) Side view of cell, (c) photograph of prototype 2 aluminium-air cell. (d) 99.999 % aluminium anode after use in prototype 2.

3.3.3 Aluminium-air battery

An aluminium-air battery was constructed according to Figure 3.12. The battery consisted of five of the prototype 2 cells connected in electrical series adding 10 cm^3 of 3 mol dm^{-3} NaOH solution to each cell. The mass of the dry battery was 52 g, while the mass of the battery with 50 cm^3 of 3 mol dm^{-3} NaOH was 109 g. Plan and side view photographs of the battery are

shown in Figure 3.13. There was 1 cm spacing between the individual cells to allow sufficient air supply to the back of the air-electrodes.

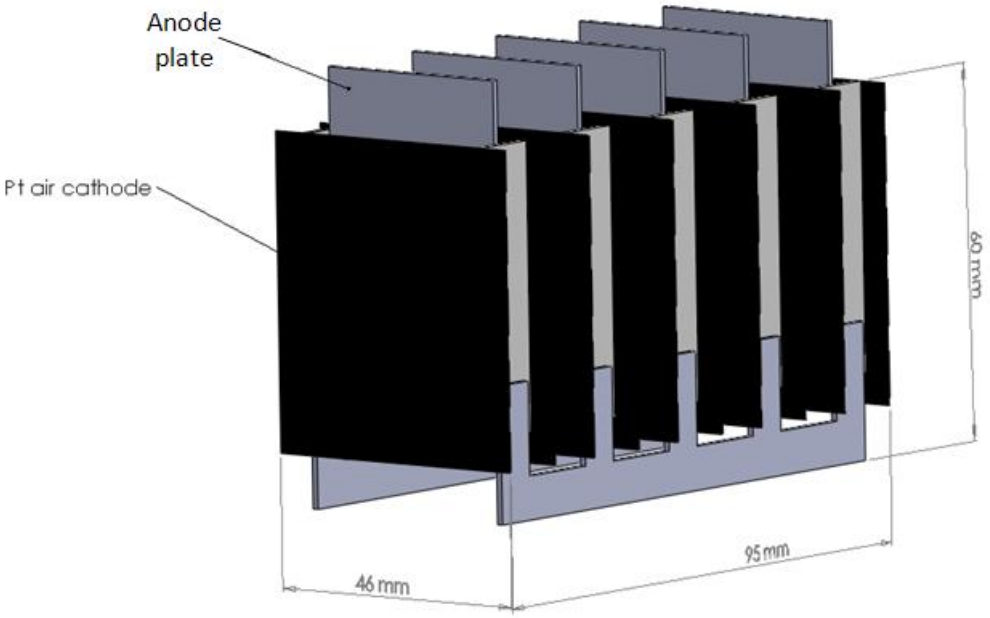

(a)

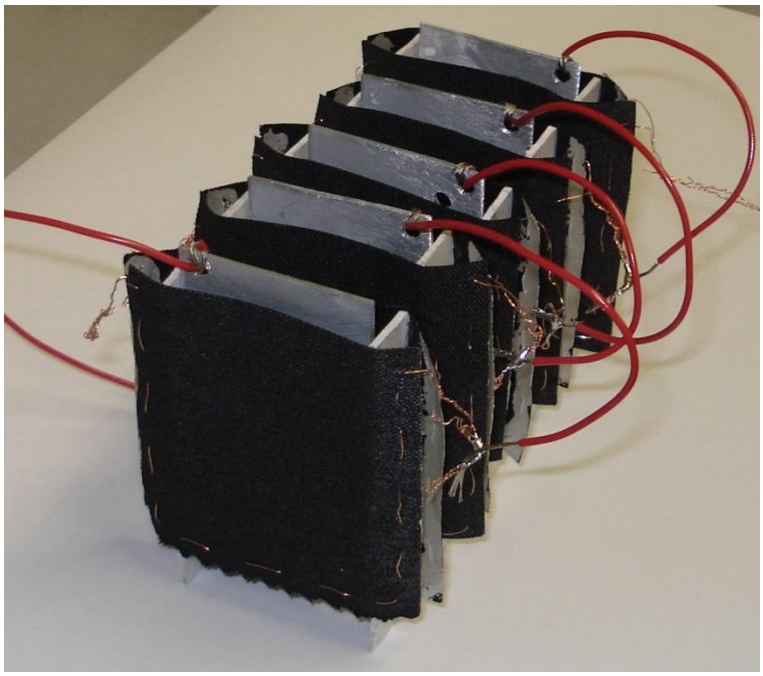

(b)

Figure 3.12: Aluminium air battery comprising five prototype 2 cells connected in series. (a) Drawing and (b) Photograph

(a)

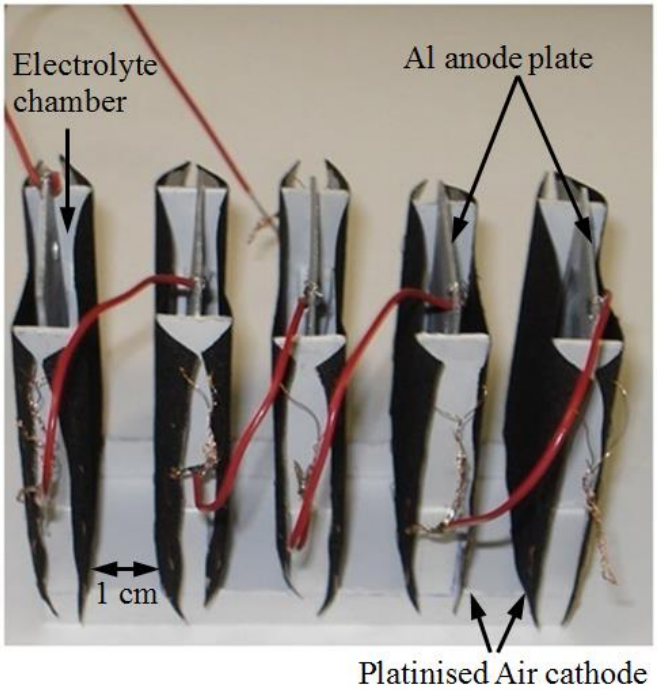

(b)

Figure 3.13: Photographs of the aluminium-air battery comprising 5 prototype 2 cells connected in series. (a) Plan view, (b) side view.

3.3.4 Prototype 3 aluminium-air cell

Prototype 3 Al-air cell, like the previous two cell designs, incorporated two electrically connected air-electrodes forming the two external faces of the cell with the aluminium anode sitting in between them. It was very similar to prototype 2 in that approximately 75 % of the cell consisted of active materials i.e. the aluminium anode, the catalysed air-cathode and the alkaline electrolyte. The major difference between prototype 2 & 3 is the greater rigidity of prototype 3. Prototype 3 shown in Figure 3.14 was constructed from a hollow polypropylene box, rectangular in cross section, with a material thickness of 0.7 mm. A slot, 3.0 × 2.4 cm, was cut into each of the two faces of the box, over each of which was placed an air-cathode adhered in place with an adhesive or Struers EpoFix epoxy. This gave a cathode area of 14 cm^2 split across the two faces of the cell. The overall dimensions of each of the air-cathode were 4.5 × 4.0 cm. The air-cathode was 1 cm wider than the box so as to easily make electrical contact with a crocodile clip. The anode sat in the middle of the cell between the two air-cathodes. Another crocodile clip made electrical contact with the top of the anode which protruded from the cell. The top of the cell was open to facilitate evacuation of the hydrogen gas, to accommodate a Luggin capillary for measuring electrode potentials and a thermocouple to measure temperature.

The Al/Mg/Sn alloy was used as the anode for the prototype 3 cell. It was solution heat treated at 600 °C for 8 hours followed by a water quench. The anode was cut to the dimensions shown in Figure 3.15 giving it an active area of 20 cm^2. Current and power densities were calculated relative to the area of the anode. The bottom edge of the anode sat on the bottom of the cell, while the top of the anode protruded 9 mm from the top of the cell. The active area of the anode was divided equally between its two faces. The upper, inactive parts of the anode were kept isolated from the electrolyte in the cell by coating these parts with EpoFix epoxy resin supplied by Struers, as indicated in Figure 3.15(c). The purpose was to ensure a constant anode area during discharge tests. The Struers EpoFix epoxy resin was more effective at isolating the inactive anode areas from the electrolyte than the green polyester tape used on the anode for prototype 2. The green polyester tape was more easily undermined by the electrolyte than the epoxy. After an aluminium sample was used for two successive cell tests, the electrolyte would have begun to undermine the epoxy layer, so the epoxy layer was ground back and a fresh layer re-applied for a subsequent test. Anodes were re-used between tests with their surfaces ground to P1200 prior to testing. Before immersing the anode in the cell, it was pre-immersed in a beaker of 4 mol dm^{-3} NaOH so that the initial

transient high corrosion phase of the alloy experienced upon immersion occurred outside of the cell to avoid bubbling away the small electrolyte volume. The electrolyte was 4 mol dm^{-3} NaOH solution. The electrolyte was made from NaOH pellets, supplied by Merck, of analytical grade with purity of between 99 – 100 %.

The prototype 3 aluminium-air cell was held in clamp during discharge tests as shown in Figure 3.16. Two pieces of PTFE insulation electrically insulated the cell from the metallic clamp. The Hg/HgO reference electrode was placed into a vertical Luggin capillary, shown in Figure 3.17, which was placed between one face of the anode and one of the air-cathodes. The Luggin capillary was held in position by a clamp attached to a retort stand. The tip of the Luggin capillary had a 90 degree angle bend, so that its end could not be blocked by hydrogen bubbles. The hermitically sealed, type T thermocouple from Omega was inserted between the other face of the anode and the other air-cathode.

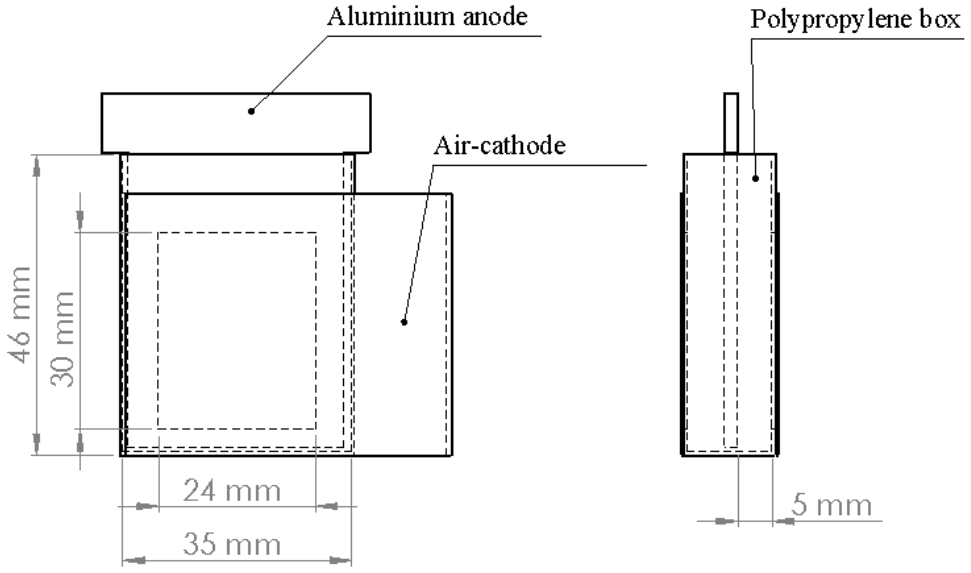

Figure 3.14: Prototype 3 Al-air cell fabricated from a polypropylene box. (a) Front view of the cell, (b) side view of the cell. Al/Mg/Sn anode, 14 g. Approx. 15 cm^3 of 4 mol dm^{-3} NaOH, initially at 22 °C. Mass of cell (inc. electrodes, cell body & electrolyte), 46 g. The gap between the faces of the aluminium anode and the air-cathode was 5 mm.

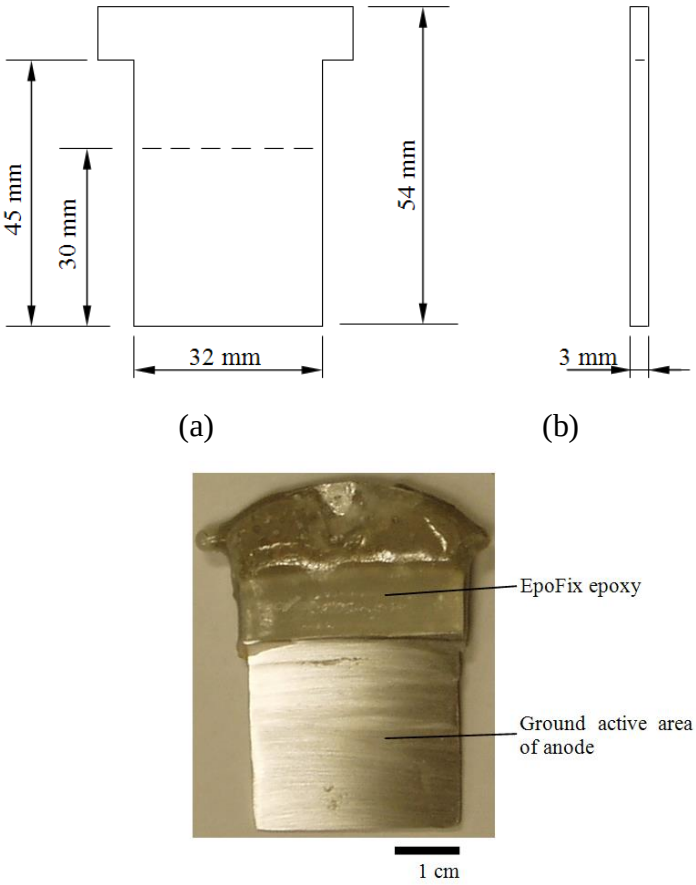

Figure 3.15: Dimensions of aluminium anode for prototype 3 aluminium-air cell. (a) Front view drawing of aluminium anode, (b) side view drawing of aluminium anode and (c) photograph showing the layer of epoxy to exclude inactive parts of the anode from the electrolyte.

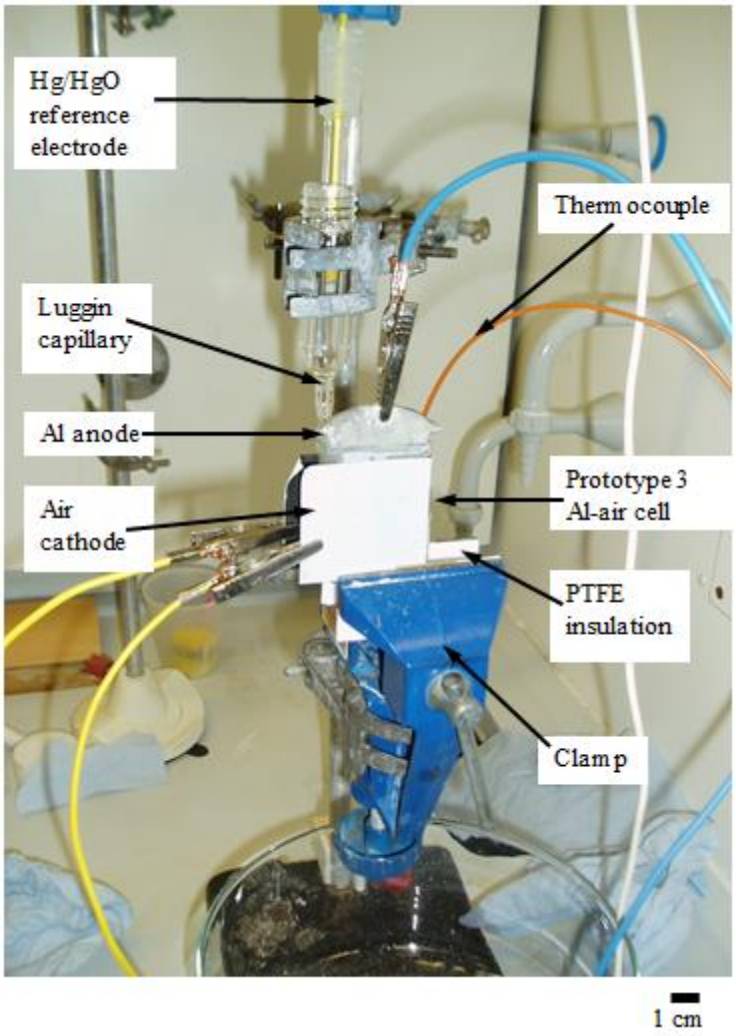

Figure 3.16: Experimental set-up during discharge tests on the prototype 3 aluminium-air cell. The cell is held in a clamp between two pieces of PTFE insulation.

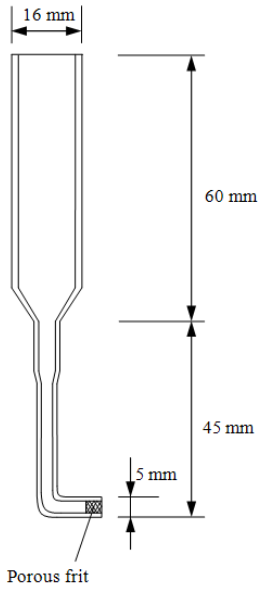

Figure 3.17: Luggin capillary for the Hg/HgO reference electrode for measuring the electrode potentials during the Al-air cell tests.

3.3.5 Electrochemical measurements on Al-air cell

Before discharge tests were conducted on an aluminium-air cell, the cell was put through a small pre-conditioning step. This involved filling the cell with the sodium hydroxide electrolyte and leaving to rest for 1 hour while keeping the anode out of the cell. This facilitated wetting of the air-cathode and its pores. When the KTH air-cathode was being used, it was pre-conditioned by applying a cathodic current density of −50 mA cm^{-2} for 1 hour between it and a platinum counter electrode. Again the anode was kept external to the cell during this pre-conditioning step.

Two types of discharge tests were used to evaluate the performance of the prototype aluminium-air cells: variable load experiments and constant current discharge. Variable load experiments were conducted on the Al-air cells and Al-air battery with the purpose of obtaining a plot showing how the cell potential varied with discharge current. They are useful for determining the cell peak power, limiting current and identifying which elements are responsible for resistive losses in the cell; whether it be activation resistance, ohmic resistance or mass transport. This experiment was conducted using the Kikusui Electronic Load, PLZ334W to apply variable currents from 1 to 5 A at intervals of 0.1 A and rest time of 60 s at each current.

Constant current discharge tests were also carried out on the prototype aluminium-air cells using the Kikusui electronic load. Tests were conducted at 100 mA cm^{-2} discharge for 1 hour. During cell testing the potentials of the anode and cathode were measured against a Hg/HgO electrode. Data acquisition was conducted with a National Instruments data acquisition system, NI 6211, and LabView software. LabView software is a graphical user interface that communicates with a National Instruments data acquisition hard-ware. LabView allows the user to specify which variables are being measured, such as voltage and temperature, to determine how they are recorded and displayed on the computer monitor. The LabView graphical interface created for measuring each of the individual cell voltages during discharge of the 5-celled battery is shown as an example in Figure 3.18. Cell temperature was measured with a Type T thermocouple connected to another National Instruments module, which was designed to compensate for cold junction temperature. The thermocouple was a hermitically sealed type to protect it against the caustic sodium hydroxide electrolyte.

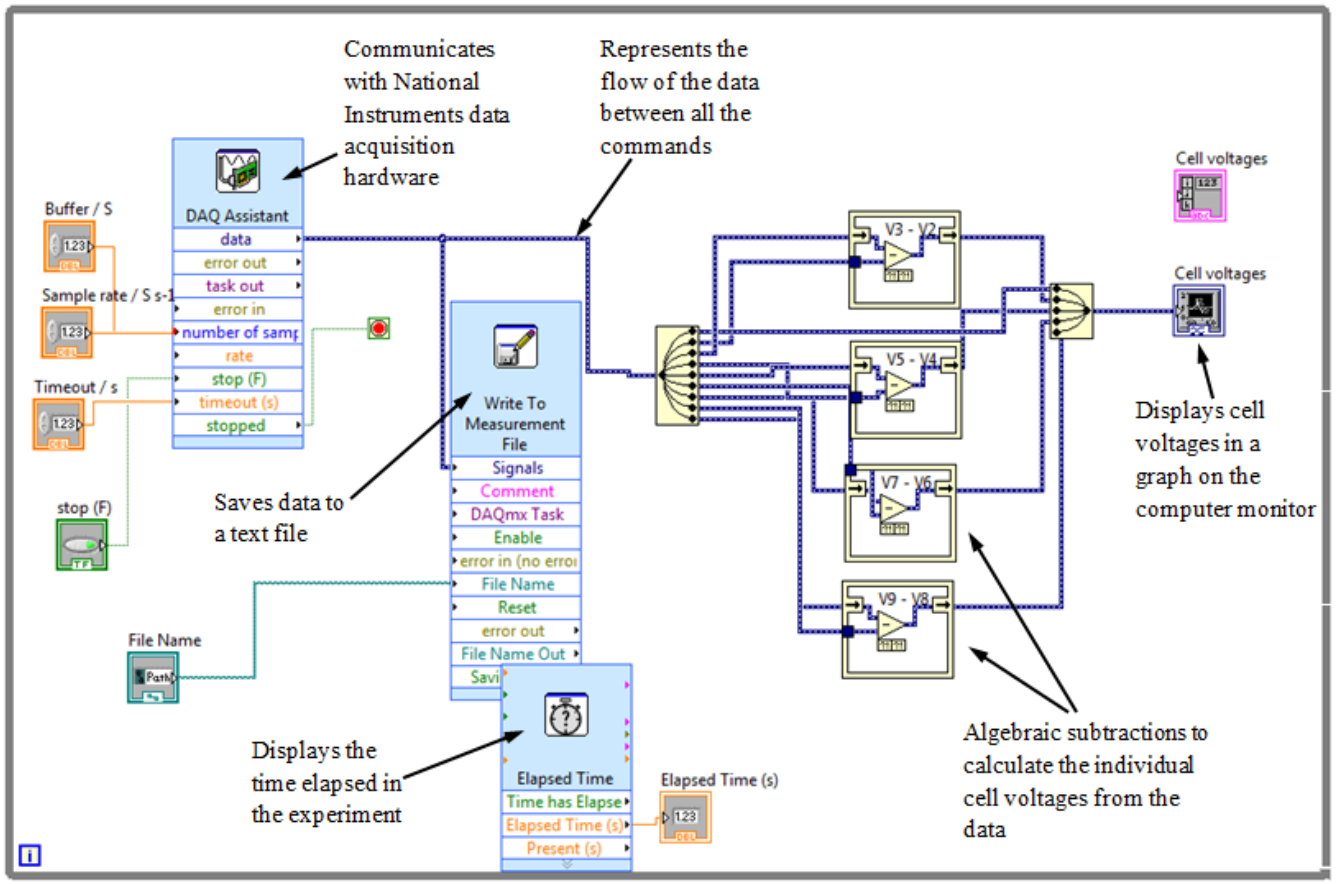

Figure 3.18: LabView data acquisition code used for measuring the voltage of each cell in the 5 cell Aluminium–air battery.

Chapter 4. Electrochemical behaviour of 99.999 % Al and aluminium alloys

4.1 Introduction

The initial part of this chapter characterises the corrosion behaviour of 99.999 %wt aluminium in alkaline solutions. This data was then compared with the oxidation and corrosion behaviour of two high-purity aluminium alloys for use as potential anodes in an aluminium-air battery. There have been many alloys evaluated in the literature as anodes in Al-air batteries, which can be discharged at extremely high current densities at low anode overpotential. The two selected from the literature to be studied in this work were Al/Mg/Sn/Ga and Al/Mg/Sn. Literature results for these alloys showed they displayed more negative potentials than pure aluminium in an Al-air battery at current densities as high as 715 mA cm^{-2} and at potentials as negative as −1.52 V *vs.* Hg/HgO, at a solution temperature of 80 °C, see Table 4.1 [24, 25]. These two alloys were differentiated by their corrosion behaviour, where Al/Mg/Sn/Ga showed corrosion currents at least ten times greater than those of Al/Mg/Sn under anodic discharge in a half-cell [25]. The solution temperature and the gallium alloying addition were the reasons for the difference in corrosion behaviour between the two alloys. The temperature at which the corrosion tests were carried out was 60 °C, which was well above the melting temperature of gallium, 29 °C. In liquid form, the gallium alloying element aggravated the self-corrosion of the Al/Mg/Sn/Ga alloy.

Alloy	Galvanostatic discharge potential *vs.* Hg/HgO	j_{cor} / mA cm^{-2} at 60 °C		
		$j_{cor,70}$	$j_{cor,200}$	$j_{cor,600}$
Al/0.5 Mg/0.07 Sn	*−1.52 V at 645 mA cm^{-2} at 80 °C	1	2	2
Al/0.7 Mg/0.09 Sn/0.03 Ga	−1.62 V at 715 mA cm^{-2} at 80 °C	374	22	28
99.999 % Al	−1.22 V at 520 mA cm^{-2} at 80 °C			

Table 4.1: Polarisation and corrosion characteristics of two aluminium alloys and 99.999 % Al in alkaline solution at elevated temperature [24, 25]. *data for an Al/0.45 Mg/0.085 Sn alloy. Galvanostatic tests were in an aluminium-air cell with a mixture of 5.5 mol dm^{-3} KOH and 0.6 mol dm^{-3} NaCl. Corrosion tests were in a half-cell with 5 mol dm^{-3} KOH. $j_{cor,70}$ is the corrosion current density when discharged at an anodic current density of 70 mA cm^{-2}.

One of the aims of this work was to investigate the electrochemical behaviour of these two alloys, Al/Mg/Sn and Al/Mg/Sn/Ga, at 22 °C, below the melting temperature of the gallium alloying element and contrast the electrochemical behaviour with that at 60 °C. The alloys in Table 4.1 were tested in KOH because KOH has a higher conductivity than NaOH and the peak conductivity occurs at a higher concentration for KOH than NaOH, as discussed in Section 2.1.2. This is beneficial because the higher the electrolyte concentration the higher the solubility for the reaction product, aluminate. In these experiments, NaOH was chosen over KOH due to purity reasons, with high purity NaOH pellets more economically affordable than KOH ones. From that analysis one alloy was chosen as being more appropriate than the other for use in an aluminium-air cell. The electrochemistry of this alloy was further examined at intermediate temperatures between 22 and 70 °C, to see how it would behave from a cold start in the prototype Al-air cell with a small volume, static electrolyte.

4.2 Oxidation and corrosion of 99.999 %wt aluminium

The purpose of these experiments on pure aluminium was to characterise its corrosion and oxidation behaviour in alkaline solutions for use as a comparison against the two alloys. These tests investigated further how the electrochemical behaviour of pure aluminium was affected by different parameters including surface preparation, electrolyte type and purity.

4.2.1 Effect of surface preparation

The effect of surface preparation on the open-circuit potential of pure Al was investigated. The aim was to choose a surface preparation protocol which was an important procedure to facilitate reuse of samples between tests. EDX analysis showed that the surface of the 99.999 %wt Al sample, as received from the manufacturer, was contaminated with iron compounds, presumably remnant from the rolling process, Figure 4.1(a). The very low hardness of the 99.999 % aluminium samples (Vickers Hardness of 17), meant that silicon carbide and carbon grit from the grinding and polishing stages embedded in the surface, as shown in Figure 4.1(b) [119]. The inset in Figure 4.1(b) shows microsized silicon and nanosized zirconia particles embedded on the surface. These contaminants are undesirable as silicon is known to aggravate the corrosion of aluminium in alkaline solutions [92].

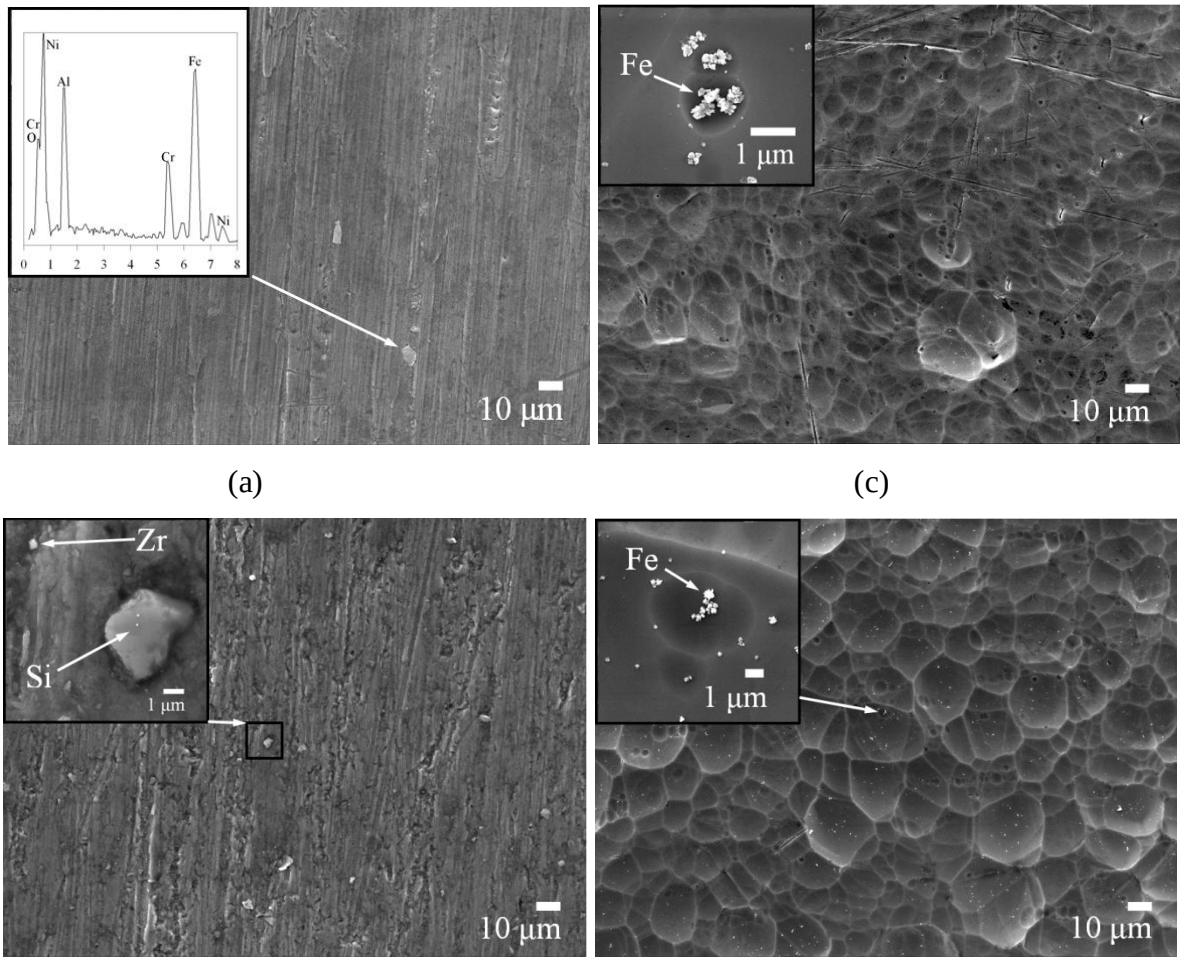

Figure 4.1: Effect of surface pretreatment on the corrosion of 99.999 % Al in 4 mol dm^{-3} NaOH. (a) Initial surface of unpolished sample, as received from manufacturer. Inset shows EDX of an iron compound on the surface from a rolling process. (b) Initial surface of the sample dry polished down to P4000 grade with SiC paper. (c) The corroded surface of unpolished sample. Insets show a magnification of a pit with an iron particle at its centre. (d) Corroded surface of sample polished with SiC paper. Inset shows a circular pit with an iron particle at its centre. Corroded samples were held at open-circuit for 4800 s in 4 mol dm^{-3} NaOH at 22 °C. Electrode area: 3.5 cm^2.

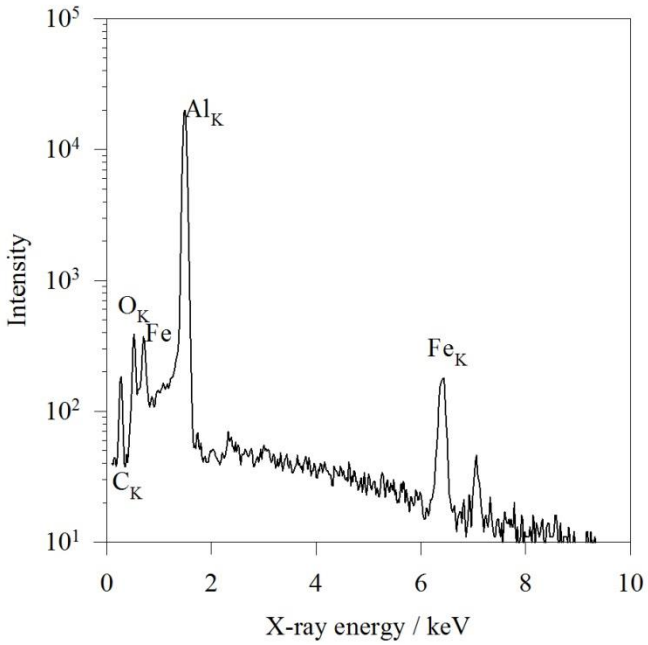

Figure 4.2: EDX analysis of the iron particle at the centre of the pit identified in Figure 4.1(d).

Samples were subsequently immersed in 4 mol dm^{-3} NaOH and their open-circuit potential compared over a 4800 s period to investigate if the surface preparation affected the open-circuit potential, as shown in Figure 4.3. Four other 99.999 % aluminium samples having different surface treatments are included in the comparison. Within the first 150 s, the potential of all samples shifted from −1.70 V *vs.* Hg/HgO to more positive values. The most positive value attained was with the unpolished sample and the sample polished with Al_2O_3 paper (−1.61 V *vs.* Hg/HgO). This was due to the iron compound identified in Figure 4.1(a) [52] or the Al_2O_3 grit from the grinding paper having a passivating effect. These samples remained at this potential for approximately 1000 s before beginning to shift more negatively. Compared to the unpolished sample and the sample polished with Al_2O_3 paper, the other specimens shifted to less positive potentials, 200 s after immersion, and remained at these potentials for a shorter time of at most 450 s before beginning to shift back towards negative potentials. This was particularly true for the two samples polished to a mirror finish whose potentials shifted to −1.63 V *vs.* Hg/HgO, the least positive potential out of the samples examined. This was because they had a cleaner surface. At the end of 4800 s, the open-circuit potential of all samples, independent of the mechanical surface preparation technique used, had slowly reached a steady state value of *ca.* −1.66 V *vs.* Hg/HgO, which is the value reported in the literature [90, 136].

Surface analysis of 99.999 % Al samples following the open-circuit studies found the surface to be characterised by a network of broad, shallow pits between 10 and 20 μm in size. This was the case for both the unpolished sample, Figure 4.1(c), and the sample polished with SiC paper Figure 4.1(d) [49]. This indicates that regardless of the surface preparation used, the aluminium surface will appear the same at open-circuit following a sufficient period of time to reach a steady-state potential. The inset in Figure 4.1(c) shows that within the shallow pits, there are smaller circular pits of 2 μm in size, some with iron particles at their centres as verified by EDX analysis in Figure 4.2. The iron particles most likely came from a rolling process during manufacture, which had not been removed during surface preparation.

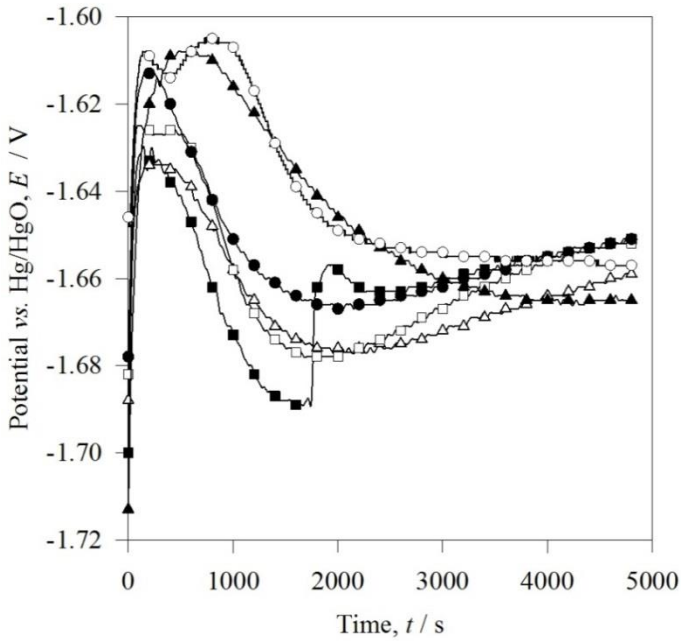

Figure 4.3: The effect of surface polishing on the open-circuit potential of 99.999 % aluminium in 4 mol dm^{-3} NaOH. ○ unpolished, ▲ ground by 9 μm Al_2O_3 paper, ● ground by P1200 SiC paper, □ ground by P4000 SiC paper, ■ mirror finish, polished with 1 μm diamond paste, △ mirror finish, polished with 0.04 μm silica suspension. Electrode area: 3.5 cm^2. Static electrolyte at 22 °C.

In an additional experiment, after holding a sample at open-circuit for 3600 s, the electrolyte was refreshed while still using the same aluminium sample in its oxidised state. Upon doing so, the sample observed a similar transient behaviour in open-circuit potential in Figure 4.4. Over the initial 1000 s in Figure 4.4 the sample in the refreshed electrolyte approached the equilibrium faster than it had done when it was first immersed in electrolyte. Despite this, there are close similarities between the variations in the open-circuit potentials in Figure 4.4

before and after the electrolyte was refreshed. When the initial electrolyte was emptied from the cell the corroded aluminium surface was exposed to the air and re-formed an aluminium oxide layer. When fresh electrolyte was poured into the half-cell, the aluminium oxide layer dissolved and was steadily replaced by a hydroxide layer. This transformation accounted for the transience observed in the open-circuit potential in Figure 4.4 upon the addition of a fresh electrolyte. This suggests that surface preparation alone did not entirely dictate the variation of open-circuit potential of pure aluminium upon initial immersion in the electrolyte and so was not further explored. It took approximately 3600 seconds for the aluminium to reach −1.66 V *vs.* Hg/HgO due to the time it took for the hydroxide layer to stabilise on the surface [36]. A steady-state needed to be reached at the surface among the different reactions taking place including the consumption of OH^- ions to form aluminate ions and consumption of water to evolve hydrogen gas. The experimental potential of −1.66 V *vs.* Hg/HgO was then a mixed potential due to all these different reactions occurring on the aluminium surface.

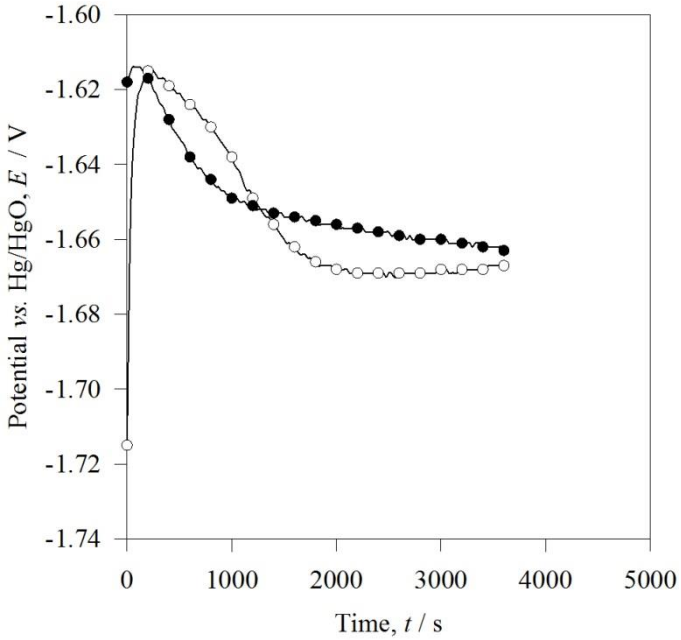

Figure 4.4: The effect of refreshing the electrolyte on the open-circuit potential of the same 99.999 % Al sample in 4 mol dm^{-3} NaOH. ○ Initial measurement, ● after refilling with fresh electrolyte. For the initial measurement, the aluminium was mechanically ground by SiC paper, grit P4000. After measuring its open-circuit potential for 3600s the electrolyte was refreshed. Electrode area: 3.5 cm^2.

4.2.2 Effect of electrolyte type

KOH solutions show a higher conductivity than NaOH solutions, with peak conductivity of 0.7 S cm^{-1} for 7 mol dm^{-3} KOH at 30 °C compared to 0.39 S cm^{-1} for 4 mol dm^{-3} NaOH [80]. As the solubility of aluminate increases with OH^- ion concentration, being able to select a higher concentration potassium hydroxide than sodium hydroxide allows for an aluminate solubility of 6 wt% [82]. A higher electrolyte concentration would also be of benefit to the oxidation of the alloys as the electrolyte solubility for the alloying elements would be greater in a higher concentration electrolyte [127]. Comparing the anodic linear sweep for 99.999 % aluminium in 7 mol dm^{-3} KOH and 4 mol dm^{-3} NaOH shows some differences in anodic behaviour as indicated in Figure 4.5.

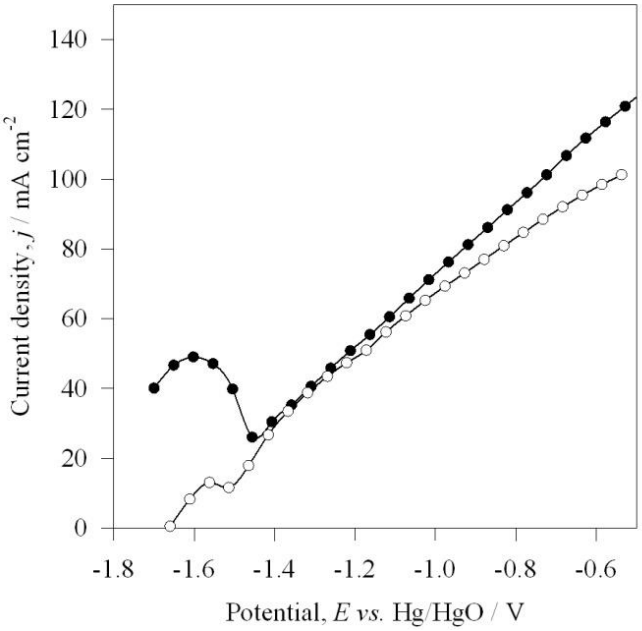

Figure 4.5: Effect of electrolyte type on the anodic polarisation of 99.999 % aluminium. Sweep rate of 1 mV s^{-1}. The electrodes were held at open-circuit for at least one hour prior to sweeping the potential. Platinum mesh counter electrode. Electrolyte temperature: 22 °C. ● 7 mol dm^{-3} KOH, ○ 4 mol dm^{-3} NaOH.

The linear sweep in Figure 4.5 for the sample in sodium hydroxide was commenced at its open-circuit, −1.66 V *vs.* Hg/HgO, recording a current density of 0 mA cm^{-2}, as expected. The sample in potassium hydroxide had a rest potential of −1.70 V *vs.* Hg/HgO prior to the anodic linear sweep. Upon commencing its linear sweep at this potential it displayed a current density of 40 mA cm^{-2} and it only emulated the behaviour of the sample in sodium hydroxide at a potential of around −1.40 V *vs.* Hg/HgO. The reason for the difference in behaviour was because of the low purity of the potassium hydroxide electrolyte, with a purity

range of 85 to 100 %, supplied by Merck. Comparing the impurity levels between the KOH and NaOH electrolytes in Table 4.2 shows that the main difference was higher Ag (10 ppm) and Pb (10 ppm) in KOH than in NaOH (5 ppm Ag and 5 ppm Pb). Perhaps the higher lead concentration in the KOH electrolyte is causing the more negative open-circuit potential and higher anodic currents between −1.70 and −1.40 V *vs.* Hg/HgO. Research elsewhere showed that 20 ppm Pb alloyed with aluminium was beneficial for shifting the open-circuit potential to more negative values and enhancing the anodic discharge rate in sodium chloride compared to pure aluminium. The lead achieved this by destabilising the passive layer. At potentials greater than −1.0 V *vs.* Hg/HgO higher current densities were attained in the KOH electrolyte than in NaOH. KOH was not chosen for further use in these studies because the lack of availability of an economical analytical grade potassium hydroxide.

	KOH 85 - 100 % Impurity / ppm	NaOH 99 - 100 % Impurity / ppm
Carbonate (Na_2CO_3)	≤ 10000	≤ 10000
Chloride (Cl)	≤ 5	≤ 5
Phosphate (PO_4)	≤ 5	≤ 5
Silicate (SiO_2)	≤ 20	≤ 10
Sulphate (SO_4)	≤ 5	≤ 5
Nitrogen	≤ 3	≤ 3
Heavy metals, Ag	≤ 10	≤ 5
Heavy metals, Pb	≤ 10	≤ 5
Aluminium (Al)	≤ 2	≤ 5
Calcium (Ca)	≤ 5	≤ 5
Cadmium (Cd)	≤ 0.1	
Copper (Cu)	≤ 1	
Iron (Fe)	≤ 5	≤ 5
Mercury (Hg)		≤ 0.1
Potassium (K)		≤ 200
Sodium (Na)	≤ 20	
Magnesium (Mg)	≤ 5	≤ 20
Nickel (Ni)	≤ 1	≤ 5
Manganese	≤ 0.5	
Zinc (Zn)	≤ 1	

Table 4.2: Comparison of the certificate of analysis for KOH and NaOH. Both were supplied by Merck, product number 105021 for KOH and product number 106469 for NaOH.

4.2.3 Effect of electrolyte purity on the open-circuit potential of 99.999 % Al in NaOH

Experiments were carried out to compare the effect of the purity of 4 mol dm^{-3} NaOH solution on the open-circuit potential of 99.999 % aluminium. Two electrolyte purities were investigated, an analytical reagent from Merck with an assay of 98.95 % and a laboratory reagent from Fisher Scientific with an assay of 97 %. Figure 4.6 shows that the open-circuit potential obtained in the analytical grade solution was −1.66 V *vs.* Hg/HgO, the experimental value for pure aluminium in alkaline solutions. In the laboratory reagent solution the steady open-circuit potential was 340 mV more negative, at −2.0 V *vs.* Hg/HgO. The closeness of the aluminium to its theoretical value of −2.45 V *vs.* Hg/HgO [36, 49] in the laboratory reagent suggests a thinner passive film on the surface than in the analytical reagent.

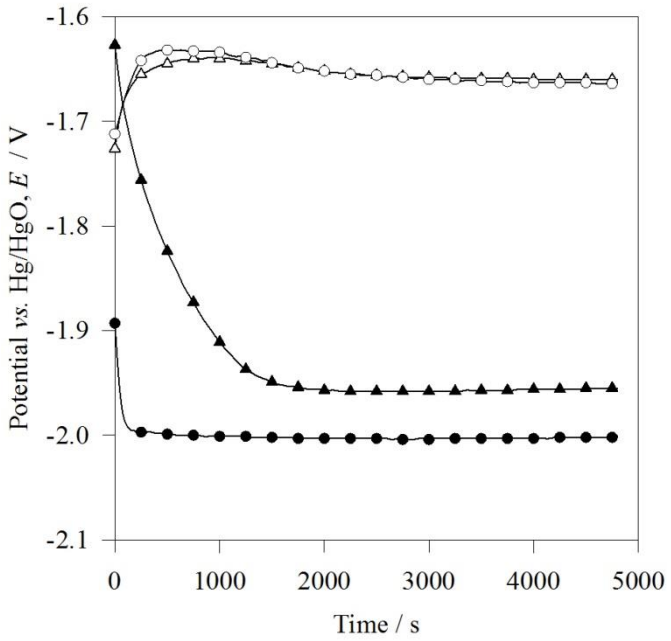

Figure 4.6: Effect of electrolyte purity on the open-circuit potential of 99.999 % Al in 4 mol dm^{-3} NaOH using two different experimental half-cells. ○ 3-electrode cell with analytical reagent NaOH, ● 3-electrode cell with laboratory reagent NaOH, △ beaker cell with analytical reagent NaOH, ▲ beaker cell with laboratory reagent NaOH. Analytical reagent NaOH had a purity of 98.95 %wt, whereas the laboratory reagent NaOH had a purity of 97 %wt.

The difference in aluminium electrode potential when using the two types of electrolyte can be explained by the difference in purity of the two electrolytes, with the laboratory reagent NaOH having higher calcium and phosphorus contents than the analytical reagent, as detailed in Table 4.3. Both calcium [227] and phosphorus [116] have been shown to shift the open-circuit potential of aluminium in NaOH to more negative values as was the case here. From

measurement of the volume of hydrogen evolving from the samples there appeared to be little difference in corrosion current density between the samples immersed in the two types of electrolyte: 19 mA cm^{-2} in the analytical one compared to 22 mA cm^{-2} in the laboratory reagent.

	Analytical reagent NaOH Impurity / ppm	Laboratory Reagent NaOH Impurity / ppm
Calcium	1.32	< 100
Carbonate	500	
Copper	0.05	< 20
Heavy metals	5	
Iron	1.28	< 20
Lead	< 0.05	< 20
Magnesium	< 0.2	< 100
Mercury	< 0.1	
Nickel	0.11	
Phosphate	5	
Potassium	122.62	< 2000
Sulfate	< 20	
Chloride	< 50	
Nitrogen	< 1	
Phosphorus	0.23	< 50
Zinc		< 500
Sulfur		< 200

Table 4.3: Comparison of the impurity contents of analytical reagent, 98.95 %wt purity, [228] and laboratory reagent, > 97 %wt purity sodium hydroxide.

The SEM image of the surface of the sample immersed in the laboratory reagent, Figure 4.7, completely contrasts with the surface of the sample immersed in the analytical reagent, Figure 4.1(c). The sample immersed in the analytical reagent was characterised by a network of shallow pits on its surface, see Figure 4.1(c). These pits were not evident on the sample that was immersed in the laboratory reagent suggesting its surface underwent uniform oxidation, as shown in Figure 4.7. To ensure that the experimental set-up using the three-electrode cell was not the reason for the more negative open-circuit potential, the two tests were repeated, this time by suspending the aluminium electrode in the solution in a glass beaker. These results agree with those from the three-electrode cell, where a more negative open-circuit potential was obtained in the laboratory reagent than in the analytical one, see Figure 4.6.

Research elsewhere showed that the purity of an alkaline electrolyte had an effect on the corrosion behaviour and potential of the aluminium electrode [36]. In experiments comparing two electrolytes, one with 0.05 ppm iron impurity and the other with 5 ppm iron impurity, the overpotential of the aluminium electrode was greatest in the electrolyte with the higher level of iron impurity [36]. This was because Fe^{2+} ions reduced on the aluminium surface, creating preferential sites for hydrogen evolution and the corrosion current was enhanced, shifting the potential to more positive values [36].

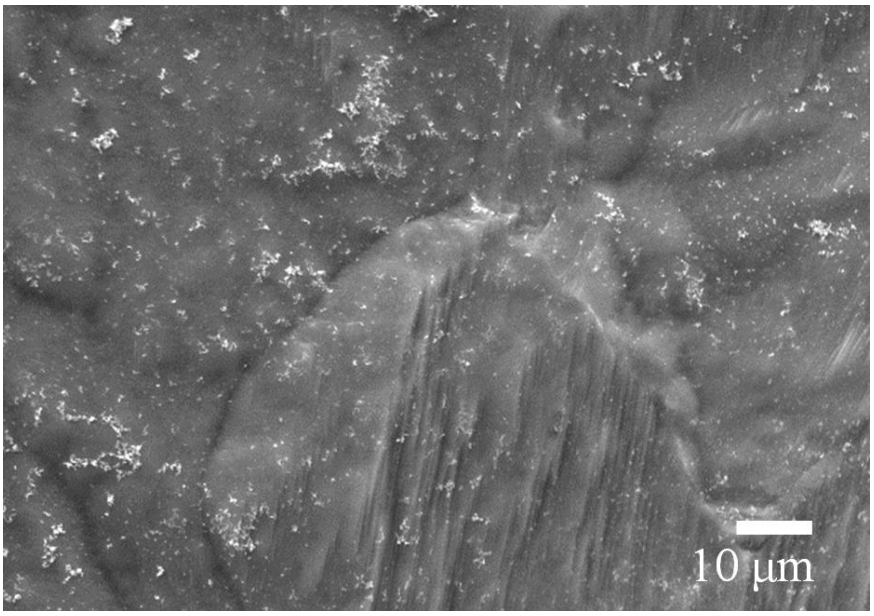

Figure 4.7: SEM image showing the effect of electrolyte purity on the surface of 99.999 % aluminium at open-circuit. Electrolyte: 4 mol dm^{-3} NaOH at 22 °C. Sample held at open-circuit for 4800 s in a laboratory reagent of > 97 %wt purity. Electrode area: 3.5 cm^2.

4.2.4 Corrosion of 99.999 %wt aluminium at open-circuit and under discharge

The technique used to quantify the corrosion of 99.999 % Al involved applying a range of anodic currents and simultaneously measuring the volume of evolved hydrogen with time [23, 36, 58, 59, 61]. Galvanostatic tests were carried out on an aluminium sample, using the three electrode cell, over the current density range of 0 to 80 mA cm^{-2}. For each current density, the electrode potential and volume of evolved hydrogen gas were measured as a function of time, as shown in Figure 4.8(a) and (b) respectively. From Figure 4.8(a), the electrode potentials at time equal to 3000 s were recorded and plotted as a function of applied current density in Figure 4.9(a). The curve in Figure 4.9(a) displays an almost linear ohmic response suggesting the oxidation of the aluminium is controlled by charge transfer. This

plot, constructed from the galvanostatic discharge experiments, is compared against that obtained from a conventional anodic linear sweep voltammogram at a slow sweep rate of 1 mV s^{-1}. There was a small difference between the results of the tests.

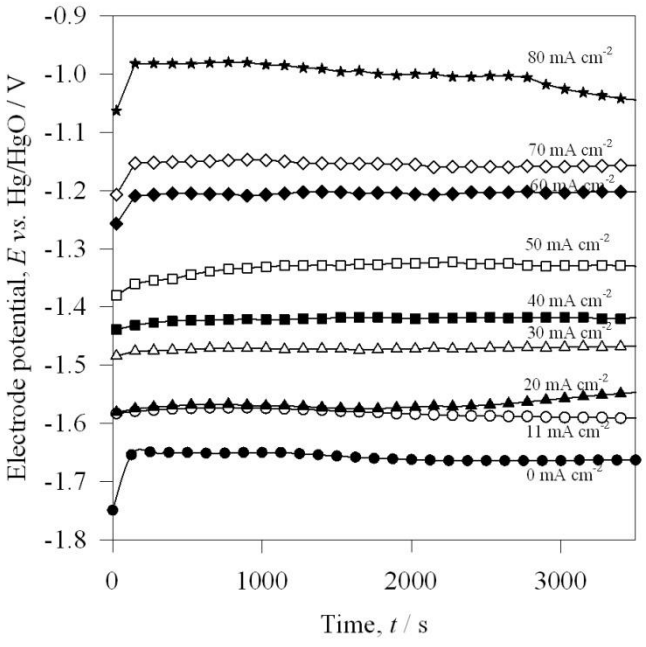

(a)

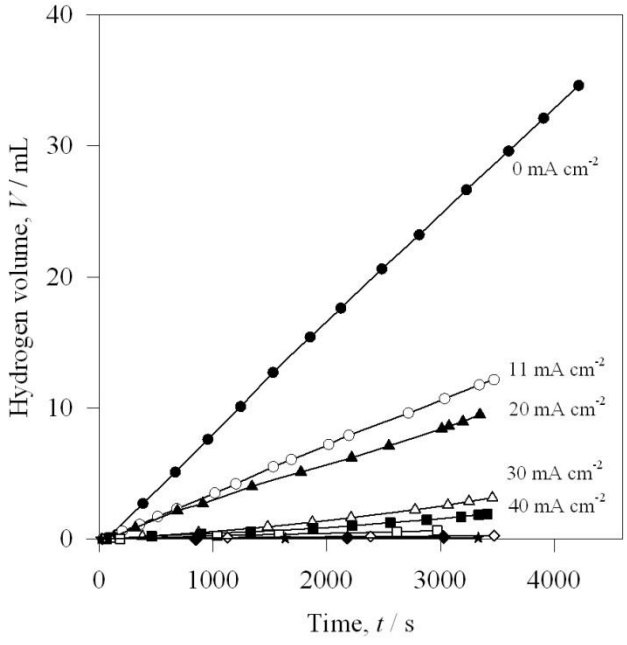

(b)

Figure 4.8: Results from galvanostatic tests on 99.999 %wt aluminium in 4 mol dm^{-3} NaOH. (a) Variation of electrode potential *vs.* time at different anodic current densities. (b) Hydrogen volume *vs.* time at different anodic current densities. Electrode area: 3.5 cm^2. Electrolyte temperature: 22 °C. Platinum mesh counter electrode.

The current density that was applied during the galvanostatic discharge tests and flowed through the external circuit was the difference between two reactions: the anodic dissolution of the aluminium and the cathodic reduction of water, occurring on the surface of the aluminium making up a galvanic cell. The corrosion current indicates the rate at which electrons were consumed in the reduction of water. It was calculated from the hydrogen volume data in Figure 4.8(b) and plotted as a function of applied current, as shown in Figure 4.9(b). The corrosion currents of 99.999 % aluminium were highest at open-circuit and reduced as the discharge rate was increased [23]. At current densities above 55 mA cm^{-2}, the discharge efficiency, calculated via equation (2.9), was greater than 99 %. Matching an aluminium-air battery to an application requiring continuous discharge at current densities greater than 55 mA cm^{-2} would achieve most use out of the aluminium anode.

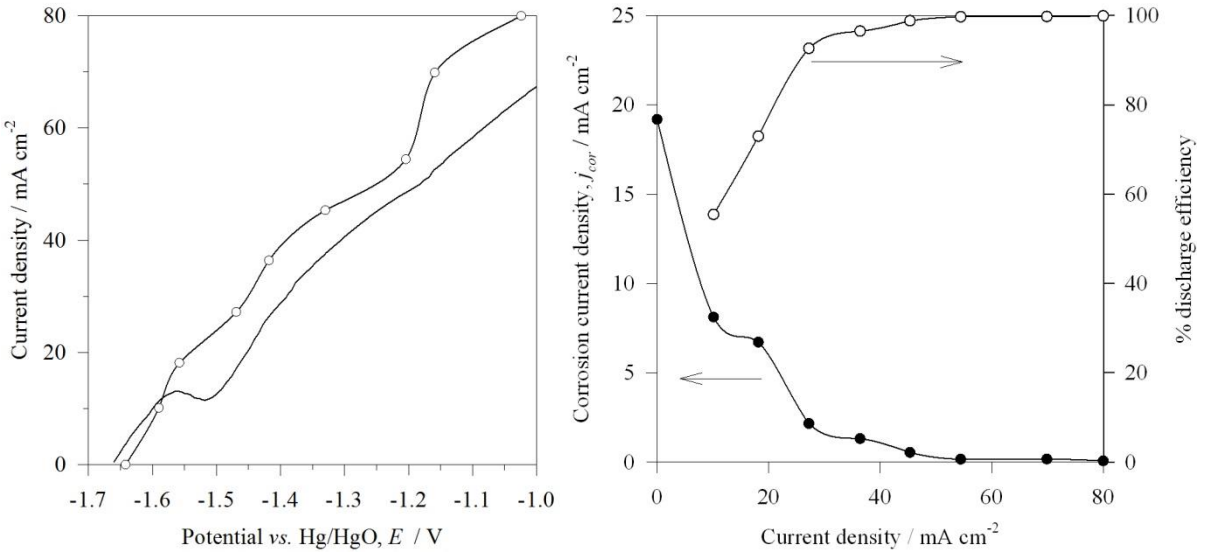

(a) (b)

Figure 4.9: Dissolution behaviour of 99.999 % Al in 4 mol dm^{-3} NaOH. (a) ○ Polarisation curve constructed from galvanostatic discharge tests over the range, 0 to 80 mA cm^{-2}. —— Linear sweep voltammogram for pure aluminium at 1 mV s^{-1} (b) Corrosion current density determined by hydrogen collection, and discharge efficiency. Electrolyte temperature: 22 °C. Electrode area: 3.5 cm^2.

4.3 Oxidation and corrosion of the alloys

4.3.1 Importance of solution heat treatment

Elements alloyed with the aluminium are only effective at enhancing the oxidation of the aluminium or inhibiting the self-corrosion when they are in solid solution [49, 88]. Alloying elements that are present as precipitates act as corrosion centres, often resulting in pronounced grain boundary attack and potential disintegration of the grain [49]. Precipitates will form during the slow cooling of the metal after casting. As the aluminium alloy begins to cool down after casting, dendrites begin to grow at 660 °C. As dendrite growth occurs, the solidification front rejects the alloying constituents which have a lower solidification temperature than aluminium. Once the solid solubility of these alloying elements at their solidification temperature is exceeded, they will concentrate as precipitates in the interdendritic region [47]. The elements can be brought into solid solution by carrying out a solution heat treatment at 600 °C for 8 hours followed by a water quench [52, 96, 100]. The rapid cooling during quenching suppresses precipitation of the alloying elements.

To illustrate the effect of precipitates on aluminium alloy oxidation in alkaline solution two forms of the Al/Mg/Sn alloy were examined: one with an un-homogenised microstructure and the other with a homogenised microstructure. The homogeneous sample was solution heat treated for 8 hours at 600 °C, followed by a cold water quench, where the water was at 20 °C. 600 °C is the temperature at which Mg and Sn have maximum solubility in aluminium, as indicated by their binary phase diagrams in Figure 4.10. At 600 °C, the maximum solubility for tin in aluminium is 0.10 % and the maximum solubility for magnesium is 3.6 % [102]. These maximum solubility's apply to a binary alloy, but could be lower for a ternary alloy. Precipitation of the alloying elements was prevented by the rapid cooling or quenching to form a solid solution alloy with a uniform composition, Figure 4.11(a). The un-homogenised sample had a non-uniform composition characterised by micrometre sized precipitates which were of higher atomic mass than the surrounding matrix and showed up as bright particles under the back-scatter electron image in Figure 4.11(b). These precipitates were richer in Mg and Sn than the surrounding metal, as indicated by the comparison of the EDX profiles for a precipitate in Figure 4.11(c) and the matrix in Figure 4.11(d). The un-homogenised Al/Mg/Sn sample was heat treated at 500 °C which clearly was not a sufficiently high temperature to allow all of the magnesium and tin alloying elements to go into solid solution with the aluminium base metal.

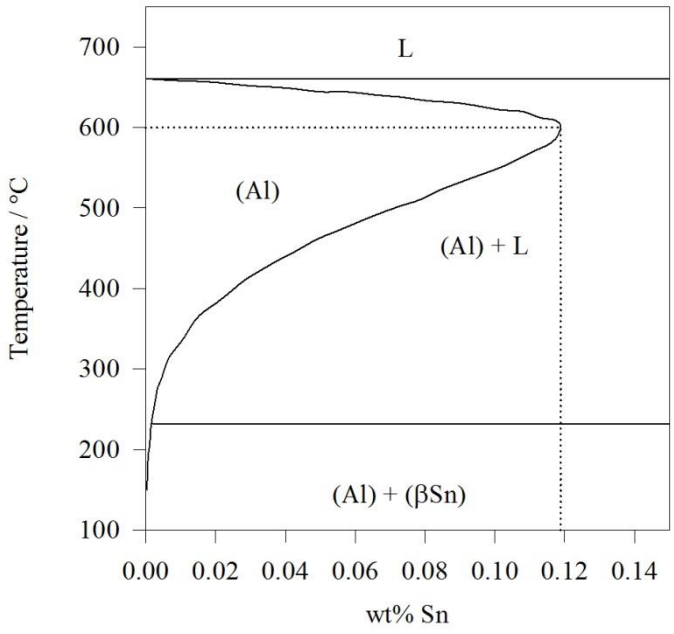

(a)

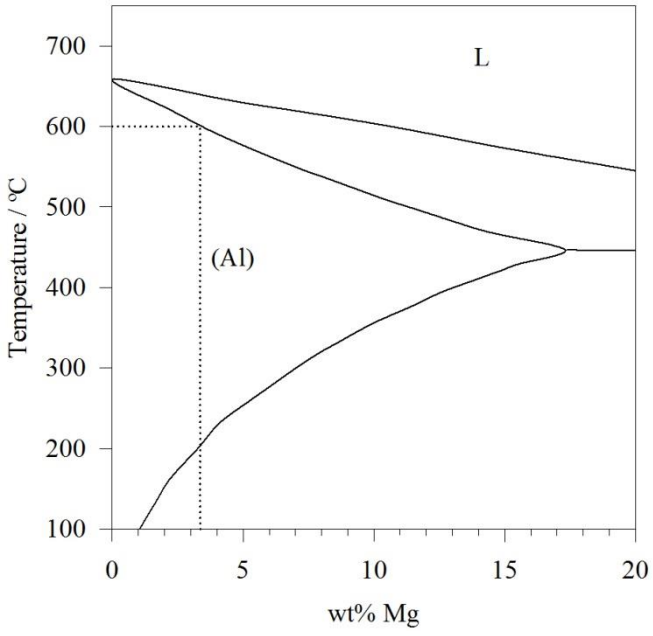

(b)

Figure 4.10: Equilibrium phase diagrams for (a) Al/Sn and (b) Al/Mg binary alloys [101]. Dotted lines indicate how the solubility limits at 600 °C are read from the graphs.

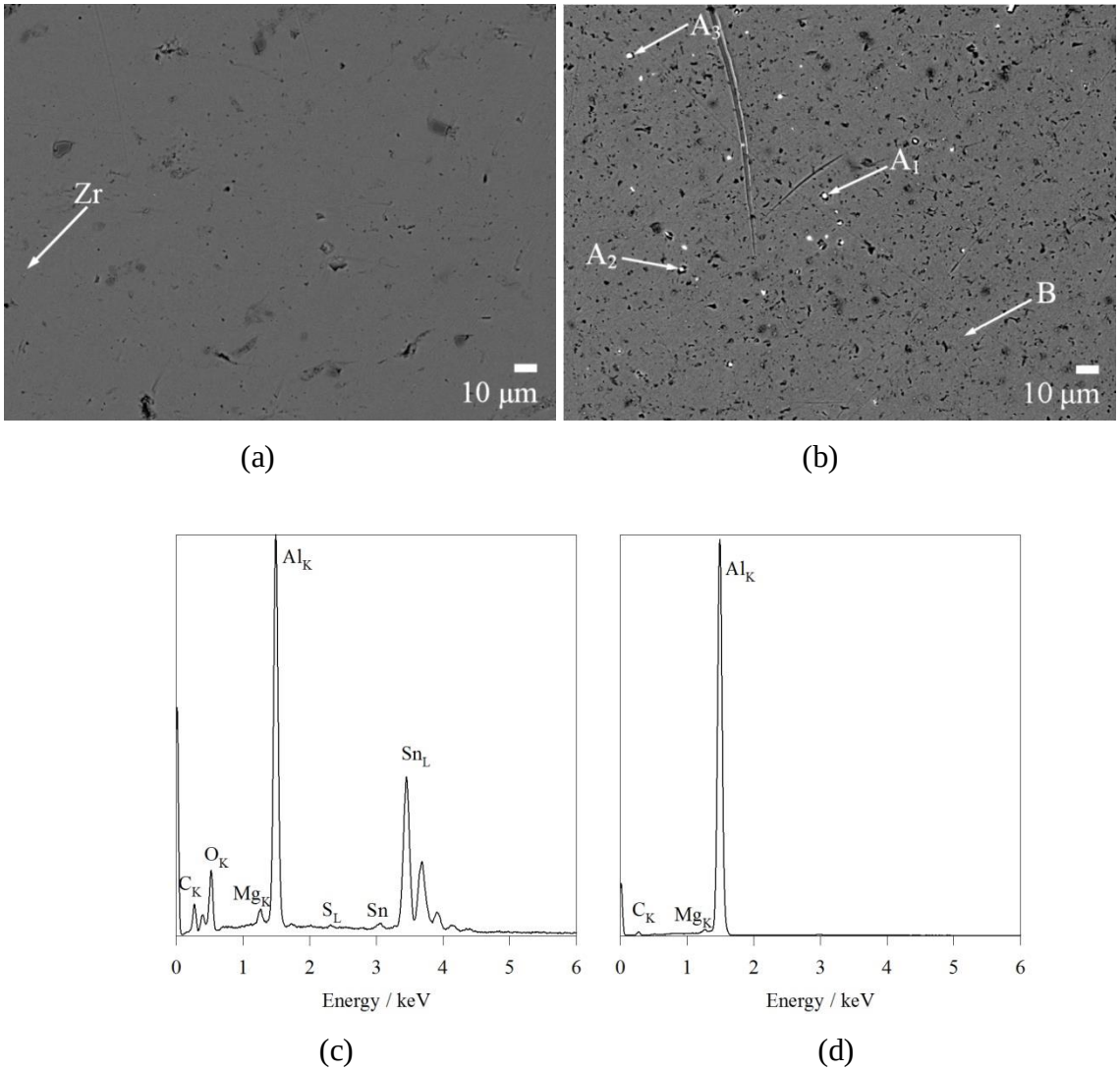

Figure 4.11: Effect of heat treatment temperature on the uniformity of the composition of the Al/Mg/Sn alloy. (a) BEI of homogenised sample, solution heat treated at 600 °C for 8 hours, followed by a water quench. The identified zirconium particle was a contaminant from polishing. (b) BEI of un-homogenised sample, heat treated at 500 °C for 6 hours. Elements of higher atomic mass than the matrix show up as white particles. (c) EDX profile for point A_1. Points A_2 and A_3 were of similar composition. (d) EDX profile for point B.

The precipitates in the un-homogenised sample acted as corrosion centres causing local break-down of the passive hydroxide layer. As a consequence its open-circuit potential fluctuated for the first 3000 s, between −2.07 and −1.78 V *vs.* Hg/HgO, see Figure 4.12(a), before stabilising at −2.07 V *vs.* Hg/HgO, more negative than the −1.66 V *vs.* Hg/HgO for 99.999 %wt aluminium. At this extremely active open-circuit potential, the formation of tin hydride, SnH_4 [49], or aluminium hydrides would have been viable, further preventing the passivation of the surface. Consequently, the self-corrosion of the un−homogenised sample

was very aggressive at open-circuit with a rapid rate of hydrogen evolution, equating to a corrosion current density of 718 mA cm^{-2}.

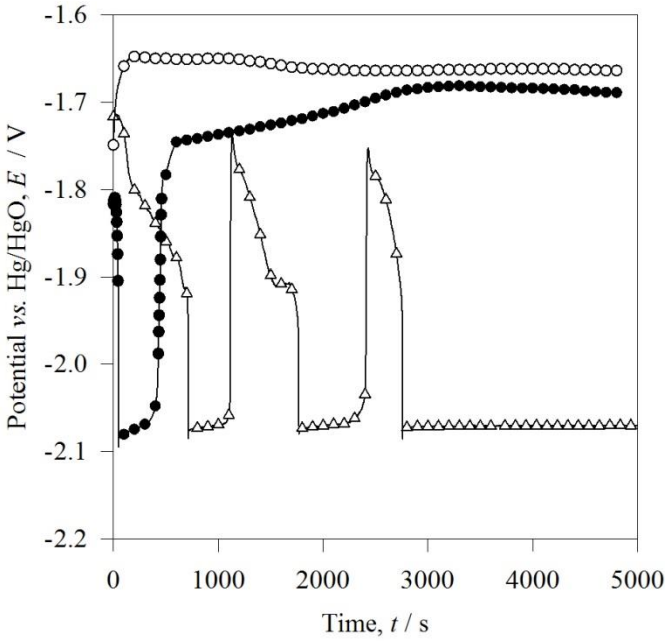

(a)

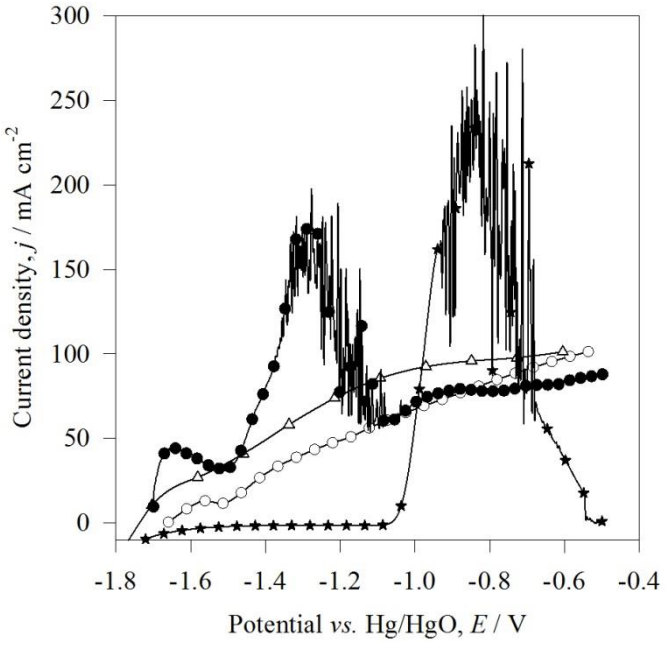

(b)

Figure 4.12: The importance of solution heat treatment on the open-circuit potential and polarisation of Al/Mg/Sn alloy. (a) Open-circuit potential, (b) Polarisation curves at 1 mV s^{-1}. Electrolyte: 4 mol dm^{-3} NaOH at 22 °C. △ Al/0.5 Mg/0.07 Sn un-homogenised, ● Al/0.5 Mg/0.07 Sn homogenised at 600 °C for 8 hours, ○ 99.999 %wt Al, ★ 99.99 % Sn. Electrode area: 3.5 cm^2. Platinum mesh counter electrode.

In contrast, the homogenised sample only displayed this high negative open-circuit potential as a transient for 400 s before stabilising at −1.70 V *vs.* Hg/HgO in Figure 4.12(a), 40 mV more negative compared to pure aluminium. This negative open-circuit potential can be explained upon examination of the anodic linear sweep for 99.99 % Sn in 4 mol dm^{-3} NaOH, shown in Figure 4.12(b), which shows the stability range of tin in alkaline solution to be −1.71 to −1.1 V *vs.* Hg/HgO. During oxidation of the alloy at open-circuit, tin also oxidised from the alloy and dissolved into the electrolyte. As aluminium is more anodic than tin, these tin ions deposited from the electrolyte onto cathodic surface sites of the aluminium alloy, shifting the potential of the alloy to the more negative end of the stability window for tin, −1.7 V *vs.* Hg/HgO. This illustrates that an appropriate alloying element for aluminium-air battery alloys is more noble that aluminium with a wide stability window in alkaline solutions. The formation of these tin deposits at cathodic sites inhibited the water reduction reaction giving the homogenised sample a much lower open-circuit corrosion current density of 7 mA cm^{-2}, compared to its un-homogenised counterpart [106].

The presence of tin and magnesium as precipitates instead of in solid solution within the un−homogenised alloy also affected anodic discharge. Anodic currents were inferior to those of the fully homogenised alloy, as can be seen from the linear sweep voltammetry in Figure 4.12(b). In comparison to pure aluminium, the homogenised Al/Mg/Sn alloy was more electrochemically active over the potential range of −1.7 to −1.1 V *vs.* Hg/HgO. At around −1.5 V there was a dip in the current of the homogenised Al/Mg/Sn alloy, which was also observed for pure aluminium. At potentials more positive than −1.5 V *vs.* Hg/HgO, the current for the homogenised Al/Mg/Sn alloy increased linearly to a maximum of 173 mA cm^{-2} at around −1.3 V *vs.* Hg/HgO. The potential range of enhanced anodic behaviour (−1.7 to −1.1 V *vs.* Hg/HgO) corresponded to the region of stability for pure tin in alkaline solutions, as predicted by the Pourbaix diagram i.e. between the $SnH_{4(g)} / Sn$ reversible potential of −1.9 V *vs.* Hg/HgO to the Sn / SnO_3^{2-} reversible potential of −1.0 V *vs.* Hg/HgO [25, 49, 105]. The anodic polarisation curve for 99.99 %wt Sn in Figure 4.12(b) verifies this. During the anodic discharge of the homogenised alloy, both the base aluminium and the tin alloying element oxidise to form aluminate and stannate ions, respectively, in the electrolyte. When the potential of the alloy was more negative than the reversible potential for Sn / SnO_3^{2-}, stannate ions in the electrolyte reduced and immersion deposited as metallic tin

onto the cathodic sites of the alloy [95]. The deposited tin destabilised the passive layer promoting further dissolution of the homogenised alloy, enhancing its anodic currents compared to the un-homogenised sample. Evidence in the literature of the presence of surface tin can be found through Auger depth profiling which indicated a higher concentration of metallic tin on the outer surface of the passive film on an Al/Sn alloy, gradually decreasing across the entire film thickness towards the bulk value in the metal [106]. Once the potential of the homogenised alloy became more positive than the Sn / SnO_3^{2-} reversible potential of −1.0 V *vs.* Hg/HgO, stannate no longer plated back from the electrolyte onto the alloy surface and the dissolution behaviour of the alloy returned to match that of super-pure aluminium, which accounted for the passivation peak at −1.3 V *vs.* Hg/HgO, shown in Figure 4.12(b).

Before this passivation peak at −1.3 V *vs.* Hg/HgO, there were current fluctuations in the anodic polarisation curve of the homogenised Al/Mg/Sn sample. Local variations in the concentration of stannate in the electrolyte could explain these [49], indicating the significance of the solubility of the alloying element in alkaline solutions. Locally, when the electrolyte became saturated with stannate, further tin from the alloy solid solution was no longer able to dissolve into the electrolyte and instead formed tin oxide causing a drop in anodic behaviour. Gradually the stannate concentration fell below the saturation level due to diffusion into the bulk electrolyte or back plating onto cathodic sites on the surface of the aluminium. Once the electrolyte was no longer locally saturated with stannate, tin once again dissolved from the alloy into the electrolyte returning the alloy to its more enhanced anodic state compared to pure aluminium. At the end of a linear sweep experiment, the potential of the homogenised alloy returned to its transient open-circuit value of −2.0 V *vs.* Hg/HgO. The commencement of an anodic linear sweep from this active potential of −2.0 V *vs.* Hg/HgO did not yield any improvement in the anodic behaviour of the homogenised Al/Mg/Sn alloy compared to the linear sweep commenced at the steady state potential of −1.7 V *vs.* Hg/HgO, see Figure 4.13. This indicates that the highly anodic state of the alloy that existed at −2.0 V *vs.* Hg/HgO was not sustained to infer any additional benefit during anodic discharge.

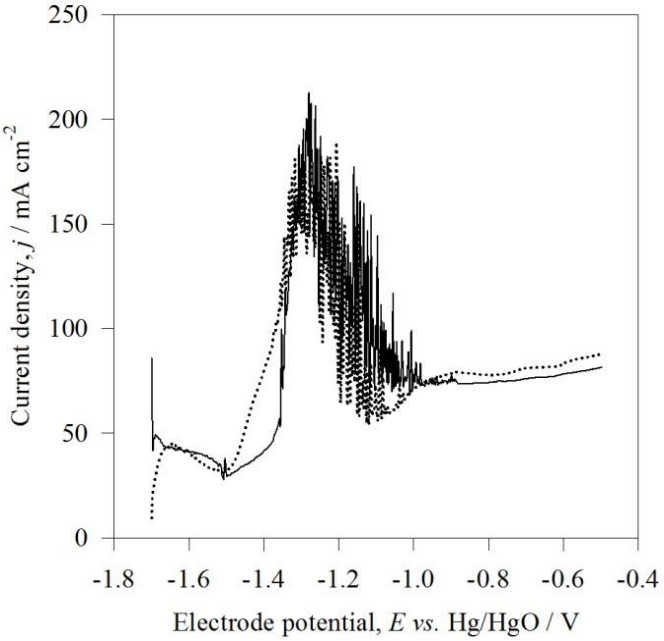

Figure 4.13: Effect of initial electrode potential on the polarisation of the homogenised Al/Mg/Sn alloy. ····· Initial potential was −1.7 V *vs.* Hg/HgO, ——— initial potential was −2.0 V *vs.* Hg/HgO. Electrolyte: 4 mol dm^{-3} NaOH at 22 °C. Sweep rate: 1 mV s^{-1}.

The above experiments showed the importance of solution heat treatment of the aluminium alloys. The same solution heat treatment procedure was used for the preparation of the Al/0.4 Mg/0.07 Sn/0.05 Ga alloy i.e. it was heat treated at 600 °C for 8 hours followed by a water quench. Analysis of the surface of the sample under a scanning electron microscope indicated the presence of second phase particles, see Figure 4.14. These particles were composed of Mg and Sn as illustrated by the EDX in Figure 4.14(b). There are a number of reasons for the presence of these precipitates. The addition of gallium may reduce further the maximum solubility limit for tin in aluminium, explaining why not all of the tin goes into solid solution. Previous work at the University of Southampton on this alloy also found the presence of tin and magnesium precipitates on untested samples [1].

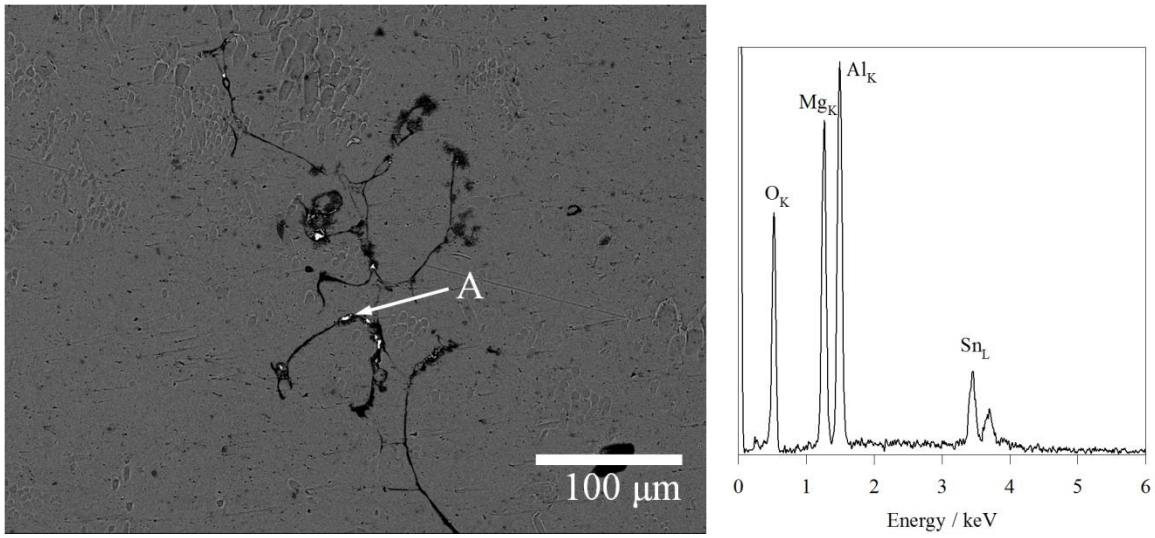

(a) (b)

Figure 4.14: Difficulty in obtaining a solid solution with the Al/Mg/Sn/Ga alloy. (a) Back-scatter electron image (b) EDX profile of the particle labelled A. Solution heat treatment for 8 hours at 600 °C followed by a water quench. 15 kV accelerating voltage.

The discussion above highlights the necessity for a solution heat treated alloy, with a homogeneous microstructure, as an anode of an Al-air cell. Subsequent experiments were conducted with solution heat treated alloys.

4.3.2 Effect of reference electrode distance

The potential of the Al/Mg/Sn alloy was highly sensitive to the distance of the reference electrode from the electrode surface. Figure 4.15 shows how the anodic profile from the Al/Mg/Sn alloy drastically varied depending on the location of the reference electrode from its surface. When the reference electrode was 5 cm form the surface of the Al/Mg/Sn working electrode the linear sweep was entirely resistive. This was because of the large distance between the reference electrode and the working electrode which meant the voltage drop between them was large given by IR_s, where I is the anodic current and R_s is the solution resistance. Theoretically that resistance would be equal to 3.1 Ω, given a conductivity of 0.39 S cm^{-1} across a cylindrical volume of cross sectional area of 4.13 cm^2 and with the reference electrode 5 cm away from the surface of the working electrode. In another instance, a Luggin Capillary was positioned so that its tip was 2 mm away from the electrode surface. This was achieved by having the tip of the Luggin capillary 1 mm back from the circular opening in the three-electrode cell to which the working electrode was clamped. Then knowing the

thickness of the rubber gasket to be 1 mm, a working distance of 2 mm could be ensured. When the reference electrode was placed in the Luggin capillary the electrode potential measured by the Luggin capillary was influenced by a smaller uncompensated resistance. The uncompensated resistance then depended on the distance between the tip of the Luggin capillary and the working electrode. Consequently the current observed from the working electrode during the linear sweep was higher when electrode potential was measured with a Luggin capillary.

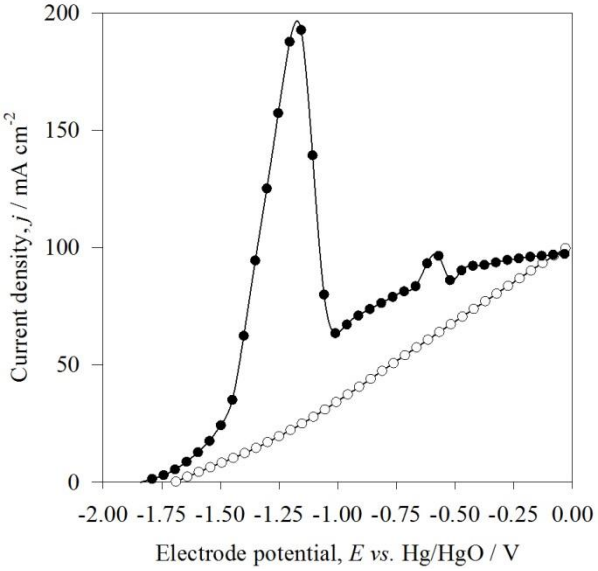

Figure 4.15: Effect of distance of reference electrode on the anodic linear sweep of the Al/Mg/Sn alloy. ● Tip of the Luggin capillary 2 mm from the Al/Mg/Sn surface. ○ Reference electrode 5 cm away from the Al/Mg/Sn surface. Alloy was solution heat treated. Electrolyte of 4 mol dm^{-3} at 22 °C.

4.3.3 Variation of corrosion rate at open-circuit

The variation of the open-circuit potential of the homogenised Al/Mg/Sn alloy was mirrored by a simultaneous variation in the volume of evolved hydrogen, as illustrated in Figure 4.16 [49]. The figure indicates that the corrosion rate of the alloy varied with time, validating the efficacy of the corrosion measurement technique used [63]. Computing corrosion rate from mass loss between the start and end of the experiment would have given an over estimate of the steady-state corrosion rate because of the transient high corrosion rate upon initial immersion in the electrolyte.

Initially the open-circuit potential of the Al/Mg/Sn alloy was −1.75 V *vs.* Hg/HgO. To examine the effect of the tin alloying element, the open-circuit potential of a 99.99 %wt tin

sample was found to be −1.1 V *vs.* Hg/HgO indicating it was passivated in 4 mol dm^{-3} NaOH. Since the potential for tin was more positive than that of pure aluminium, −1.66 V *vs.* Hg/HgO, during the oxidation of the Al/Mg/Sn alloy tin ions from the electrolyte back-plated onto the alloy surface. The presence of metallic tin on the surface of the alloy shifted its potential to the negative end of the region of stability of tin. In the case of the magnesium alloying element, as it is more anodic than aluminium it would facilitate breakdown of the aluminium passive layer but it would not plate back from the electrolyte onto the alloy surface.

The open-circuit potential of the Al/Mg/Sn alloy initially increased abruptly from −1.81 to −2.08 V *vs.* Hg/HgO. The high negative potential of −2.08 V *vs.* Hg/HgO may be due to the presence of tin hydrides, which have been detected experimentally [64, 65], creating an almost film-free aluminium surface [49]. A very low polarisation resistance of 0.35 Ω, indicated in Figure 4.17, supported the theory of a film-free surface. The bare surface of the alloy was then exposed to the electrolyte, resulting in a high hydrogen evolution rate of 1.75 cm^3 min^{-1}, as indicated by the steep slope over the initial 400 s in Figure 4.16 [49], which equated to a corrosion current density as high as 146 mA cm^{-2}, see Figure 4.18. This hydrogen evolution rate far surpassed that of 99.999 % aluminium at 0.5 cm^3 min^{-1}.

After 400 s, the potential of Al/Mg/Sn dropped from −2.1 to −1.75 V *vs.* Hg/HgO and stabilised at −1.7 V *vs.* Hg/HgO. A dramatic reduction in the rate of hydrogen evolution to 0.17 cm^3 min^{-1} in Figure 4.16 and lower corrosion currents, shown in Figure 4.18, accompanied this positive shift in potential. Passivation of the surface with a hydroxide layer increased the polarisation resistance to a peak of 3 Ω before stabilising at approximately 2 Ω, higher than the 1.65 Ω for 99.999 % Al. The higher polarisation resistance of the passive layer on Al/Mg/Sn was reflected in the lower open-circuit corrosion current density of 6 mA cm^{-2}, compared to 20 mA cm^{-2} for 99.999 % Al, shown in Figure 4.18. The formation of tin deposits on the alloy surface and tin's higher hydrogen overpotential accounted for this lower corrosion current [97]. The rate of hydrogen evolution from pure aluminium was constant at a rate of 0.5 cm^3 min^{-1} for the duration of the period that it was held at open-circuit due to the absence of any large deviations in its potential.

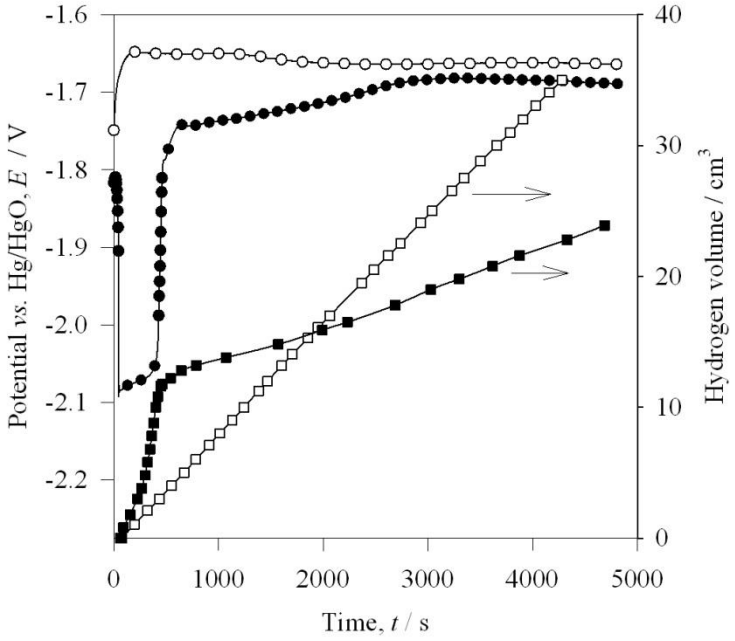

Figure 4.16: Variation of open-circuit potential and hydrogen volume for ●, ■ Al/Mg/Sn and ○, □ 99.999 %wt Al. Electrolyte: 4 mol dm^{-3} NaOH at 22 °C. Electrode area: 3.5 cm^2. Platinum mesh counter electrode.

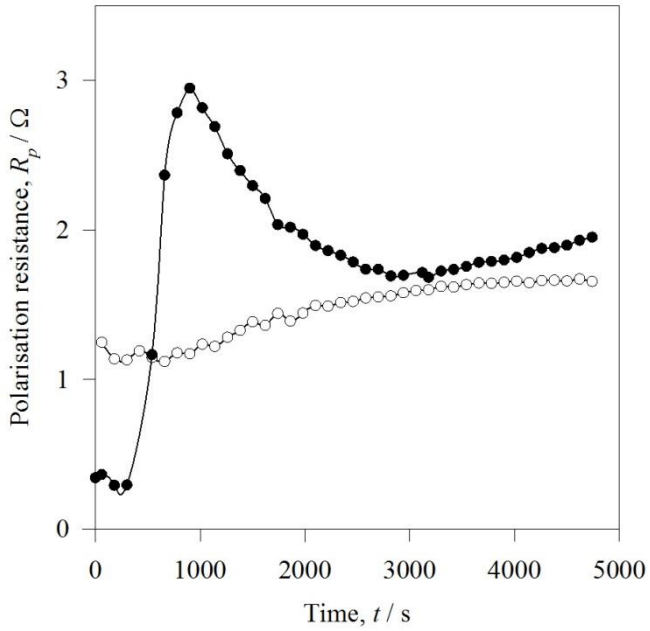

Figure 4.17: Polarisation resistance of the Al/Mg/Sn alloy compared to that of 99.999 %wt aluminium. Electrolyte: 4 mol dm^{-3} NaOH at 22 °C. Electrode area: 3.46 cm^2. ● Al/Mg/Sn ○ 99.999 %wt Al.

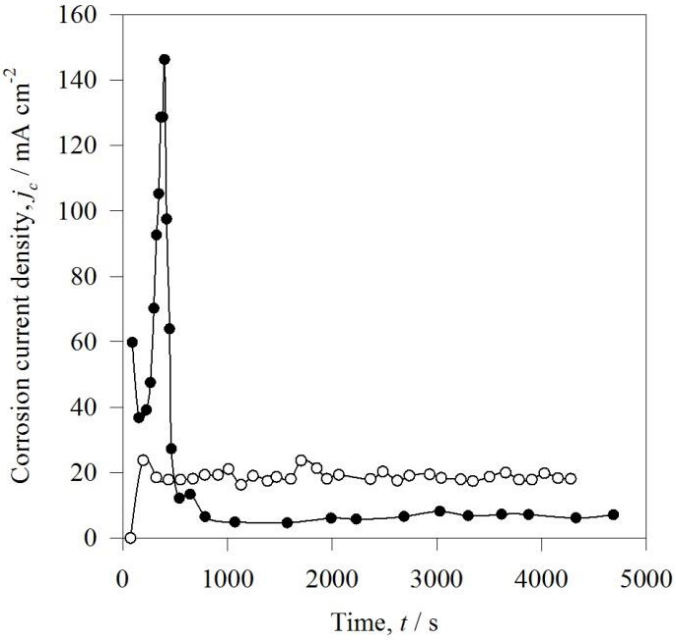

Figure 4.18: Variation with time of the open-circuit corrosion current density of Al/Mg/Sn compared to that of 99.999 %wt Al. Electrolyte: 4 mol dm^{-3} NaOH at 22 °C. ● Al/0.5 % Mg/0.07 % Sn, ○ 99.999 %wt Al. Electrode area: 3.5 cm^2. Platinum mesh counter electrode.

The stability of this passive layer with the tin deposits on the Al/Mg/Sn alloy at open-circuit was examined by investigating the effect of refreshing the electrolyte in the three-electrode cell once the open-circuit potential of the alloy had initially stabilised. Figure 4.19 shows the characteristic transient open-circuit potential of the alloy observed over the initial 4800 s, at which point the 4 mol dm^{-3} NaOH electrolyte was emptied out and filled afresh, while leaving the sample configuration the same. Upon doing so, the transient behaviour associated with the open-circuit potential was not re-observed and neither were the high corrosion currents as indicated in Figure 4.19(b). The transient behaviour was then dependent on the surface condition of the aluminium. Upon initial immersion into the electrolyte the surface of the aluminium alloy was covered by an oxide layer and all the Mg and Sn alloying elements were in the solid solution microstructure of the alloy. When the potential of the alloy stabilised, its surface was covered by a passive hydroxide layer and tin plated onto cathodic sites [106], a surface which remained stable even after emptying and refilling the electrolyte. In order to avoid the transient behaviour from occurring upon initial immersion within the prototype Al-air cell the Al/Mg/Sn alloy could be preconditioned by holding at open-circuit for at least 600 s in a NaOH solution external to the cell, until the stable open-circuit potential of −1.7 V *vs.* Hg/HgO is reached. Otherwise encountering the rapid hydrogen evolution

transient phase within the prototype cell, which has a small electrolyte volume, would consume water needed for the reduction of oxygen at the air-cathode, could cause electrolyte leakage by aggressive bubbling and increase the electrolyte pH through generation of OH^- ions. Alternatively allowing the alloy to experience the transient phase within the prototype Al-air cell may be beneficial for heating the cell's electrolyte which would in turn enhance the anodic behaviour of the alloy. The effect of temperature on the alloy behaviour is subsequently discussed.

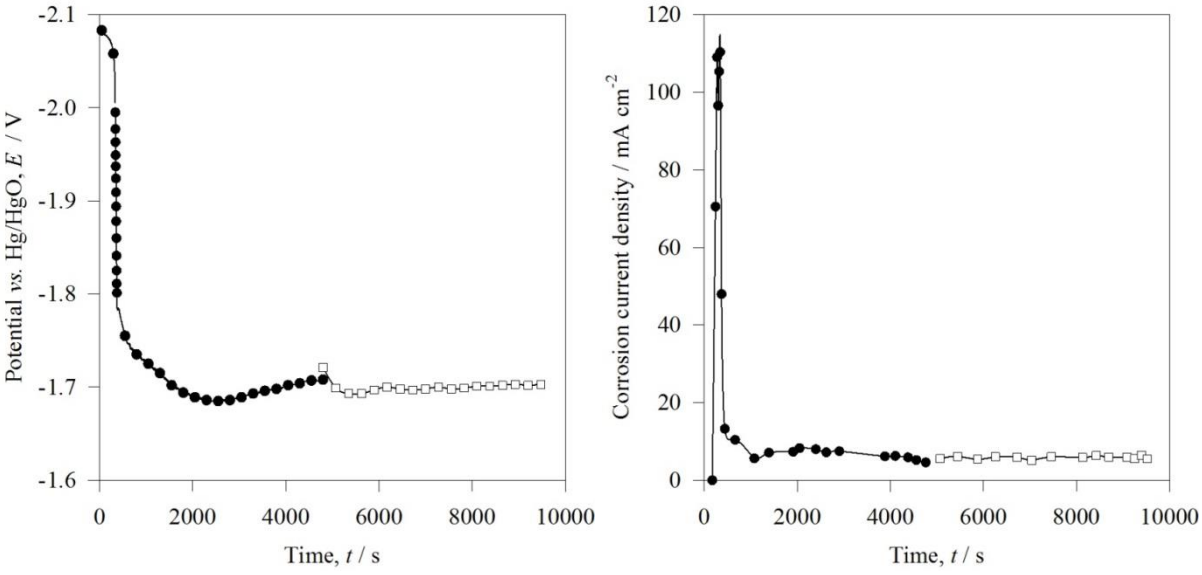

(a) (b)

Figure 4.19: Dependence of the transient, extremely negative open-circuit potential of Al/Mg/Sn on the surface condition of the alloy. (a) Open-circuit potential with time. (b) Corrosion current density at open-circuit. ● Sample held at open-circuit for 4800 s, □ Electrolyte refreshed and sample held at open-circuit for a further 4800 s. Electrolyte: 4 mol dm^{-3} NaOH at 22 °C. Electrode area: 3.5 cm^2.

The surface of the Al/Mg/Sn alloy, after holding at open-circuit for 4800 s, was characterised by corrosion along grain boundaries as well as corrosion of the grain surface, see Figure 4.20. The grains, visible to the naked eye, are extremely large, with some as wide as 1.2 mm. It may be worth investigating if the electrochemistry of the alloy and its corrosion rate would change with a finer grain size [130]. A benefit of a finer grain size would be that if a grain were to become detached from the surface due to corrosion the mass of aluminium lost would be less than if it were a larger grain. There are pits present, both within the grains and at the grain boundaries. The surface morphology of the grains is not uniform, with some areas showing a coarser surface as in Figure 4.21(a), than others as in Figure 4.21(b). The coarse

structured regions showed up as bright areas under the back-scatter detector, see Figure 4.20. They were characterised by ridges and cracks, see Figure 4.21(a). If a sample was analysed after a shorter time than 4800 s at open-circuit, it is predicted that there would be a greater abundance of the coarse structured regions. It is also recognised the cracks may have formed during analysis of the sample under the SEM where the vacuum in the SEM chamber drew water out from the surface, creating the cracks. The fine structured regions in Figure 4.21(b) were characterised by a patchy passive film consisting of a mesh of interconnected black regions and isolated white regions.

The EDX profile for the white regions, Figure 4.21(e), showed a higher ratio of oxygen to aluminium peak intensity, compared to the EDX profile of the black regions in Figure 4.21(f). This suggests that a non-uniform passive layer covered these fine structured regions, with the white regions having a thicker passive layer than the black regions. When the sample was withdrawn from the electrolyte its surface would have reacted with oxygen in the air. The uniqueness of the patchy passive film, however, relative to other areas on the surface suggests it formed while held at open-circuit in the 4 mol dm^{-3} NaOH.

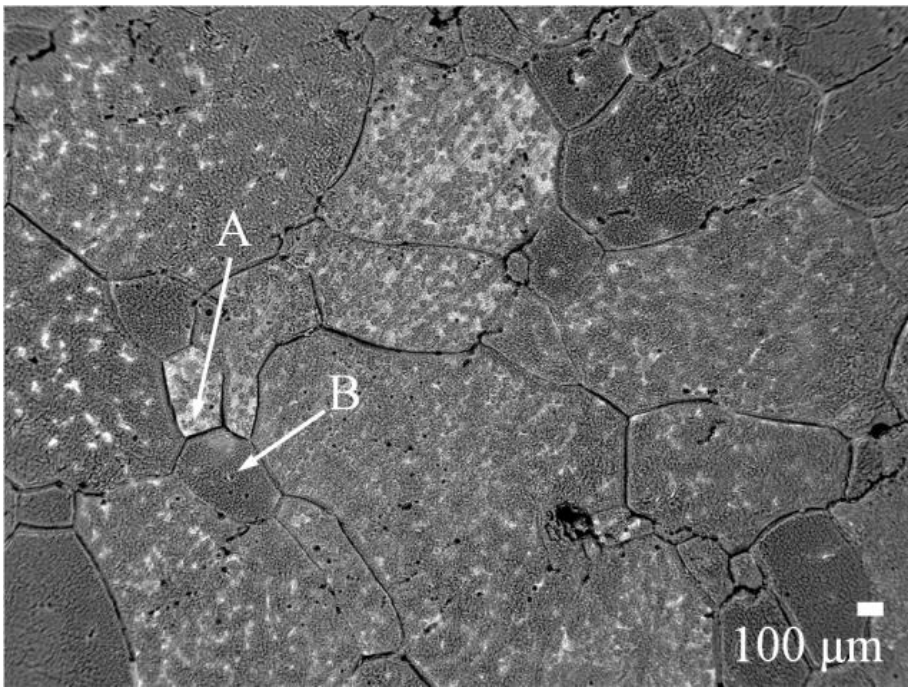

Figure 4.20: Back-scatter electron image showing surface microstructure of the Al/Mg/Sn alloy at open-circuit. Sample held at open-circuit for 4800 s in 4 mol dm^{-3} NaOH. Points A and B highlight two different surface morphologies, which are shown at higher magnification in Figure 4.21(a) and (b) respectively.

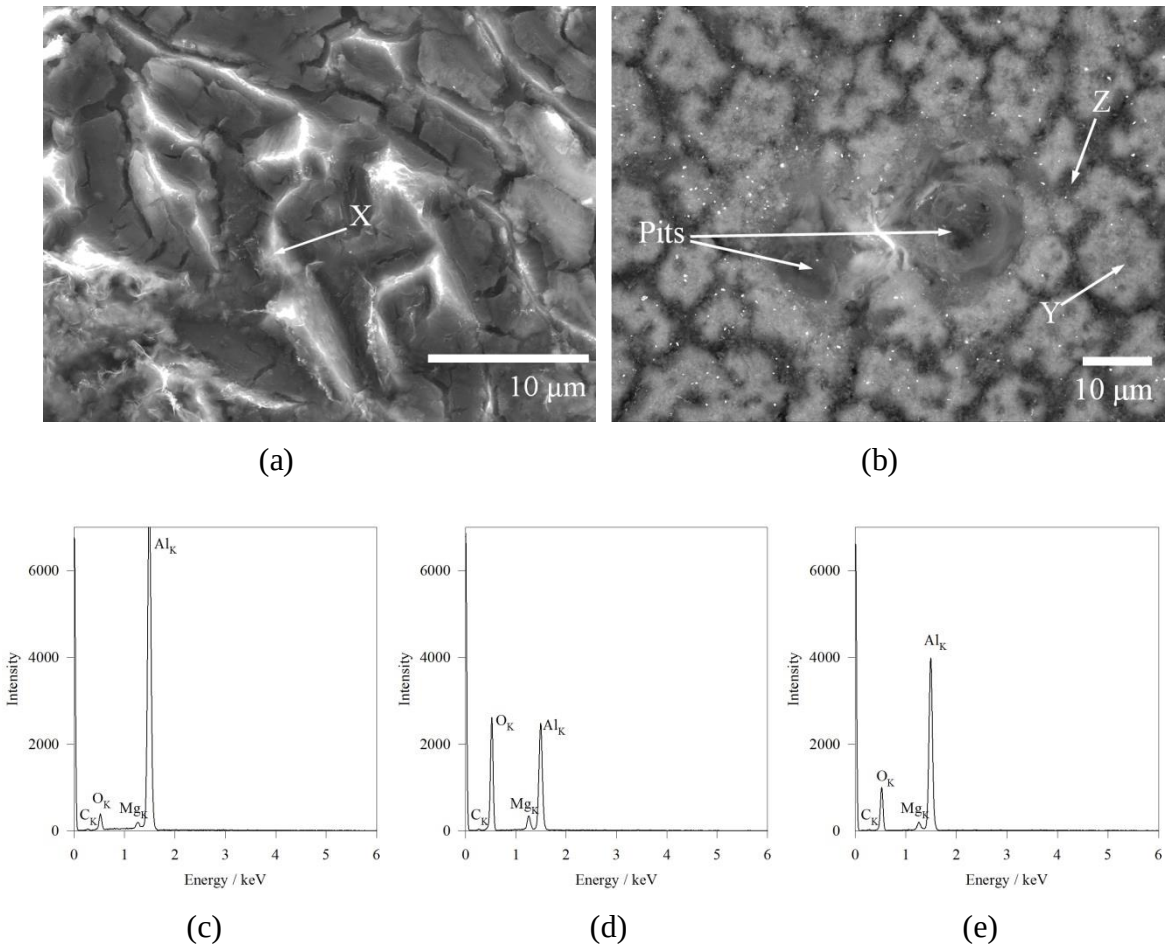

Figure 4.21: Non-uniform surface morphology and passive layer of the Al/Mg/Sn alloy after being held at open-circuit for 4800 s in 4 mol dm^{-3} NaOH. (a) Morphology 1; SEM image showing a coarse surface with ridges and cracks. (b) Morphology 2; BEM image showing a finer surface characterised by a mesh of interconnected black regions surrounding white areas. (c) EDX profile of point X. (d) EDX profile of point Y. (e) EDX profile of point Z.

Examining the cross-section of the corroded surface after open-circuit under SEM did not reveal much below the surface of the passive layer as shown in Figure 4.22. The resolution was insufficient to resolve the image a few nanometres below the surface. Figure 4.22 shows that the alloying elements remained in solid solution in the bulk regardless of corrosion reactions occurring at the surface. The Cu/S particle was perhaps a contaminant left over from the sectioning or grinding processes.

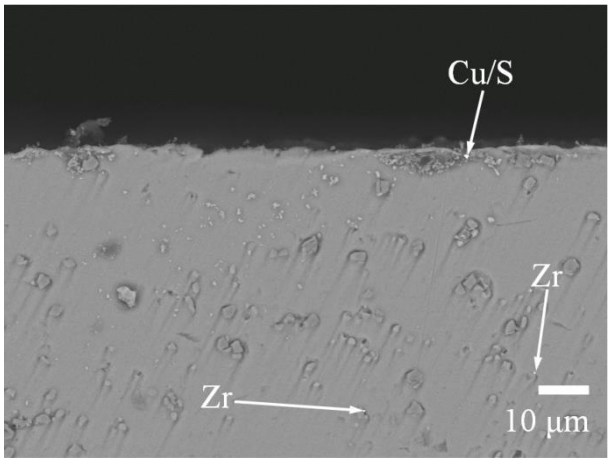

Figure 4.22: Back-scatter electron image showing the cross-section of the Al/Mg/Sn alloy. The face perpendicular to the top edge was immersed in 4 mol dm^{-3} NaOH at 22 °C at open-circuit for 4800 s.

4.3.4 Comparison of the alloys

An ideal alloy for an aluminium-air battery would have a high anodic discharge rate but a low corrosion rate. The anodic behaviour of the two alloys, Al/Mg/Sn/Ga and Al/Mg/Sn, were initially compared in 4 mol dm^{-3} NaOH at room temperature, 22 °C. The open-circuit potential for Al/Mg/Sn/Ga, −1.8 V *vs.* H/HgO, was more negative than that of Al/Mg/Sn, −1.7 V *vs.* Hg/HgO. Consequently the anodic linear sweep of Al/Mg/Sn/Ga commenced at a more negative potential than that for Al/Mg/Sn, as shown in Figure 4.23. This figure shows that Al/Mg/Sn/Ga exhibited potentials 40 – 90 mV more negative than those of Al/Mg/Sn over the current density range of 0 and 230 mA cm^{-2}. Beyond that the Al/Mg/Sn showed more favourable anodic currents at a given potential with a peak current density of 357 mA cm^{-2} at −1.1 V *vs.* Hg/HgO. The Al/Mg/Sn/Ga alloy exhibited a peak current density of 300 mA cm^{-2} at −1.07 V *vs.* Hg/HgO. The peak current density for both alloys occurred at the oxidation potential for tin in alkaline solution. At more positive potentials the alloys experienced passivation and their current density reduced to match that of 99.999 %wt aluminium at −0.8 V *vs.* Hg/HgO. In general both alloys observe a similar anodic linear sweep with a region of enhanced anodic currents compared to 99.999 %wt aluminium that fell over a potential range for the region of stability of tin in alkaline solution. The reason why tin dominated the behaviour of the Al/Mg/Sn/Ga alloy rather than the gallium alloying element was due to the lower melting temperature of gallium, 30 °C, compared to tin, 230 °C. The gallium was able to back diffuse more quickly than the tin from where it had plated onto the alloy surface back into the alloy bulk [49]. The diffusion coefficient for gallium in

aluminium is 9 × 10^{-4} cm^2 s^{-1} [100]. The slower back diffusion of the tin meant it was retained for longer on the alloy surface and so dominated the alloy's anodic behaviour. The fluctuations in the linear sweep were not observed at the point at which the alloys passivated as was the case in Figure 4.12, since in this case the linear sweeps were conducted at a fast rate of 20 mV s^{-1}.

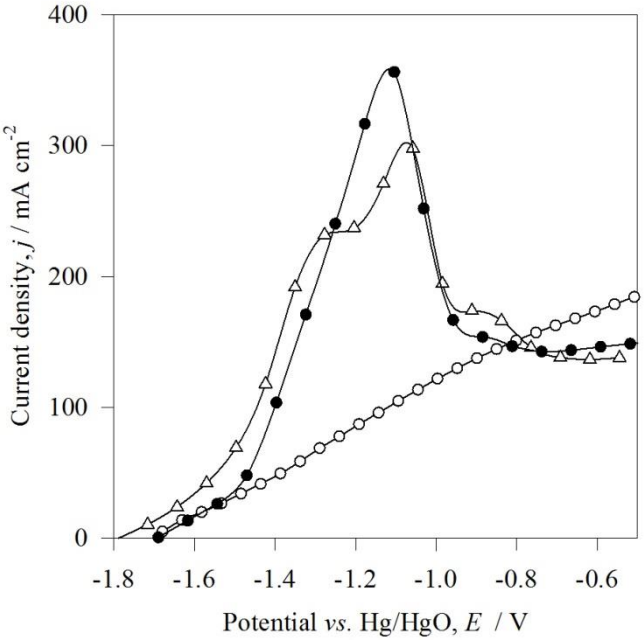

Figure 4.23: Comparison of the linear sweep behaviour of the two aluminium alloys in 4 mol dm^{-3} NaOH at 22 °C. Sweep rate: 20 mV s^{-1}. The electrodes were held at open-circuit for at least one hour prior to the potential sweep. ● Al/Mg/Sn, △ Al/Mg/Sn/Ga, ○ 99.999 %wt Al. The alloys were solution heat treated.

There was a 230 mV higher order of magnitude potential difference under galvanostatic discharge at 100 mA cm^{-2} in favour of the Al/Mg/Sn/Ga alloy indicated in Figure 4.24. This may be due to an apparent activation step where the potential of Al/Mg/Sn/Ga jumped from −1.47 V *vs.* Hg/HgO to −1.54 V *vs.* Hg/HgO within the first 20 s of discharge. This activation step may have locally heated the electrolyte owing to the large sample area (3.46 cm^2), which could explain the subsequent slow rise in potential from −1.54 V *vs.* Hg/HgO to −1.57 V *vs.* Hg/HgO over the one hour duration of the test.

The Al/Mg/Sn alloy also appeared to display this activation step, but it was extremely short-lived, as evidenced by the fluctuating potential when discharged at 100 mA cm^{-2}, see Figure 4.24. The fluctuations were characterised by the potential varying from −1.28 V to −1.30 V *vs.* Hg/HgO and back again to −1.28 V *vs.* Hg/HgO over duration of 330 s followed by a

large single or double negative spike in potential to a value of at least −1.45 V *vs.* Hg/HgO. This negative spike in potential was extremely short-lived over a one second time-frame before returning to a potential of −1.28 V *vs.* Hg/HgO and the trend repeated itself.

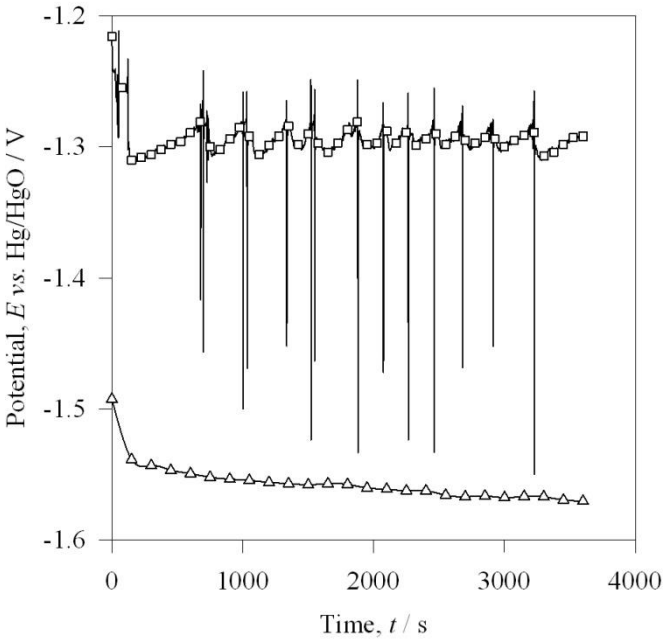

Figure 4.24: Comparison of the galvanostatic discharge for the two alloys at 100 mA cm^{-2}. Electrode area: 3.46 cm^2. Electrolyte: 4 mol dm^{-3} NaOH at 22 °C. Static electrolyte. □ Al/Mg/Sn, △ Al/Mg/Sn/Ga. Alloys were solution heat treated.

The fluctuations in discharge potential of Al/Mg/Sn in Figure 4.24 could have been due to periodic build-up and subsequent destruction of a passive hydroxide layer or due to a tin deposit on the alloy surface [5, 63]. Rapid oxidation of Al at active sites lowered the local OH^- concentration and the sites became passivated by aluminium oxide or hydroxide [63]. The subsequent low rate of discharge at the passivated sites allowed the OH^- ion concentration to increase again, dissolving the passive layer, resulting in the large negative spike in potential. However since these fluctuations in potential did not occur for 99.999 % Al at 22 °C in Figure 4.25(a), there must be another reason. Variations in the local concentration of SnO_3^{2-} ion in the electrolyte could have caused the potential fluctuations for the Al/Mg/Sn alloy [49]. When the local saturation level for the SnO_3^{2-} ion in the electrolyte was reached, additional tin exposed during alloy oxidation could not dissolve into the electrolyte and instead formed SnO_2 on the surface, passivating it. Auger depth profiles found the presence of tin oxides on the outer few layers of the hydroxide layer on a Al/0.1 Sn alloy after discharge in 1 mol dm^{-3} NaOH [106]. As the local stannate concentration fell below the

saturation level via dispersion in the electrolyte or back plating onto the aluminium surface, the SnO_2 dissolved into the electrolyte causing a negative jump in potential.

The fluctuations in the potential of Al/Mg/Sn under galvanostatic discharge at 22 °C occurred at 50 mA cm^{-2} and at 100 mA cm^{-2}, see Figure 4.25. The frequency of the fluctuations was higher and their amplitude smaller at the higher current density. At 60 °C these periodic fluctuations were not observed because of higher solubility of aluminium hydroxide and stannate in the electrolyte at elevated temperature, see Figure 4.25. At both 50 and 100 mA cm^{-2}, the electrode potential for the Al/Mg/Sn alloy was more negative when discharged at the higher temperature of 60 °C. This was because of a thinner passive film. Also if the anodic currents were concentrated at surface pits with tin at their centre, then the diffusion of the bulk aluminium through the surface tin to be oxidised in the electrolyte would have been accelerated at the higher temperature. There is a theory that if the anodic currents were concentrated at surface pits then the local temperature at these pits could be raised high enough to melt the tin surface deposit to allow quick diffusion of aluminium through the tin.

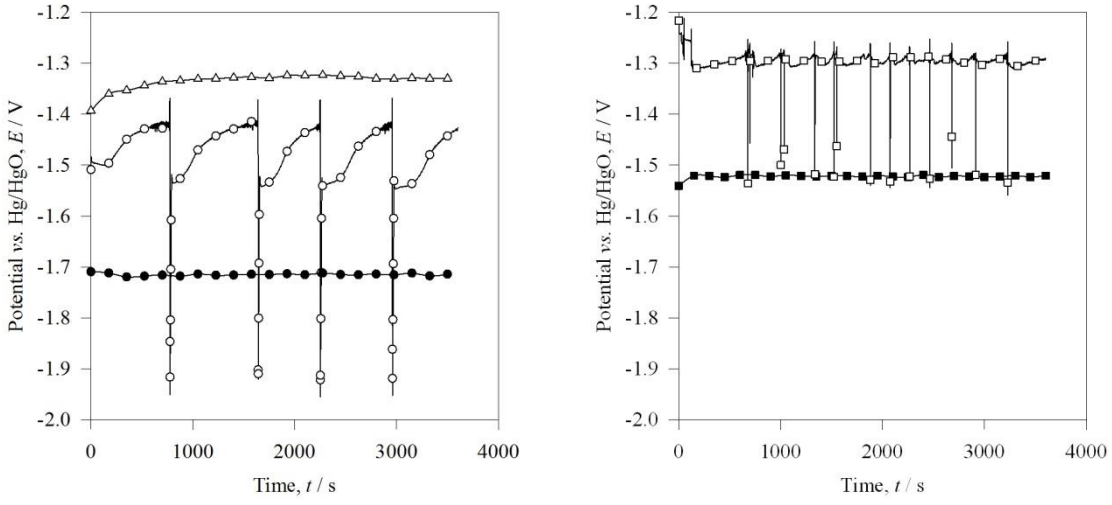

Figure 4.25: Effect of temperature on the galvanostatic discharge. (a) 50 mA cm^{-2} discharge of Al/Mg/Sn at two different temperatures and compared against pure aluminium and (b) 100 mA cm^{-2} discharge of Al/Mg/Sn. Electrode area: 3.46 cm^2. Electrolyte: 4 mol dm^{-3} NaOH. Static electrolyte. △ 99.999 % Al at 22 °C; ○, □ Al/Mg/Sn at 22 °C; ●, ■ Al/Mg/Sn at 60 °C.

In terms of corrosion currents, both alloys observed lower steady-state values at open-circuit compared to pure aluminium at 22 °C, with Al/Mg/Sn yielding a higher inhibition efficiency of 63 % compared to 54 % for Al/Mg/Sn/Ga, as detailed in Table 4.4. The rates of parasitic

hydrogen evolution were highest at open-circuit and reduced proportionally with the rate of discharge [23]. The discharge efficiencies for both alloys at 22 °C were above 94 % at current densities higher than 50 mA cm^{-2}.

At higher temperature of 60 °C, the separating factor between the two alloys was the higher corrosion rate of Al/Mg/Sn/Ga with an open-circuit corrosion current of 56 mA cm^{-2}, almost twice that of Al/Mg/Sn, see Table 4.4. During an attempted linear sweep voltammetry test on a 2 mm thick sample of Al/Mg/Sn/Ga, the electrolyte penetrated right through the material along the grain boundaries leaking through to the other side. This occurred at some point over the course of the 1 hour experiment indicating the speed of the corrosion. For this reason galvanostatic discharge tests at 60 °C were not carried out on the alloy. The higher corrosion rates were due to the liquefying of the gallium portion of the Al/Mg/Sn/Ga alloy [100]. In agreement, other research showed that the self-corrosion of binary Al/Ga alloys at 60 °C was very aggressive [19, 24, 99].

The loss of structural integrity of Al/Mg/Sn/Ga at 60 °C excludes its use as an anode in the alkaline prototype aluminium-air cell. Although its corrosion rate was 54 % less than that of pure aluminium at 22 °C, once the Al/Mg/Sn/Ga anode is immersed in the cell's electrolyte the exothermic oxidation of aluminium and reduction of water on its surface would raise the electrolyte temperature to values of 60 °C in the prototype aluminium-air cell [23]. Since the electrolyte temperature in the lightweight aluminium-air cell will be unregulated, once it surpasses the melting point of the gallium alloying element the self-corrosion of the Al/Mg/Sn/Ga alloy will accelerate, invalidating its use.

Examination of the surface morphology of the Al/Mg/Sn alloy in Figure 4.26 after discharge at 100 mA cm^{-2} shows a non-uniform surface. After the discharge, the grains were visible to the naked eye with widths of upwards of 1.2 mm as previously indicated in Figure 4.20. The SEM image in Figure 4.26 shows an uneven surface with some areas corroded to a greater depth than others. Perhaps this indicates variable corrosion of different grains and the boundaries between the areas of the surface of differing depth are the grain boundaries. Note that at the end of the galvanostatic discharge, the sample was briefly held at open-circuit while removing the sample from the experimental cell.

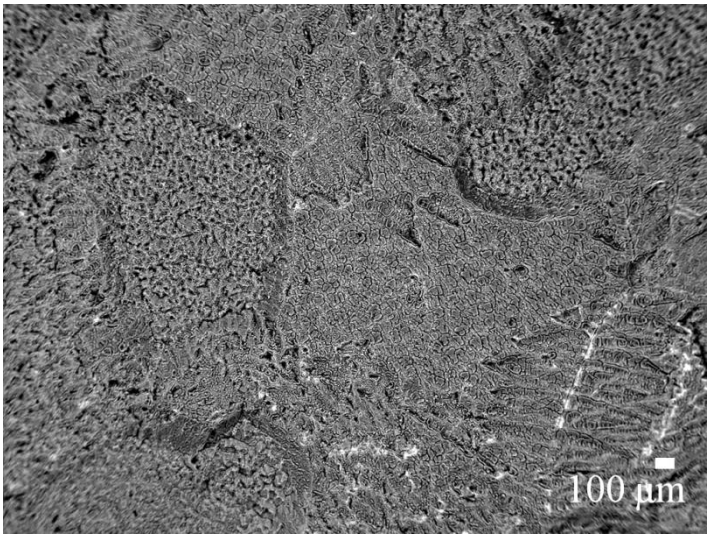

Figure 4.26: Surface morphology of the Al/Mg/Sn alloy under discharge at 22 °C. Back-scatter electron image. The alloy was discharged at 100 mA cm^{-2} for 3600 s in 4 mol dm^{-3} NaOH.

4.3.5 Effect of electrolyte temperature

The anodic discharge rates of pure aluminium and aluminium alloys can be enhanced by elevating the temperature [23, 103]. Figure 4.27(a) illustrates the effect of repetitive sweeps for Al/Mg/Sn undertaken at different temperatures from 22 to 70 °C. The maximum anodic behaviour for the alloy was observed at 70 °C which corresponds to the optimum temperature found in the literature for the Al/Mg/Sn alloy [21]. The enhanced anodic behaviour at elevated temperature was partly due to an increased solubility for aluminate reaction product, $Al(OH)_4^-$ allowing more of the $Al(OH)_3$ passive film to dissolve into the electrolyte. The thinner passive film had less resistance to the transfer of OH^- ions through it, increasing the rate of aluminium dissolution [23]. In the literature, an Al/0.089 Sn alloy had a more active behaviour than pure aluminium at a temperature of 60 °C, highlighting the role of tin in enhancing the alloy's oxidation at the higher temperature [49]. A higher temperature would enhance the rate of stannate ion reduction from the electrolyte onto the alloy surface forming tin deposits and it would also promote the diffusion of aluminium through these tin deposits.

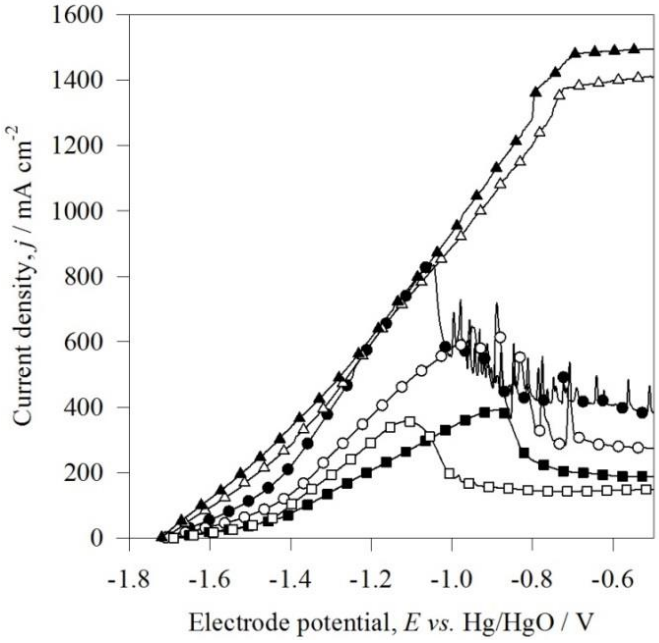

(a)

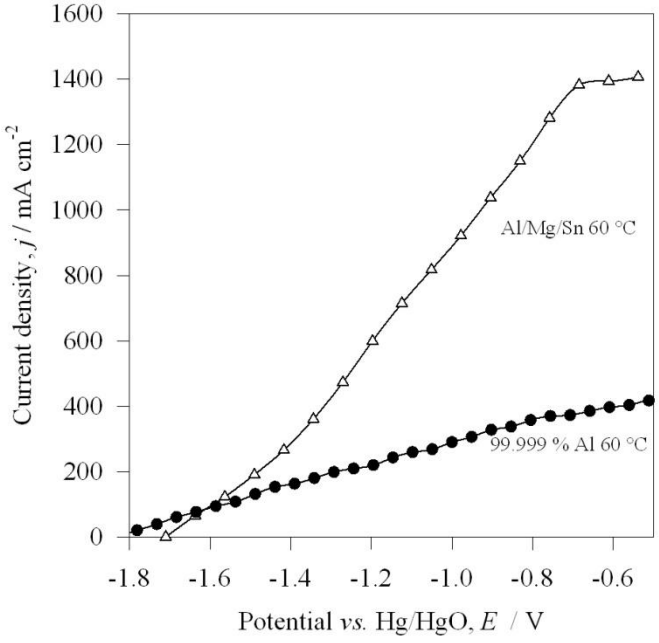

(b)

Figure 4.27: Effect of temperature on the anodic behaviour of Al/Mg/Sn alloy. Electrode area: 3.46 cm^2. Electrolyte: 4 mol dm^{-3} NaOH. Sweep rate 20 mV s^{-1}. (a) Linear sweep of Al/Mg/Sn alloy at different temperatures □ 22 °C, ■ 30 °C, ○ 40 °C, ● 50 °C, △ 60 °C, ▲ 70 °C. (b) Anodic linear sweep of Al/Mg/Sn and pure aluminium at 60 °C. Alloy was solution heat treated.

Another change in behaviour at 60 °C for the Al/Mg/Sn alloy was that its voltammogram was approximately linear over the potential range examined. The enhanced anodic currents of the alloy compared to 99.999 % aluminium at 60 °C, illustrated in Figure 4.27(b), were not confined to a defined potential window of −1.7 to −1.1 V *vs.* Hg/HgO as was the case at intermediate temperatures, 22 to 50 °C. The potential under galvanostatic discharge at 60 °C was also steadier than the 'saw-tooth' fluctuations observed at 22 °C in Figure 4.12. An increased solubility for tin in alkaline solution explains the absence of these periodic fluctuations at 60 °C. Rotating disc electrode studies support this mechanism. Figure 4.28(a) shows fluctuations in electrode potential were observed at a static disc. Under rotation, these fluctuations were no longer observed since the electrolyte motion enhanced the diffusion of $Al(OH)_4^-$ and SnO_3^{2-} ions away from the electrode surface. Enhanced diffusion of stannate away from the electrode surface would keep the local levels of stannate below their saturation level and in turn allow further tin to dissolve from the electrode surface into the electrolyte instead of passivating the surface. Similarly research in the literature showed that for a binary Al/0.074 In alloy, increasing the electrolyte flow from 100 to 300 cm^3 min^{-1} reduced the presence of potential oscillations when discharged at 467 mA cm^{-2} in 4 mol dm^{-3} NaOH solution at 60 °C [49]. In this study, increasing rotation smoothed the discharge potential of the Al/Mg/Sn alloy. Yet it did not reduce the overpotential during the discharge suggesting that charge transfer was the rate determining step. This is in agreement with rotating disc studies found in the literature which showed that in high concentration alkaline solutions of 4 mol dm^{-3} NaOH at 25 °C, the reaction of 99.999 % aluminium was not limited by the transport of OH^- and $Al(OH)_4^-$ ions through the solution [23, 36, 79]. Rather it was limited by the diffusion of OH^- ions through the hydroxide layer on the aluminium surface [23].

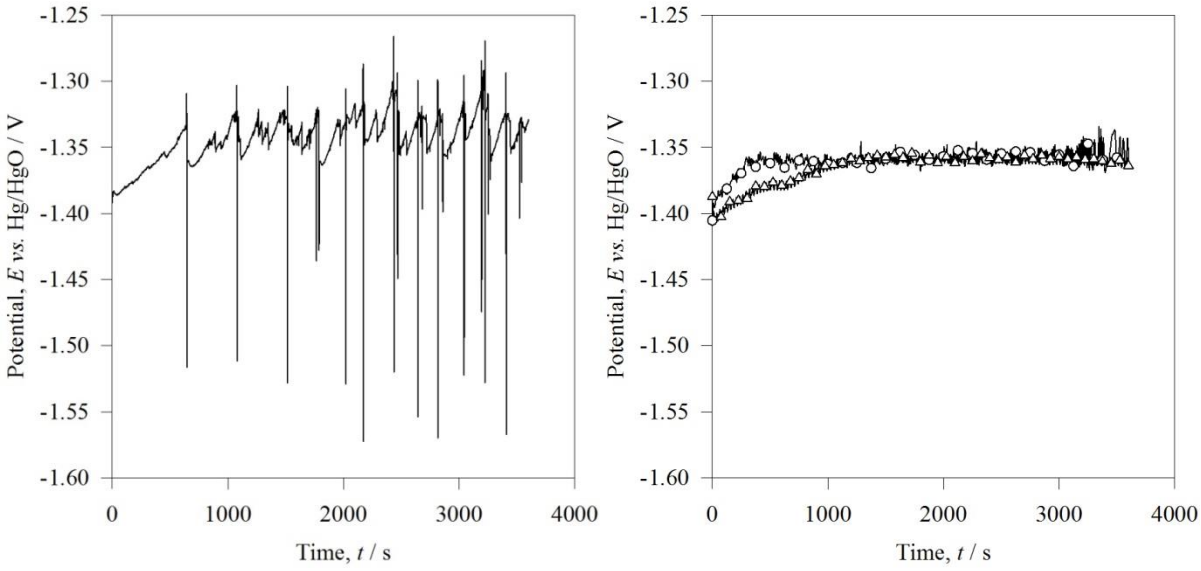

Figure 4.28: Effect of rotation rate on the galvanostatic discharge at 100 mA cm^{-2} of Al/Mg/Sn at 22 °C. Electrolyte: 4 mol dm^{-3} NaOH. Rotation rate: (a) 0 rpm, (b) ○ 200 rpm, △ 400 rpm. Alloy was solution heat treated.

Alloy	T / °C	j_{oc} / mA cm^{-2}	% φ_{inh}	% φ_{dis} at j in mA cm^{-2}				E *vs.* Hg/HgO / V			
				50	100	200	600	E_{oc}	E_{50}	E_{100}	E_{600}
99.999 % Al	20	19		99				-1.65	-1.33		
Al/Mg/Sn not SHT	20	718	-3631					-2.01			
Al/Mg/Sn	20	7	63	94	97	passive		-1.69	-1.43	-1.32	
Al/Mg/Sn/Ga	20	9	54	99	99			-1.77	-1.66	-1.57	
99.999 % Al	60										
Al/Mg/Sn	60	31		99	100			-1.79	-1.71	-1.52	
Al/Mg/Sn/Ga	60	56						-1.78			

Table 4.4: Comparison of the inhibition and discharge efficiencies of the aluminium alloys. Samples studied in a 4 mol dm^{-3} NaOH solution. Electrode area: 3.46 cm^2. Static electrolyte. Alloys were solution heat treated (SHT) unless otherwise stated.

4.4 Summary of aluminium alloy dissolution

1. The open-circuit potential of 99.999 %wt aluminium showed a transient behaviour upon immersion in sodium hydroxide.
2. The open-circuit potential was dependent on electrolyte purity.
3. A method of quantifying the corrosion of aluminium in alkaline solutions, at open-circuit and under discharge, was developed employing a hydrogen collection technique.
4. Two cast aluminium alloys, Al/0.5 Mg/0.07 Sn and Al/0.4 Mg/0.07 Sn/0.05 Ga both heat treated at 600 °C for 8 hours followed by a water quench, were studied as candidate anodes for a lightweight, aluminium-air cell. Experiments were conducted in a static 4 mol dm^{-3} NaOH solution at 22 °C and 60 °C.
5. Solution heat treatment of the Al/Mg/Sn alloy following casting was vital for discharging at high anodic rates compared to 99.999 % aluminium. The alloying elements needed to be in solid solution with the aluminium. The presence of Mg and Sn precipitates detrimentally increased the rate of hydrogen evolution from the surface of the Al/Mg/Sn alloy.
6. The open-circuit corrosion rate of the Al/Mg/Sn alloy varied with time, being highest upon initial immersion in the electrolyte.
7. The tin alloying element strongly influenced the anodic behaviour of Al/Mg/Sn at 22 °C. The potential range over which the alloy showed enhanced anodic behaviour compared to 99.999 % aluminium was defined by tin's potential range of stability in pH 14 electrolyte.
8. The anodic behaviour of both Al/Mg/Sn and Al/Mg/Sn/Ga was enhanced at 60 °C, which was the optimal operational temperature for Al/Mg/Sn.
9. At 22 °C the discharge efficiency for both alloys was above 94 %.
10. At 60 °C, self-corrosion of the Al/Mg/Sn/Ga alloy significantly increased leading to electrode disintegration.
11. The behaviour of the Al/Mg/Sn alloy was limited by charge transfer although enhancing mass transfer steadied the electrode potential under galvanostatic discharge at 100 mA cm^{-2} at 22 °C.

Chapter 5. Evaluation of the gas diffusion electrode

5.1 Introduction

A major advantage of aluminium-air batteries for energy storage is that one of the reactants, oxygen, is readily available from the air, giving them a high energy to weight ratio or high specific energy ratio. Oxygen normally reacts at a gas diffusion electrode where it is reduced to hydroxyl ions [19]:

$$O_2 + 2H_2O + 4e^- \rightarrow 4OH^- \qquad E_c = 0.30 \text{ V } \textit{vs.} \text{ Hg/HgO} \qquad (5.1)$$

A three-phase, i.e. gas, liquid electrolyte, solid electrocatalyst, oxygen-diffusion electrode has a layered structure [141, 229], consisting of (i) a hydrophobic air permeable membrane such as polytetrafluoroethylene, PTFE, (ii) an electrically conductive framework such as nickel mesh and (iii) a catalytic layer, e.g. platinised carbon. The catalytic layer is made of a catalyst, a hydrophilic catalyst support such as carbon black and is bound together with a hydrophobic binder such as PTFE. A single layer air-electrode, as illustrated in Figure 5.1(a), has an active layer whose function is to maximise the diffusion of electrolyte and oxygen to the catalyst. In a double layer air-electrode the diffusion of oxygen is facilitated by a separate gas diffusion layer between the PTFE membrane and active layer. This additional gas diffusion layer would not have any catalyst present in it and would have a high percentage of PTFE binder of 70 % so as to maximise the number of hydrophobic air-channels.

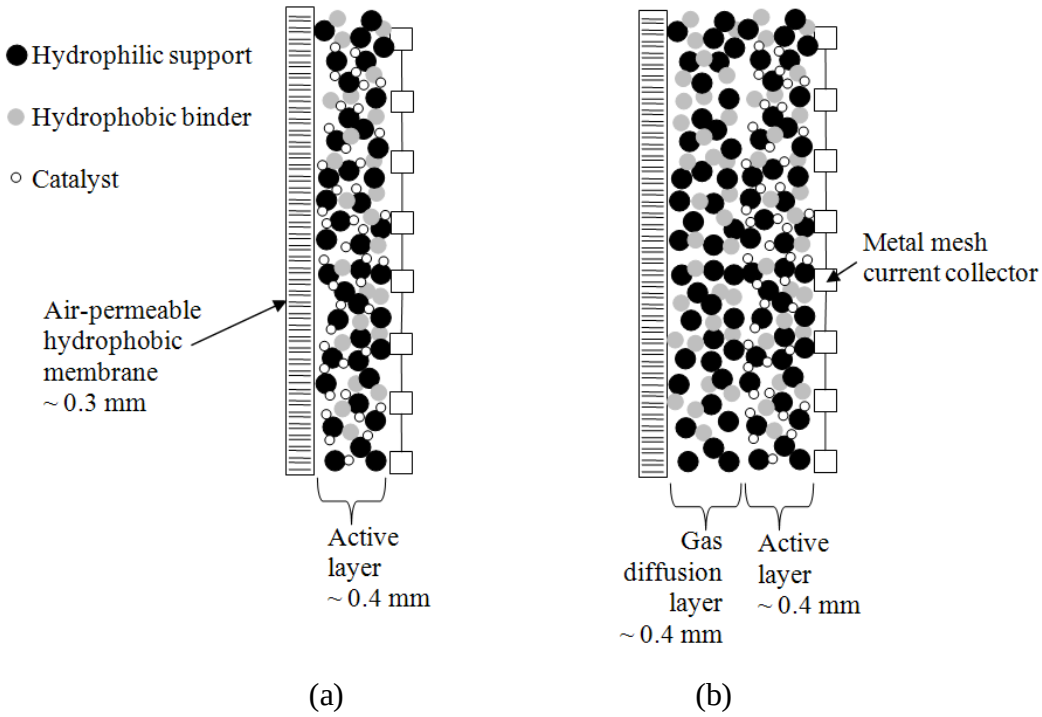

Figure 5.1: Illustration of the structure of two types of gas diffusion electrodes (a) Single layer electrode (b) Double layer electrode.

The aim of these experiments was to compare the electrochemical behaviour of commercial gas diffusion electrodes with an air electrode fabricated by a project collaborator: comparison was made based on structural and electrochemical properties. The air electrode supplied by a project collaborator was fabricated at KTH University in Sweden. Conveniently it has been labelled as KTH for discussion in the results. All the other seven commercial air-electrodes are labelled according to their name given by their respective manufacturer and are detailed in Table 5.1. Included in this table are structural and physical properties of the air electrodes which are discussed in the next section.

Electrode name, supplier	Catalyst	Catalyst size / μm	Thickness / mm	Mesh spacing / mm	Total specific pore area / $m^2\ g^{-1}$	Mean pore diameter / nm	Pycnometric % porosity
KTH	$LaCaCoO_3$ / $LaCaMnO_3$	3	0.67	0.24			
E5, Electric Fuel Ltd.	Cobalt based	1	0.5	1.4	17	87	60
OxAg, Gaskatel	AgO_x	3	0.85	0.58			
W18365 ELE0072 Graphite paper	4 mg cm^{-2} Platinum	-	0.23	no mesh	4.4	1166	67
MOC, Gaskatel	Manganese oxide	6 – 40	0.7	0.55	39	32.3	61
E4A, Electric Fuel Ltd.	Manganese oxide based	32	0.5	1.1	27	46.4	61
E4, Electric Fuel Ltd.	Manganese oxide based	38 – 80	0.5	1.1	36	36.9	66
W11529-346 Graphite paper	0.5 mg cm^{-2} Platinum	-	0.35	no mesh	3.9	1320	63

Table 5.1: Comparison of the structural and physical properties of the air-electrodes examined.

5.2 Structure of the air-electrodes

The E5 commercial gas diffusion electrode acquired from Electric Fuel Ltd. had a three-layer structure: an active layer of cobalt catalyst in porous carbon and silicon, which was pressed into a nickel mesh and backed with a PTFE layer. A magnified view of the front face of this air electrode is shown in Figure 5.2 highlighting a part of the nickel mesh pressed into the active layer of sintered carbon/PTFE. Energy dispersive x-ray analysis of the catalyst micro-particle indicated that it is a cobalt and iron compound with fluorine also present. This suggests that the catalysts could be a porphyrin or a phthalocyanine based catalyst [156], such as cobalt tetramethoxyphenylporphyrin [88, 144, 157]. The manufacturer did not provide a detailed description of the air electrode, so deductions needed to be made from the microscopic investigation.

In the case of the KTH electrode, back-scatter electron imaging revealed a surface covered with bright particles with two of these particles pointed out in Figure 5.4(a). EDX analysis of these particles in Figure 5.4(a) and (b) showed the catalyst to contain several elements including Ca, Mg, Co, Ce and O. Literature from the manufacturer suggests the use of a catalyst mixture combined of perovskites such as $La_{0.6}Ca_{0.4}CoO_3$ or $La_{0.1}Ca_{0.9}MnO_3$ [170], although lanthanum was not identified in the EDX analysis at a k_α of 33 keV. Porphyrins, such cobalt-tetraphenyl-porphyrin (CoTPP) could be another possibility. A perovskite is a mixed metal oxide with an ABO_3-type crystal structure. The A site is typically occupied by a rare-earth metal ions such as lanthanum and the B site is occupied by transition metal ions [230]. The KTH electrode has a rough discontinuous surface as indicated in Figure 5.5(a). Higher magnification indicated that this surface is textured with spherical-like nanostructures as indicated in Figure 5.5(b), conferring a high surface area. These nanostructures are approximately 50 nm in size which is the typical order of magnitude for carbon black particles used in battery applications [142]. The high surface area was most likely achieved through the use of high surface area carbon in the active layer such as Ketjen Black EC and Vulcan XC-72 which have surface areas upwards of 1300 and 250 $m^2\ g^{-1}$ respectively [149]. A high-surface area carbon would have a higher number of internal micro-pores to facilitate greater diffusion of the water to and OH^- ions away from reaction sites, and shorter diffusion pathway for the peroxide ions, HO_2^- from the carbon support to the catalyst [149, 154]. The absence of agglomerates on the surface of the KTH electrode suggests that thermal treatments were followed by cooling in the oven, which avoided their formation [153].

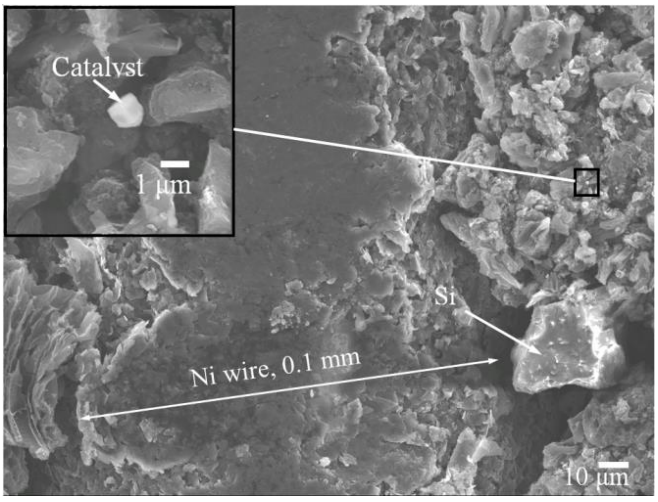

(a)

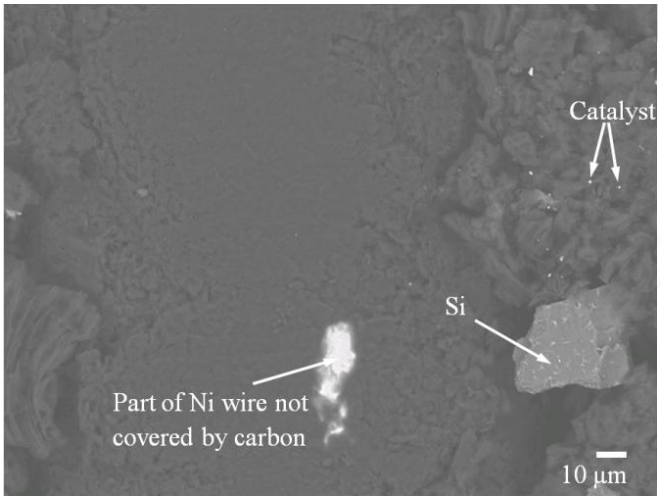

(b)

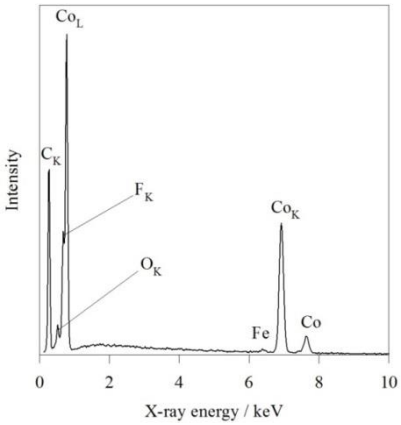

(c)

Figure 5.2: Surface images of the face of the commercial gas diffusion electrode, E5, looking at the catalysed carbon interspersed between the pores of the nickel mesh current collector (a) SEM image. (b) Back-scattered electron image of image 'a' where the bright particles are the catalyst microparticles, (c) EDX analysis of the catalyst.

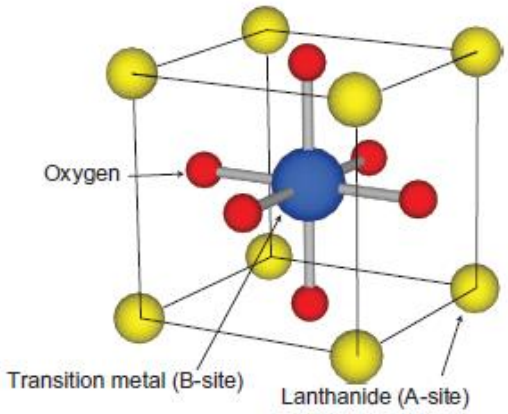

Figure 5.3: The ABO_3 crystal structure of perovskites [230].

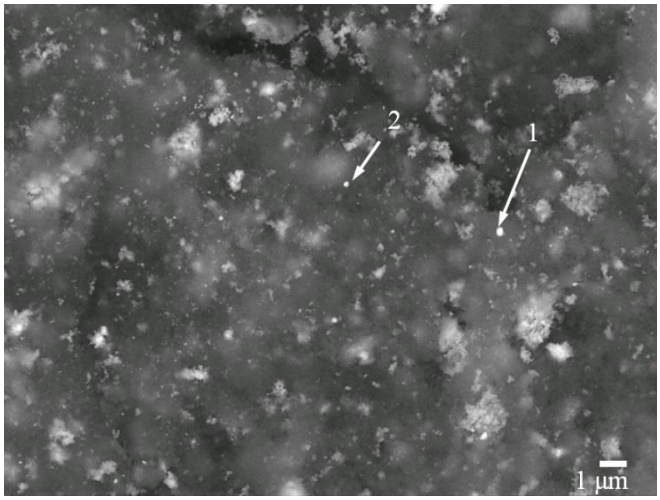

(a)

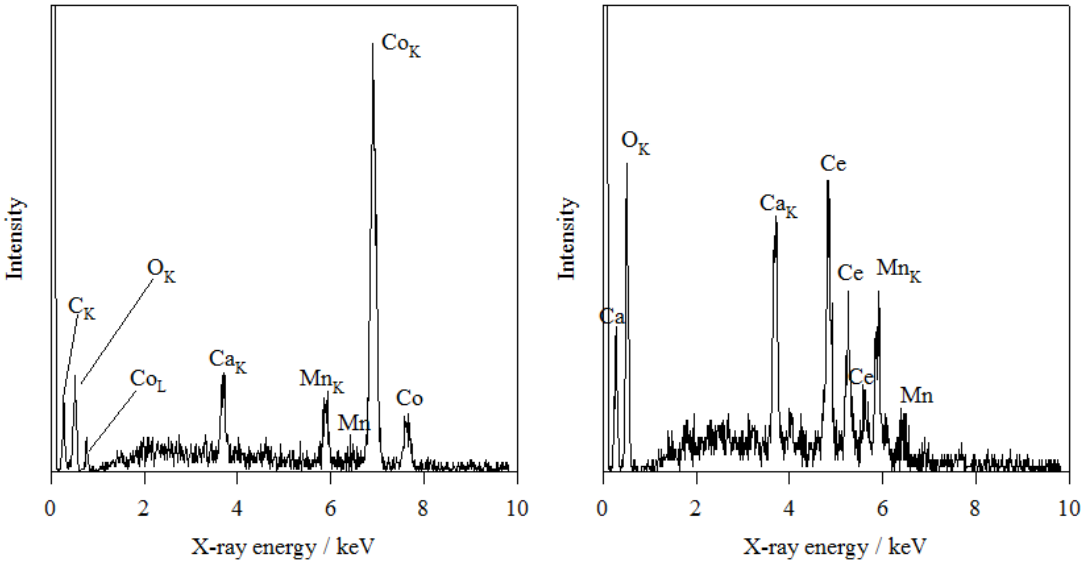

(b) (c)

Figure 5.4: (a) Back-scattered electron image of KTH electrode showing two particles of the catalyst identified as 1 and 2. (b) EDX of particle 1. (c) EDX of particle 2.

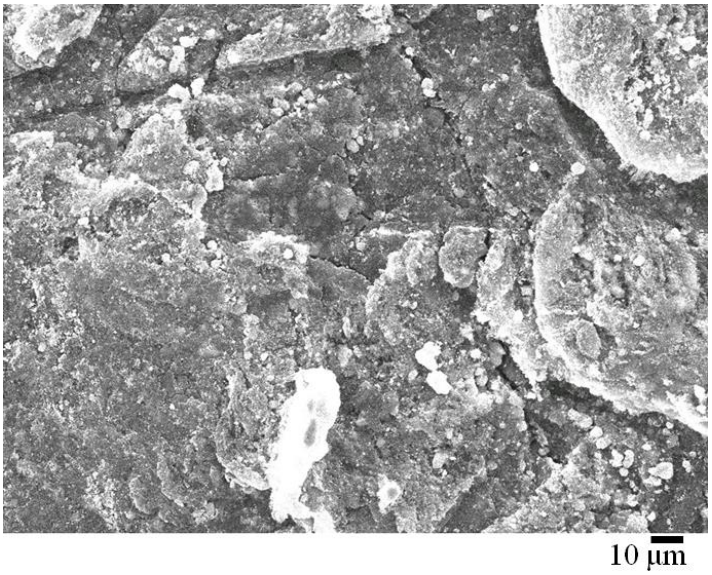

(a)

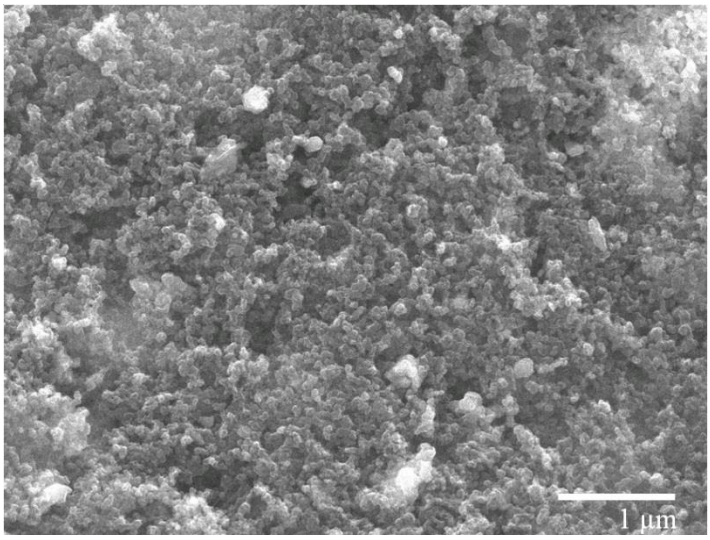

(b)

Figure 5.5: Scanning electron microscopy image of the KTH electrode surface at two magnifications.

Examination of the cross section of the KTH electrode under the scanning electrode microscope indicated that it was a double layer gas diffusion electrode i.e. there was a separate highly hydrophobic gas diffusion layer and a more hydrophilic active layer [153]. Both layers were the same thickness, 334 µm, as highlighted in Figure 5.6a. The active layer contains the catalyst mixed with carbon and PTFE, with the catalyst showing up brightly in the SEM images in Figure 5.6. The dark colour of the gas-diffusion layer indicates the lack of catalyst in that layer. The catalysts are of varying size with some larger than 1 µm as shown in the left inset in Figure 5.6(b). EDX analysis in Figure 5.6(c) of one of the catalyst particles

this time identified La along with Ca, Mg and O hinting at a $La_{0.1}Ca_{0.9}MnO_3$ catalyst. The active layer appears to have a much more porous structure than the compactness of carbon in the diffusion layer, as seen in the right hand inset in Figure 5.6(b). This would have been a design feature dependent on the type of carbon chosen for the respective layers. The more open pores in the active layer would facilitate greater wetting by the electrolyte, while the compactness of the diffusion layer would prevent its flooding, enabling diffusion of air into the electrode.

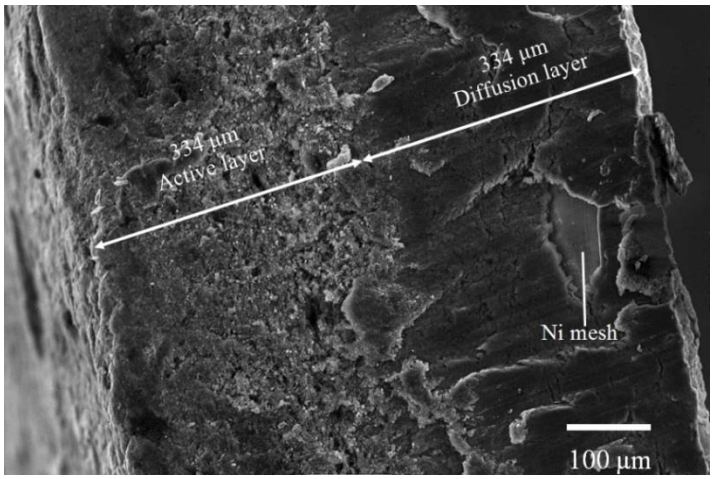

(a)

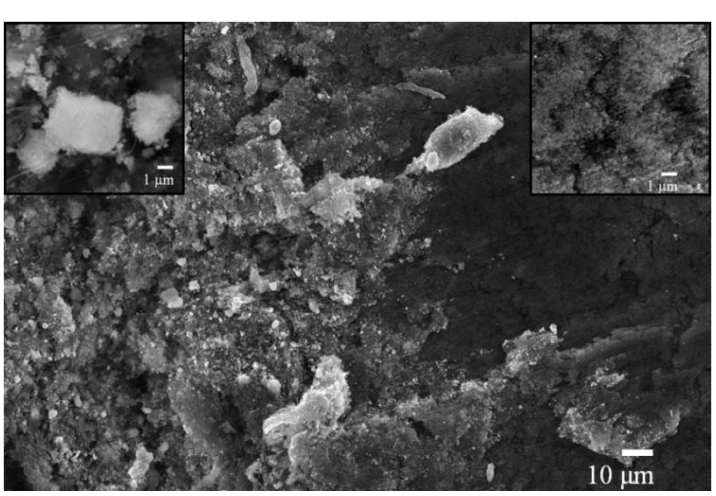

(b)

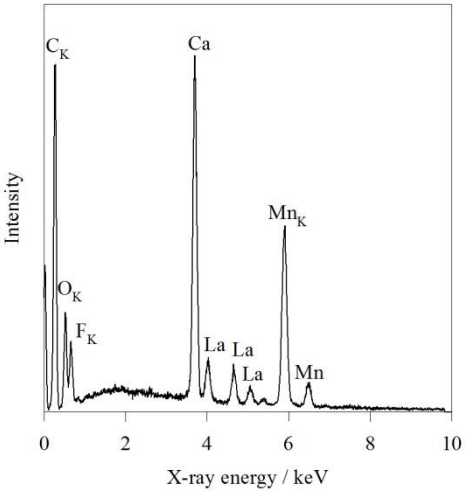

(c)

Figure 5.6: Cross-section of the KTH electrode examined under scanning electron microscopy. (a) Plan view showing electrode thickness, (b) interface between active and gas-diffusion layers, (c) EDX analysis of the catalyst.

In comparison to the KTH electrode, the surface of the OxAg electrode appears to consist of agglomerates of arbitrary shape with dimensions of the order of 3 μm as shown in Figure 5.7(a) and (b). As can be seen in Figure 5.7(b), the surface consists of a mixture of bright and dark particles. EDX analysis showed that the bright particles had higher composition of the Ag, Figure 5.7(c), while the darker particles had more carbon present, Figure 5.7(d).

The cross section of the OxAg electrode is shown in Figure 5.8. This electrode does not contain two distinct layers of sintered carbon as the KTH electrode did. Instead the active layer consisted of carbon/catalyst/PTFE mixture and the diffusion layer was a porous Teflon membrane laminated on the left face of the electrode (the PTFE membrane is not visible in the image because it had been removed). The magnified back-scatter electron image in Figure 5.8(b) indicates a high loading concentration of the catalyst, showing up as the bright particles and confirmed by EDX analysis, which is shown in the left inset. The AgO catalyst is inter-dispersed with carbon particles showing up as the darker regions as confirmed by EDX shown in the right inset of Figure 5.8(b). The thickness of the active layer is 388 μm, which is the same order of magnitude as thickness of the active layer in the KTH electrode.

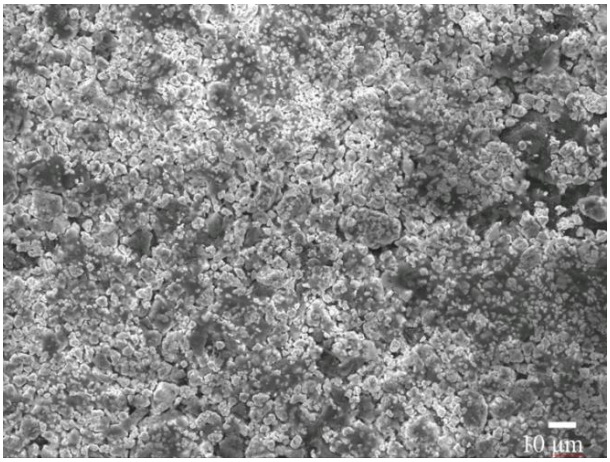

(a)

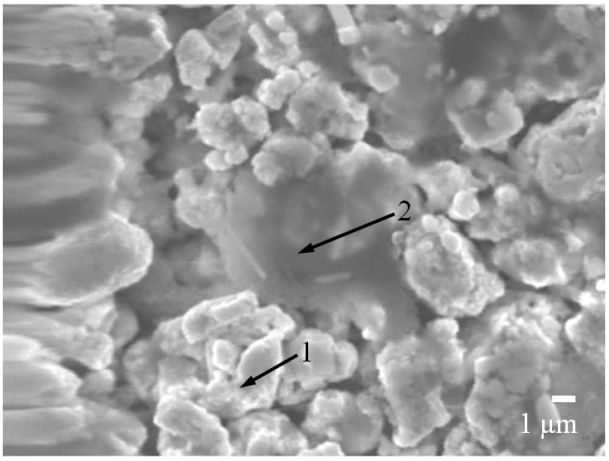

(b)

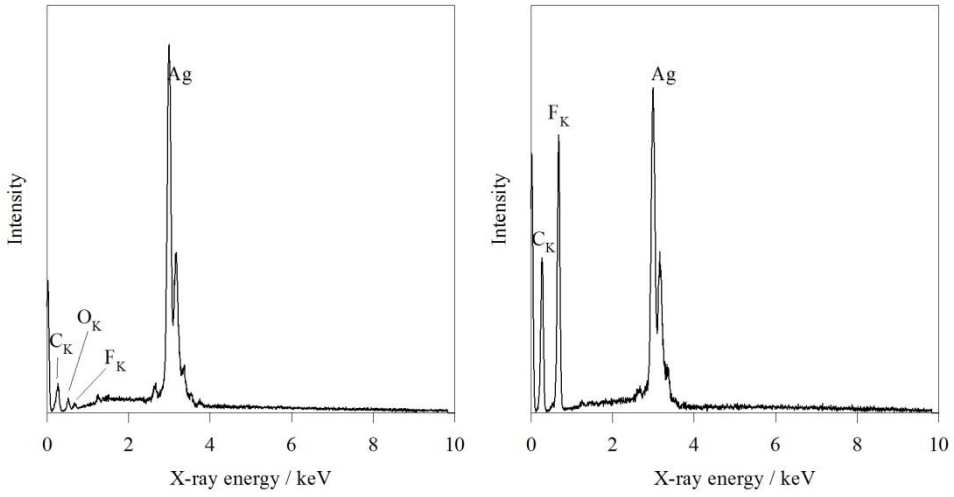

(c) (d)

Figure 5.7: Scanning electron microscopy image of the surface of the OxAg electrode at two different magnifications including EDX. (c) EDX of point labelled 1, (d) EDX of point labelled 2.

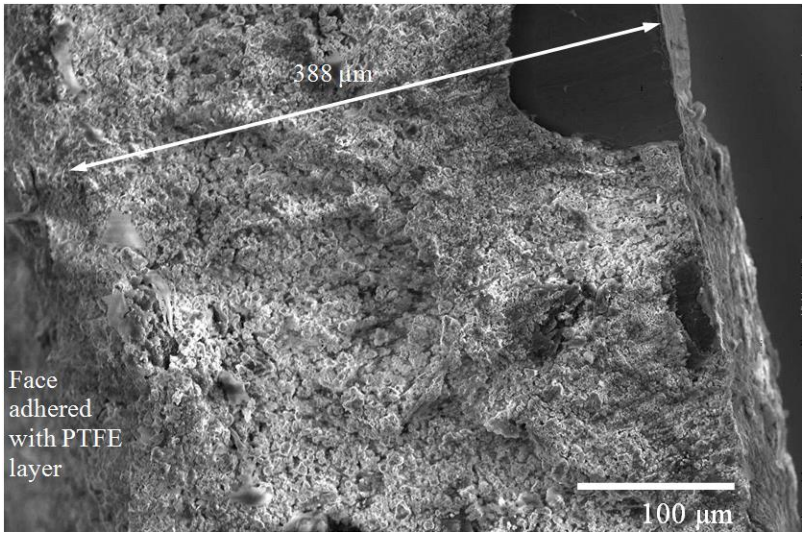

(a)

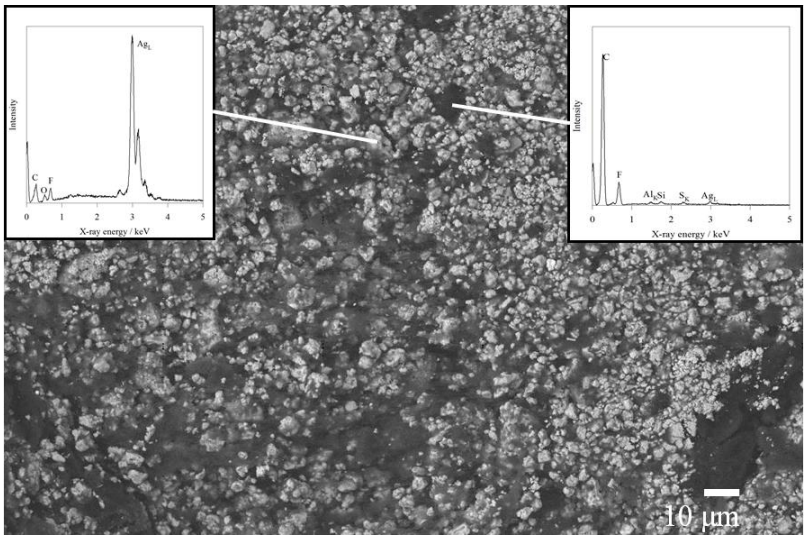

(b)

Figure 5.8: Cross section of the OxAg electrode examined via scanning electron microscopy. (a) Plan view of the thickness of the electrode, (b) Back-scattered electron image with EDX analysis insets.

Scanning electron microscopy images of E4A are shown in Figure 5.9(a), showing the sintered carbon/PTFE/catalyst mixture pressed between the nickel mesh, which had a spacing of 1.1 mm. The area highlighted by the white rectangle in Figure 5.9(a) is illustrated at higher magnification in Figure 5.9(b) where a rectangular shaped catalyst can be identified. The catalyst was quite large, 32 µm in size. The relatively low cost of MnO_x offered flexibility over catalyst size. Higher magnification of the edge of the catalyst in Figure 5.9(c) indicates the porosity between the carbon conductor and catalyst edge that allows diffusion of the oxygen and electrolyte reactants.

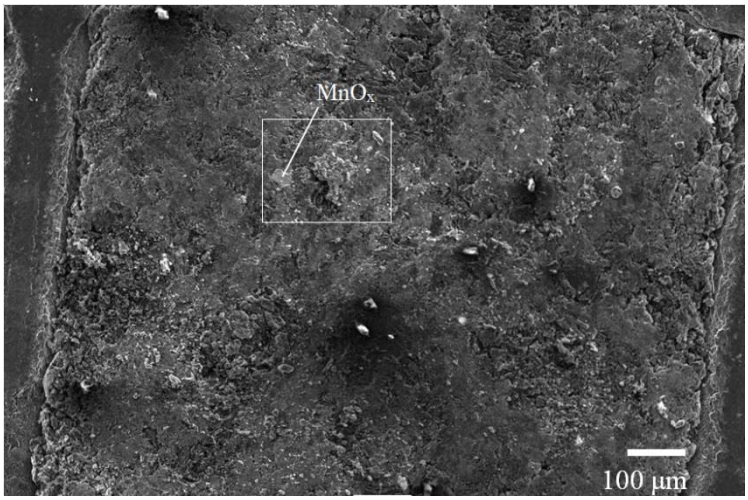

(a)

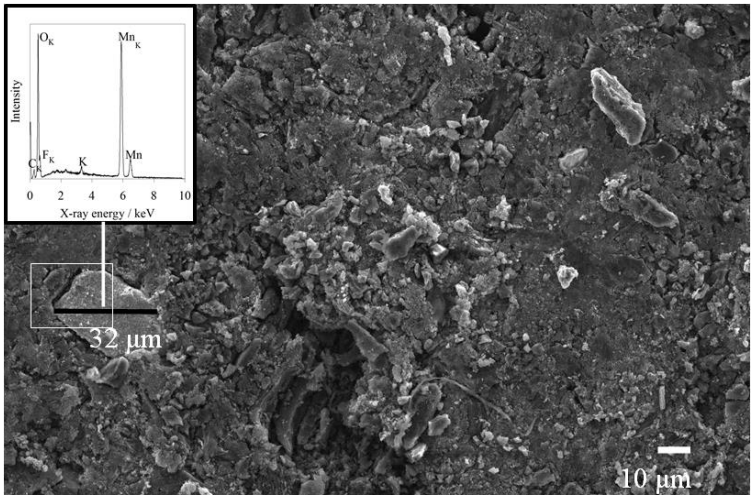

(b)

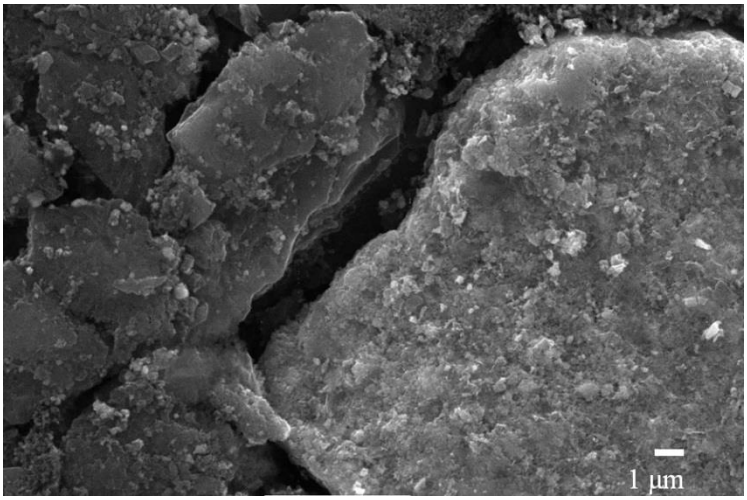

(c)

Figure 5.9: Scanning electron microscopy image of the E4A air-electrode at different magnifications. (a) Image showing active layer between metal mesh, (b) Magnification of area highlighted by the white square in image ‘a’, (c) magnification of area highlighted by the white square in image ‘b’.

Scanning electron microscopy images for the E4 MnO_x air electrode supplied by Electric Fuel Ltd. are shown in Figure 5.10(a) where three MnO_x catalysts are identified. The catalysts shown are also large, between 38 and 80 μm in size. A magnified view of the area highlighted by the white square in Figure 5.10(a) is shown in Figure 5.10(b).

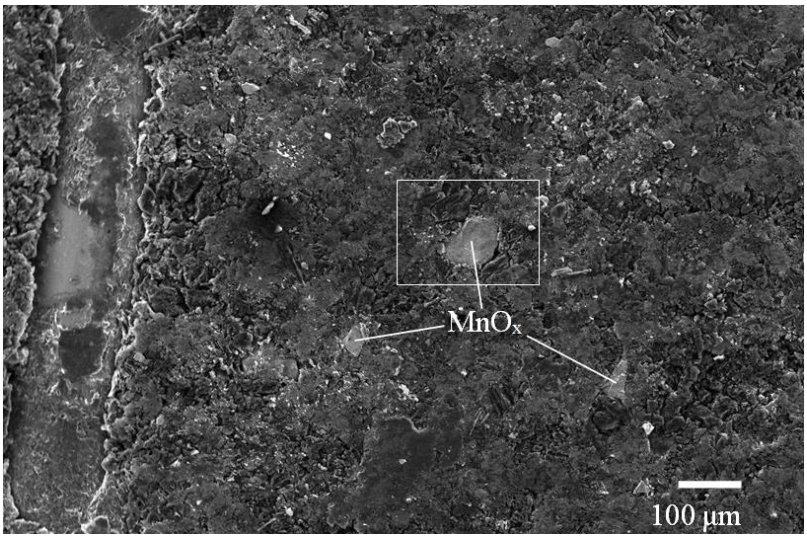

(a)

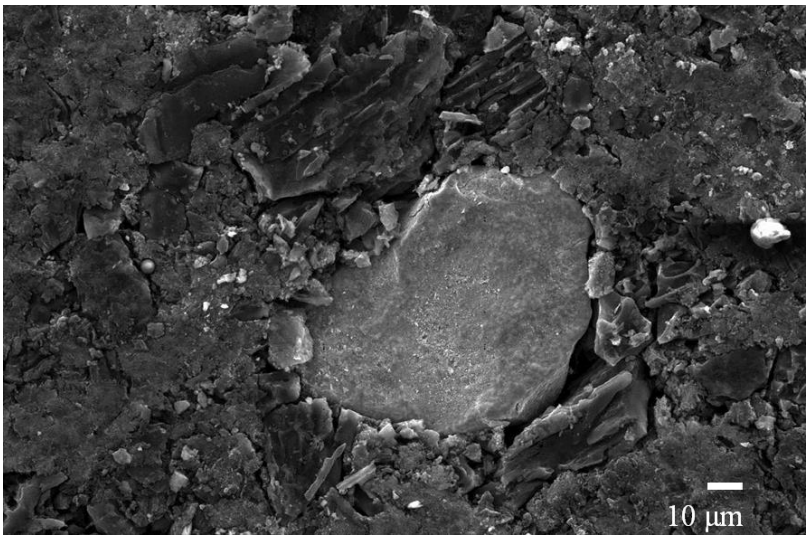

(b)

Figure 5.10: Scanning electron microscopy image of the E4 electrode at different magnitudes. (a) Low magnification image with three MnO_x catalyst particles identified, (b) High magnification of area highlighted by the white square in image 'a'.

The MOC electrode, which was a MnO_x electrode supplied by Gaskatel, appeared to have a higher catalyst loading than either E4 or E4A electrodes. This is indicated in the back-scatter electron image of Figure 5.11(a) where the heavier MnO_x catalyst shows up brightly against

the surrounding carbon interspersed between a nickel mesh. The MOC electrode had a finer mesh size of 0.55 × 0.55 mm, compared to the 1.1 × 1.1 mm of the E4A air-cathode, facilitating better current distribution. The catalysts used in the MOC electrode were of varying size. Those identified in the inset of Figure 5.11(b) ranged from 6 to 40 μm wide.

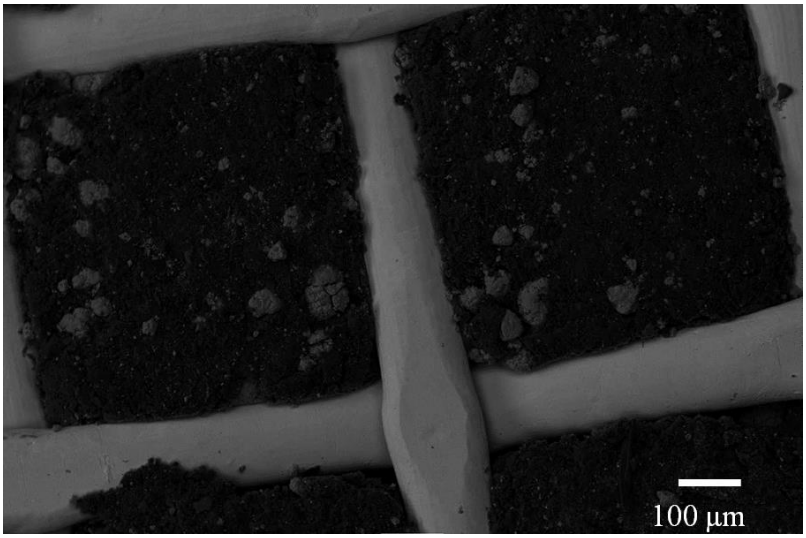

(a)

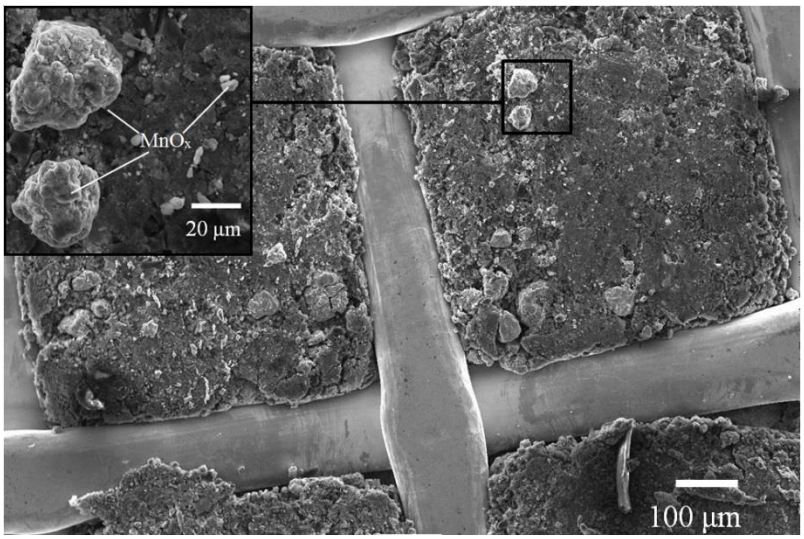

(b)

Figure 5.11: (a) Back scattered electron image of MOC electrode. (b) The same image as in image 'a' as viewed under the scanning electron microscope, with a magnified view of the catalyst inset.

Both the 0.5 mg cm^{-2} and 4 mg cm^{-2} Pt loaded electrodes did not have metal mesh current collectors embedded in their structure. This is because they were designed for use in fuel cells where electrical contact would be made via compressive contact with a metal or carbon flow

field plate. The 0.5 mg cm^{-2} Pt electrode was a carbon cloth with platinum on carbon forming the active layer. The 4.0 mg cm^{-2} platinum electrode was made from graphite paper with platinum particles on carbon forming the active layer. The rear face of both of these electrodes was treated with a hydrophobic coating to prevent electrolyte leakage. The absence of a metal mesh also meant that these electrodes lacked structural strength, with the carbon cloth being flexible and the graphite paper very brittle.

The surface of the 4 mg cm^{-2} Pt electrode was quite fractured with cracks 12 μm wide, as indicated in Figure 5.12(a). These cracks could have formed following manufacture, during drying of the suspension of nafion, platinum catalyst and carbon powder after it was brushed onto the top of the graphite sheet which formed the air diffusion layer. These cracks would be disadvantageous making the electrode susceptible to electrolyte flooding. Alternatively the cracks could have formed following the application of the ultra-high vacuum in the SEM chamber in which the images were taken. This could be ruled out by observation under an optical microscope. Attempts were made to identify a catalyst particle on the surface. The backscatter image in Figure 5.12(b) shows bright particles sub-micrometer in size. The inset in Figure 5.12(b) shows a magnified view of one of these particles, labelled as point 1, with a width of 200 nm. Clarification of the particle as platinum was not achievable. Energy dispersive x-ray analysis of the particle shown in Figure 5.12(c) indicated a platinum intensity peak similar to that for the EDX of the surrounding material in Figure 5.12(d). The surface of the 0.5 mg cm^{-2} Pt electrode was also ‘mud-cracked’ with cracks of 1.8 μm wide making it also susceptible to electrolyte flooding, see Figure 5.13.

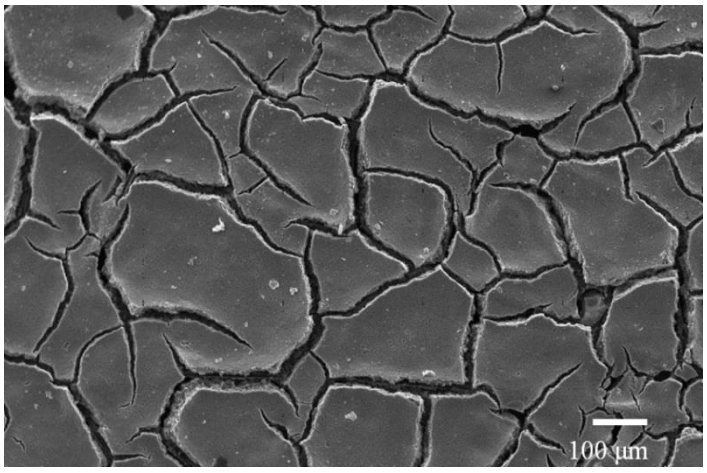

(a)

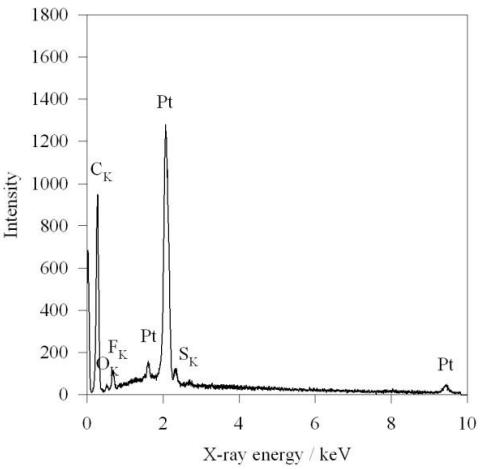

(c)

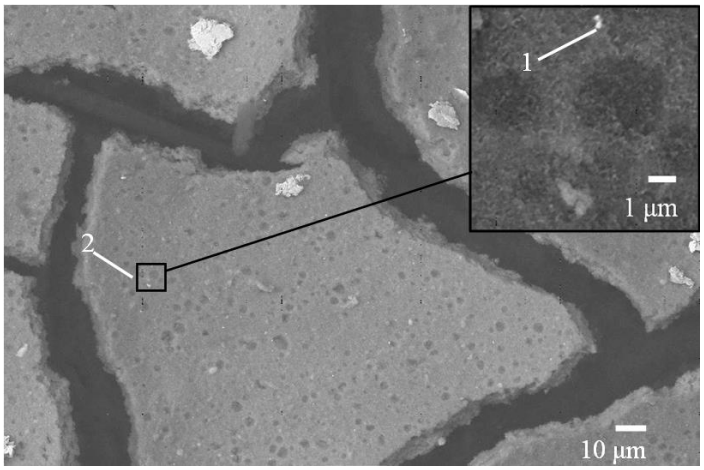

(b)

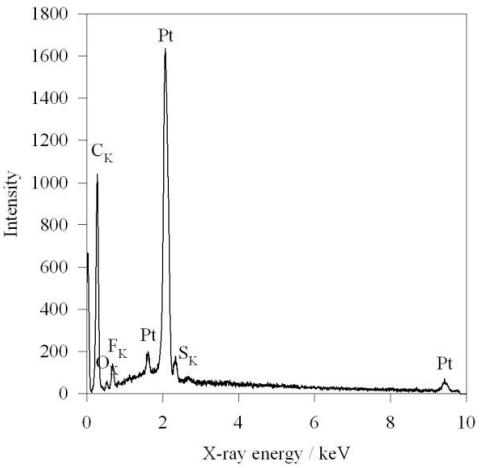

(d)

Figure 5.12: Scanning electron microscopy images of the 4 mg cm^{-2} platinum electrode at different magnifications. (a) Scanning electron microscopy image of the face of the active layer, (b) back scatter electron image with inset showing magnified view of selected area, (c) EDX of point 1, (d) EDX of point 2.

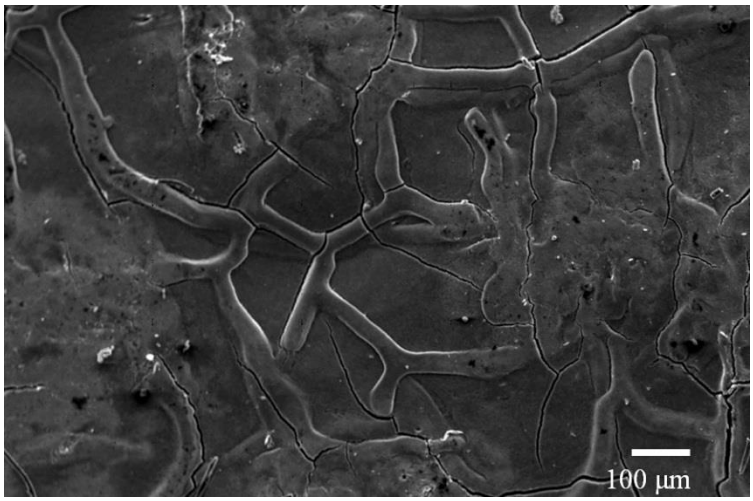

(a)

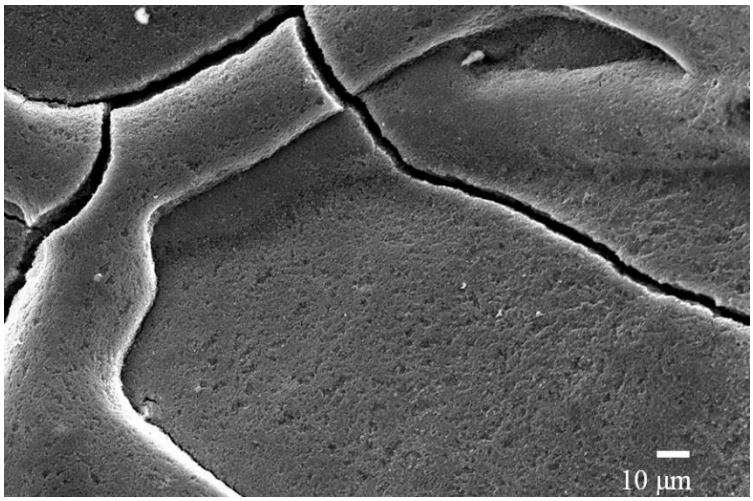

(b)

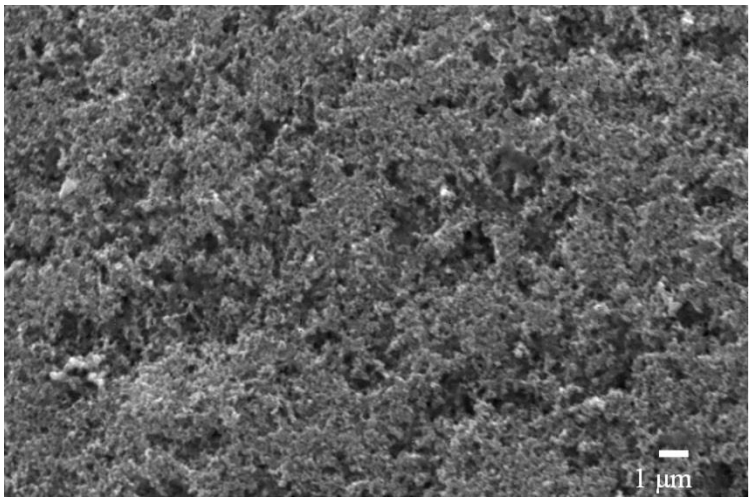

(c)

Figure 5.13: Scanning electron microscopy images of the 0.5 mg cm^{-2} Pt electrode at three magnifications.

Mercury porosimetry analysis was another technique used to analyse and compare the structural properties of the different gas diffusion electrodes. The mercury porosimetry experiments were conducted in collaboration by researchers at the University of Plymouth. The data is presented as the amount of the intruded mercury against pore diameter in Figure 5.14. The figure shows that the 4 mg cm^{-2} platinum electrode experienced a large volume of intruded mercury at pore diameters above 10 μm. This was due to the 12 μm wide cracks on its surface as indicated earlier in Figure 5.12. The cracks meant this structure may have been wetted more easily compared to the other electrodes and so suffered flooding of active sites which limited the current densities at which it could reduce oxygen. This is understandable as these electrodes are designed for a PEMFC to be in contact with a solid Nafion electrolyte rather than an aqueous liquid electrolyte. In PEMFC, pore structure is largely designed to facilitate removal of product water when the H^+ ions react with reduced oxygen.

Using the data from the pore distribution curves in Figure 5.14, the intrusion gradient with respect to the logarithm of the pore diameter was calculated and shown in Figure 5.15 for four of the commercial electrodes: E4A, MOC, E4 and E5. Comparing the four figures indicates similarities in the occurrence of peaks in the intrusion gradient over two pore ranges: 10 to 40 nm and 1×10^3 to 1×10^4 nm. This could suggest the presence of a bi-modal pore network in the gas diffusion electrodes [146], made up from a network of two different pore sizes. The smaller pores act as a hydrophilic network and the larger pores are responsible for the gas transport [146]. It has been postulated that the smaller pores are present within the carbon particles themselves while the larger particles formed between the carbon particles. The larger pores are hydrophobic due to the presence of the PTFE which is pressed into them during lamination [146]. Typically, carbon particles are approximately 50 nm in size [144], so the pore sizes should be of a similar order of magnitude, with the micropores within the carbon being even smaller than 50 nm. The mercury porosimetry appears to support this statement as the calculated mean pore diameter for the E5, E4, E4A and MOC electrodes fell between 32 and 87 nm, as indicated in Table 5.1.

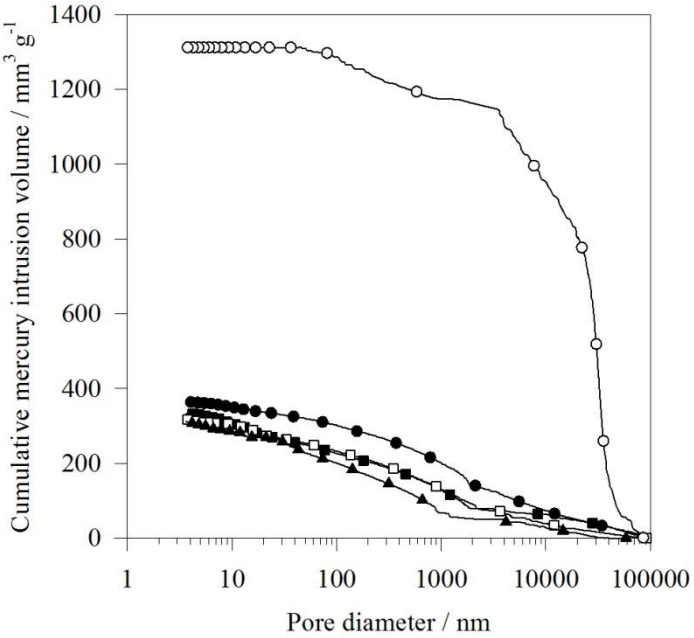

Figure 5.14: Pore distribution curves for the commercial gas diffusion electrodes calculated from mercury intrusion data. ▲ Gaskatel MOC, □ E4A ■ E4, ● E5, ○ 4 mg cm^{-2} Pt.

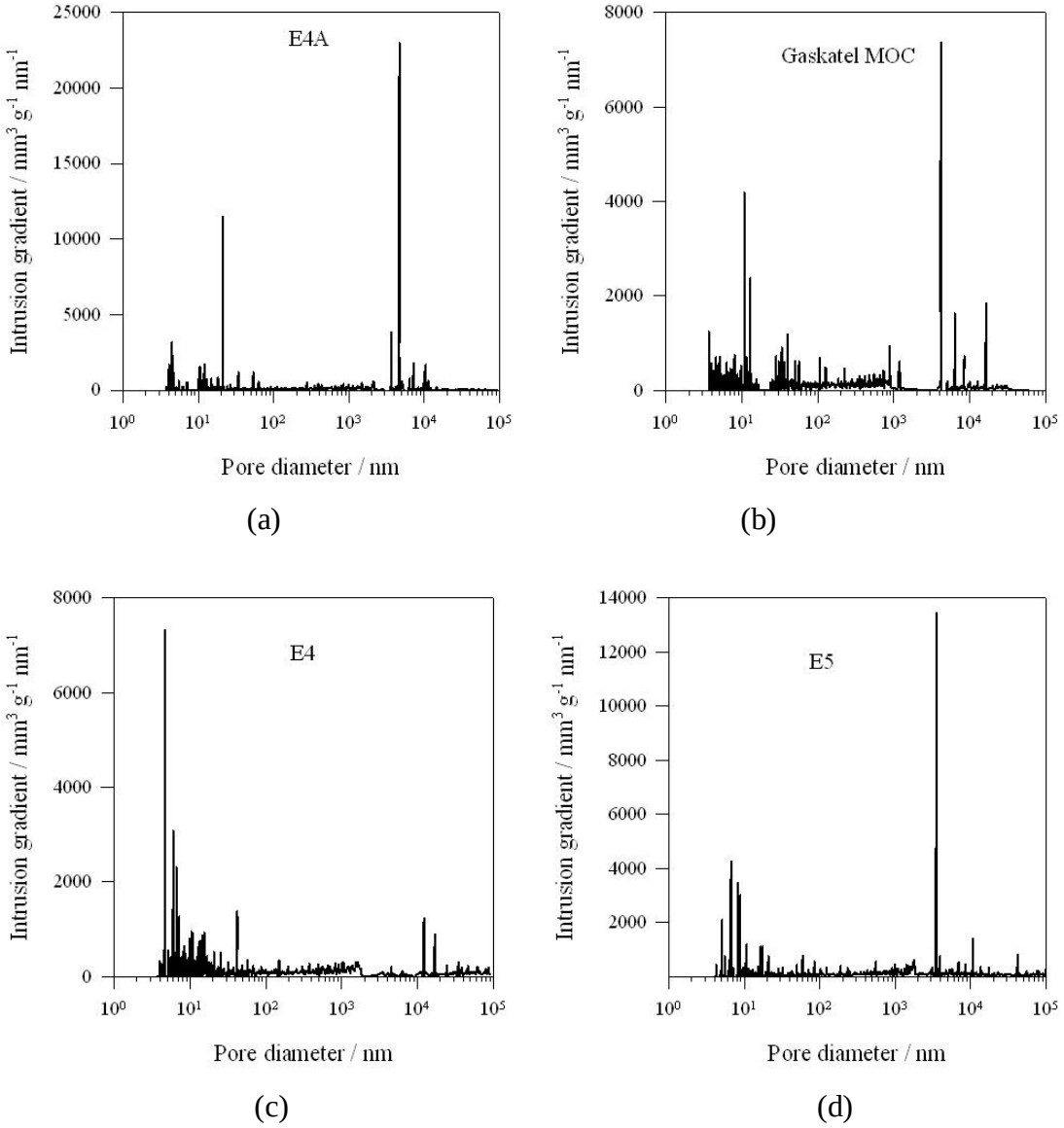

Figure 5.15: Intrusion gradient for four of the commercial gas diffusion electrodes. (a) E4A, (b) MOC, (c) E4, (d) E5.

5.3 Importance of electrode preconditioning

The processes used to manufacture the KTH air-electrode rendered the top surface of the active layer hydrophobic. A thin layer of PTFE could have formed on the surface during manufacture imparting the hydrophobicity. Visually a water droplet placed onto the surface would roll off instead of absorbing into it. For that reason the KTH electrode needed preconditioning, the purpose of which was to ensure wetting of the surface and the internal pores of the electrodes to facilitate the presence of the three phases necessary for oxygen reduction. Other studies have also used a preconditioning step which included a pre-discharge

at 50 mA cm^{-2} for 25 minutes [231] or a pre-discharge followed by immersion in the electrolyte for 12 hours [3].

Several preconditioning procedures were examined with the KTH electrode, followed by a linear sweep voltammogram to compare the effect of each procedure, as shown in Figure 5.16. The results show that holding the electrode at open-circuit for 1 hour prior to the linear sweep was insufficient for facilitating discharge at high current densities with a limiting current density for oxygen reduction of only −200 mA cm^{-2} at −0.37 V *vs.* Hg/HgO. Carrying out a galvanostatic discharge at −50 mA cm^{-2} was a more effective preconditioning procedure, with that sample reaching a limiting current density of −460 mA cm^{-2} at −0.49 V *vs.* Hg/HgO. A similar limiting current density was obtained by holding the electrode at open-circuit for 24 hours prior to the linear sweep. Another procedure of a predischarge at −100 mA cm^{-2} saw further improvements with a limiting current density of −470 mA cm^{-2} at −0.42 V *vs.* Hg/HgO.

The accuracy of the procedure where the sample was held for 24 hours needs to be questioned. As the electrodes were porous, the long pre-immersion time may have allowed the electrolyte not only to penetrate the depth of the electrode but also to internally diffuse laterally in the electrode outside the diameter defined by the rubber gasket. As this possibility could not be ruled out, a pre-discharge of −50 mA cm^{-2} was selected as the preconditioning procedure for the KTH electrode [170].

Although, knowledge that the KTH electrode was fully pre-conditioned following 24 hours exposure to electrolyte is useful when selecting the storage procedure for a commissioned aluminium-air cell. It means it would be favourable to store a commissioned cell with the electrolyte present but with the aluminium anode absent, until needed, to avoid its degradation from corrosion. Another option is to pour in the electrolyte when the cell is going to be used. However, these results have shown that the air-cathode needs to be preconditioned by immersion in the electrolyte to facilitate wetting of its pores.

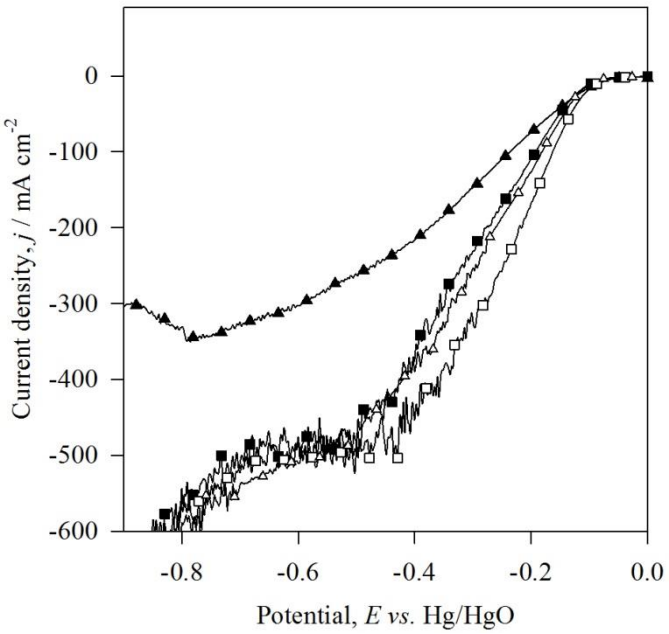

Figure 5.16: The importance of electrode preconditioning on the linear sweep voltammogram of the KTH electrode in 4 mol dm^{-3} NaOH solution at 22 °C. The preconditioning procedures were: ▲ ocp 1 hour, ■ −50 mA cm^{-2} 1 hour discharge, △ ocp for 24 hours, □ −100 mA cm^{-2} 1 hr discharge. The back of the electrode was open to atmosphere. Sweep rate: 1 mV s^{-1}.

5.4 Effect of nitrogen purging on polarisation of GDE

The effect of bubbling nitrogen through the electrolyte on the polarisation behaviour of the E5 gas diffusion electrode was examined. The purpose of bubbling with nitrogen was to remove the dissolved oxygen from solution to examine what role it played as a reactant at the air-electrode. Two samples of the E5 commercial gas diffusion electrode were evaluated, one in a degassed solution, the other in a normal solution of 4 mol dm^{-3} NaOH at 295 K. Nitrogen was bubbled through the solution for 40 minutes. The solubility limit for oxygen in 4 mol dm^{-3} NaOH at 298 K is 0.36 mmol dm^{-3} [81].

In the normal solution, atmospheric oxygen and oxygen dissolved within the electrolyte were reduced at the electrode while in the de-gassed solution only atmospheric oxygen was reduced. The results in Figure 5.17 indicate that removing oxygen from the solution unfavourably shifted the cathodic polarisation curve of the GDE 8 mV more negative. This increase was considered so small that, in other tests, the electrolyte was not degassed with nitrogen.

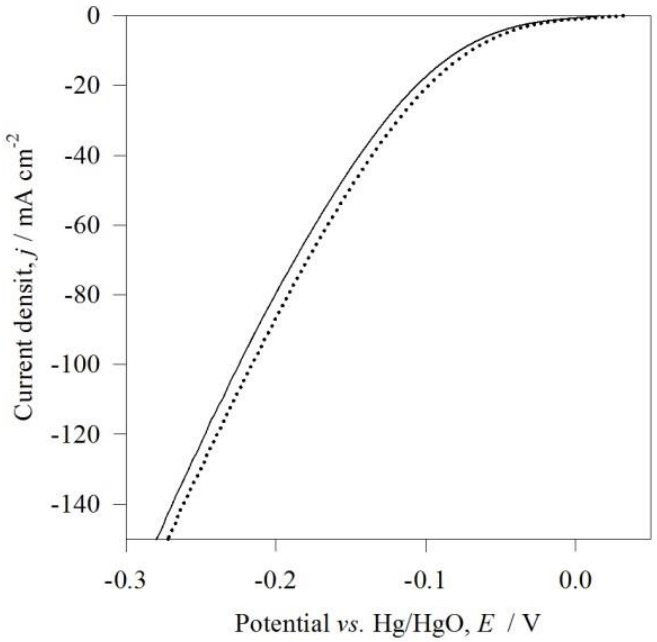

Figure 5.17: The effect of degassing the electrolyte on the polarisation of the E5 commercial gas diffusion electrode. ——— Solution degassed with N_2 for 40 minutes, ····· Non-degassed normal solution. Electrolyte: 4 mol dm^{-3} NaOH. Sweep rate: 1 mV s^{-1}. Temperature: 295 K. The back of the air-electrode was open to atmosphere.

5.5 Effect of electrolyte concentration and type on polarisation of GDE

The effect of the sodium hydroxide concentration on the polarisation of the Co-based, E5 commercial gas diffusion electrode was investigated. Three samples of E5 were tested by linear sweep voltammetry in the three-electrode glass cell at a sweep rate of 1 mV s^{-1}. The overpotential for cathodic polarisation for the Co-based electrode was larger in 1 mol dm^{-3} NaOH than in either 4 or 8 mol dm^{-3} NaOH, as shown in Figure 5.18. The solubility of oxygen is 0.8 mmol dm^{-3} in 1 mol dm^{-3} NaOH, higher than it is in 4 mol dm^{-3} NaOH at 0.36 mmol dm^{-3}. The difference in oxygen solubility then cannot explain the difference in electrode behaviour. Since the difference in behaviour is found to occur in the ohmic region of the linear sweep, the higher conductivity of 4 mol dm^{-3} NaOH of 0.39 S cm^{-1} compared to 0.18 S cm^{-1} for 1 mol dm^{-3} NaOH could explain the difference. There was no further improvement in reactivity for oxygen reduction by increasing electrolyte concentration from 4 to 8 mol dm^{-3} NaOH because the conductivity of NaOH is maximum at 4 mol dm^{-3} [79].

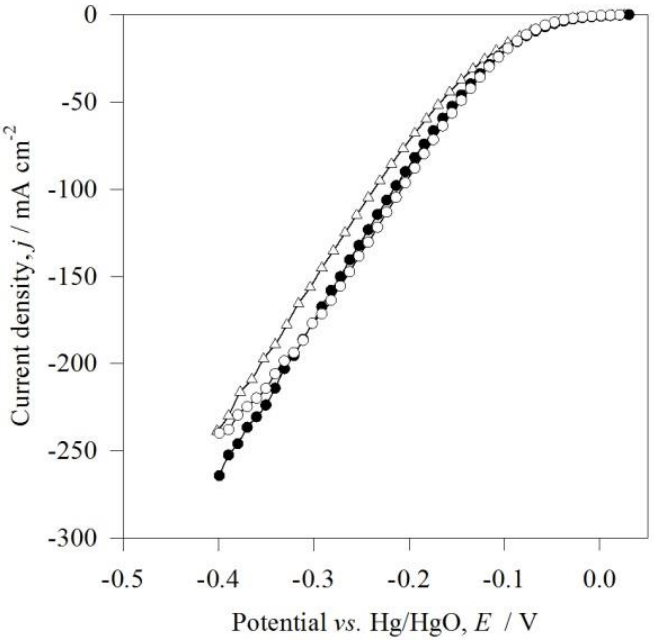

Figure 5.18: Effect of electrolyte concentration on the polarisation of the Co-based GDE, E5, in NaOH. △ 1 mol dm^{-3}; ● 4 mol dm^{-3}; ○ 8 mol dm^{-3}. Sweep rate: 1 mV s^{-1}. The back of the air−electrode was open to air at atmospheric pressure. Electrolyte temperature: 22 °C. Electrode area: 3.46 cm^2.

Examining different alkaline electrolytes, Figure 5.19 shows that there was no difference in the oxygen reduction reactivity of the E5 commercial gas diffusion electrode in 4 mol dm^{-3} NaOH compared to 7 mol dm^{-3} KOH. The higher solubility for oxygen, higher oxygen diffusion coefficients and lower viscosity of potassium hydroxide did not lower the overpotential for oxygen reduction [81]. Even the superior conductivity of 7 mol dm^{-3} KOH (0.7 S cm^{-1} [80]) compared to that of 4 mol dm^{-3} NaOH (0.39 S cm^{-1} [79]) did not infer any advantage. This suggests that the performance of the air cathode is not limited by the diffusion of water to and OH^- ions away from the reaction sites but most likely by the utilisation of the catalyst. Contributing to this are the effective diffusion of oxygen through the GDE and the actual number of 3-phase regions in the gas diffusion electrode where water, oxygen and an electron can simultaneously be at a catalyst reaction site in order for oxygen to reduce.

The effect of electrolyte type was not examined on any of the other air-electrodes because sodium hydroxide was being chosen over purity reasons for the aluminium anode as discussed in Section 4.2.3

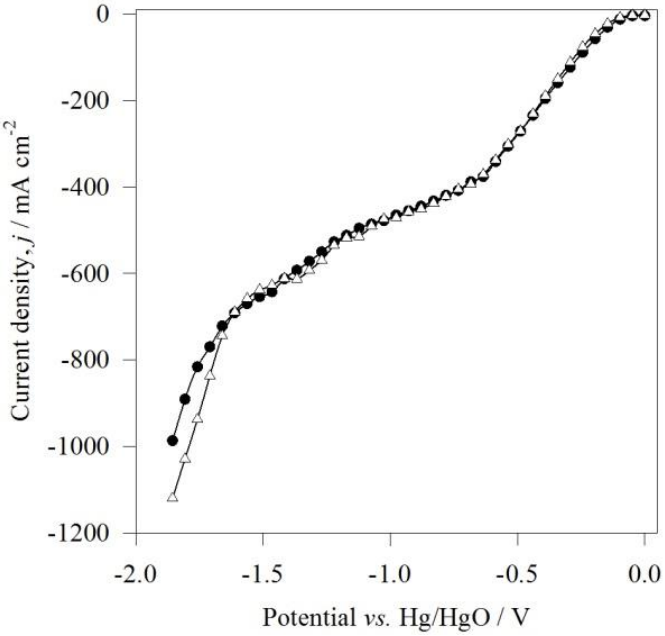

Figure 5.19: The effect of electrolyte type on polarisation of the commercial air electrode, E5. ● 4 mol dm^{-3} NaOH, △ 7 mol dm^{-3} KOH. Sweep rate 1 mV s^{-1}. The back of the electrode was open to atmosphere. Electrolyte temperature: 22 °C. Electrode area: 3.5 cm^2. Platinum mesh counter electrode of area 1.5 cm × 1.5 cm.

5.6 Effect of electrolyte temperature and boiling water treatment of gas diffusion electrode

A sample of the E5 commercial gas diffusion electrode was pretreated by placing it in boiling water for 10 minutes. It was considered that this would increase hydration of the catalytic layer and also open up the pores to increase the access to the 3-phase regions [232]. Figure 5.20 indicates that boiling the E5 electrode did not deliver any improvement in the oxygen reduction reactivity. The reason for this may be because the porosity of this electrode may already be sufficient to allow diffusion of electrolyte to catalyst sites.

Increasing the electrolyte temperature to 60 °C did not enhance the performance of the E5 electrode. One of the reasons for this may be that adsorption of gases on the electrode surface can be affected adversely with temperature [233]. These would negate the positive effects of decreased activation polarisation and electrolyte resistance with increasing temperature.

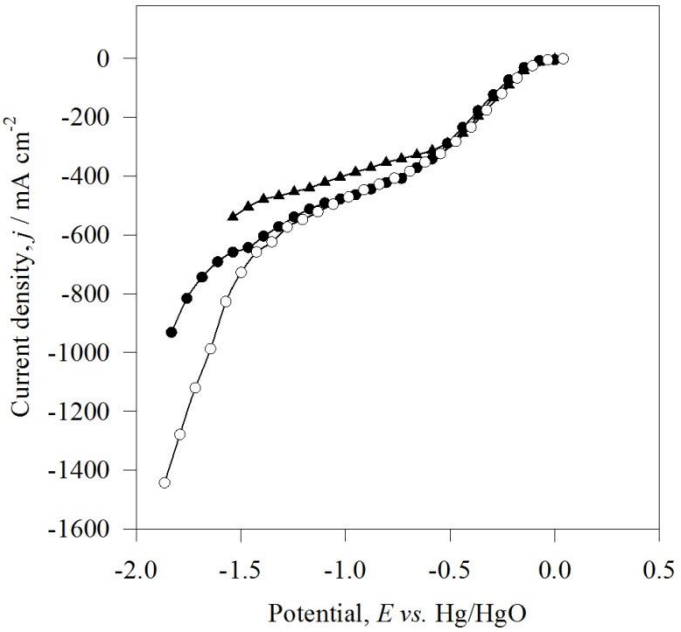

Figure 5.20: The effect of electrolyte temperature and electrode pre-treatment on the oxygen reduction reactivity of the E5 commercial gas diffusion electrode. Sweep rate 1 mV s^{-1}. Rear face of the electrode was open to the atmosphere. Electrolyte: 4 mol dm^{-3} NaOH. Electrode area: 3.46 cm^2. Platinum mesh counter electrode of area 1.5 cm × 1.5 cm. ● 22 °C, ▲ 60 °C, ○ pretreated with boiling water.

The KTH electrode showed more sensitivity to the electrolyte temperature than the E5 one. Figure 5.21(a) shows that raising the electrolyte temperature to 60 °C greatly increased the maximum current density from − 270 mA cm^{-2} to – 413 mA cm^{-2} at – 0.525 V *vs.* Hg/HgO. The lower discharge currents at 22 °C were because of an earlier onset of mass transport limitations, at − 0.374 V *vs.* Hg/HgO. This is more clearly seen in Figure 5.21(b) showing the Tafel plots of the linear sweeps, where the current reached a plateau beyond −0.374 V *vs.* Hg/HgO because of mass transport limitations. The initial hydrophobic nature of the KTH electrode surface, as discussed at the start of Section 5.3, could explain the earlier onset of mass transport effects at 22 °C i.e. limitation of the mass transfer of electrolyte through the electrode to the catalyst. Raising the electrolyte temperature to 60 °C may have broken down the hydrophobicity of the KTH surface to allow improved mass transport of electrolyte into the electrode to discharge at higher current densities. Raising the electrolyte temperature may be an additional way of pre-conditioning the KTH electrode similar to the application of a cathodic current density. To confirm this, the linear sweep voltammogram of the KTH electrode following a pre-discharge of −50 mA cm^{-2} at 22 °C is included for comparison in Figure 5.21(a). The enhanced currents observed at 60 °C were also observed following the

pre-discharge of –50 mA cm^{-2}. This indicates that the enhanced current densities at 60 °C compared to at 22 °C may not be due to an improvement in catalytic activity but a breakdown of the hydrophobicity of the electrode leading to improved mass transport. The overpotential in the kinetic region during the linear sweep response at 60 °C was larger than it was after the pre-discharge of −50 mA cm^{-2} because gas evolved rapidly from the electrode surface during the linear sweep at 60 °C. Consequently the linear sweep following the pre-discharge of −50 mA cm^{-2} at 22 °C saw a high limiting current density for oxygen reduction of −460 mA cm^{-2} at –0.49 V *vs.* Hg/HgO. This was better than that attained from the linear sweep at 60 °C of –413 mA cm^{-2} at −0.525 V *vs.* Hg/HgO. The gas evolution observed from the surface of the sample at 60 °C could have been due to decomposition of the oxide catalyst, releasing oxygen. The evolved bubbles partially blocked the electrode surface area, which explained the fluctuating potential observed in the linear sweep at 60 °C.

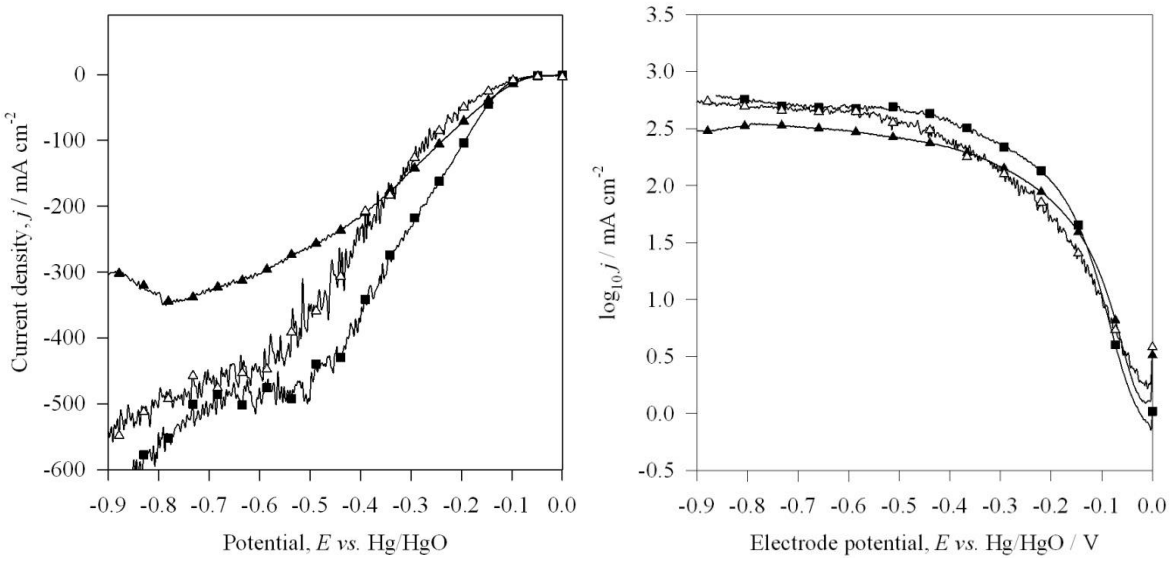

(a) (b)

Figure 5.21: The effect of temperature on linear sweep voltammetry at the KTH electrode. (a) Cathodic linear sweep voltammetry, (b) Tafel plots of these voltammetry sweeps. ▲ 22 °C, △ 60 °C, ■ 22 °C, after a −50 mA cm^{-2} pre-discharge. Electrolyte: 4 mol dm^{-3} NaOH. Electrode area: 3.8 cm^2. The rear face of the electrode was open to the air. Sweep rate: 1 mV s^{-1}.

5.7 Effect of gas diffusion electrode design and current collection

The design of the gas diffusion electrode is critical to minimise its overpotential during oxygen reduction. Tests were carried out with the 4 mg cm^{-2} Pt GDE investigating the effect of a current collector on the overpotential for oxygen reduction. A stainless steel foil with a

circular hole in it was used as a current collector by placing it in compressive contact with the rear face of the gas diffusion electrode. The results in Figure 5.22 show that the overpotential was lower when using a current collector than without it, emphasising the importance of the design of the gas diffusion electrode on its performance. The improvement in the linear sweep occurred in the ohmic region of the plot indicating the metallic current collector helped reduce resistive losses.

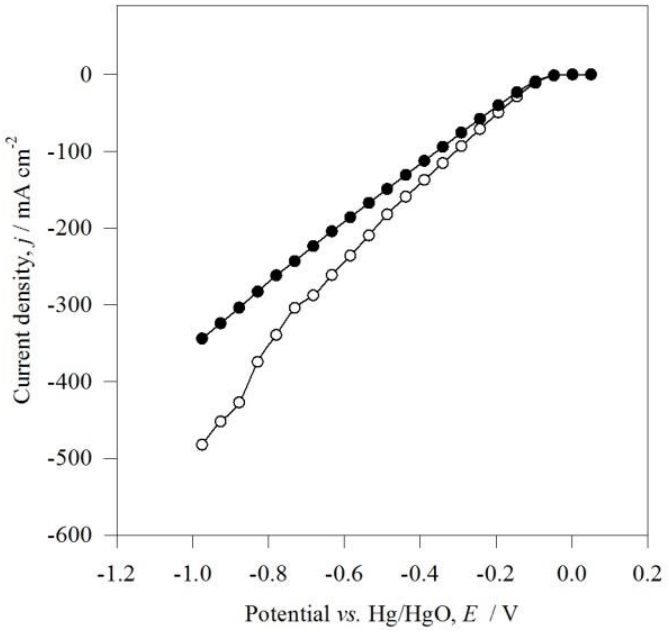

Figure 5.22: The effect of current collection on oxygen reduction reactivity of 4 mg cm^{-2} Pt gas diffusion electrode in alkaline solution. Static 4 mol dm^{-3} NaOH solution at 22 °C. Electrode area: 3.46 cm^2. Sweep rate: 1 mV s^{-1}. ● 4 mg cm^{-2} Pt GDE without current collector, ○ 4 mg cm^{-2} Pt GDE with current collector. The current collector was a stainless steel foil with a hole in its centre to allow air access at the back of the electrode.

5.8 Comparison of gas diffusion electrodes

Linear sweep voltammetry was used to compare the oxygen reduction reactivity of the KTH electrode with the seven commercial gas diffusion electrodes as shown in Figure 5.23(a). A magnified view of the same graph comparing the linear sweep voltammograms showing the behaviour of the electrodes at current densities below −200 mA cm^{-2} is shown in Figure 5.22(b). The limiting current densities for oxygen reduction at the electrodes are compared in Table 5.2. The KTH air cathode exhibited the highest limiting current density for oxygen reduction of −463 mA cm^{-2} at −493 mV *vs.* Hg/HgO.

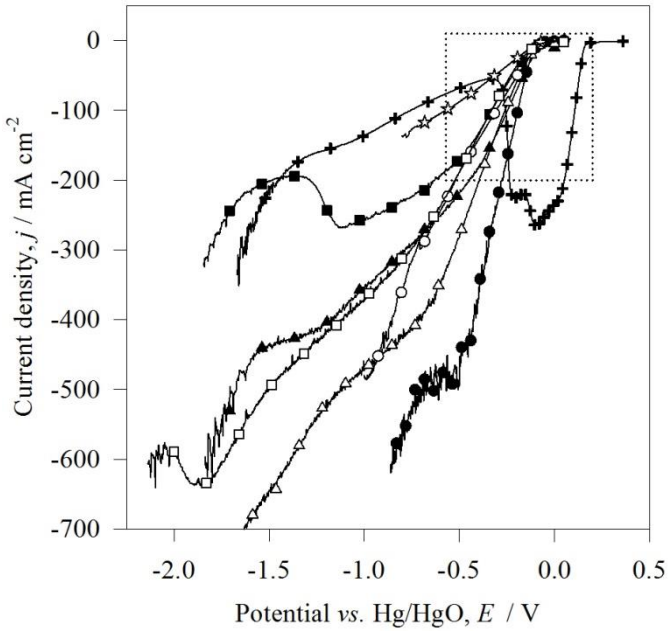

(a)

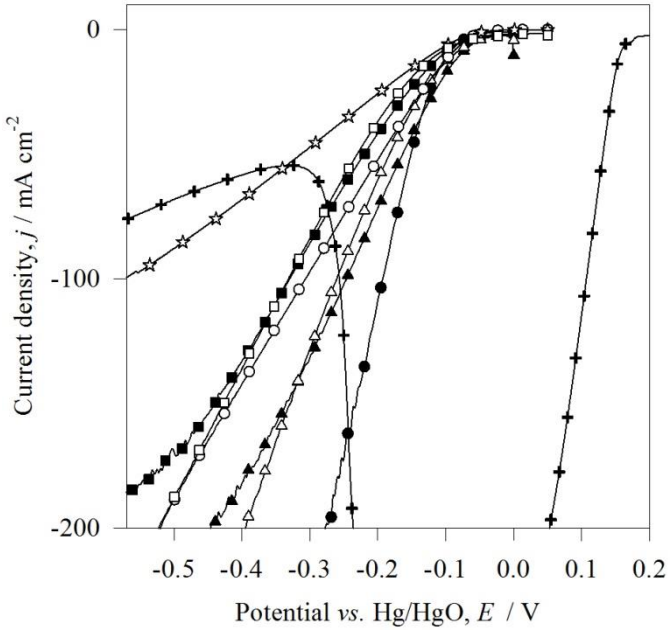

(b)

Figure 5.23: (a) Comparison of KTH electrode with the commercial gas diffusion electrodes. The area highlighted by the dotted square is shown in graph 'b'. (b) Close-up of linear sweep at current density below −200 mA cm^{-2}. Linear sweep scans carried out in 4 mol dm^{-3} NaOH at 22 °C. Sweep rate: 1 mV s^{-1}. Area: 3.46 cm^2. The rear face of the electrode was open to air at atmospheric pressure. ✯ 0.5 mg cm^{-2} Pt, ○ 4.0 mg cm^{-2} Pt, ■ E4 MnO_x, ▲ E4A MnO_x, □ MOC, △ E5 Co-catalysed air cathode, ✚ OxAg, ● KTH.

Two of the electrodes were Pt/C electrodes, with a platinum/carbon active layer pasted onto a carbon cloth (0.5 mg cm^{-2} Pt) and a porous graphite gas-diffusion layer (4 mg cm^{-2} Pt). The limiting current density for the 0.5 mg cm^{-2} and 4.0 mg cm^{-2} platinum electrodes were −120 and −300 mA cm^{-2} respectively. The higher platinum loading can account for the lower resistance, 0.64 Ω, of the 4 mg cm^{-2} platinum electrode compared to the 0.5 mg cm^{-2} Pt one, 1.39 Ω, which was calculated over the linear ohmic region of the linear sweep curves. The higher the loading of catalyst, the faster the rate of oxygen reduction. Research on the effect of platinum loading can be found elsewhere [234]. The Pt/C electrodes would have a lower cathodic overpotential if they incorporated a metal mesh in their structure to enhance the current distribution across the electrode. Also the presence of the cracks in the surface of both of the platinum electrodes could have resulted in flooding of some parts of the electrode.

Compared to the platinum loaded electrodes, the major design difference with the other gas diffusion electrodes studied was a metal mesh current collector incorporated into their laminated structure. They consisted of a porous PTFE membrane and active layer of catalysed carbon laminated with the metal mesh. Three manganese based air electrodes were studied: E4 and E4A supplied by Electric Fuel and MOC supplied by Gaskatel. In the ohmic controlled region below −200 mA cm^{-2} the resistance of E4 is similar to that of the 4 mg cm^{-2} Pt GDE, 0.63 Ω, although the platinum gas diffusion electrode had a superior limiting current density, see Table 5.2. The E4A electrode had a resistance of 0.49 Ω. Of the three manganese based electrodes, MOC had the superior limiting current density of −220 mA cm^{-2} at −0.56 mV *vs.* Hg/HgO. The superior limiting current density for oxygen reduction of the MOC electrode compared to E4 and E4A may be due to several reasons. Firstly SEM analysis discussed in the structure section found MOC to have a higher catalyst loading and finer mesh size than either E4 or E4A. Also the nickel mesh current collector of the MOC electrode was gold plated, with gold supporting the reduction of oxygen through the peroxide two electron pathway. The limiting current density of the manganese based electrodes was limited by their propensity to promote the two-electron pathway for oxygen reduction [14]. For this reason they may not be suited to a high-power density Al-air cell.

Comparing the E4A and E5 electrodes indicates their ohmic region was of a similar slope of 0.49 and 0.42 Ω respectively. As both of these electrodes were manufactured by the same company, perhaps the design of the electrode contributed to the potential drop in the ohmic region. Design similarities between the E4A and E5 electrodes were metal mesh of similar

spacing indicating a similar means of current distribution. Also the lamination pressure and PTFE content between the electrodes could have been similar, determining the number of air and water diffusion pathways in the electrodes. The main difference between these two electrodes was a Co-based catalyst for E5 and a MnO_x catalyst for E4A. The superior activity of the E5 catalyst compared to the E4A MnO_x catalyst meant that E5 had a higher limiting current density of −358 mA cm^{-2} at −0.62 V *vs.* Hg/HgO compared to −160 mA cm^{-2} at −0.54 V *vs.* Hg/HgO for E4A.

The OxAg electrode designed by Gaskatel underwent two reduction steps during its cathodic polarisation. If the species of silver oxide in the air-electrode contained some of the higher oxide, AgO, which has been shown to be $Ag_2O_3.Ag_2O$ [235], it would have reduced via two mechanisms firstly to monovalent silver oxide, Ag_2O,

$$2AgO + H_2O + 2e^- \rightarrow Ag_2O + 2OH^- \qquad E_c = 0.46 \text{ V } vs. \text{ Hg/HgO} \qquad (5.2)$$

Then finally to Ag,

$$Ag_2O + H_2O + 2e^- \rightarrow 2Ag + 2OH^- \qquad E_c = 0.20 \text{ V } vs. \text{ Hg/HgO} \qquad (5.3)$$

The OxAg electrode observed the most positive open-circuit potential of 0.35 V *vs.* Hg/HgO, compared to the other electrodes, which fits in between the theoretical potentials for the reactions (5.2) and (5.3). The first reduction step commenced at 0.2 V *vs.* Hg/HgO and proceeded to yield currents at more positive potentials compared to the other air-electrodes. This first reduction reaction reached a limiting current density of −265 mA cm^{-2} at −0.094 V *vs.* Hg/HgO when all the AgO had reduced to Ag [236, 237]. After the first reduction step of AgO to Ag the electrode continued to discharge as an oxygen reduction electrode but at significantly more negative potentials compared to the other air-electrodes. This was surprising considering that silver is known to promote the direct 4-electron oxygen reduction pathway [140]. The larger overpotentials of the AgO electrode for oxygen reduction at potentials negative of −0.3 V *vs.* Hg/HgO compared to the other electrodes could be due to its constituent elements. Oxygen reduction is effective once a three-phase boundary is created between the catalyst, water and oxygen. Clearly a two-phase boundary existed between the catalyst and water in order for reduction of AgO to Ag to occur. Also the low resistance of

the electrode during the AgO reduction step of 0.14 Ω suggested that electrical conduction to the catalyst was not an issue. The issue may be the availability of oxygen at the active sites [238].

Unlike the reduction of oxygen, the duration of the initial reduction phase of AgO to Ag was dependent on the capacity of the AgO or Ag_2O present. This is clearly illustrated in Figure 5.24, where the electrode observed a variable discharge potential at −100 mA cm^{-2} for 900 s, before a sharp negative shift in potential signifying the end of discharge. During the initial 900 s the discharge potential was most likely attributable to the reduction of AgO to Ag rather than the reduction of oxygen [236]. There also seems to have been two potential steps in the discharge profile over the initial 900 s. This is characteristic of an electrode made of divalent AgO, whereby the first potential step was attributed with the reduction of AgO to Ag_2O followed by reduction of Ag_2O to Ag [239, 240]. Once all the AgO was reduced the negative drop in potential occurred after 900 s of discharge. Visual analysis of the electrode surface after discharge in Figure 5.25 shows that the discharged area of the electrode was light grey in colour suggesting the change in the electrode composition from AgO to Ag.

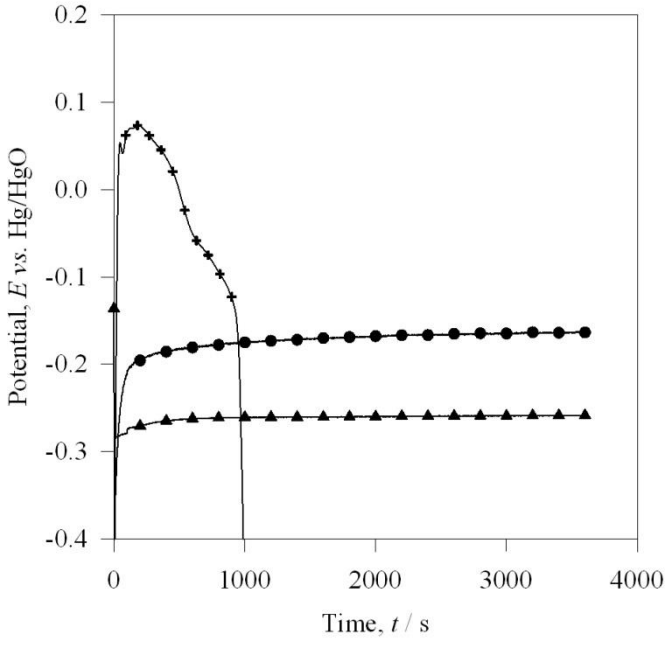

Figure 5.24: Comparison of the gas diffusion electrodes under galvanostatic discharge at 100 mA cm^{-2}. Electrolyte: 4 mol dm^{-3} NaOH at 22 °C. Electrode area: 3.46 cm^2. A larger area of 3.8 cm^2 was used for KTH. ▲ E4A, ● KTH, ✚ AgO. The back of the electrodes were open to the air at ambient pressure.

The KTH and E4A electrodes showed steadier, more consistent potentials for an hour under galvanostatic discharge at −100 mA cm^{-2}, compared to the OxAg electrode, as illustrated in Figure 5.24. The potential of the KTH electrode was −0.16 V *vs.* Hg/HgO, more desirable than that of the E4A electrode, −0.26 V *vs.* Hg/HgO. These potentials were inferior to those delivered by the OxAg electrode under the same current density. Higher power could be potentially obtained with the OxAg electrode in the Al-air cell although to increase its discharge time a larger and more expensive loading of AgO would be needed.

Electrode name	Catalyst	I_L / mA cm^{-2}	E at I_L *vs.* Hg/HgO / V	Resistance in IR region / Ω
KTH	$LaCaCoO_3$ / $LaCaMnO_3$	-463	-0.493	
E5	Cobalt based	-358	-0.620	0.42
OxAg Gaskatel at 55°C	AgO	-335*	-0.084	
W18365 ELE0072 Graphite paper	4 mg cm^{-2} platinum	-300	-0.726	0.64
OxAg Gaskatel at 22°C	AgO	-265*	-0.094	0.141
MOC	Manganese oxide	-220	-0.56	0.55
E4A	Manganese oxide based	-160	-0.54	0.49
E4	Manganese oxide based	-150	-0.44	0.63
W11529-346 Graphite paper	0.5 mg cm^{-2} platinum	-120	-0.416	1.390

Table 5.2: Electrochemical comparison of the commercial air-electrodes. I_L is limiting current density for oxygen reduction with the exception of OxAg electrode. E is the potential at the limiting current density for oxygen reduction. * limiting current density for AgO reduction.

Longer duration stability test of the E4A MnO_x electrode under galvanostatic discharge at −150 mA cm^{-2}, found the overpotential for oxygen reduction increased over the 72 hour period as shown in Figure 5.26. Beyond 10 hours the potential shifted from −0.30 V to −0.34 V *vs.* Hg/HgO, indicating a reduction in electrode performance. Visually carbon particles were seen in the electrolyte indicating evidence of corrosion of the catalyst support and the electrolyte was discoloured faintly black because of corrosion of the carbon. Carbon is slowly oxidised by the HO_2^- radical that is formed as an intermediate during oxygen reduction [13]. Also, as galvanostatic discharge proceeds, the electrolyte pH will increase due to the generation of OH^- ions, which will also accelerate corrosion [13].

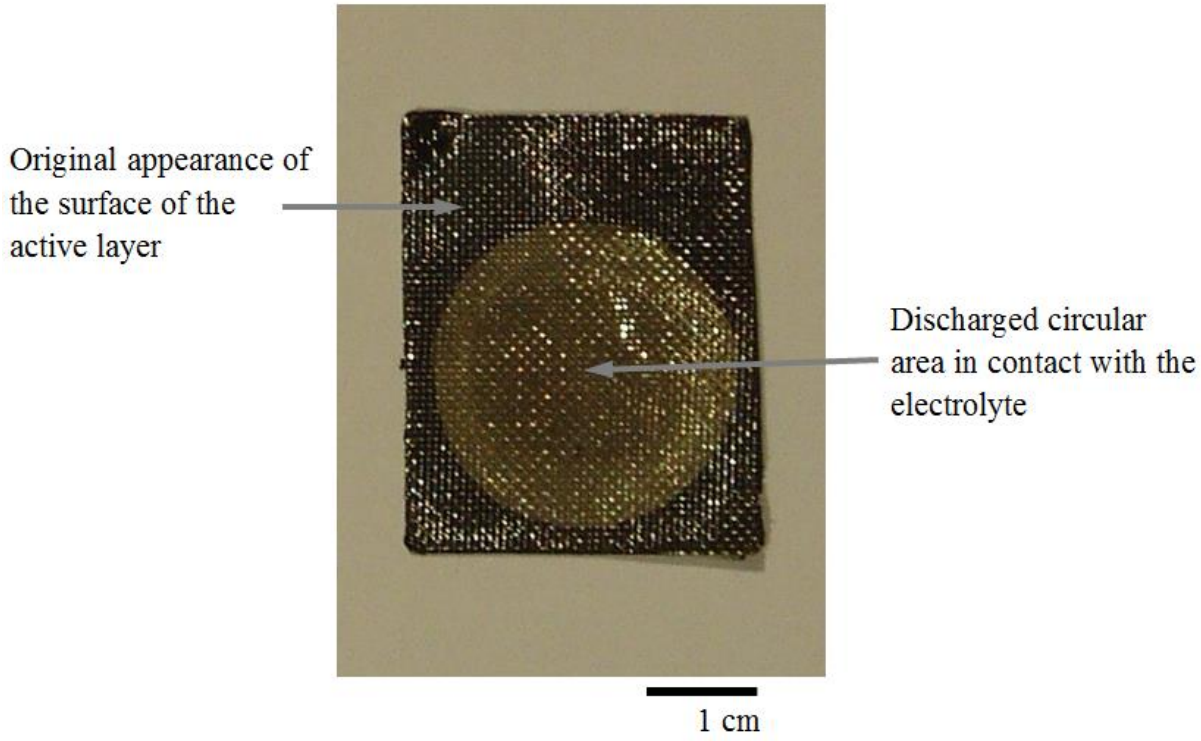

Figure 5.25: Photograph of discharged OxAg electrode. The light-grey circular area was the discharged area in contact with the electrolyte. The surrounding black area was untested parts of the electrode.

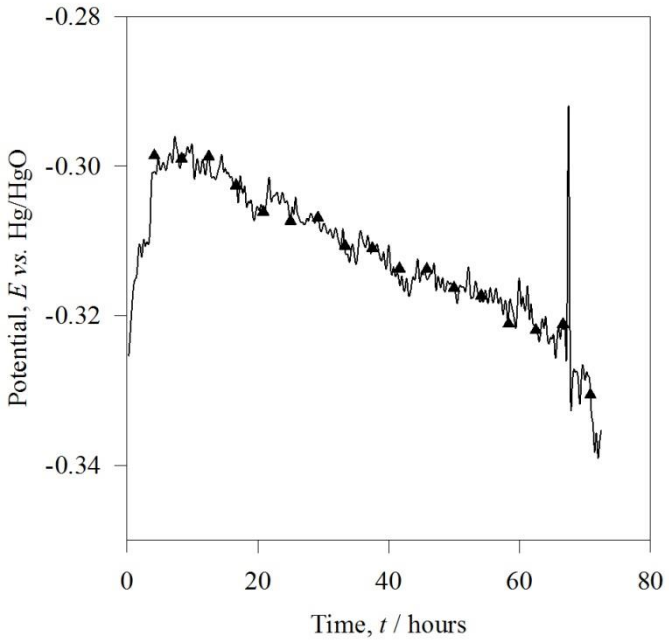

Figure 5.26: Stability of E4A gas diffusion electrode under galvanostatic discharge at −150 mA cm^{-2}. Electrolyte: 4 mol dm^{-3} NaOH at 22 °C. Electrode area: 3.46 cm^2. The rear face of the electrode was open to air at atmospheric pressure. ▲ E4A MnO_x

5.9 Summary of air cathode experiments

The platinum based electrodes were designed for use in a proton-exchange membrane fuel cell and so were designed without a metal mesh current collector, in the absence of which their performance as air-cathodes suffered. The 4 mg cm^{-2} Pt electrode had cracks on its surface meaning it may have been susceptible to electrolyte flooding.

Three manganese oxide air electrodes were studied, E4, E4A and MOC. Of the three, the MOC air-electrode had the most superior limiting current density for oxygen reduction of −220 mA cm^{-2} at −0.56 V *vs.* Hg/HgO. This was because of its higher catalyst loading compared to the other two, as found from scanning electron microscopy imaging.

The OxAg electrode behaved more like an AgO electrode than an oxygen reduction electrode. Its linear sweep showed the most positive onset potential for cathodic currents at 0.2 V *vs.* Hg/HgO owing to the reaction involving the reduction of AgO to Ag. This reaction reached a limiting current density of −265 mA cm^{-2} at −0.094 V *vs.* Hg/HgO. After which the current density reduced as the electrode proceeded to reduce oxygen at overpotentials far greater than those observed from the other electrodes studied. Although the reduction of AgO occurred at more positive potentials than the oxygen reduction reaction, its capacity was limited by the quantity of AgO present. Galvanostatic discharge experiments found that the capacity for the reduction of AgO to Ag was low, maintaining an average potential of −0.08 V *vs.* Hg/HgO for only 900 s.

The KTH electrode showed the most promising oxygen reduction behaviour with a limiting current density of −463 mA cm^{-2} at −0.49 V *vs.* Hg/HgO. The reason for its high activity for oxygen reduction was a high loading of perovskite catalysts which promote the direct four-electron oxygen reduction. This was a double layered electrode that had a separate active layer and a gas diffusion layer. The active layer had a high surface area to facilitate diffusion of electrolyte to the catalyst.

Chapter 6. Performance of the Al-air cell

6.1 Introduction

This chapter discusses the experimental work carried out on the development of the Al-air cell. These studies explored the use of a foam anode, different aluminium materials, the Al-air cell construction and a selection of the gas diffusion cathodes tested previously. Three prototype cells were investigated with each subsequent cell providing lessons for the next generation. Prototype 1 Al-air cell compared aluminium foams against flat plate anodes made from commercial aluminium and a super-pure aluminium alloy. Prototype 2 investigated what electrode area would be required from the light-weight aluminium-air cell to deliver reasonable power output at current densities upwards of 200 mA cm^{-2}. This cell incorporated a solution heat treated aluminium alloy, Al/Mg/Sn, that was alloyed with elements that lowered the self-corrosion compared to the previous alloy, Al/Mg/Sn/Ga. Prototype 2 used the platinum air electrodes as previously as well as a commercial Co-based air-electrode with superior electrode design. Finally Prototype 3 offered greater rigidity to the cell and was the final prototype tested. This cell was used to examine the advantage of the Al/Mg/Sn alloy over pure aluminium and how the cell behaviour changed with exothermic heating of the small volume electrolyte. Quantitative analysis was made based on measurement of reference potentials and cell temperature during variable load and galvanostatic discharge experiments. An air-electrode designed by a project collaborator was tested using Prototype 3 and compared against two of the commercial air-electrodes which used MnO_x and AgO catalysts.

6.2 Prototype 1

6.2.1 Investigation of anode structure

Electrodes in a battery should have a large electrode area to enable discharge at high currents, without compromising on the weight of the battery. One way to achieve this is through the use of a 3-dimensional structure such as an aluminium foam anode. Commercial foams of two different pore densities, 10 and 20 pores per linear inch (ppi) were investigated in the prototype 1 aluminium-air cell. The cell potential under controlled load while using the foams as anodes is shown in Figure 6.1. The cell potential with both foams was identical up until 50 mA cm^{-2}, at which time the 20 ppi foam in contact with the electrolyte lost its structural

integrity and disintegrated. This was because of the thinner struts of the 20 ppi foam (0.2 mm) compared to that of the 10 ppi foam (0.34 mm). Also, as the foams were made from an Al 6101 alloy with a minimum aluminium content of 97.7 %wt, their low purity contributed to the disintegration of the 20 ppi foam as evidenced by aggressive hydrogen evolution. Al 6101 is made up of 0.5 %wt iron and 0.1 %wt copper, both of which have low overpotentials for hydrogen evolution, aggravating the self-corrosion of the aluminium alloy via galvanic effects [49]. Examining the reference potentials from the prototype 1 cell with the 10 ppi foam shows that the 0.5 mg cm^{-2} Pt air-cathode dominated the cell response with a resistance of 0.15 Ω, compared to a value of 0.04 Ω for the anode, measured between 30 to 60 mA cm^{-2}. The anode also benefited from increased reactivity as the electrolyte heated due to the exothermic oxidation of aluminium and reduction of water to form hydrogen, with the temperature recorded as 62 °C at the end of the variable load experiment.

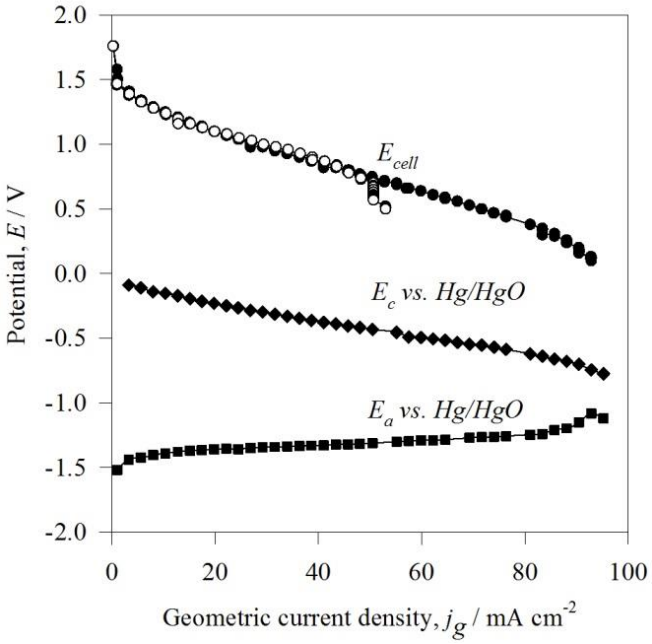

Figure 6.1: Behaviour of an Al 6101 foam anode in Prototype 1 Al-air cell. Electrolyte: 3 mol dm^{-3} NaOH initially at 22 °C. The electrolyte temperature increased due to Joule heating. Geometrical area of anode: 43 cm^2. The air cathode was a Pt/C GDE with 0.5 mg cm^{-2} platinum loading: ●, ◆, ■ 10 ppi Al 6101 foam, ○ 20 ppi Al 6101 foam. The electrodes were not solution heat treated before use.

Under galvanostatic discharge at 1 A, the cell containing 20 ppi or 10 ppi foam displayed a variable voltage over the duration of the discharge as shown in Figure 6.2. After 22 minutes, the 20 ppi foam lost its structural integrity, disintegrating as illustrated in Figure 6.3, and its cell voltage dropped from 0.67 V to 0.2 V. A compromise between maximising the anode

surface area while maintaining structural integrity is important. The thicker struts of the 10 ppi foam meant it continued to discharge for a further 38 minutes, with the cell voltage dramatically fluctuating between 0.6 V and 0.9 V. The fluctuating potential was due to intermittent loss and regaining of electrical contact as the struts of the foam dissolved and its active area began to disintegrate, as illustrated in Figure 6.3(b). The thinning of the struts of the Al 6101 foam could also explain the fluctuating discharge profile. This is illustrated by comparison with another 3-D anode made from Al/Mg/Sn/Ga which had much thicker struts of 1.5 mm and showed a more stable discharge profile as shown in Figure 6.2. The cell voltage with the Al/Mg/Sn/Ga 3-D anode was similar to that of an Al/Mg/Sn/Ga anode plate, which maintained a relatively constant average voltage of 1.04 V for at least 100 minutes. The charge efficiency, calculated from mass loss data, of the cell with the Al/Mg/Sn/Ga was 65 %, higher than that with the 10 ppi Al 6101 foam at 20 %.

The disintegration of the Al/Mg/Sn/Ga plate around its large grains, which were visible to the unassisted eye, accounted for this increase in anode overpotential. The disintegration of the active area of the 0.6 mm thick plate indicated it suffered aggressive corrosion which was targeted along the grain boundaries [49].

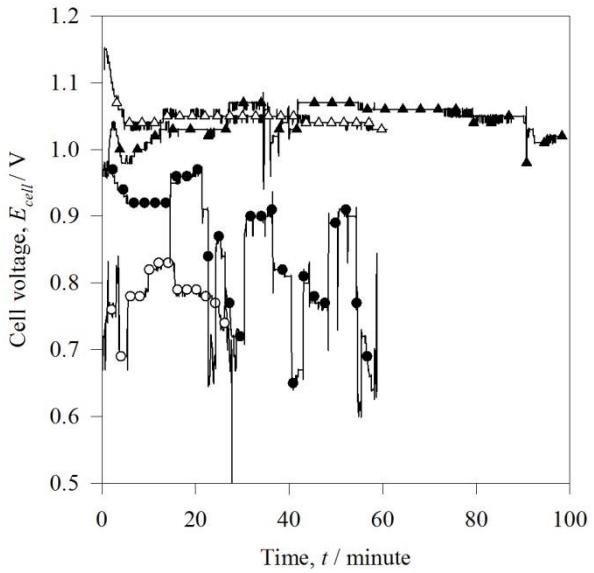

Figure 6.2: Cell voltage *vs.* time for the prototype 1 aluminium-air cell employing four different types of aluminium anode: ○ Al 6101 20 ppi foam, ● Al 6101 10 ppi foam, ▲ Al/Mg/Sn/Ga plate, △ Al/Mg/Sn/Ga perforated plate. Electrolyte: 50 cm^3 of 3 mol dm^{-3} NaOH. Discharge current: 1 A. The air cathode was a Pt/C GDE with a 0.5 mg cm^{-2} platinum loading. Samples were not solution heat treated.

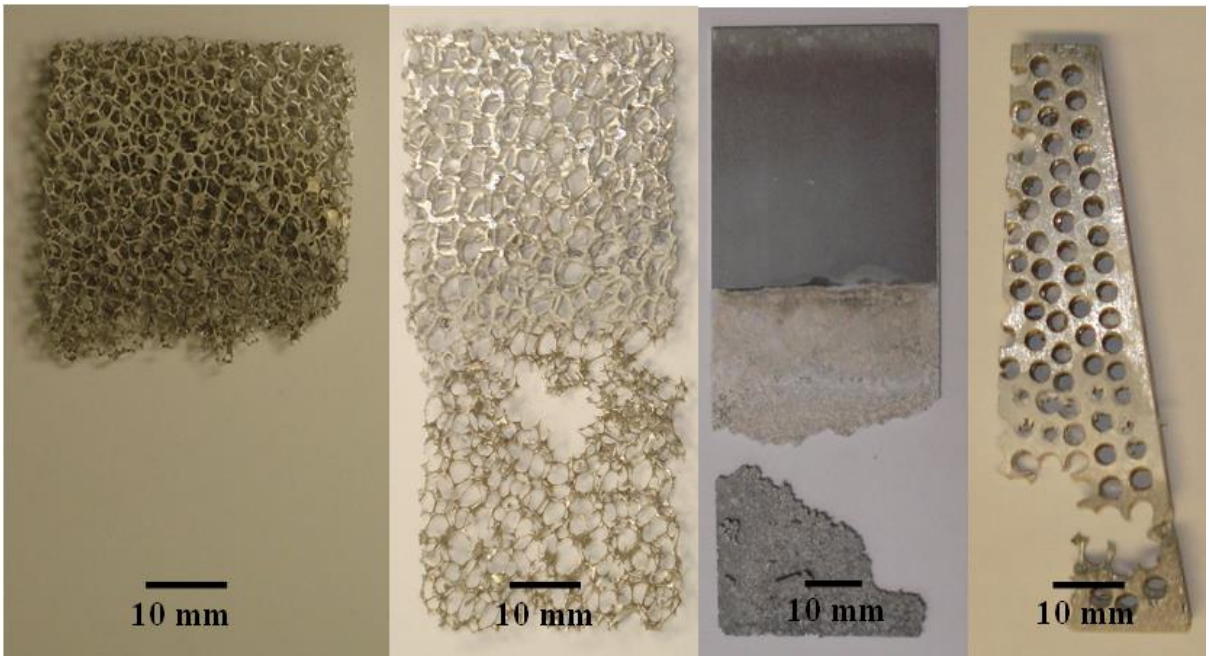

(a) (b) (c) (d)

Figure 6.3: Photographs of (a) Al 6101 20 ppi foam, (b) Al 6101 10 ppi foam, (c) Al/Mg/Sn/Ga plate, (d) Al/Mg/Sn/Ga perforated plate, after constant current discharge at 1 A in the prototype 1 aluminium-air cell. Electrolyte: 50 cm^3 of 3 mol dm^{-3} NaOH. The air cathode was a Pt/C GDE with 0.5 mg cm^{-2} platinum loading.

Measurement of the electrode potentials during the experiment with the 10 ppi foam indicated a difference between the measured cell potential and that calculated from the difference in cathode and anode potentials as indicated in Figure 6.4. This is attributable to the large inter-electrode gap, 1.6 cm, of prototype 1 with a theoretical resistance of 0.27 Ω, given a conductivity of 0.39 S cm^{-1} across an area of 5 × 3 cm. The cathode reference potential unfavourably shifted negatively from −0.251 V *vs.* Hg/HgO at the start of the experiment to −0.29 V *vs.* Hg/HgO at the end. The build up of reaction product on its surface could account for this. There was an unfavourable positive shift in the 10 ppi foam anode potential from an average value of −1.32 V *vs.* Hg/HgO to –1.30 V *vs.* Hg/HgO compared with the start and end of the experiment.

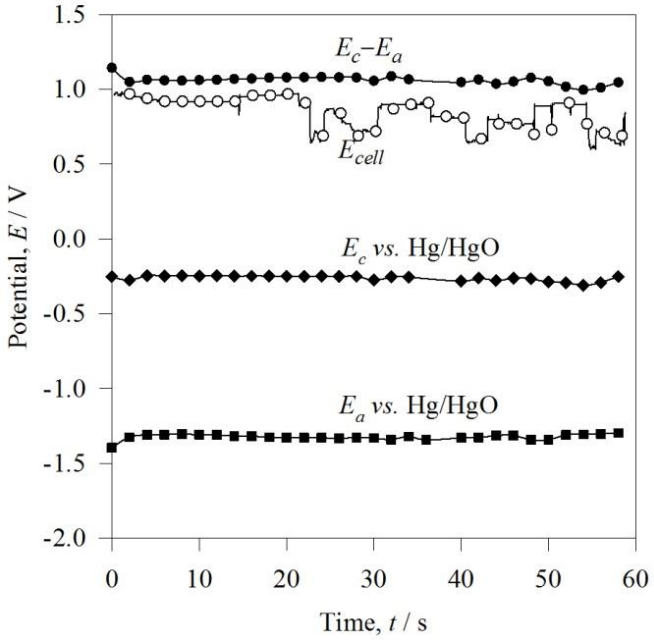

Figure 6.4: Measurement of electrode potentials during galvanostatic discharge of the prototype 1 aluminium-air cell using an Al 6101 10 ppi foam anode discharged at 1 A. Electrolyte: 50 cm^3 of 3 mol dm^{-3} NaOH. Air cathode: 0.5 mg cm^{-2} Pt/C GDE. The anode was not heat treated.

6.2.2 Effect of electrolyte concentration

The effect of electrolyte concentration on the performance of the prototype 1 aluminium-air cell was investigated. Load tests were carried out on the Al/Mg/Sn/Ga plate using 3 and 8 mol dm^{-3} NaOH. The air cathode was a fresh 0.5 mg cm^{-2} Pt/C GDE in each experiment. The active area of the anode was 35 cm^2 in 3 mol dm^{-3} NaOH and 38 cm^2 in 8 mol dm^{-3} NaOH, initially at 22 °C. The same electrolyte volume was used between the tests of 70 cm^3. The anode area was larger in the test with 8 mol dm^{-3} NaOH than in the 3 mol dm^{-3} one because the reference electrode was placed inside the cell in the 8 mol dm^{-3} NaOH test, raising the height of the electrolyte in contact with the anode. The reference electrode was absent from the cell for the 3 mol dm^{-3} NaOH test. The area of the cathodes was smaller than those of the anodes: 20 cm^2 in 3 mol dm^{-3} NaOH and 22 cm^2 in 8 mol dm^{-3} NaOH. The results shown in Figure 6.5(a) and Figure 6.5(b) indicate that the performance in the prototype 1 Al-air cell was the same when using either 8 mol dm^{-3} NaOH or 3 mol dm^{-3} NaOH since the conductivity of NaOH is at a maximum at a concentration of 4 mol dm^{-3} [79].

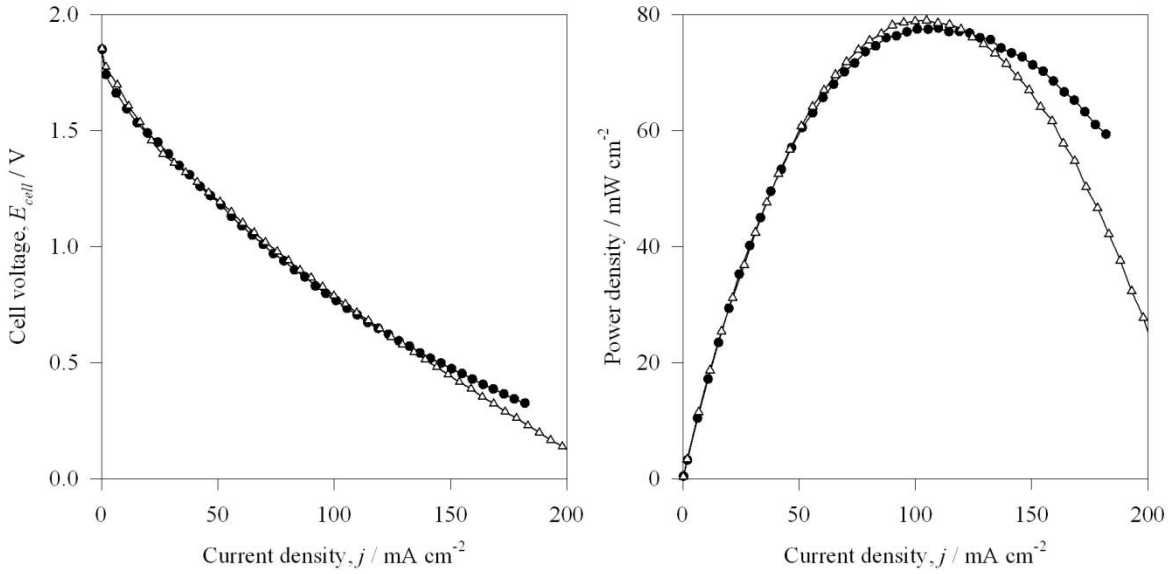

(a) (b)

Figure 6.5: Effect of electrolyte concentration on the prototype 1 Al-air cell performance. △ 3 mol dm^{-3} NaOH, ● 8 mol dm^{-3} NaOH. (a) Cell voltage *vs.* current density and (b) Power density *vs.* current density. Current and power densities were calculated per unit geometrical area of cathode. The air cathode used was a Pt/C GDE with 0.5 mg cm^{-2} Pt loading. Electrolyte volume of 70 cm^3. Aluminium anodes were not solution heat treated before use.

6.3 Prototype 2

Several valuable lessons were learned from the prototype 1 aluminium-air cell, which were used in the development of the prototype 2 cell. The first of these was the need to scale down the cell size to reduce its weight and volume to a more lightweight design. On the air-cathode side, the prototype 1 experiments highlighted the need to examine different air-cathodes with improved design with better current collection and cheaper electrocatalysts that would negate any catalyst loading constraints.

6.3.1 Determining the active area required to deliver reasonable power

The design of the prototype 2 aluminium-air cell involved investigating how small the electrode areas could be while still being able to withdraw high current from the cell at reasonable cell voltages. Two of the prototype 2 cells were evaluated. In one cell, the anode area was 22 cm^2; in the other, the anode area was 11 cm^2 (the areas of the cathodes were 20 and 10 cm^2, respectively). Green polyester tape from Cole Parmer were applied over the anode and cathode in the cell with the smaller electrode areas so as restrict the active area

available to the electrolyte. Comparing the cell polarisation curves in Figure 6.6 indicates that the cell with the smaller anode area had a narrow current operating range up to 2.1 A. It delivered a maximum power of 0.7 W at 1.1 A. This cell voltage-current curve is almost entirely resistive, with a resistance of 0.5 Ω measured between 1.0 and 1.5 A. Previous tests on the prototype 1 cell, where the reference potentials were measured, showed that the resistive response of the air-cathode dominated the cell response, see Figure 6.1. In the case of the prototype 2, in the test with the smaller cathode area of 10 cm^2, the dominant effect of the air-cathode would have been amplified, resulting in the observed resistive response. In comparison, the cell with an anode area of 22 cm^2 showed a more characteristic S-shaped voltage-current behaviour, with activation, resistive and mass transport controlled regions all evident. Its cell resistance was lower at 0.14 Ω, measured between 2.0 and 4.0 A. This cell delivered a reasonable maximum power output of 3 W at a current of 3.9 A and a cell voltage of 0.75 V. This anode area of 22 cm^2 was chosen for subsequent aluminium-air cell tests.

The inter-electrode gap of the prototype 2 cell was 5 mm. A smaller inter-electrode gap of 2 mm was evaluated but was found to be too small to accommodate the large hydrogen bubbles which formed during the first few minutes when the aluminium was exposed to the electrolyte. The bubbles reached the top of the cell resulting in loss of electrolyte. This would be worse when using either the Al/Mg/Sn or Al/Mg/Sn/Ga alloy because of their propensity to show a transient high hydrogen evolution rate upon initial immersion in the electrolyte.

Figure 6.6(b) shows that when the power and current for both cells are normalised with respect to electrode area, the performance of the cell with the smaller electrode area does not scale to match up with that of the cell with the larger electrode area. This suggests that the current density was unevenly distributed across the surface of air-cathodes and the aluminium anodes and was unique to each cell, depending strongly on the area employed. This could be caused by non-uniform distribution of catalyst within the air-cathode. Also, the oxygen reduction reaction occurs only at a site where an electrocatalyst is present at a 3−phase boundary i.e. an electrocatalyst in contact with both oxygen and electrolyte reactants. In the case of the aluminium, current may be concentrated at pits particularly in the case of aluminium alloys.

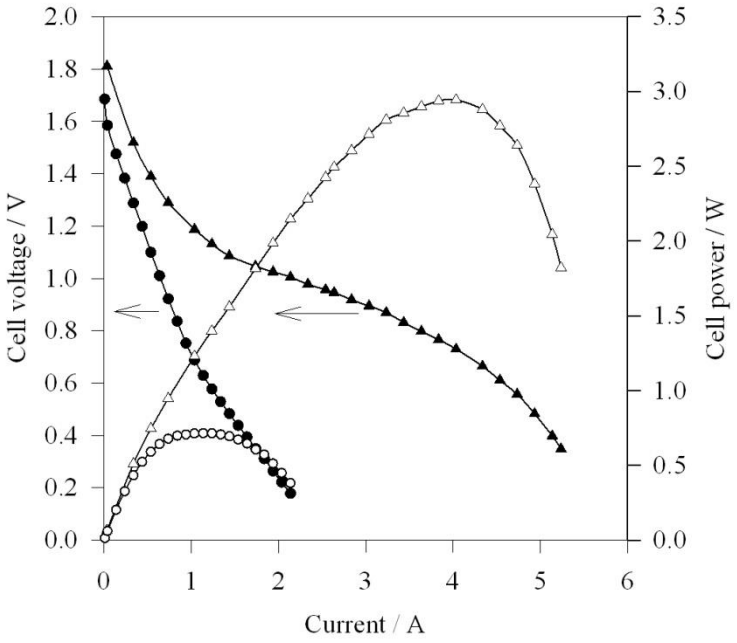

(a)

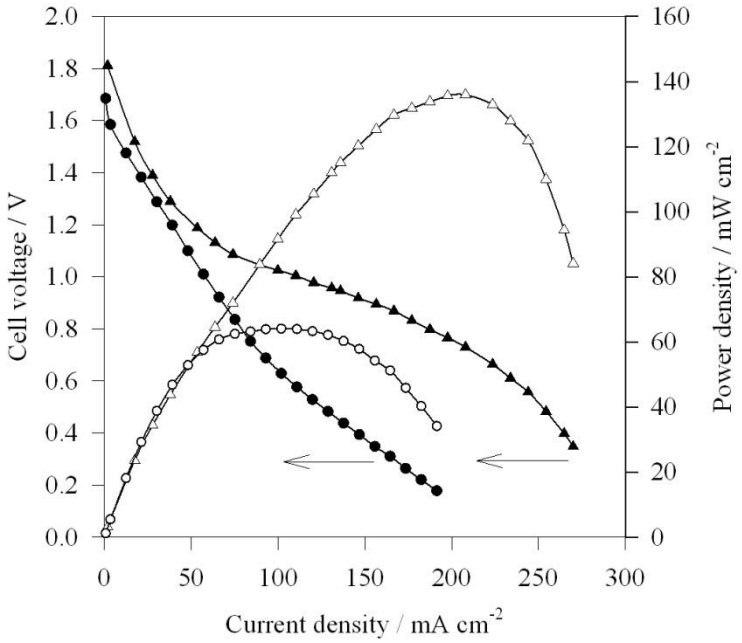

(b)

Figure 6.6: Determining the area required for a prototype 2 cell. (a) Cell voltage and power versus current. (b) Cell voltage and power density versus current density. ▲ & △ active area of 22 cm^2, ● & ○ active area of 11 cm^2. 99.999 %wt aluminium anode and E5 Co-catalysed commercial gas diffusion electrode. Electrolyte: 4 mol dm^{-3} NaOH initially at 22 °C.

6.3.2 Effect of anode to cathode area ratio on cell performance

Employing 3-D electrodes in a battery is advantageous as it increases the surface area of the electrode per unit mass, alloying for higher currents to be attained. Optimal foam thickness is an issue to consider when using a 3-D electrode because the voltage drop becomes bigger proportionally with thickness due to increasing inter-electrode gap and mass transport limitations in the electrolyte [241]. Other issues to consider when selecting an appropriate 3−D electrode include cost, availability, ease of scale up, ease of current connections and IR within the solid phase. While considering the development of an aluminium foam anode, an experiment was conducted to examine if there was an advantage in having an aluminium electrode with an active area much larger than that of the gas diffusion electrode.

An Al-air cell was tested, based on the design of prototype 2, where the projected area of the aluminium anode was four times the area of the gas diffusion cathode. Application of green polyester tape to the air-cathode restricted its active area in contact with the electrolyte so that its active area was four times smaller than that of the anode. The cell performance is compared with that of a cell where the ratio of projected anode to cathode area was unity, see Figure 6.7. The results indicate that having an aluminium electrode with a larger projected area that the GDE was advantageous in the kinetic and mass transfer controlled regions. The cell with the larger aluminium anode observed more of a resistive response suggesting the air-cathode was dominating the cell response. This differs to the typical S-shaped curve observed for the cell with the anode:cathode area of 1:1 ratio. The cell with the anode:cathode area of 4:1 showed higher cell voltages over the current ranges of 0.2 to 2.5 A and 3.8 to 6.0 A. It observed an ohmic response up until a current of 6.0 A, with no mass transport control evident. This had the advantage of shifting the peak power point from 3.0 W at 3.9 A to 3.2 W at 6.0 A.

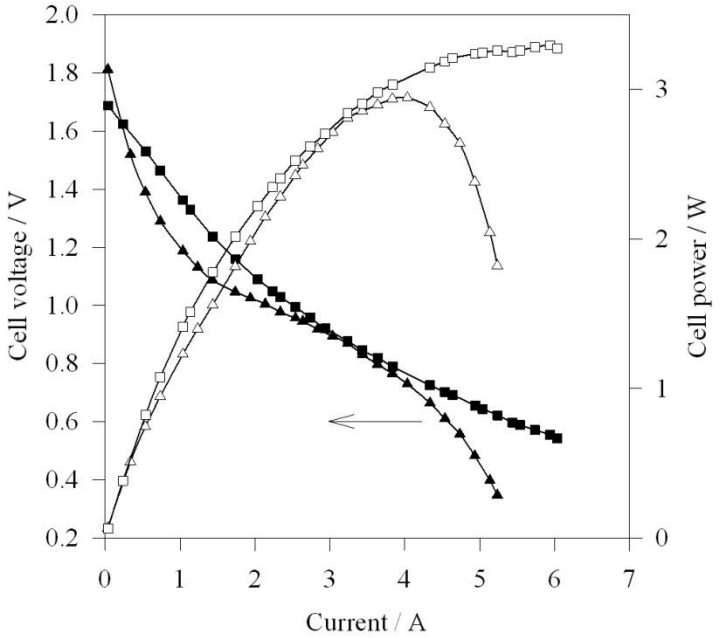

Figure 6.7: Effect of ratio of anode to cathode area on the performance of the prototype 2 Al-air cell. □ & ■ anode:cathode area of 4:1. △ & ▲ anode:cathode area of 1:1. Electrolyte: 4 mol dm^{-3} NaOH, initially at 22 °C. 99.999 %wt aluminium anode and commercial E5 GDE air cathode.

6.3.3 Effect of gas diffusion electrode design

Another limitation was the absence of a metal mesh current collector in the design of the Pt gas diffusion electrode. This platinum gas diffusion electrode is intended for use in O_2/H_2 fuel cell stack assemblies where sufficient electrical contact is made via compression against a metal or carbon current collector. An illustration of the benefit of improving the current collection from the air-cathode can be seen in Figure 6.8. This compares two of the prototype 2 cells, each with different means of collecting current from the air-cathodes: one with a copper wire, 0.63 mm diameter, woven through the carbon felt of the cathode and silver paint applied over it and the other cell without copper wire and current collection made via a single crocodile clip. The addition of the copper wire lowered the cell resistance from 0.6 Ω to 0.36 Ω, delivering higher cell voltages at a given current. The cell voltage improved in the resistive and mass transfer controlled regions, increasing the maximum operating current density from 84 to 167 mA cm^{-2}. The performance of the air-cathode was further improved by increasing the catalyst loading from 0.5 to 4.0 mg cm^{-2}, as illustrated in Figure 6.8. The higher platinum loading yielded higher power and cell voltages at a given current density compared to the cell using the lower platinum loading in Figure 6.8(a) and Figure 6.8(b). The

cell resistance was lower when employing the GDE with the higher platinum loading, 0.3 Ω compared to 0.36 Ω.

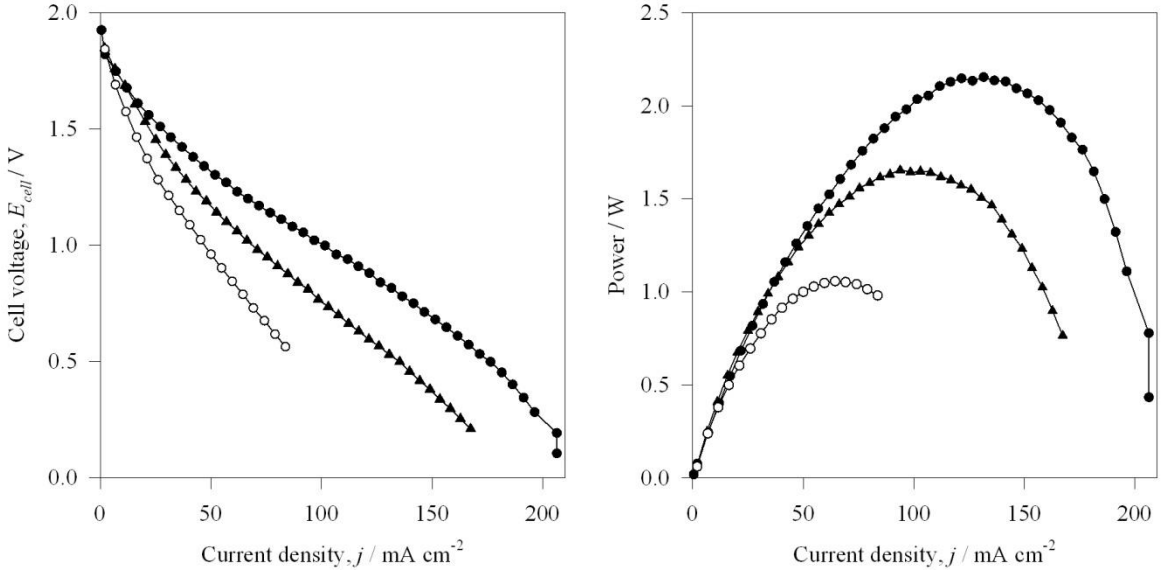

(a) (b)

Figure 6.8: Effect of air-cathode current collection and platinum loading on cell performance. (a) Cell voltage and (b) Power density *vs.* current density for the prototype 2 Al-air cell employing three different air-cathodes: ○ 0.5 mg cm^{-2} Pt, no copper wire, ▲ 0.5 mg cm^{-2} Pt, with copper wire, ● 4.0 mg cm^{-2} Pt, with copper wire. Current densities relative to area of the air-cathode of 20 cm^2. Anode area of 21.5 cm^2. The cells were tested using an Al/Mg/Sn/Ga plate anode immersed in 10 cm^3 of 3 mol dm^{-3} NaOH, initially at 20 °C. The alloy was not solution heat treated before these studies.

6.3.4 Load tests on an Al-air battery

A load experiment was carried out on an aluminium-air battery made up of five of the prototype 2 cells connected in series. It delivered a maximum power of 14 W at 3.1 A as shown in Figure 6.9(a). Dividing the maximum power by five indicates a 2.8 W contribution from each cell within the battery. This differs from the maximum power recorded from the individual cell test, 1.6 W, the result of which is shown above in Figure 6.8(b). The reason for this discrepancy was that during the individual cell test the air electrode was electrically grounded, in error, resulting in leakage current. The resistance of the battery, 1.0 Ω or 0.2 Ω per cell was lower than the resistance calculated from the individual cell test, 0.36 Ω. This issue is discussed in more detail in Section 6.4.1.

In another test on the Al-air battery, measurement of the individual cell potentials found there was differential loading on the individual cells. The results in Figure 6.10 show that at a given load current the potential of cell 5 was lower than it was for cell 1. The difference in cell potentials may have been due to differences in the extent of corrosion of the anode in each cell. Examination of the anodes at the end of the variable load test in Figure 6.11 shows that the anode in cell 5 underwent greater dissolution/corrosion than the anode in cell 1. The anode in cell 1 formed the battery negative terminal while cathode in cell 5 was the positive one. The anode in cell 5 encountered some disintegration of its structure compared to the other anodes and consequently its active area became smaller than that of the others. A smaller active area could explain why the potential of cell 5 was lower at a given current compared to the potentials of the other cells in the battery. Since these anodes had not been solution heat treated prior to testing the presence of precipitates in their microstructures would have aggravated their self-corrosion by providing local galvanic microcells [49].

At the end of the variable load test, the electrolyte in each cell was grey with white globules in suspension. These white globules were crystallised aluminium hydroxide, which deposited on the air cathodes reducing their active area. The variable load test shown in Figure 6.9 was conducted for 44 minutes during which time the total electrolyte volume in the battery had reduced from 50 to 30 cm^3. The aggressive reactivity of the Al/Mg/Sn/Ga alloy accounts for this electrolyte loss due to water evaporation and reduction of water on the aluminium surface to form hydrogen. Use of an alloy less prone to corrode would experience a slower rate of electrolyte loss. This was a limitation of this battery design that was addressed in the prototype discussed later. The battery, with 5 cells connected in series, powered a small 7.2 V motor/propeller assembly of adjustable resistance, as shown in Figure 6.12, drawing a maximum current of 0.5 A.

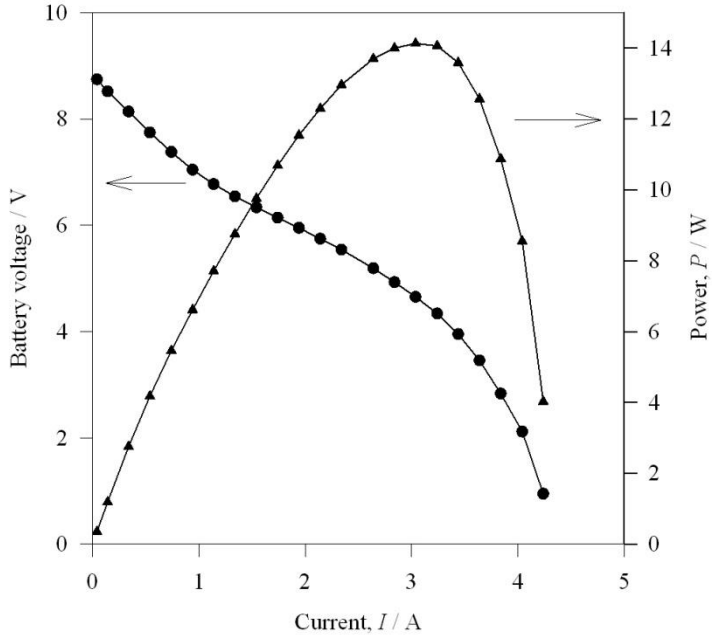

(a)

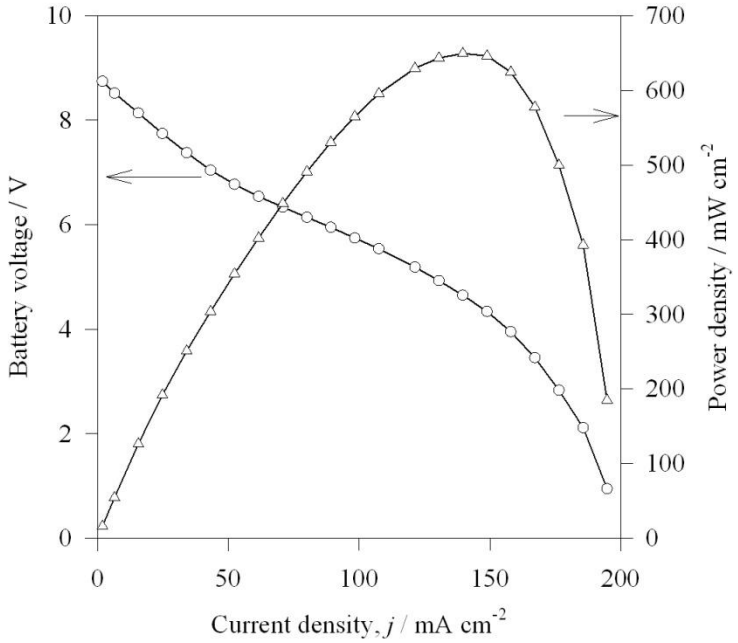

(b)

Figure 6.9: Variable load test on aluminium-air battery consisting of 5 of the prototype 2 Al-air cells connected in series. (a) Battery voltage and power *vs.* current (b) Battery voltage and power density *vs.* current density. Alloy, Al/Mg/Sn/Ga plate (22 cm^2), not heat treated. 0.5 mg cm^{-2} Pt/C GDE. 50 cm^3 of 3 mol dm^{-3} NaOH solution, initially at 22 °C. Current and power densities were calculated per unit projected area of the cathode.

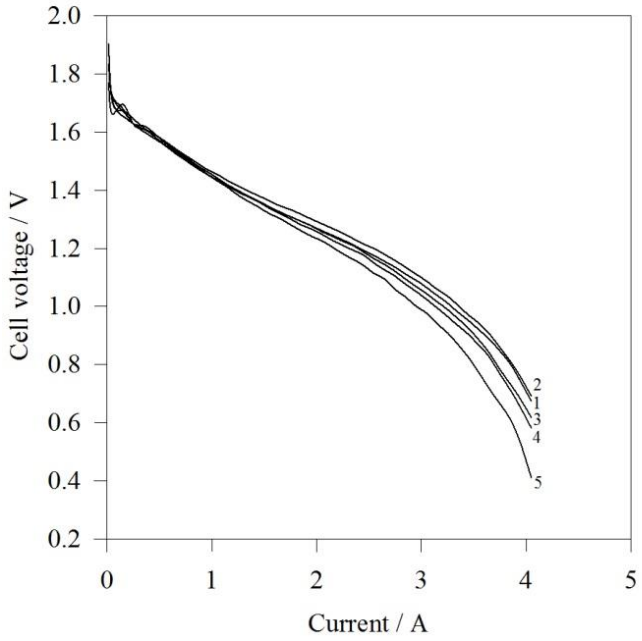

Figure 6.10: Variation of cell voltage with current for each of the five cells connected in series to form the light-weight aluminium-air battery shown in Figure 6.12(a). The cells were tested with an Al/Mg/Sn/Ga plate anode and a gas diffusion electrode with 0.5 mg cm^{-2} platinum loading. The electrolyte was 3 mol dm^{-3} NaOH, initially at 22 °C. The anode of cell 1 formed the battery negative terminal, while the cathode of cell 5 formed the battery positive terminal. The aluminium anodes were not solution heat treated before use.

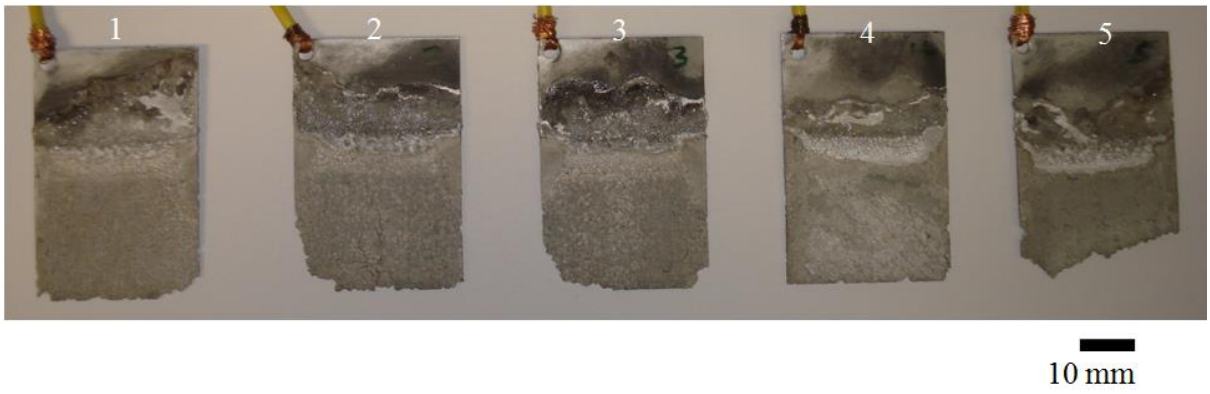

Figure 6.11: The five Al/Mg/Sn/Ga anodes after performing a load test on the Al-air battery. Original dimensions: 50 × 30 × 1 mm. The battery consisted of 5 cells in series, each cell containing 10 cm^3 of 3 mol dm^{-3} NaOH, initially at 22 °C. In each cell the cathode was a 0.5 mg cm^{-2} loaded Pt/C GDE. The active area of each anode was 22 cm^2. The anodes pictured above belong to cells 1 through 5 from left to right. Anode in cell 1 formed the negative terminal of the battery while cathode in cell 5 formed the positive terminal. The aluminium anodes were not solution heat treated.

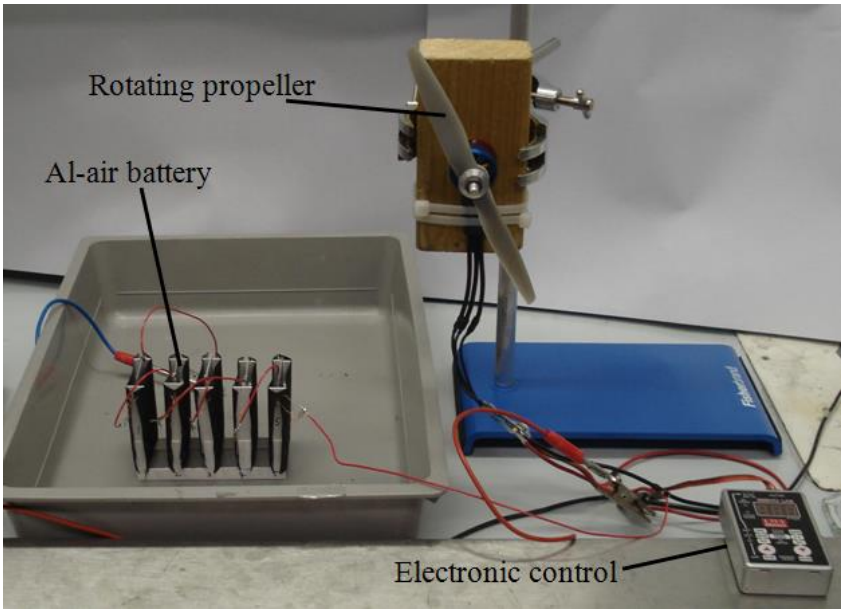

Figure 6.12: 5 cell aluminium-air battery driving the motor, delivering 0.5 A (24 mA cm^{-2}) at 7.7 V. Each cell is made from a U-shaped PVC body, with an air cathode glued to the front and back faces and a flat plate Al anode in the centre. Wet mass 109 g. The motor was driving a ca. 180 mm diameter 2-blade, propeller at adjustable speed.

6.4 Prototype 3

The experience gained from the prototype 1 and 2 experiments led towards an improved Al-air cell design, prototype 3. The experiments on prototype 3, discussed in subsequent sections, involved utilising a more corrosion resistant aluminium anode and air-electrodes with enhanced electrical conductivity and non-noble catalysts.

6.4.1 Importance of cell insulation

Prototype 3 Al-air cell, as in the previous two cell designs, incorporated two electrically connected air-electrodes, which formed the two external faces of the cell with the aluminium anode sitting in between them. When the Al-air cell was held in a clamp for testing it was important that an insulator was placed between the clamp and the outward face of each air electrode, as illustrated in Figure 6.13 and will be referred to as an insulated cell. Otherwise the performance of the cell was drastically different if there was electrical contact between the clamp and the outward face of the air-electrodes, referred to as a grounded cell. This was particularly the case for the KTH electrode, as shown in Figure 6.14(a), which had its metal mesh conductor on its outward face. There was a marked difference between the behaviour of

an insulated cell and a grounded cell in Figure 6.14(a) when the air-electrode was the KTH type. The insulated cell had a lower cell resistance, 0.1 Ω measured between 60 and 170 mA cm^{-2}, compared to the grounded cell. Examination of the electrode potentials indicated that the greater resistance of the grounded cell was because of the higher resistance of the air-cathode when it made electrical contact with the clamp, 0.12 Ω measured between 75 and 150 mA cm^{-2}, compared to 0.076 Ω when the cell was insulated from its surroundings.

This issue was only of a concern when the outward face of the air-cathode was electrically conductive. For example in comparison to the KTH electrode, the outward face of the E4A air cathode was an electrically insulating PTFE layer: the conductive metal mesh current collector of this electrode was on its inward face. Therefore, there was no degradation in cell performance when the cell body was grounded by making contact with the rear of the E4A air cathode, as shown in Figure 6.14(b). The electrical grounding could have meant that the electrons from the oxidation of aluminium were parasitically consumed in another reduction reaction instead of for the intended oxygen reduction reaction.

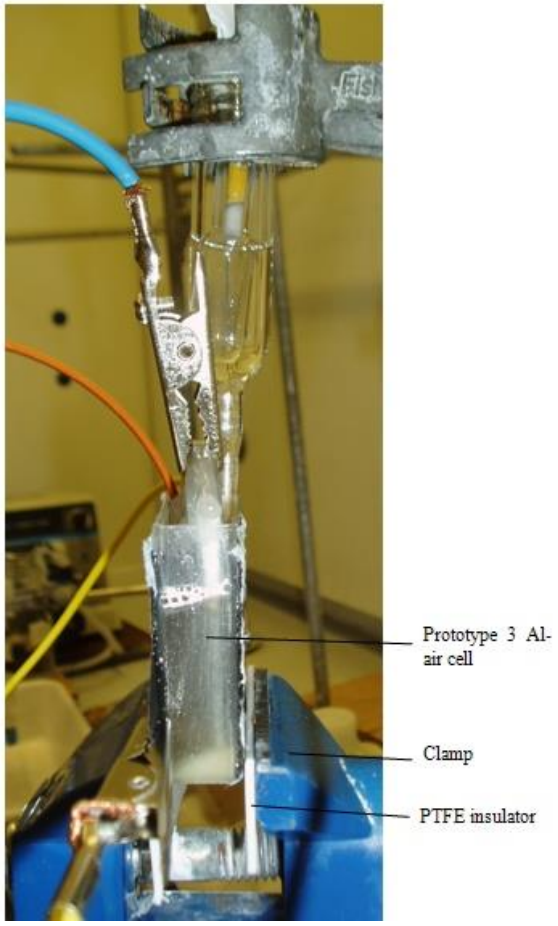

Figure 6.13: Side view of prototype 3 Al-air cell held between PTFE insulators in the clamp.

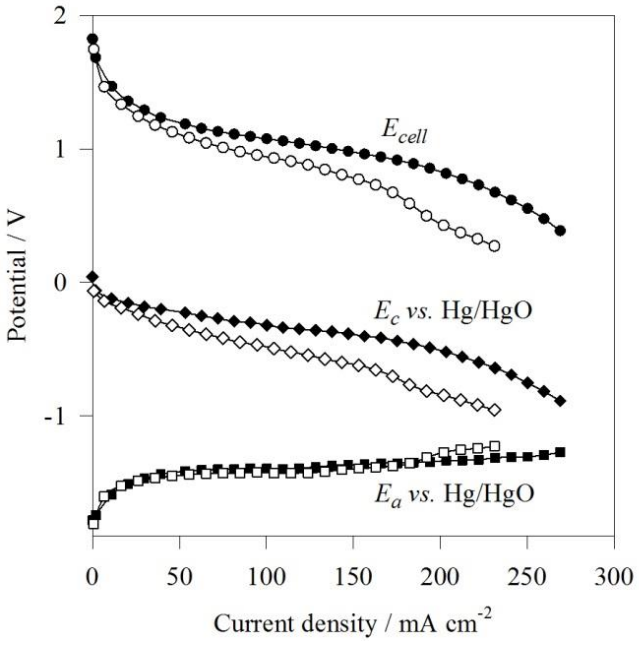

(a)

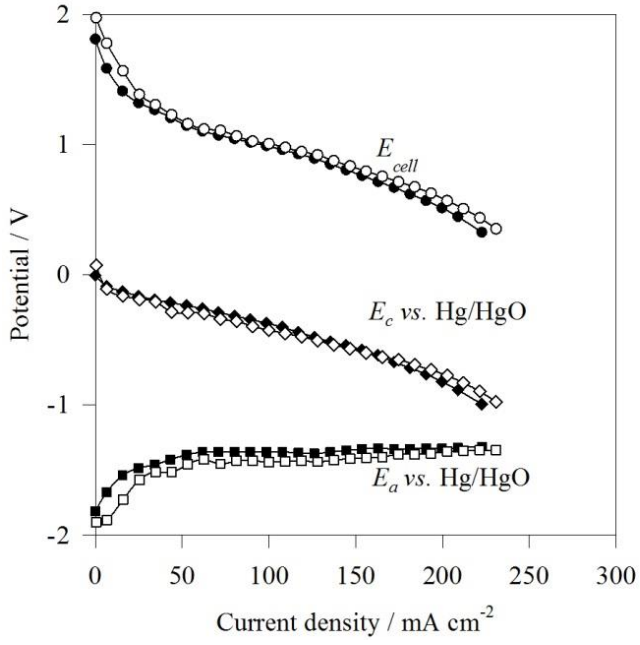

(b)

Figure 6.14: Importance of insulating the Al-air cell to isolate it from its surroundings. ●, ◆, ■ insulated cell. ○, ◇, □ grounded cell. (a) Al-air cell with the KTH cathode (b) Al-air cell with the E4A cathode. Anode: Al/Mg/Sn. Electrolyte: 4 mol dm^{-3} NaOH, initially at 22 °C. Cathode area: 14.4 cm^2. Current density relative to an anode area of 20 cm^2.

6.4.2 The importance of aluminium alloy material

Experiments discussed earlier using the 3-electrode cell to measure the hydrogen evolution and oxidation characteristics of the Al/Mg/Sn alloy showed it to observe lower corrosion rates and higher oxidation rates compared to 99.999 % aluminium. Experiments were then conducted in the prototype 3 aluminium-air cell to see how those advantages were beneficial to cell performance. The open-circuit cell potential versus time, in Figure 6.15, of the cell with Al/Mg/Sn showed a transient behaviour similar to that observed during the half-cell studies (Figure 4.16). After 80 s the open-circuit cell potential rose from 1.71 V to 2.07 V, which is 630 mV less than the theoretical potential for an Al-air cell. This is because tin hydrides on the surface of the Al/Mg/Sn alloy created an almost film-free surface, as discussed in Chapter 4 [49]. During this transient high potential over the initial 600 s at open-circuit, large volumes of hydrogen evolved from the surface of the Al/Mg/Sn anode and the discharge products clouded the electrolyte. These discharge products could block the pores of the air-cathode. In a working cell it is recommended to allow the Al/Mg/Sn electrode to go through this transient period before being placed into the cell. This transient period was completely different to that observed for the cell using 99.999 % Al. Upon immersion, the potential of 99.999 %wt Al was −1.76 V *vs.* Hg/HgO, before it stabilised at −1.64 V *vs.* Hg/HgO after passivation by a hydroxide layer.

The cell voltage and power *vs.* current density curves for the Al-air cell using Al/Mg/Sn are shown in Figure 6.16(a), along with data for pure aluminium as a comparison. The open-circuit cell voltage was higher with Al/Mg/Sn, 1.8 V, than with pure aluminium, 1.69 V. Over the activation-polarisation region between 0 and 70 mA cm^{-2}, the cell voltage with pure aluminium observed a 0.73 V drop, of which 0.40 V or 56 % was due to the activation polarisation of the anode, calculated from the measurement of anode potential. Similarly, 56 % of the potential drop over the activation region for the cell with Al/Mg/Sn was attributed to the alloy.

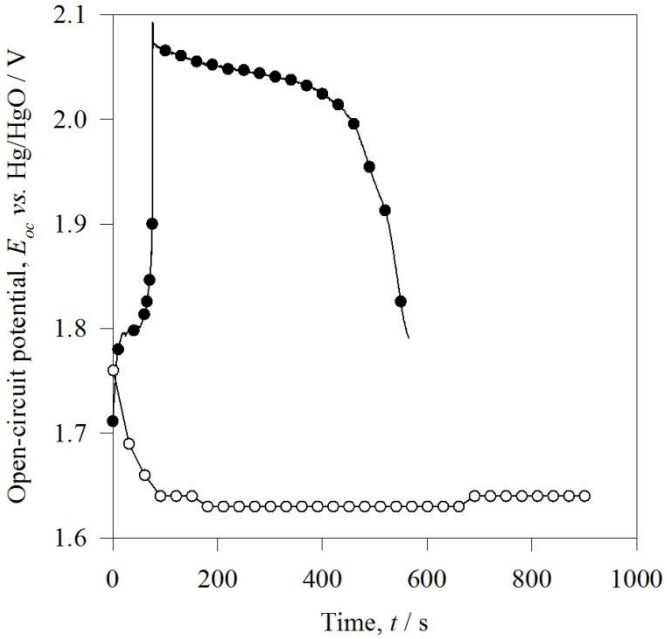

Figure 6.15: Transient behaviour of the open-circuit cell potential of the prototype 3 Al-air cell. ● Al/Mg/Sn, ○ 99.999 % Al. Air cathode: E5 Co-catalyst. 15 cm^3 of 4 mol dm^{-3} NaOH electrolyte, initially at 22 °C. Interelectrode gap: 5 mm.

Beyond 70 mA cm^{-2}, the cell with the Al/Mg/Sn alloy exhibited an ohmic response with a resistance of 0.098 Ω, measured between 60 and 170 mA cm^{-2}. In contrast, the cell with pure aluminium displayed a steady cell voltage of 0.96 V up until 170 mA cm^{-2}, owing to the variable potential of the pure aluminium anode counteracting the ohmic response of the air-cathode. Until a current density of 145 mA cm^{-2}, the cell with the Al/Mg/Sn alloy inferred a marginal advantage over the cell with pure aluminium, when the electrolyte temperature was still below 45 °C. As the KTH air-cathodes were the same in both cells, the difference was due to the behaviour of the different anodes and the cell temperature. A magnified view of the anode reference potentials is shown in Figure 6.16(b). Compared to the Al/Mg/Sn alloy, pure aluminium observed a lower potential between open-circuit and 145 mA cm^{-2}, reaching its most positive value of −1.24 V *vs.* Hg/HgO at 70 mA cm^{-2}, after which it began to shift towards negative values. The negative shift in potential of pure aluminium beyond 70 mA cm^{-2} follows a change in the temperature gradient to its peak rate of 3.0 °C per 10 mA cm^{-2}, suggesting the elevated temperature enhanced the anode activity. By 145 mA cm^{-2} the potential of pure aluminium favourably matched the potential of the alloy of −1.36 V *vs.* Hg/HgO.

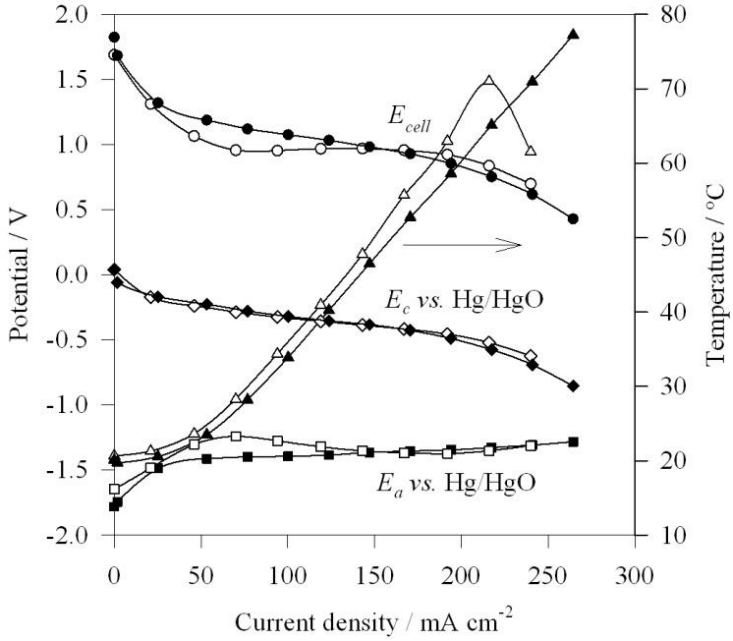

(a)

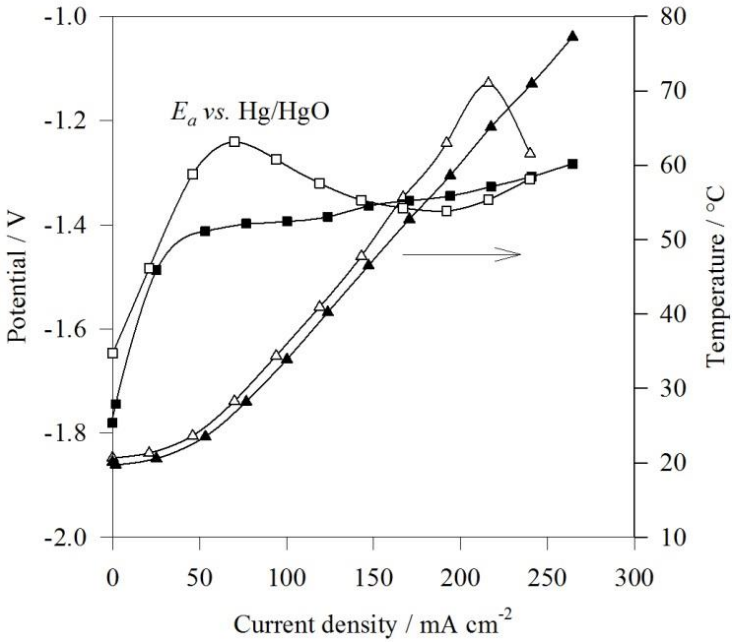

(b)

Figure 6.16: Effect of aluminium alloy on the performance of the Al-air cell. (a) Potential and cell temperature versus current density, (b) Magnified view of anode potential and cell temperature versus current density. ●, ◆, ■, ▲ cell with Al/Mg/Sn. ○, ◇, □, △ cell with 99.999 % Al. Current density relative to anode area, 22 cm^2. Cathode area: 15 cm^2. KTH air-electrode. Electrolyte: 15 cm^3 of 4 mol dm^{-3} NaOH initially at 22 °C. 5 mm interelectrode gap.

Comparison of the anode potentials in the prototype cell in Figure 6.16(b) and how they are influenced by temperature suggests that, at current densities below 145 mA cm^{-2}, the Al/Mg/Sn alloy gains an advantage over pure aluminium at low electrolyte temperatures. Support for this observation can be found from the linear sweep experiments conducted on Al/Mg/Sn and 99.999 % Al at 60 °C in the three-electrode glass cell. Below 250 mA cm^{-2}, which is the upper current density limit tested in the prototype cell tests, the linear sweep experiments showed that the difference in electrode potential between the alloy and pure aluminium was smaller than it was at current densities above 250 mA cm^{-2}. The electrode potentials from the Al-air cell were not in complete agreement with the three-electrode cell experiments because a smaller electrolyte volume used in the Al-air prototype (15 cm^3 compared to 80 cm^3), allowed the reaction product to have a greater influence on the anode potential in the prototype Al-air cell [21].

The maximum cell power with the KTH air-electrode and an Al/Mg/Sn anode was 174 mW cm^{-2} at a current density of 208 mA cm^{-2} at 60 °C, see Table 6.1. After the experiment the alloy grain boundaries were clearly visible to the naked eye.

6.4.3 The influence of temperature

Temperature has an impact on the cell start-up during galvanostatic discharge, with a more pronounced effect on 99.999 % aluminium than on the Al/Mg/Sn alloy. Figure 6.17 shows that in the first 900 s of discharge, the temperature rose rapidly from 24 to 40 °C at a rate of 1.7 °C min^{-1}, before slowing down to a rate of 0.08 °C min^{-1}. During this temperature rise, the Al/Mg/Sn anode potential shifted from −1.24 V to −1.43 V *vs.* Hg/HgO. With continuing discharge, the alloy potential gradually shifted back to more positive values with a potential of −1.32 V *vs.* H/HgO at the end of the experiment. This was due to the accumulation of discharge products in the electrolyte which lower the solution conductivity. The E4A air-cathode also showed an improvement in potential with discharge time, shifting from its initial value of −0.44 V to −0.34 V *vs.* Hg/HgO after 1400 seconds.

At start-up, the Al/Mg/Sn alloy was advantageous over 99.999 % aluminium, which had a more positive potential of −0.74 V *vs.* Hg/HgO because of the cold electrolyte temperature, 22 °C. As the electrolyte warmed up over the initial 900 seconds of discharge the potential of pure aluminium approached that of the alloy, −1.40 V *vs.* Hg/HgO. By the end of the

experiment the potential of pure aluminium also shifted back in the positive direction with a final reading of −1.24 V *vs.* Hg/HgO. Since the alloy experienced a less dramatic change in potential with rising temperature compared to pure aluminium, a cold battery start would be feasible and electrolyte pre-heating would not be necessary. This approach has been used by other battery systems used in military applications such as silver/zinc batteries, which are stored in a dry state for several years until needed for use [235].

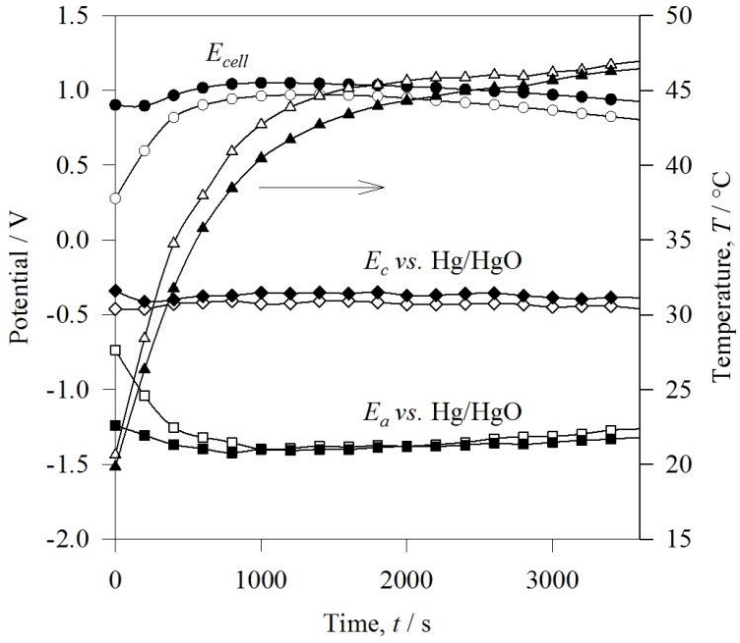

Figure 6.17: Comparison of the Al/Mg/Sn alloy and 99.999 % aluminium in the Al-air cell under galvanostatic discharge at 100 mA cm^{-2}. E4A air cathode. Electrolyte: 4 mol dm^{-3} NaOH. Anode area: 21 cm^2. Cathode area: 15 cm^2. 5 mm inter-electrode gap. ●, ◆, ■, ▲ for Al/Mg/Sn. ○, ◇, □, △ are for 99.999 % aluminium

Upon discharge at the peak power point at 170 mA cm^{-2} in Figure 6.18 for the cell with Al/Mg/Sn alloy there were greater fluctuations in the cathode potential than were observed at 100 mA cm^{-2}. Within the first 1000 s, there was a favourable potential shift from −0.92 V to −0.73 V *vs.* Hg/HgO, increasing the cell voltage to 0.68 V. Based on the variable load test results shown in Figure 6.14(b) a cathode potential of −0.67 V *vs.* Hg/HgO was expected. This steady state potential was not attained because the current was increased too fast, in a single step from open circuit to the limiting current density of the E4A air cathode. This suggests that in order to discharge the cell at the peak power point, a slow current-ramp up rate is required to operate close to the limiting current density of the air-cathode. The anode potential shifted negatively from an initial value of −1.18 V *vs.* Hg/HgO to a value of −1.49 V *vs.* Hg/HgO after 630 s, coinciding with a cell temperature of 55 °C. The temperature of

the cell also became higher when discharged at 170 mA cm^{-2} compared to at 100 mA cm^{-2}, although the trend of the rise in temperature was similar between the two. In this instance, the temperature rose rapidly at a rate of 3.3 °C min^{-1} over the first 600 s of discharge before slowing down to a steady rate of 0.2 °C min^{-1}, resulting in a final cell temperature of 71 °C.

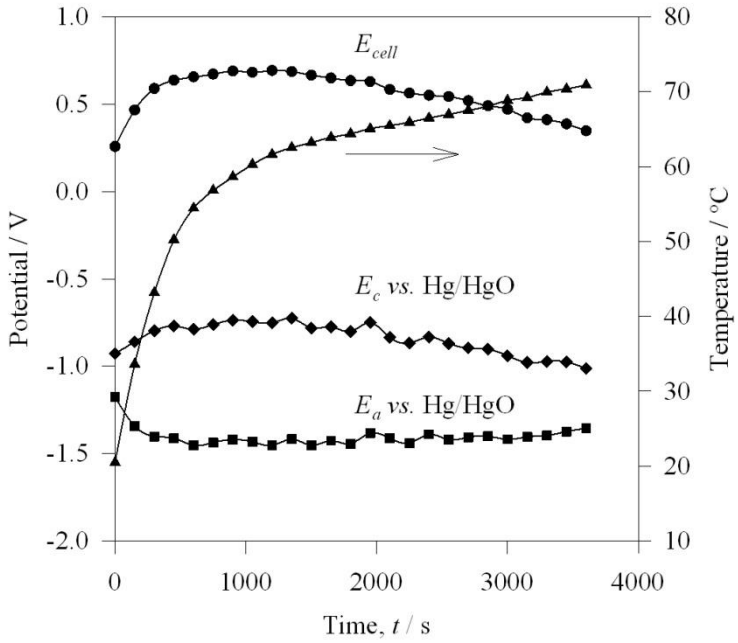

Figure 6.18: Discharge of the aluminium-air cell at the peak power point at 170 mA cm^{-2}. Anode: Al/Mg/Sn, area 22 cm^2. Cathode: E4A MnOx, area 15 cm^2. Electrolyte: 15 cm^3 of 4 mol dm^{-3} NaOH.● E_{cell}, ◆ E_c, ■ E_a, ▲ Temperature.

6.4.4 The importance of the air-electrode

The effect of different air-electrodes on the performance of the Al-air cell was examined. Three of the electrodes tested in the half-cell experiments were chosen: KTH and OxAg, the two electrodes with the highest limiting current densities at the lowest overpotential, and E4A, an in-expensive MnOx air electrode. The Al/Mg/Sn alloy was used as the anode in all instances. The variable load results in Figure 6.19 indicate that the highest open-circuit cell voltage was attained with the OxAg electrode at 2.06 V compared to 1.82 V for the cells using the other two air-cathodes. The higher open-circuit cell voltage with the OxAg electrode was due to a high positive rest potential for that electrode, 0.39 V *vs.* Hg/HgO. Under discharge the cell with OxAg air-electrode observed higher cell voltages than with the other air-electrodes up until a current density of 90 mA cm^{-2}. By this time the experiment was running for 21 minutes, and the potential of the OxAg electrode dramatically shifted more negatively to a value of −1.05 V *vs.* Hg/HgO to the detriment of the cell voltage which

dropped to 0.31 V before trailing off to 0.1 V, signifying the end of discharge of the cell with the OxAg electrode. It is likely that the predominant reaction at the OxAg was the reduction of Ag_2O to Ag rather than the reduction of oxygen, as discussed previously in Section 5.8. Once all the Ag_2O was reduced after 80 C cm^{-2} the cell stopped discharging.

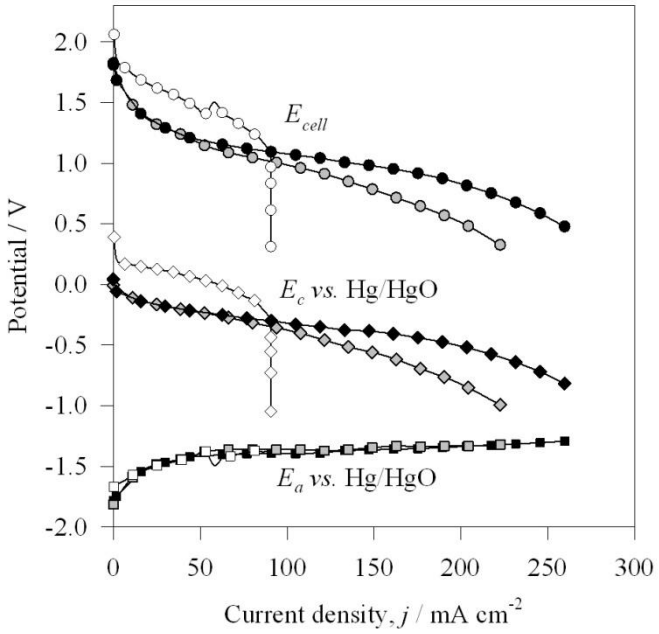

Figure 6.19: Comparison of the performance of the aluminium-air cell using different air electrodes. □, ◇, ○ OxAg; ●, ◆, ■ KTH; ◍, ◈, ▣ E4A. Anode, Al/Mg/Sn solution heat treated. Electrolyte: 15 cm^3 of 4 mol dm^{-3}, initially at 22 °C. Cathode area: 15 cm^2. Current density calculated relative to an anode area of 21 cm^2.

The cells with the KTH and E4A air cathodes showed a similar potential up until 100 mA cm^{-2}, see Figure 6.19, beyond which the IR drop was smaller for the KTH electrode. In the ohmic region, the resistance of the KTH electrode was 0.076 Ω, half the resistance for the E4A cathode of 0.16 Ω. The higher resistance of the E4A electrode can be attributed to the preference of the MnO_x catalyst to promote the two-electron transfer oxygen reduction [14]. The resistance of the E4A air-cathode accounted for 100 % of the ohmic resistance of the cell, whereas that of the KTH electrode accounted for only 78 %. This was calculated from the ratio of the resistance of the air-cathode to the cell resistance measured in the ohmic region from the *E-j* curve. So the air-electrode was still the limiting element of the cell in the ohmic region, although the KTH electrode offered some improvement. In the activation region the activation polarisation of the anode played a bigger impact compared to the cathode on the cell activation. The lower resistance of the KTH cathode meant that the cell was discharged at a current density of 270 mA cm^{-2}.

The performance of the Al-air cell with the three different air electrodes under galvanostatic discharge at 100 mA cm^{-2}, or 140 mA cm^{-2} normalised to the area of the air-cathode, can be seen in Figure 6.20(a). Three of the air-cathodes were compared: E4A, KTH and OxAg. The cell discharge with the OxAg electrode was extremely short at 100 s. It displayed a cell voltage of 0.48 V for 100 s before sharply declining to 0.20 V for the remainder of the test. The decline was due to the increase in overpotential of the air cathode from −0.84 V to −1.25 V *vs.* Hg/HgO. The calculated charge density for the AgO electrode from the Al-air cell test was 14 C cm^{-2}. This was below expectations given the results from the half-cell tests where the AgO electrode was discharged at 100 mA cm^{-2} for 900 s before its overpotential increased, which equates to a charge density of 90 C cm^{-2}. Perhaps the sudden onset of the high discharge current from the Al-air cell was a shock to the OxAg electrode and a gradual ramp-up rate is required. The increase in overpotential was attributable to the AgO becoming completely reduced. It is not known how the current of this electrode was divided between AgO reduction and oxygen reduction. To enhance its discharge time would involve increasing the AgO loading, at the expense of cathode cost. The AgO electrode is interesting from the point of view that the Al-AgO cell is an alternative to an Al-air cell offering higher cell voltages [236].

Examining the influence of the KTH and E4A air-cathodes on the performance of the Al-air cell shows a small difference in their discharge profile, see Figure 6.20(a). The data from the variable load cell experiments in Figure 6.19 indicates that at 100 mA cm^{-2} the cathode potentials for KTH and E4A should be −0.31 V and −0.37 V *vs.* Hg/HgO at 34 °C. During the galvanostatic discharge experiment, the air-cathode potentials start out far more negative and only shift to these more positive potentials after at least 1100 s in the case of the KTH electrode at which point the cell temperature reached 43 °C, see Figure 6.20(b). This suggests that there was a run-in time period before the electrodes began operating at their minimum overpotential. In the case of KTH, over the first 1100 s its potential favourably shifted from −0.57 to −0.32 V *vs.* Hg/HgO before moving to −0.41 V *vs.* Hg/HgO at the end. The more superior potential of the KTH electrode compared to E4A was due to its lower ohmic resistance. Toward the end of the experiment, the potential of both air-cathodes became inseparable owing to the build-up of aluminium hydroxide reaction product within the small electrolyte volume partially blocking the electrode pores.

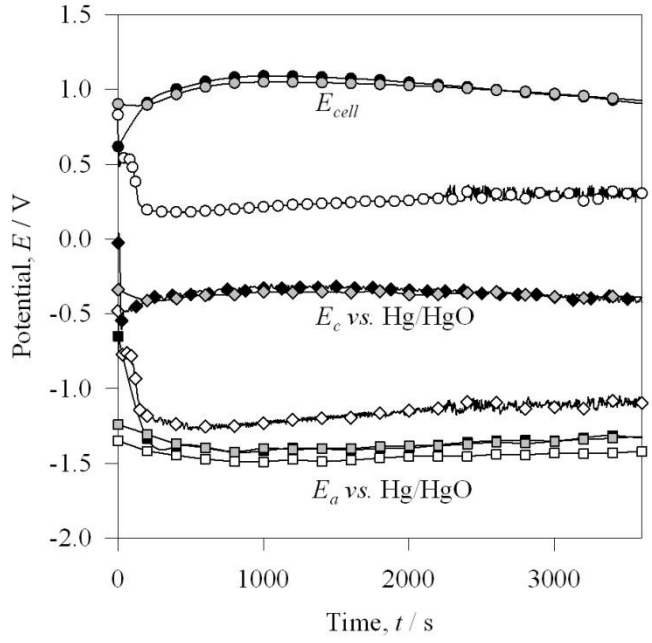

(a)

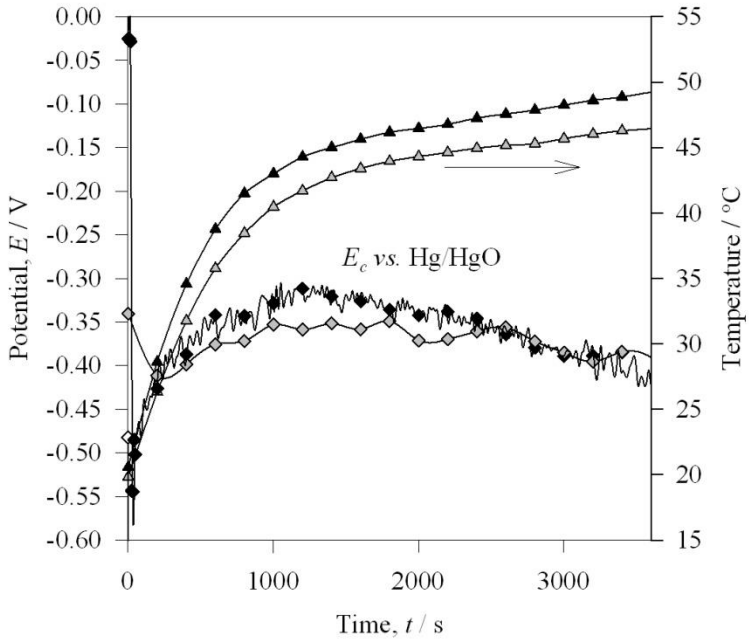

(b)

Figure 6.20: The influence of the different air-cathodes on the galvanostatic discharge of the Al-air cell at 100 mA cm^{-2}. □, ◇, ○ OxAg; ●, ◆, ■, ▲ KTH; ●, ◆, ■, ▲ E4A. (a) Comparison of cell and reference potentials versus time. (b) Comparison of cathode reference potential for cells with KTH and E4A air-electrodes. Anode Al/Mg/Sn, solution heat treated. Electrolyte: 15 cm^3 of 4 mol dm^{-3} NaOH, initially at 20 °C. Anode area: 21 cm^2. Cathode area: 15 cm^2. Interelectrode gap: 5 mm.

6.5 Summary of the performance of the Al-air cells

The peak power density attained from the prototype 1 aluminium-air cell was 79 mW cm^{-2} at 104 mA cm^{-2}, as shown in Table 6.1. These values were attained using an Al/Mg/Sn/Ga alloy as anode and a 0.5 mg cm^{-2} Pt electrode as air-cathode. The lack of a metal mesh current collector in the design of the 0.5 mg cm^{-2} Pt gas diffusion electrode meant that resistive losses in collecting current from the air-electrode limited the cell power density. The same cell had gravimetric energy and power densities of 5 W h kg^{-1} and 2.9 W kg^{-1}. The energy density was very low because of the bulkiness of the cell with a mass of 361 g and due to disintegration of the 1 mm thick Al/Mg/Sn/Ga plate anode. The Al/Mg/Sn/Ga anode disintegrated due to aggressive corrosion in alkaline electrolyte. This alloy was deemed unsuitable for use in an alkaline electrolyte, in agreement with the literature, as corrosion along grain boundaries was aggressive leading to disintegration of the anode plate. The energy density of the prototype 1 cell with Al 6101 foam was even lower at 2.5 W h kg^{-1} because this alloy too disintegrated with corrosion causing break-down of the strands of the foam. The Al 6101 alloy material contained impurities like iron and copper which have low overpotentials for the hydrogen evolution reaction and aggravated the self-corrosion of the aluminium. The high surface area offered by aluminium foams needs to be traded off against the need to maintain structural integrity during galvanostatic discharge.

Prototype 2 was lighter and smaller than the prototype 1 aluminium-air cell. A prototype 2 cell using a 0.5 mg cm^{-2} Pt air-electrode, as was used in the prototype 1 cell, delivered a power density of 51 mW cm^{-2}. This value was improved to 74 mW cm^{-2} by improving the method of current collection from the air-cathode. Further improvement again was achieved of 105 mW cm^{-2} by using a higher platinum loading of 4 mg cm^{-2}. The highest peak power density for a prototype 2 cell was 137 mW cm^{-2} at 213 mA cm^{-2}, as shown in Table 6.1. This was with a 99.999 % aluminium anode and a commercial E5 air-cathode. The superior power density of prototype 2 over prototype 1 was because of the use of an improved air-cathode, E5 from Electric Fuel, compared to the 0.5 mg cm^{-2} Pt gas diffusion electrode used in prototype 1. Comparing anode area of 11 and 22 cm^2 in the prototype 2 cell found that an area of 22 cm^2 was desirable to discharge at currents upwards of 5.0 A. An aluminium anode with an area much larger than that of the air-cathode inferred the advantage of having a lower cell voltage drop in the activation and mass transport regions of the *E-j* curve. It yielded less

advantage in the ohmic region of the *E-j* curve where the cell performance was dominated by the resistance of the air-cathode.

The prototype 3 aluminium-air cell was of similar size to the prototype 2 but improved the structural rigidity of the cell. Cell performance was characterised by variable loading and galvanostatic discharge experiments. Detailed analysis was made from measurement of cell temperature, electrode reference potentials and their inter-relationship. Compared to the other two prototypes, prototype 3 used a solution heat treated Al/Mg/Sn alloy that was prone to less corrosion than the Al/Mg/Sn/Ga alloy, tested in the earlier prototypes, in alkaline solution. The Al/Mg/Sn alloy maintained its structural integrity when discharged in an alkaline solution. The small electrolyte volume, 15 cm^3, in the prototype 3 Al-air cell meant that the cell exothermically heated itself, helping to improve anode reactivity. While the electrolyte temperature was low the Al/Mg/Sn alloy inferred more anodic potentials than 99.999 % aluminium. However once the electrolyte temperature rose, the potential of 99.999 % aluminium mirrored that of the Al/Mg/Sn alloy. A number of commercial air-electrodes were compared against an air-electrode designed by a project collaborator in the prototype 3 cell. The best performance was attained with the KTH air-electrode, with a power density of 174 mW cm^{-2} at a current density of 208 mA cm^{-2}.

The prototype 3 cell that was developed in this study could be further optimised by using a thinner aluminium anode and a smaller inter-electrode gap to reduce the weight of the cell and improve its energy density. Currently with a 3 mm thick aluminium anode and 15 cm^3 of electrolyte with a 5 mm inter-electrode gap the cell had a mass of 30 g. The current prototype had an energy density of 66 W h kg^{-1} after being discharged at 100 mA cm^{-2} for 1 hour. From Faraday's laws of electrolysis, the mass of the aluminium anode, of area 20 cm^2, consumed over an hour duration at 2.0 A discharge via reaction (2.2) would be (assuming aluminium dissolution via a 3 electron change and no other anode secondary reactions):

$$m = \frac{MIt}{zF} = \frac{\left(26.982\ \text{g mol}^{-1}\right)\left(2.0\ \text{A}\right)\left(3600\ \text{s}\right)}{\left(3\right)\left(96,485\ \text{C mol}^{-1}\right)} = 0.67\ \text{g} \qquad (6.1)$$

Given an anode area of 20 cm^2, split across two faces of the anode, the thickness that equates to 0.67 g of aluminium being consumed during 1 hour discharge at 100 mA cm^{-2} would be 0.24 mm.

$$d = \frac{m}{A\rho} = \frac{0.67 \text{ g}}{\left(10 \text{ cm}^2\right)\left(2.7 \text{ g cm}^{-3}\right)}\left(10 \text{ mm cm}^{-1}\right) = 0.24 \text{ mm} \qquad (6.2)$$

For structural purposes if an anode of 1 mm thickness and area of 20 cm^2 was selected it would have a mass of 5.4 g. Redesigning the prototype 3 cell with the thinner anode and an inter-electrode gap of 4 mm would mean 8 cm^3 of electrolyte would be needed instead of the current 15 cm^3. These adjustments would bring the cell mass to 20 g. This would see an energy density improvement from 66 W h kg^{-1} to 106 W h kg^{-1} over a 1 hour discharge period at 100 mA cm^{-2}, equating to a specific power of 106 W kg^{-1}. This energy density could be further improved if galvanostatic discharge experiments were conducted for a longer duration.

The original design brief at the outset of this study required an Al-air battery with a cell voltage of 7.8 V capable of delivering a maximum power of 34 W and an average power of 20 W for 1 hour. To achieve these requirements, the battery would require 8 of the current prototype 3 cells connected in electrical series each operating at an average voltage of 1.0 V at 100 mA cm^{-2} each at an average power of 2 W delivering a total battery power of 16 W at 8 V. Such a battery would have a mass of 240 g.

		Variable load experiments		Galvanostatic discharge experiments	
Anode	Cathode	Peak power density / mW cm^{-2}	Current density for peak power density / mA cm^{-2}	Specific power / W kg^{-1}	Energy density / W h kg^{-1}
Prototype 1					
Al/Mg/Sn/Ga, 3M NaOH	0.5 mg cm^{-2} Pt	79	104	2.9	5
Al/Mg/Sn/Ga perforated plate	0.5 mg cm^{-2} Pt				
Al/Mg/Sn/Ga, 8 M NaOH	0.5 mg cm^{-2} Pt	77	109		
Al 6101 10 ppi foam	0.5 mg cm^{-2} Pt	60	94	2.5	2.5
Al 6101 20 ppi foam	0.5 mg cm^{-2} Pt	57	72	2.1	1.1
Prototype 2					
Al/Mg/Sn/Ga	0.5 mg cm^{-2} Pt, no Cu wire	51	64		
Al/Mg/Sn/Ga	0.5 mg cm^{-2} Pt	74	92		
Al/Mg/Sn/Ga	4.0 mg cm^{-2} Pt	105	128		
99.999 % Al, 11 cm^2	E5	66	110		
99.999 % Al, 22 cm^2	E5	137	213	75	76
99.999 % Al, 82 cm^2	E5	161	291		
Prototype 3					
Al/Mg/Sn	KTH	174	208	62	66
99.999 % Al	KTH	182	206	-	-
Al/Mg/Sn	E4A	117	154	63	67
99.999 % Al	E4A	121	179	59	63
Al/Mg/Sn	OxAg	101	85	14	14

Table 6.1: Comparison of cell performances with different air-cathodes and anodes.

Chapter 7. Conclusions and Further Work

7.1 Conclusions

This project investigated the development of a lightweight, alkaline aluminium-air cell and the characterisation of its electrochemical behaviour. A prototype, lightweight aluminium-air cell was developed using a solution heat-treated Al/0.5 Mg/0.07 Sn alloy and a $LaCaCoO_3/LaCaMnO_3$ air-cathode, which was designed by a project collaborator. The cell had a peak power density of 174 mW cm^{-2} at a discharge current density of 208 mA cm^{-2} or 3.5 W at a discharge current of 4.2 A. Under galvanostatic discharge at 100 mA cm^{-2} for 1 hr the cell had gravimetric energy and power densities of 66 W h kg^{-1} and 62 W kg^{-1} respectively. The experimental work involved in developing the prototype aluminium-air cell explored three areas: the aluminium anode, the air-cathode and the development of a prototype lightweight aluminium-air cell. The main findings from those three pieces of work are:

1. A review of the literature concerning the anodic and corrosion behaviour of high-purity aluminium and its alloys was undertaken. An understanding has been developed of the reasons behind choosing certain elements to alloy with aluminium and the mechanisms by which they influence the oxidation and corrosion behaviour.

2. Two high purity aluminium alloys were evaluated in this work, Al/0.5 Mg/0.07 Sn and Al/0.4 Mg/0.07 Sn/0.05 Ga and their anodic and corrosion behaviours in NaOH were compared against that of 99.999 %wt Al.

3. Solution heat treatment of Al/Mg/Sn was very important in order to oxidise it at lower overpotentials compared to 99.999 %wt aluminium and also for the alloying elements, mainly tin, to be effective at increasing the overpotential for hydrogen evolution. If the alloying elements were present as precipitates, the parasitic corrosion reaction became problematic.

4. At 22 °C, linear sweep voltammetry eludes to show similarities between the anodic behaviour of the alloys. However galvanostatic discharge showed that the potential of

Al/Mg/Sn had a fluctuating discharge profile at 22 °C, compared to the relatively steadier and more negative potential of Al/Mg/Sn/Ga alloy. Based on literature research, the low melting point of the gallium alloying addition facilitated discharge of the Al/Mg/Sn/Ga alloy with lower overpotential at 22 °C.

5. In terms of corrosion at 22 °C the Al/Mg/Sn/Ga alloy exhibited a higher open-circuit corrosion rate of 9 mA cm^{-2} compared to 7 mA cm^{-2} for Al/Mg/Sn. Corrosion rates experienced at open-circuit reduce under galvanostatic discharge and discharge efficiencies were as high as 94 % above 50 mA cm^{-2}.

6. At 60 °C, Al/Mg/Sn/Ga alloy experiences aggravated corrosion along grain boundaries with a corrosion current density of 56 mA cm^{-2} at open-circuit almost double that of Al/Mg/Sn. Consequently Al/Mg/Sn/Ga was unsuitable for use in an alkaline aluminium-air battery, in agreement with reports in the literature.

7. Linear sweep voltammetry showed that the Al/Mg/Sn alloy was best suited for use at 60 °C, at which it displayed its highest limiting current density for aluminium oxidation of 1380 mA cm^{-2} at −0.72 V *vs.* Hg/HgO

8. A review was undertaken of gas-diffusion electrodes with high activity for oxygen reduction. From this literature survey, a collaboration was established with a researcher at KTH University, Sweden, whom had expertise in the field of air-electrode optimisation and fabrication. They agreed to supply some of their electrode for evaluation in this study.

9. Several commercial gas diffusion electrodes were tested and compared against the electrode designed by researchers at the KTH University, Sweden.

10. Two commercial platinum on carbon electrodes, with loadings of 0.5 and 4.0 mg cm^{-2}, supplied by E-TEK showed the importance of electrode design. These two electrodes were designed for use in a PEM fuel cell where electrical contact would be made via compression against a conductive plate, which was why these electrodes had no metal mesh current collector.

11. Three commercial MnO_x electrodes were evaluated; E4 and E4A supplied by Electric Fuel and MOC supplied by Gaskatel. The MOC electrode had a superior limiting current density of 220 mA cm^{-2} compared to the two supplied by Electric Fuel because of a higher loading of MnO_x catalyst. The commercial Co-based gas diffusion electrode by Electric Fuel could be a porphyrin which is a good catalyst choice due to it propensity to promote four-electron oxygen reduction. The commercial OxAg electrode supplied by Gaskatel did not behave very well as an oxygen reduction electrode. During discharge, the main reaction was likely to be the reduction of AgO to Ag.

12. The KTH electrode designed at KTH University, Sweden was the best air-electrode tested with a limiting current density of 463 mA cm^{-2} at −0.49 V *vs.* Hg/HgO. The superior behaviour of this electrode was down to several reasons: use of a combination of high-activity catalyst of $LaCaCoO_3$/$LaCaMnO_3$, high surface area carbons, a double-layer structure and high catalyst loading.

13. Three prototype aluminium-air cells were investigated during the course of the project. Prototype 1 was larger than the latter two. It was used to explore aluminium foam materials and the Al/Mg/Sn/Ga alloy as an anode. Individual electrode potential measurements found that the air-cathode overpotential was larger than that of the aluminium foam anode indicating that focus was needed on identifying a better cathode than developing a 3-D anode.

14. The peak power density attained with a prototype 1 cell was 79 mW cm^{-2} at 104 mA cm^{-2}, using an Al/Mg/Sn/Ga anode and 0.5 mg cm^{-2} Pt gas diffusion electrode. Under galvanostatic discharge at 1.0 A for 100 min the same cell delivered energy and power densities of 5 W h kg^{-1} and 3 W kg^{-1}. These values were low because of the large weight of prototype 1, 361 g.

15. The aggressive nature of the corrosion of the Al/Mg/Sn/Ga alloy was observed in prototype 1 experiments, with disintegration of 1 mm thick plate.

16. Prototype 2 improved upon prototype 1 with a smaller and lighter design weighing 30 g. Experiments on prototype 2 found that an anode area of 21 cm^2 was required to be able to discharge up to currents of 5 A. Peak power density with a prototype 2 cell was 137

mW cm^{-2} at 213 mA cm^{-2} or 3 W at 4 A owing to the use of an improved commercial air-cathode called E5 from Electric Fuel. Prototype 2 had a gravimetric energy density of 76 W h kg^{-1}.

17. Prototype 2 was replaced with prototype 3 which was of similar size and shape at 32 g, but was more robust. Experiments comparing the different air-cathodes and examining the behaviour of Al/Mg/Sn were conducted using prototype 3 Al-air cell. This was the final prototype design. Its cell performance was characterised by measurement of electrode potentials and cell temperature under galvanostatic discharge and variable loading.

18. Galvanostatic discharge tests at 100 mA cm^{-2} found that the Al/Mg/Sn alloy inferred advantage over 99.999 %wt aluminium mainly over the initial 1000 s following a cold-start up when the overpotential on 99.999 %wt aluminium was greatest. However once the electrolyte temperature rose to 40 °C there was no difference between the reference potentials of the two samples during galvanostatic discharge at 100 mA cm^{-2}.

19. As an air-electrode for the prototype 3 cell, the KTH electrode was compared against two commercial air-electrodes, E4A from Electric Fuel and OxAg from Gaskatel. Comparing the different air-cathodes from the variable load cell tests indicates up until 150 mA cm^{-2} the commercial OxAg electrode delivered the highest cell voltages. Beyond 150 mA cm^{-2} the highest cell voltages were delivered with the KTH electrode.

20. Galvanostatic discharge tests showed that an Al-AgO cell delivered higher cell-voltages than an Al-air cell. Although the capacity of the cell with the OxAg electrode was limited by the quantity of AgO, suggesting oxygen reduction was not its primary reaction unlike the other air electrodes.

21. Variable load tests showed that the ohmic region of the cathode potential contributed most to the cell voltage compared to the Al/Mg/Sn anode potential, which tended to reach a plateau over this current density range. This indicates that the air-cathode was limiting the performance of the cell. Galvanostatic discharge experiments were conducted for an hour duration, at the end of which the Al/Mg/Sn anode potential would

begin to unfavourably shift positively due to the build-up of reaction products in the small electrolyte volume.

7.2 Further work

As outlined in the summary section of Chapter 6, further optimisation of the current prototype could involve reducing the weight by making the anode and cell thinner, thus allowing for a smaller electrolyte volume. Prototype 3 cell was galvanically discharged for one hour duration. Longer galvanostatic discharge experiments would be worthwhile to find the maximum energy density for the cell and explore how the electrode potentials are influenced by increasing discharge product in the electrolyte. Zero resistance amperometry could be used to look at bimetallic corrosion and the parametric effects in the battery along with the voltage components of the individual electrodes.

Further work should examine the shortening of solution heat treatment time, during anode production, to vary the grain size and examine the effect on anodic polarisation and corrosion behaviour.

The behaviour of a 3-D aluminium anode could be further looked at. Questions need to be answered regarding the ideal strut thickness of a 3-D anode so as to maximise the area while ensuring the anode retains its structural integrity for the required discharge time. Two avenues could be explored here. One includes using the replication process to make a foam anode using the Al/Mg/Sn alloy. A lower cost alternative could investigate commercial aluminium foams. The corrosion of these commercial foams could be minimised and their oxidation enhanced by selecting appropriate additives to add to the alkaline electrolyte. For example 1×10^{-2} Na_2SnO_3.

References

1. Nestoridi, M., et al., *The study of aluminium anodes for high power density Al/air batteries with brine electrolytes.* J. Power Sources, 2008. **178**(1): p. 445-455.
2. Kay, A.D., *Novel Aluminium Air Batteries for Ultralight Micro-Aircraft* in *School of Engineering Sciences / School of Chemistry*. 2005, University of Southampton.
3. Nestoridi, M., *The study of aluminium anodes for high power density Al-air batteries with brine electrolytes*, in *Faculty of Engineering, Science and Mathematics*. 2009, University of Southampton.
4. Nestoridi, M., et al., *Further studies of the anodic dissolution in sodium chloride electrolyte of aluminium alloys containing tin and gallium.* J. Power Sources, 2009. **193**(2): p. 895-898.
5. Birkin, P.R., M. Nestoridi, and D. Pletcher, *Studies of the anodic dissolution of aluminium alloys containing tin and gallium using imaging with a high-speed camera.* Electrochim. Acta, 2009. **54**(26): p. 6668-6673.
6. Teal Group Corporation. 2010 [cited 2011 25 March]; Available from: http://www.tealgroup.com/index.php?option=com_content&view=article&id=62:uav-study-release&catid=3&Itemid=16.
7. Wu, H.S., *Micro Air Vehicle: Configuration, Analysis, Fabrication and Test.* IEEE/ASME Transactions on Mechantronics, 2004. **9**(1): p. 108 - 117.
8. Cameron, K. and V. Kowalenko, *Portable Unmanned Aircraft System Concept Investigation*. 1995, Defence Science and Technology Organisation Aeronautical and Maritime Research Laboratory Australia.
9. *Heavyweight power from lightweight cell*, in *New Scientist*. 1987. p. 38.
10. Rao, B.M.L. and G.M. Scamans. *Advances in aluminium-air batteries*. in *Proc. 10th International Seminar on Primary and Secondary Battery Technology Applications*. 1993. Deerfied Beach, Florida.
11. Hunter, J.A., G.M. Scamans, and W.B. O'Callaghan, *Aluminium batteries*. 1990: United States.
12. Martin, J.J., et al., *Air cathodes for metal-air batteries and fuel cells.* Electrical Power & Energy Conferece (EPEC), IEEE, 2009: p. 1-6.
13. Bidault, F., et al., *Review of gas diffusion cathodes for alkaline fuel cells.* J. Power Sources, 2009. **187**: p. 39-48.
14. Neburchilov, V., et al., *A review on air cathodes for zinc-air fuel cells.* J. Power Sources, 2010. **195**: p. 1271-1291.
15. Spendelow, J.S. and A. Wieckowski, *Electrocatalysis of oxygen reduction and small alcohol oxidation in alkaline media.* Phys. Chem. Chem. Phys., 2007. **9**: p. 2654-2675.
16. Fujiwara, N., et al., *Reversible air electrodes integrated with an anion-exchange membrane for secondary air batteries.* J. Power Sources, 2011. **196**: p. 808-813.
17. Zaromb, S., *The use and behaviour of aluminium anodes in alkaline primary batteries.* J. Electrochem. Soc., 1962. **109**(12): p. 1125-1130.
18. Cooper, J.F., R.V. Homsey, and J.H. Landrum, *The aluminium-air battery for electric vehicle propulsion.* 15th Intersociety Energy Conversion Engineering Conference, 1980. **2**: p. 1487-1495.
19. Tuck, C.D.S., *Modern Battery Technology*. 1991: Ellis Horwood.
20. *Aluminium batteries come to the fore.* New Scientist, 1987: p. 31.
21. Doche, M.L., et al., *Characterisation of different grades of aluminium anodes for aluminium/air batteries.* J. Power Sources, 1997. **65**: p. 197-205.

22. Scamans, G.M., et al., *Further developments of the aluminium-air telecommunications reserve power source,* in *Telecommunications energy conference, INTELEC '92., 14th International*. 1992: Washington, DC, USA. p. 413-417.
23. Chu, D. and R.F. Savinell, *Experimental data on aluminium dissolution in KOH electrolytes.* Electrochim. Acta, 1991. **36**(10): p. 1631-1638.
24. Hunter, J.A., et al., *Aluminium batteries*. 1991: United States.
25. Hunter, J.A., G.M. Scamans, and J. Sykes, *Anodes for high energy density aluminium air batteries.* Power Sources 13: International Power Sources Symposium 17, 1991: p. 193-211.
26. Dougherty, T.A., et al., *Aluminium-air reserve power unit for use in a 6 kW standby power system,* in *17th International Telecommunications Energy Conference*. 1995: The Hague, Netherlands. p. 821-827.
27. Egan, D.R.P., C.T.J. Low, and F.C. Walsh, *Electrodeposited nanostructured lead dioxide as a thin film electrode for a lightweight lead-acid battery.* J. Power Sources, 2011. **196**: p. 5725-5730.
28. Shkolnikov, E.I., A.Z. Zhuk, and M.S. Vlaskin, *Aluminium as an energy carrier: Feasibility analysis and current technologies overview.* Renewable and Sustainable Energy Reviews, 2011. **15**(9): p. 4611-4623.
29. Li, Q. and N.J. Bjerrum, *Aluminum as anode for energy storage and conversion: a review.* J. Power Sources, 2002. **110**(1): p. 1-10.
30. International Energy Agency. *Technology Roadmap Electric and plug-in hybrid electric vehicles*. [cited 2012 7 August]; Available from: http://www.iea.org/papers/2009/EV_PHEV_Roadmap.pdf.
31. Altek Fuel Group. *Alkaline aluminium-air fuel cell power supply system APS 100*. [cited 2012 7 August]; Available from: http://altekfuel.com/userfiles/File/SDS_APS100_12-24_V-04.pdf.
32. Yardney. [cited 2012 7 August]; Available from: www.yardney.com/AluPower/alupower.html.
33. Miranda, D., C.M. Costa, and S. Laceros-Mendez, *Lithium-ion rechargeable batteries: State of the art and future needs of microscopic theoretica models and simulations.* J. Electroanal. Chem., 2015. **739**: p. 97-110.
34. Morris, R.K., et al., *The Aluminium-Air Cell: A Hands-on Approach to the Teaching of Electrochemical Technology.* International Journal of Engineering Education, 2002. **18**(3): p. 379-388.
35. Pourbaix, M., *Atlas of electrochemical equilibria in aqueous solutions*. 1966: Pergamon Press.
36. Doche, M.L., et al., *Electrochemical behaviour of aluminium in concentrated NaOH solutions.* Corros. Sci., 1999. **41**: p. 805-826.
37. Bernard, J., M. Chatenet, and F. Dalard, *Understanding aluminium behaviour in aqueous alkaline solution using coupled techniques Part I. Rotating ring-disc study.* Electrochim. Acta, 2006. **52**: p. 86-93.
38. Armstrong, R.D. and V.J. Braham, *The mechanism of aluminium corrosion in alkaline solutions.* Corros. Sci., 1996. **38**(9): p. 1463-1471.
39. Hamlen, R.P., et al., *Applications of aluminium-air batteries.* IEEE AES Systems Magazine, 1991: p. 11-14.
40. Dougherty, T.A., et al. *Aluminum-air: status of technology and applications [secondary cells]*. in *Energy Conversion Engineering Conference, 1996. IECEC 96. Proceedings of the 31st Intersociety*. 1996.
41. Wu, H., *Design and optimisation of pivotal materials in electrolyte aluminium metallurgy and aluminium air battery industry chain using large-scale non-grid-*

connected wind power, in *World Non-Grid-Connected Wind Power and Energy Conference (WNWEC), 2010*. 2010, IEEE: Nanjing, 2010.
42. Fitzpatrick, N. and G. Scamans, *Aluminium is a fuel for tomorrow*, in *New Scientist*. 1986. p. 34-37.
43. Wang, H.Z., et al., *A review on hydrogen production using aluminium and aluminium alloys.* Renewable and Sustainable Energy Reviews, 2009. **13**: p. 845-853.
44. Sequeira, C.A.C., *Environmental Oriented Electrochemistry*. 1994: Elsevier.
45. Yang, S. and H. Knickle, *Design and analysis of aluminium/air battery system for electric vehicles.* J. Power Sources, 2002. **112**: p. 162-173.
46. Zhang, X., S.H. Yang, and H. Knickle, *Novel operation and control of an electric vehicle aluminium/air battery system.* J. Power Sources, 2004. **128**: p. 331-342.
47. Lemieux, E., W.H. Hartt, and K.E. Lucas, *A critical review of aluminium anode activation, dissolution mechanisms and performance*, in *Corrosion* 2001, NACE International: Houston, Texas.
48. Zhang, J., M. Klasky, and B.C. Letellier, *The aluminum chemistry and corrosion in alkaline solutions.* J. Nucl. Mater., 2009. **384**(2): p. 175-189.
49. Hunter, J., *The anodic behaviour of aluminium alloys in alkaline electrolytes*. 1989, University of Oxford.
50. Reding, J.T. and J.J. Newport, Materials Protection, 1966. **5**(12): p. 15.
51. Valand, T., O. Mollesad, and G. Nilsson, *Al-air cells-potential small electric generators for field use.* Power Sources 8: Proceedings of the 12th intnernational power sources symposium, 1980: p. 523-533.
52. Jeffrey, P.W., W. Halliop, and F.N. Smith, *Aluminium anode alloy*. 1988: United States.
53. Coin, R.J., C.W.B. Jr., and J.M. Noscal, *Metal hydroxide crystalliser and filter*. 1991, Eltech Systems Corporation: United States.
54. Abedin, S.Z.E., et al., *Electrodeposition of nano- and microcrystalline aluminium in three different air and water stable ionic liquids.* Chem. Phys. Chem., 2006. **7**: p. 1535-1543.
55. Gálová, M., *Electrodeposition of aluminium from organic aprotic solvents.* Surf. Tech., 1980. **11**: p. 357-369.
56. Linden, D. and T.B. Reddy, *Handbook of Batteries*. 3rd ed. 2001: McGraw-Hill.
57. Pyun, S.-I. and S.-M. Moon, *Corrosion mechanism of pure aluminium in aqueous alkaline solution.* J. Solid State Electrochem., 2000. **4**(5): p. 267-272.
58. Real, S., M. Urquidi-MacDonald, and D.D. MacDonald, *Evaluation of alloy anodes for aluminium-air batteries II. Delineation of anodic and cathodic partial reactions.* J. Electrochem. Soc., 1988. **135**(7): p. 1633-1636.
59. Scott, D.H., *The effect of manganese additions on the performance of aluminium air battery anode alloys*. 1982, Lawrence Livermore National Laboratory.
60. MacDonald, D.D. and C. English, *Development of anodes for aluminium/air batteries — solution phase inhibition of corrosion.* J. Appl. Electrochem., 1990. **20**(3): p. 405-417.
61. Brown, O.R. and J.S. Whitley, *Electrochemical behaviour of aluminium in aqueous caustic solutions.* Electrochim. Acta, 1987. **32**(4): p. 545-556.
62. Boinet, M., et al., *Understanding aluminium behaviour in aqueous alkaline solution using coupled techniques Part II: Acoustic emission study.* Electrochim. Acta, 2010. **55**: p. 3454-3463.
63. Wilhelmsen, W., et al., *The electrochemical behaviour of Al-In alloys in alkaline electrolytes.* Electrochim. Acta, 1991. **36**(1): p. 79-85.

64. Adhikari, S., J. Lee, and K.R. Hebert, *Formation of aluminium hydride during alkaline dissolution of aluminium.* J. Electrochem. Soc., 2008. **155**(1): p. C16-C21.
65. Adhikari, S. and K.R. Hebert, *Participation of aluminium hydride in the anodic dissolution of aluminium in alkaline solutions.* J. Electrochem. Soc., 2008. **155**(5): p. C189-C195.
66. Wang, X.Y., et al., *The effects of polyethylene glycol (PEG) as an electrolyte additive on the corrosion behaviour and electrochemical performances of pure aluminium in an alkaline zincate solution.* Mater. Corros., 2010. **61**(9999): p. 1-4.
67. Hamlen, R.P., et al., *Battery powered light source*. 1988, Alupower, Inc.: United States.
68. Drazic, D.M., et al., *Neutral Electrolyte Aluminium-Air Battery.* Power Sources 7, 1976: p. 353-363.
69. Budevski, E., et al., *Investigations of a large-capacity medium-power saline aluminium-air battery.* J. Appl. Electrochem., 1989. **19**(3): p. 323-330.
70. Bin, H.G., Liang., *Neutral electrolyte aluminium air battery with open configuration.* Rare Metals, 2006. **25**(10): p. 360.
71. Graver, B., A.T.J.v. Helvoort, and K. Nisancioglu, *Effect of heat treatment on anodic activation of aluminium by trace element indium.* Corros. Sci., 2010. **52**: p. 377-3781.
72. Anawati, M.P. Halvorsen, and K. Nisancioglu, *Activation of aluminium by small alloying additions of bismuth.* J. Electrochem. Soc., 2012. **159**(5): p. C211-C218.
73. Gudic, S., I. Smoljko, and M. Kliskic, *Electrochemical behaviour of aluminium alloys containing indium and tin in NaCl solution.* Mater. Chem. Phys., 2010. **121**: p. 561-566.
74. Smoljko, I., et al., *Electrochemical properties of aluminium anodes for Al/air batteries with aqueous sodium chloride electrolyte.* J. Appl. Electrochem., 2012. **42**: p. 969-977.
75. Müller, S., et al., *Aluminium alloys in sulfuric acid Part II: Aluminium-oxygen cells.* J. Appl. Electrochem., 1996. **26**(12): p. 1217-1223.
76. Rota, M., et al., *Bipolar Al/0₂ battery with planar electrodes in alkaline and acidic electrolytes.* J. Appl. Electrochem., 1995. **25**(2): p. 114-121.
77. Holzer, F., et al., *Aluminium alloys in sulphuric acid Part I: Electrochemical behaviour of rotating and stationary disc electrodes.* J. Appl. Electrochem., 1993. **23**(2): p. 125-134.
78. Hsueh, K.-L., E.R. Gonzalez, and S. Srinivasan, *Electrolyte effects on oxygen reduction kinetics at platinum: a rotating ring-disc electrode analysis.* Electrochim. Acta, 1983. **28**(5): p. 691-691.
79. Streicher, M.A., *The dissolution of aluminium in sodium hydroxide.* J. Electrochem. Soc. , 1949. **96**(3): p. 170-194.
80. See, D.M. and R.E. White, *Temperature and concentration dependence of the specific conductivity of concentrated solutions of potassium hydroxide.* J. Chem. Eng. Data, 1997. **42**: p. 1266-1268.
81. Jin, W., et al., *Comparison of the oxygen reduction reaction between NaOH and KOH solutions on a Pt electrode: The electrolyte-dependent effect.* J. Phys. Chem. B, 2010. **114**: p. 6542-6548.
82. Tseung, A.C.C., R.L. Quarshie, and Z.G. Lin, *Batteries having an aqueous alkaline electrolyte*. 1988: World Intellectual Property Organisation.
83. Walters, B.N., *A study of the anodic behaviour of aluminium alloys in alkaline electrolytes*, in *Chemical Energy Research Centre, Department of Chemistry*. 1988, City University: London.

84. Samson, E., J. Marchand, and K.A. Snyder, *Calculation of ionic diffusion coefficients on the basis of migration test results.* Materials and Structures, 2003. **36**: p. 156-165.
85. E.L.Cussler, *Diffusion: Mass transfer in fluid systems*. 3rd ed. 2009: Cambridge.
86. Scamans, G., *Advances in battery technology: development of the aluminium/air battery.* Chem. Ind. , 1986: p. 192-196.
87. Niksa, M.J. and A.J. Niksa, *Primary aluminium-air battery*. 1990: United States
88. Rudd, E.J. and D.W. Gibbons, *High energy density aluminium/oxygen cell.* J. Power Sources, 1994. **47**: p. 329-340.
89. Feliu, S. and M.J. Bartolomé, *Influence of alloying elements and etching treatment on the passivating films formed on aluminium alloys.* Surf. Interface Anal., 2007. **39**(4): p. 304-316.
90. Patnaik, R.S.M., et al., *Heat management in aluminium/air batteries: sources of heat.* J. Power Sources, 1994. **50**: p. 331-342.
91. Ghali, E., *Corrosion resistance of aluminium and magnesium alloys. Understanding, performance and testing.* 2010: Wiley.
92. Mazhar, A.A., S.T. Arab, and E.A. Noor, *Electrochemical behaviour of Al-Si alloys in acid and alkaline media.* Bulletin of Electrochemistry, 2001. **17**(10): p. 449-458.
93. Albert, I.J., et al., *Characterisation of different grades of commercially pure aluminium as prospective galvanic anodes in saline and alkaline battery electrolyte.* J. Appl. Electrochem., 1989. **19**(4): p. 547-551.
94. Roald, B. and M.A. Streicher, *Corrosion rate and etch structures of aluminium; effect of heat treatment and impurities.* J. Electrochem. Soc., 1950. **97**(9): p. 283-289.
95. Hunter, J.A., *Aluminium batteries*. 1989: European.
96. Scamans, G., et al., *Advances in the development of Aluminium/air batteries.* Power Sources 11, 1986: p. 267-279.
97. Bockris, J.O.M., et al., *Comprehensive Treatise of Electrochemistry Vol 2: Electrochemical Processing*. 1981: Plenum Press.
98. Hampel, C.A., *The Encyclopedia of Electrochemistry*. 1964: Reinhold Publishing Corporation.
99. Scamans, G.M., et al., *The present status of Aluminium/air battery development*, in *21st Intersociety Energy Conversion Conference*. 1986, American Chemical Society: San Diego. p. 1057-1061.
100. Tuck, C.D.S., J.A. Hunter, and G.M. Scamans, *The Electrochemical Behavior of Al-Ga Alloys in Alkaline and Neutral Electrolytes.* J. Electrochem. Soc., 1987. **134**(12): p. 2970-2981.
101. Baker, H., *ASM Handbook Volume 3 Alloy Phase Diagrams*. 1992: ASM International.
102. Horn, K.R.V., *Aluminium Vol. 1. Properties, Physical Metallurgy and Phase Diagrams*. 1967: American Society for Metals.
103. MacDonald, D.D., S. Real, and M. Urquidi-Macdonald, *Evaluation of Alloy Anodes for Aluminum-Air Batteries III. Mechanisms of Activation, Passivation, and Hydrogen Evolution.* J. Electrochem. Soc., 1988. **135**(10): p. 2397-2409.
104. Reboul, M.C., P.H. Gimenez, and J.J. Rameau, *A proposed activation mechanism for Al anodes.* Corros. NACE, 1984. **40**(7).
105. Lee, K.-K. and K.-B. Kim, *Electrochemical impedance characteristics of pure Al and Al-Sn alloys in NaOH solution.* Corros. Sci., 2001. **43**: p. 561-575.
106. Nisancioglu, K. and L. Odden, *Activation of aluminium anodes by tin*, in *Proceedings of the second symposium on electrode materials and processes for energy conversion and storage*. 1987, The Electrochemical Society. p. 499-512.

107. MacDonald, D.D., *The history of the Point Defect Model for the passive state: A brief review of film growth aspects.* Electrochim. Acta, 2011. **56**: p. 1761-1772.
108. Ziebarth, J.T., et al., *Liquid phase-enabled reaction of Al-Ga and Al-Ga-In-Sn alloys with.* Int. J. Hydrogen Energy, 2011. **36**: p. 5271-5279.
109. Sheng, H.W., K. Lu, and E. Ma, *Melting and freezing behaviour of embedded nanoparticles in ball-milled Al-10 wt% M (M = In, Sn, Bi, Cd, Pb) mixtures.* Acta Mater., 1998. **46**(14): p. 5195-5205.
110. Mideen, A.S., et al., *Development of new alloys of commercial aluminium (2S) with zinc, indium, tin and bismuth as anodes for alkaline batteries.* J. Power Sources, 1987. **27**: p. 235-244.
111. Paramasivam, M., M. Jayachandran, and S.V. Iyer, *Influence of alloying additives on the performance of commercial grade aluminium as galvanic anode in alkaline zincate solution for use in primary alkaline batteries.* J. Appl. Electrochem., 2003. **33**: p. 303-309.
112. Paramasivam, M. and S.V. Iyer, *Influence of alloying additives on corrosion and hydrogen permeation through commercial aluminium in alkaline solution.* J. Appl. Electrochem., 2001. **31**: p. 115-119.
113. Paramasivam, M., et al., *Different commercial grades of aluminium as galvanic anodes in alkaline zincate solutions.* J. Appl. Electrochem., 1991. **21**: p. 452-456.
114. Abedin, S.Z.E. and A.O.Saleh, *Characterisation of some aluminium alloys for applications as anodes in alkaline batteries.* J. Appl. Electrochem., 2004. **34**: p. 331-335.
115. McPhail, D.J., *The anodic behaviour of aluminium alloys in alkaline solutions*, in *Department of Chemical Engineering*. 1993, University of Canterbury: Christchurch.
116. MacDonald, D.D., et al., *Evaluation of alloy anodes for aluminium-air batteries: corrosion studies.* Corros. Sci., 1988. **44**(9): p. 652-657.
117. Tang, T., et al., *The effect of zinc on the aluminium anode of the aluminium-air battery.* J. Power Sources, 2004. **138**: p. 313-318.
118. Zhang, Y., Y.-s. Song, and Y.-s. Wang, *Synergetic effect of stannate with o-aminophenol on inhibiting H(subscript2) evolution of Al anode in strong alkaline media.* J. Shanghai Uni., 2007. **11**(4): p. 426-431.
119. Warmuzek, M., *Metallographic techniques for aluminium and its alloys*, in *ASM Handbook, Volume 9: Metallography and microstructures*. 2004, ASM.
120. Frankel, G.S., *Pitting corrosion of metals.* J. Electrochem. Soc., 1998. **145**(6): p. 2186-2198.
121. Szklarska-Smialowska, Z., *Pitting corrosion of aluminium.* Corros. Sci., 1999. **41**: p. 1743-1767.
122. Jeffrey, P.W., W. Halliop, and F.N. Smith, *Aluminium anode alloy*. 1987: European.
123. Scamans, G., J. Hunter, and C. Tuck, *Further developments of aluminium batteries.* Proceedings of the 16th International Power Sources Symposium 1988: Power Sources 12, 1988: p. 363.
124. Hunter, J.A., *Aluminium batteries*. 1991, Alcan International Ltd: United States.
125. Gunderson, J.T.B., et al., *Effect of heat treatment on electrochemical behaviour of binary aluminium model alloys.* Corros. Sci., 2004. **46**: p. 697-714.
126. Bohnstedt, W., *The influence of electrolyte additives on the anodic dissolution of aluminium in alkaline solutions.* J. Power Sources, 1980. **5**: p. 245-253.
127. Dodson, M.W., *Aluminium alloys for battery anodes in alkaline solutions*, in *Department of Chemistry*. 1992, University of Southampton.
128. Norman, C.F.W., *Corrosion of aluminium*, in *Faculty of Science Department of Chemistry*. 1986, University of Southampton.

129. Tarcy, G.P. and R.M. Mazgaj, *Aluminium alloy and associated anode*. 1989: United States.
130. Ralston, K.D. and N. Birbilis, *Effect of grain size on corrosion: a review.* Corros., 2010. **66**(7): p. 0750051-12.
131. Shu-quan, L., et al., *Effect of rolling processing on microstructure and electrochemical properties of high active aluminium anode.* Trans. Nonferrous Met. Soc. China, 2010. **20**: p. 942-949.
132. The Aluminium Association. *Aluminium-air fuel cell becoming commercially viable*. 2003 [cited 2012 7 August]; Available from: http://aluminum.org/AM/Template.cfm?Section=Home&template=/CM/HTMLDisplay.cfm&ContentID=15793.
133. Moussa, M.N., et al., *Carboxylic acids as corrosion inhibitors for aluminium in acidic and alkaline solutions.* Anti-corrosion methods and materials, 1990. **37**(3): p. 4-8.
134. Al-Rawashdeh, N.A.F. and A.K. Maayta, *Cationic surfactant as corrosion inhibitor for aluminium in acidic and basic solutions.* Anti-corrosion methods and materials, 2005. **52**(3): p. 160-166.
135. Abdel-Gaber, A.M., et al., *Novel package for inhibition of aluminium corrosion in alkaline solutions.* Mater. Chem. Phys., 2010. **124**: p. 773-779.
136. Wang, X.Y., et al., *Influences of zinc oxide and organic additive on the electrochemical behaviour of pure aluminium in an alkaline solution.* J. Appl. Electrochem., 2005. **35**: p. 213-216.
137. Wang, B., *Recent development of non-platinum catalysts for oxygen reduction reaction.* J. Power Sources, 2005. **152**: p. 1-15.
138. Litser, S. and G. McLean, *PEM fuel cell electrodes.* J. Power Sources, 2004. **130**: p. 61-76.
139. Cheng, F., *Metal-air batteries: from oxygen reduction electrochemistry to cathode catalysts.* Chem. Soc. Rev., 2012. **41**: p. 2172-2192.
140. Jorissen, L., *Bifunctional oxygen/air electrodes.* J. Power Sources, 2006. **155**: p. 23-32.
141. Fang, Z.-q., et al., *Preparation and electrochemical property of three-phase gas diffusion oxygen electrodes for metal air battery.* Electrochim. Acta, 2006. **51**: p. 5654-5659.
142. Dicks, A.L., *The role of carbon in fuel cells.* J. Power Sources, 2006. **156**: p. 128-141.
143. Watanabe, M., M. Tomikawa, and S. Motoo, *Experimental analysis of the reaction layer structure in a gas diffusion electrode.* J. Electroanal. Chem., 1985. **195**: p. 81-93.
144. Maja, M., et al., *Effect of structure of the electrical performance of gas diffusion electrodes for metal air batteries.* Electrochim. Acta, 2000. **46**: p. 423-432.
145. Tomantschger, K. and K.V. Kordesch, *Structural analysis of alkaline fuel cell electrodes and electrode materials.* J. Power Sources, 1989. **25**: p. 195-214.
146. Muller, S., K. Striebel, and O. Haas, *La0.6Ca0.4CoO3: a stable and powerful catalyst for bifunctional air electrodes.* Electrochim. Acta, 1994. **39**(11/12): p. 1661-1668.
147. Gharibi, H. and R.A. Mirzaie, *Fabrication of gas-diffusion electrodes at various pressures and investigation of synergetic effects of mixed electrocatalysts on oxygen reduction reaction.* J. Power Sources, 2003. **115**: p. 194-202.
148. Poux, T., et al., *Dual role of carbon in the catalytic layers of perovskite/carbon composites for the electrocatalytic oxygen reduction reaction.* Catalytic Materials for Energy: Past, Present and Future, 2012. **1**: p. 83-92.
149. Muller, S., et al., *A study of carbon-catalyst interaction in bifunctional air electrodes for zinc-air batteries.* J. New Mater. Electro. Sys., 1999. **2**: p. 227-232.

150. Kiros, Y., T. Quatrano, and P. Bjornbom, *Determination of the thickness of the active layer and cathode limiting currents in AFC.* Electrochem. Comm., 2004. **6**: p. 526-530.
151. Yang, X.-h. and Y.-y. Xia, *The effect of oxygen pressures on the electrochemical profile of lithium/oxygen battery.* J. Solid State Electrochem., 2010. **14**: p. 109-114.
152. Hayashi, M., et al., *Enhanced electrocatalytic activity for oxygen reduction over carbon-supported LaMnO3 prepared by reverse micelle method.* Electrochem. Solid State Lett., 1998. **1**(6): p. 268-270.
153. Kiros, Y., *Oxygen reduction electrode*. 2002.
154. Kiros, Y. and S. Schwartz, *Pyrolyzed macrocycles on high surface area carbons for the reduction of oxygen in alklaine cells.* J. Power Sources, 1991. **36**: p. 547-555.
155. Gojkovic, S.L.j., S. Gupta, and R.F. Savinell, *Heat-treated iron(III) tetramethoxyphenyl porphyrin chloride supported on high-area carbon as an electrocatalyst for oxygen reduction Part II. Kinteics of oxygen reduction.* J. Electroanal. Chem., 1999. **462**: p. 63-72.
156. Cheng, N., et al., *Reduction reaction by porphyrin-based catalysts for fuel cells.* Electrocatal., 2012. **3**: p. 238-251.
157. Zhu, A.L., et al., *Low temperature pyrolyzed cobalt tetremethoxyy phenylporphyrin catalyst and its applications as an improved catalyst for metal air batteries.* J. Power Sources, 2010. **195**: p. 5587-5595.
158. Cheng, F., et al., *Selective synthesis of manganese oxide nanostructures for electrocatalytic oxygen reduction.* Appl. Mater. and Interfaces, 2009. **1**(2): p. 460-466.
159. Lai, S.C.S. and M.T.M. Koper, *Ethanol electro-oxidation on platinum in alkaline media.* Phys. Chem. Chem. Phys., 2009. **11**: p. 10446-10456.
160. Chervin, C.N., et al., *Redesigning air cathodes for metal-air batteries using MnOx-functionalised carbon nanofoam architectures.* J. Power Sources, 2012. **207**: p. 191-198.
161. Bidault, F., et al., *A new application for nickel foam in alkaline fuel cells.* Int. J. Hydrogen Energy, 2009. **34**: p. 6799-6808.
162. Kloke, A., et al., *Strategies for the fabrication of porous platinum electrodes* Adv. Mater., 2011. **23**: p. 4976-5008.
163. Pollet, B.G., E.F. Valzer, and O.J. Curnick, *Platinum sonoelectrodeposition on glassy carbon and gas diffusion layer electrodes.* Int. J. Hydrogen Energy, 2011. **36**: p. 6248-6258.
164. Zhang, D., T. Sotomura, and T. Ohsaka, *Dual catalysts system based on nano-manganese oxide and multiwall carbon nanotube for four-electron oxygen reduction.* Chem. Lett., 2006. **35**(5): p. 520-521.
165. El-Deab, M.S., et al., *Non-platinum electrocatalysts: manganese oxide nanoparticle-cobaltporphyrin binary catalysts for oxygen reduction.* J. Appl. Electrochem., 2008. **38**: p. 1445-1451.
166. El-Deab, M.S. and T. Ohsaka, *Manganese oxide nanoparticles electrodeposited on platinum are superior to platinum for oxygen reduction.* Surf. Chem., 2006. **45**: p. 5963-5966.
167. Mukherjee, A. and I. N. Basumallick, *Metallized graphite as an improved cathode material for aluminium/air batteries.* J. Power Sources, 1993. **45**(2): p. 243-246.
168. Yuasa, M., et al., *Reverse micelle-based preparation of carbon-supported La(1-x)Sr(x)Mn(1-y)Fe(y)O(3+d) for oxygen electrode.* J. Electrochem. Soc., 2004. **151**(10): p. A1690-A1695.

169. Shimizu, Y., et al., *Bi-functional oxygen electrode using large surface area La1-X,CaxCoO3 for rechareable metal-air battery*. J. Electrochem. Soc., 1990. **137**(11): p. 3430-3433.
170. Bursell, M., M. Pirjamali, and Y. Kiros, *La0.6Ca0.4CoO3, La0.1Ca0.9MnO3 and LaNiO3 as bifunctional oxygen electrodes.* Electrochim. Acta, 2002. **47**: p. 1651-1660.
171. Hayashi, M., et al., *Reverse micelle assisted dispersion of lanthanum manganite on carbon support for oxygen reduction cathode.* J. Electrochem. Soc., 2004. **151**(1): p. A158-A163.
172. Lukaszewicz, J.P., et al., *New approach towards preparation of efficient gas diffusino-type oxygen reductin electrode.* J. Mater Sci., 2006. **41**(6215-6220): p. 6215.
173. Guangchuan, L., et al., *Preparation of nanometer La(1-x)Sr(x)MnO(3) and application in air-cathode.* J. Rare Earths, 2007. **25**: p. 264-267.
174. Yuasa, M., et al., *High-perforamnce oxygen reduction catalyst using carbon-supported La-Mn-based perovskite-type oxide.* Electrochem. Solid-State Lett. , 2011. **14**(5): p. A67-A69.
175. Lamminen, J., et al., *Preparation of air electrodes and long run tests.* J. Electrochem. Soc., 1991. **138**(4): p. 905-908.
176. Li, N., et al., *Electrocatalytic activity of spinel-type oxides LiMn(2-x)Co(x)O(4) with large specific surface areas for metal-air battery*. J. Power Sources, 1998. **74**: p. 255-258.
177. Li, N., et al., *Spinel-type oxides LiMn(2-x)M(x)O(4) [M=o, Fe, (CoFe)] as electrocatalyst for oxygen evolution/reduction in alkaline solution.* J. Appl. Electrochem., 1999. **29**: p. 1351-1354.
178. Nissinen, T., et al., *Microwave synthesis of catalyst spinel MnCo(2)O(4) for alkaline fuel cell.* J. Power Sources, 2002. **106**: p. 109-115.
179. Guerin, S., et al., *A combinatorial approach to the study of particle size effects on supported electrocatalysts: oxygen reduction on gold.* J. Comb. Chem., 2006. **8**: p. 679-686.
180. Guerin, S. and B.E. Hayden, *Physical vapor deposition method for the high-throughput synthesis of solid-state material libraries.* J. Comb. Chem., 2006. **8**: p. 66-73.
181. Jiang, R. and D. Chu, *An electrode probe for high-throughput screening of electrochemical libraries.* Rev. Sci. Instrum., 2005. **76**: p. 062213.
182. Jiang, R., *Combinatorial electrochemical cell array for high throughput screening of micro-fuel cells and metal/air batteries.* Rev. Sci. Instrum., 2007. **78**: p. 072209-1-072209-7.
183. m pore. [cited 2012 7 August]; Available from: www.m-pore.de.
184. MetalFoam. *Aluminium metal foam suppliers list*. [cited 2012 7 August]; Available from: http://www.metalfoam.net/.
185. Salavagione, H., et al., *3D Electrodes from aluminium foams prepared by replication process.* J. Appl. Electrochem., 2010. **40**(2): p. 241-246.
186. Goodall, R. and A. Mortensen, *Microcellular Aluminium?-Child's Play!* Advanced Engineering Materials, 2007. **9**(11): p. 951-954.
187. Li, C., et al., *Metallic Aluminum Nanorods: Synthesis via Vapor-Deposition and Applications in Al/air Batteries.* Chem. Mater., 2007. **19**(24): p. 5812-5814.
188. Popovich, N.A. and R. Govind, *Studies of granular aluminium anode in an alkaline fuel cell.* J. Power Sources, 2002. **112**: p. 36-40.
189. Ferrando, W.A., *Development of a novel composite aluminium anode.* J. Power Sources, 2004. **130**: p. 309-314.

190. Mohamad, A.A., *Electrochemical properties of aluminium anodes in gel electrolyte-based aluminium-air batteries.* Corros. Sci., 2008. **50**: p. 3475-3479.
191. Wu, G.M., S.J. Lin, and C.C. Yang, *Alkaline Zn-air and Al-air cells based on novel solid PVA/PAA polymer electrolyte membranes.* J. of Membr. Sci., 2006. **280**(1-2): p. 802-808.
192. Wang, J.M., et al., *Corrosion and electrochemical behavious of pure aluminium in novel KOH-ionic liquid-water solutions.* Mater. Corros., 2009. **60**(12): p. 977-981.
193. Wang, J.-B., et al., *The corrosion and electrochemical behaviour of pure aluminium in alkaline methanol solutions.* J. Appl. Electrochem., 2007. **37**: p. 753-758.
194. Abd-el-Nabey, B.A., N. Khalil, and E. Khamis, *Alkaline corrosion of aluminium in water-organic solvent mixtures.* Surface Technology, 1984. **22**: p. 367-376.
195. Shao, H.B., et al., *Anodic dissolution of aluminium in KOH ethanol solutions.* Electrochem. Commun., 2004. **6**: p. 6-9.
196. Mukherjee, A. and I.N. Basumallick, *Complex behaviour of aluminium dissolution in alkaline aqueous 2-propanol solution.* J. Power Sources, 1996. **58**: p. 183-187.
197. Meng, H. and P.K. Shen, *Novel Pt-free catalyst for oxygen electroreduction.* Electrochem. Comm., 2006. **8**: p. 588-594.
198. Kishimoto, N., et al. *Charge-Discharge Properties of Aluminum Anode in Ionic Liquid for Aluminum-Air Batteries*. in *ECS Meeting Abstracts*. 2008. Honolulu, HI.
199. Abedin, S.Z.E., et al., *Additive free electrodeposition of nanocrystalline aluminium in a water and air stable ionic liquid.* Electrochem. Commun., 2005. **7**: p. 1111-1116.
200. Plechkova, N.V. and K.R. Seddon, *Applications of ionic liquids in the chemical industry.* Chem. Soc. Rev., 2008. **37**: p. 123-150.
201. Armand, M., et al., *Ionic-liquid materials for the electrochemical challenges of the future.* Nat Mater, 2009. **8**(8): p. 621-629.
202. Endres, F., A.P. Abbott, and D.R. MacFarlane, *Electrodeposition from Ionic Liquids*. 2008: Wiley-VCH.
203. Simka, W., D. Puszczyk, and G. Nawrat, *Electrodeposition of metals from non-aqueous solutions.* Electrochim. Acta, 2009. **54**: p. 5307-5319.
204. Hamilton, T. *Betting on a Metal-Air Battery Breakthrough*. 2009 [cited 2012 7 August]; Available from: http://www.technologyreview.com/energy/23877/page1/.
205. Licht, S., et al., *The effect of water on the anodic dissolution of aluminum in non-aqueous electrolytes.* Electrochem. Commun., 2000. **2**(5): p. 329-333.
206. Moustafa, E.M., et al., *Electrodeposition of Al in 1-Butyl-1-methylpyrrolidinium Bis(trifluoromethylsulfonyl)amide and 1-Ethyl-3-methylimidazolium Bis(trifluoromethylsulfonyl)amide Ionic Liquids: In situ STM and EQCM studies.* J. Phys. Chem. B, 2007. **111**: p. 4693-4704.
207. Endres, F. and S.Z.E. Abedin, *Air and water stable ionic liquids in physical chemistry*. Phys. Chem. Chem. Phys., 2006. **8**: p. 2101-2116.
208. Abbott, A.P., et al., *Double layer, diluent and anode effects upon the electrodeposition of aluminium from chloroaluminate based ionic liquids.* Phys. Chem. Chem. Phys., 2010. **12**: p. 1862-1872.
209. Ingale, N.D., et al. *Aluminium as anode material electrodeposited from ionic liquids for secondary rechargeable batteries*. in *219th ECS Meeting*. 2011. Montreal, QC, Canada.
210. Jiang, T., et al., *Electrodeposition of aluminium from ionic liquids: Part I - electrodeposition and surface morphology of aluminium from aluminium chlorde 1-ethyl-3-methylimidazolium chloride ([EMIm]Cl) ionic liquids.* Surf. Coat. Technol., 2006. **201**: p. 1-9.

211. Zhao, Y. and T.J. VanderNoot, *Review: Electrodeposition of aluminium from nonaqueous organic electrolytic systems and room temperature molten salts.* Electrochim. Acta, 1997. **42**(1): p. 3-13.
212. Zhao, Y. and T.J. VanderNoot, *Electrodeposition of aluminium from room temperature AlCl3-TMPAC molten salts.* Electrochim. Acta, 1997. **42**(11): p. 1639-1643.
213. Zhang, J., *Air dehydration membranes for non-aqueous Li-air batteries.* J. Electrochem. Soc. , 2010. **157**(8): p. A940-A946.
214. Kuboki, T., et al., *Lithium-air batteries using hydrophobic room temperature ionic liquid electrolyte.* J. Power Sources, 2005. **146**: p. 766-769.
215. Morimitsu, M. *Charge-Discharge Behaviors of the Air Electrode/Ionic Liquid Half Cell*. in *ECS Meeting Abstracts*. 2007. Chicago, Illinois: ECS.
216. Silvester, D.S. and R. Compton, *Electrochemistry in room temperature ionic liquids: a review and some possible applications.* Z. Phys. Chem, 2006. **220**: p. 1247-1274.
217. Ernst, S., L. Aldous, and R.G. Compton, *The electrochemical reduction of oxygen at boron-doped diamond and glassy carbon electrodes: A comparative study in a room-temperature ionic liquid.* J. Electroanal. Chem., 2011. **663**: p. 108-112.
218. Petzow, G., *Metallographic etching: metallographic and ceramographic methods for revealing microstructure*. 1978: American Society for Metals.
219. Davis, J.R., *Corrosion: Understanding the basics*. 2000: ASM International.
220. Goodhew, P.J., J. Humphreys, and R. Beanland, *Electron microscopy and analysis*. 2001.
221. Zoski, C.G., *Handbook of Electrochemistry*. 2007.
222. Kear, G., C.P.-d.-L. Albarran, and F.C. Walsh, *Reduction of dissolved oxygen at a copper rotating-disc electrode.* Chemical Engineering Education, 2005. **39**(1): p. 14-21.
223. Yang, C.-C., *Preparation and characterisation of electrochemical properties of air cathode electrode.* Int. J. Hydrogen Energy, 2004. **29**: p. 135-143.
224. Electric Fuel Ltd. *Air-electrode supplier*. [cited 2015 5 March]; Available from: www.electric-fuel.com/airelectrode/index.html.
225. Gaskatel. *Air-electrode supplier*. [cited 2015 5 March]; Available from: www.gaskatel.de/eng/produkte/biplex/eng_biplex_index.html.
226. Giesche, H., *Mercury porosimetry: a general (practical) overview.* Part. Part. Syst. Charact., 2006. **23**: p. 1-11.
227. Shao, H.B., et al., *The cooperative effect of calcium ions and tartrate ions on the corrosion inhibition of pure aluminium in an alkaline solution.* Mater. Chem. Phys., 2002. **77**: p. 305-309.
228. Merck. *Sodium hydroxide pellets for analysis 106469*. [cited 2015 5 March]; Available from: www.merckmillipore.com/IE/en/product/Sodium-hydroxide,MDA_CHEM-106469.
229. Yuasa, M., et al., *Structural optimisation of gas diffusino electrodes loaded with LaMnO3 electrocatalysts.* J. Appl. Electrochem., 2010. **40**: p. 675-681.
230. Suntivich, J., et al., *Design principles for oxygen reduction acitivity on perovskite oxide catalysts for fuel cells and metal air batteries.* Nature Chemistry, 2011: p. 1-5.
231. Landi, H.P., *Catalytic membrane air electrodes for fuel cells and fuel cells containing same*. 1972: United States.
232. Qi, Z. and A. Kaufman, *Enhancement of PEM fuel cell performance by steaming or boiling the electrode.* J. Power Sources, 2002. **109**: p. 227-229.

233. Ergul, M.T., L. Turker, and I. Eroglu, *An investigation on the performance optimisaion of an alkaline fuel cell.* Int. J. Hydrogen Energy, 1997. **22**(10/11): p. 1039-1045.
234. Prasanna, M., et al., *Effects of platinum loading on performance of proton-exchange membrane fuel cells using surface-modified Nafion membranes.* J. Power Sources, 2006. **160**: p. 90-96.
235. Smith, D.F. and C. Brown, *Aging in chemically prepared divalent silver oxide electrodes for silver/zinc reserve batteries.* J. Power Sources, 2001. **96**: p. 121-127.
236. Tuck, C.D.S. and R.R. Bessette, *A high capacity aluminium-silver oxide battery*, in *Power Sources Symposium IEEE 35th International*. 1992. p. 53-55.
237. Gulzow, E., N. Wagner, and M. Schulze, *Preparation of gas diffusion electrodes with silver catalysts for alkaline fuel cells.* Fuel Cells, 2003. **3**(1-2): p. 67-72.
238. Janowitz, K., et al., *Method for producing gas diffusion electrodes*. 2007, Uhde GmbH
Gaskatel GmbH: United States.
239. Ruestschi, P., *Silver-zinc battery and method for obtaining a substantially flat voltage discharge curve*. 1963, The Electric Storage Battery Company: United States.
240. Cahan, B.D., et al., *The silve-silver oxide electrode.* J. Electrochem. Soc., 1960. **107**(9): p. 725-731.
241. Nava, J.L., et al., *Modelling of the concentration-time relationship based on global diffusion charge transfer parameters in a flow reactor with a 3D electrode.* Electrochim. Acta 2006. **51**: p. 4210-4217.